Nano-Engineered Surfaces Developed For Mercury Sensing

Ylias Mohammad Sabri
B.Eng. (Hons)

A thesis submitted in fulfillment of the requirements for the degree of Doctor of Philosophy

School of Applied Sciences
RMIT University
March 2010

Declaration

I certify that except where due acknowledgement has been made, the work is that of the author alone; the work has not been submitted previously, in whole or in part, to qualify for any other academic award; the content of the thesis is the result of work which has been carried out since the official commencement date of the approved research program; and, any editorial work, paid or unpaid, carried out by a third party is acknowledged.

Ylias M Sabri

Acknowledgments

I gratefully acknowledge the constant encouragement, support and guidance of my supervisors Prof. Suresh Bhargava, Adj. Prof. Dinesh Sood and Dr Samuel Ippolito throughout this project. Prof. Suresh Bhargava has been a wonderful example to learn from in all facets of life and without his continuous support this work would have been far from over. The knowledge, skill and dedication of Prof. Dinesh Sood as a research scientist is an inspiration and I could not have hoped for a better mentor. I cannot thank Dr. Samuel Ippolito enough for his input, encouragement, consideration and invaluable assistance that enabled me to experience a great deal of success throughout my PhD research program.

I thank the Commonwealth Government Postgraduate Award (APA) scholarship program as well as Australian Research Council – Linkage (ARC-L), BHP Billiton and ALCOA, Australia for providing me with financial support from the beginning of my PhD program. The Authors is grateful to AINSE for funding the use of SIMS instrument at ANSTO, Sydney as well as awarding travel grant to visit IMCS conference in USA.

My deepest sense of gratitude to Dr. Vipul Bansal, Dr. James Tardio and Dr. Mohammad Al kobaisi for their incredible support throughout the course of my PhD studies, their invaluable scientific discussions, criticism and positive approach to problems will be my guide for life.

Special thanks to Dr. Ian Harrison, Mr. Mark Mullet, Dr. Steven Grocott, Dr. Steven Rosenberg and Mr. Eric Boom for their invaluable help, direction and input. I can never forget the input, help and support from the industrial aspect of the project that I got from Mr. Mark Mullet.

I thank Dr. Kathryne Prince and Mr. Armand Anatacio for their scientific discussions during my visit to ANSTO and also Dr. Dennis Mather and Ms. Rhiannon Still for their hospitality.

I thank Dr. Anthony O'Mullane, Dr. Kourosh Kalantar Zadeh, Ms. Heather Wymer, Mr. Firew Beshah, Dr. Abdul-Cadir Hussein, Ms. Hailey Reynolds, Prof. Ashish Garg, Mr. Mohammad Omar, Dr. Pandiyan Murugaraj, Dr. Margaret Tate, Mr. Abdurahman Anod, Dr. Prashant Sawant, Dr. Deepak Dhawan, Dr. Dinesh Vinkatachalam, Mrs. Gopa Karr, Dr. Glen Matthews, Mr. Blake Plowman and Dr. Lisa Hodgson for providing a friendly and energetic atmosphere and being there when ever I needed their help.

My heartful thanks go to all my colleagues, technical, administrative and laboratory staff at RMIT University. Thanks specially to Mrs. Nadia Zakhartchouk, Mrs. Zahra Homan, Mr. Yuxun Cao, Mr Karl lang, Mr. Paul Jones, Mr. Howard Anderson, Mr. Peter Laming, Mrs. Chi-Ping Wu, Mrs. Diane Mileo, Mrs Ruth Cepriano-hall, Mr. Paul Morrison, Mr. Frank Antolasic, Mr. David Welsh, Mr. Bob Kealy and last but not least Mr. Phillip Francis, whom have all taken extra stressful steps at times to help me throughout my research project.

I would also like to take this opportunity to express my sincerest love to my parents, brothers, sisters, and extended family, their love, support and understanding and whom without their sacrifices and help I wouldn’t be who I am, and I am thankful for who I am.

Ylias M. Sabri

This thesis is dedicated to my family,

my parents, Zargoona and Mohammad Asif

and brothers and sisters, Khalid, Farshta, Idress, Harees, Arif, and Mezhgon

Abstract

Mercury is highly toxic but often neglected element that is readily emitted into the environment via a number of industrial processes. In Australia, coal-fired power plants and the alumina industry are the two largest emitters of mercury. In order to maintain the alumina industry's commitment to reduce the environmental impact of its processes and remain economically sustainable, innovative technologies are required that can monitor mercury concentrations within its processes. The aim of this research project was to develop robust quartz crystal microbalance (QCM) based sensors for measuring Hg vapour levels in challenging industrial environments, such as those found in the alumina industry (i.e. Hg concentrations of 1-40 mg/m^3 at 20-90°C).

In order to gain a deeper understanding of Hg vapour interactions with the surface of the QCM electrodes, parameters such as Hg sorption and desorption rates, sticking probability and Hg diffusion were studied in detail. When Hg diffusion in ultra-thin films of Au was studied, it was observed that Hg accumulation occurred at the interface between the Au sensitive and SiO_2 layers. These observations lead to the exploration of two different electrochemical methods for the direct formation of Hg selective and sensitive nanostructured Au films directly on QCM crystals. In the first case, galvanic replacement (GR) reactions were employed to form Ni-Au hybrid nanoclusters. This method resulted in Hg sensors with 93-100% recovery, excellent selectivity towards Hg in the presence of ammonia and humidity and ~27% higher sensitivity than the Au control QCM. The second case involved forming highly oriented and ornate Au nanostructures (nanospikes) with controlled crystallographic facets onto the QCM electrode by a single step electrodeposition method. These sensors were tested towards Hg vapour in the presence of ammonia and humidity at ~90°C for a 50 day period in a specially designed and developed 8-channel computer controlled gas calibration system. The testing sequences were made to simulate some of the conditions found in Hg-emitting industries. The nanospike QCM showed high selectivity, recovery and around 4.7 times higher sensitivity than the Au control QCM, with low degradation in response magnitude over the long testing period.

The high sensitivity of the nanospikes was found to be not only due to high surface area but also due to the increased number of surface defect sites created during the electrodeposition step. Due to its excellent performance, a nanospike QCM was then tested towards Hg in the presence of several volatile organic compounds (VOCs) that either had high affinity towards Au or was present in alumina effluent streams. The nanospikes based QCM was tested against VOCs such as acetone, dimethyl disulphide, methylethyl ketone, ethyl mercaptan, acetaldehyde as well as ammonia and humidity. The nanospike QCM was observed to maintain high selectivity and sensitivity towards Hg vapour when compared to Au control

QCM. The success of the data presented in this thesis has resulted in a PCT patent of the developed nanospikes and is due to undergo preliminary testing at industry partners' sites. If successful, the developed sensor will assist industries in complying with mercury emission targets and would be a significant technological breakthrough with potential for many other applications in pollution control.

Table of contents

List of figures

List of tables

Chapter I

Introduction and Literature Review

The motivation behind this research project, the objectives of the project and a critical review of the relevant literature are given in this chapter. Topics discussed and reviewed include the effects of mercury (Hg) on human health and the environment, major industrial sources of Hg emissions, and the currently available technologies for measuring these emissions. The rationale for the approach undertaken for developing a new device for measuring Hg from industrial sources - the development of a nano-engineered mass sensing device - is also discussed.

1.1 Introduction

This section addresses the research motivation, objectives, the author's achievements and thesis organisation.

1.1.1 Motivation

Mercury (Hg) is a toxic element that is emitted into the environment via natural processes such as volcanic eruptions, and a number of processes developed by man such as coal fired electricity generators. The adverse effects of mercury on human health and the environment have been well documented over the last four decades and have led many governments to introduce policies that limit industrial mercury emissions. Of the numerous industries that emit mercury the coal fired electricity generation industry is the largest source of man-made mercury emissions worldwide. Other significant contributors include the waste treatment industry (mostly via incineration based processes) and the alumina industry.[1,2] In Australia the alumina industry is the second largest emitter of mercury. The mercury emitted from the alumina industry is of particular concern as it is almost exclusively gaseous elemental mercury - a form of mercury that can travel long distances and is therefore difficult to control once it is deposited on the surface.[3]

Hg reduction targets set by industry and regulators have spurred attempts to develop real time monitoring technologies for evaluating the efficiency of mercury removal processes.[4] Hg vapour sensors can form part of an early warning system, notifying the appropriate authorities or provide the feedback signals to a process control system making them an integral part of monitoring and controlling Hg emissions.[5,6]

New technologies to reduce mercury are being trialed at various alumina refineries; for example, either upgrading existing or installing additional condensers. Furthermore, the trial of sulphide dosing of carbon to perform possible emission controls for oxalate kilns and calciners in the Bayer process is also being conducted.[7] In order to better understand mercury emission sources, migration, and environmental and societal impacts of Hg vapour, continuous emissions monitors (CEMs) located at strategic points within the Bayer process in alumina refineries are imperative. The sensor could be located at the digestion or evaporation stacks, or at the output of a Regenerable Thermal Oxidizer (RTO) to allow operators to determine where mercury is most likely to escape in the gas phase.[8,9]

Commercially available sensors are mostly based on cold vapour atomic absorption spectrometry (CV-AAS) technology. These systems are sensitive and are suited to detecting low Hg concentrations. However industries such as the alumina and many coal fired power plants are reported to emit high concentrations of Hg vapour in the milligrams rather than

micrograms per cubic meter range.[10-13] More so, in practice, spectrometry based sensors face many obstacles including undesired photochemical reactions from interferent gases and are not viable to be used as CEMs.[14-17] Additionally, the spectrometry techniques posses several challenges to long-term, low maintenance operation, the most significant of which include sample collection and flue gas conditioning. Thus the use of these types of instrumentation by the myriad of small- and medium-sized emitters is not believed to ever be economically feasible.[17,18]

The most common approach for measuring Hg emissions from anthropogenic point sources consist of sampling train methods.[19] These impinger-based wet chemistry methods rely on isokinetically sampling, filtering and diluting the flue gas sample followed by transportation through various liquid and/or solid sorbents and finally analysis of the collected gas using the common CV-AAS technique. To date, Hg monitoring approaches are costly, time consuming, labor intensive and are limited to time-average data collection.[20]

In light of the presented issues, the Australian research council (ARC) together with two large alumina industries, namely, BHP Billiton and Alcoa World Alumina has granted the current research project to RMIT University through an ARC-Linkage grant. It was postulated that through this project a cheap, robust, selective and sensitive Hg vapour sensor may be developed which is applicable to the alumina refineries and possibly other Hg emitting industries with highly concentrated effluent gases. The industry's imposed conditions were operating temperature range of 20 – 90℃, Hg vapour concentrations of 1 – 40 mg/m^3 and Hg in the presence of various levels of ammonia and humidity interferent gases. The current commercially available sensors utilized by such industries have been found to be susceptible to significant cross sensitivity issues in the presence of these interferent gases when they are used as CEMs thus producing the need to research and develop an online Hg vapour CEM.

1.1.2 Objectives

The aim of this research program is to investigate the interaction between mercury vapour in simulated alumina refinery effluent stream and gold surfaces, with a view to develop a sensor, based on enhanced Hg-Au interaction, for on-line monitoring of mercury vapour in these effluents. The prototype sensor developed from this research must be nano-engineered to achieve high selectivity and sensitivity towards Hg vapour in the presence of ammonia and humidity interferent gases. In order to develop such a sensor, this research program embraced the following main objectives,

- To design and construct a sensor test chamber and supporting calibration and mixing assembly of mercury, humidity and ammonia gases,

- Develop a firm understanding of the interaction between Au surfaces and Hg vapour by investigating the influence of the following parameters
    - Au film thickness
    - Au Surface morphologies
    - Hg diffusion in Au films
    - Differentiation of Hg adsorption from that of amalgamation/diffusion
    - Operating temperatures on sorption/desorption of Hg
- Investigate enhancements of this interaction via nano-scale surface modification (electrochemical techniques) of gold thin films to produce Hg selective surface layers on sensitive quartz crystal microbalance (QCM) electrodes.
- To investigate
    - Desorption behaviour of the adsorbed Hg and
    - The effect of the presence of ammonia and/or humidity interferent gases

  on the modified sensors under conditions similar to those encountered in alumina refineries.

Furthermore, the developed sensitive layers are characterized by Scanning Electron Microscopy (SEM), Energy Dispersive X-ray Spectroscopy (EDX), Atomic Force Microscopy (AFM), X-ray Photoelectron Spectroscopy (XPS), X-ray Diffraction Spectroscopy (XRD) and Secondary Ion Mass Spectrometry (SIMS) where relevant.

1.1.3 Outcomes and Author's Achievements

Based on a critical review of literature and initial experimental results, the author made an informed decision to investigate novel Au nanostructured QCMs employing intermediate Ti adhesion layers as sensitive and selective Hg vapour sensor. As a result, this PhD program has lead to many novel outcomes and contributions to the body of knowledge in the field of surface science and QCM based Hg vapour sensors. To the best of the author's knowledge, there have been no reports published in the public domain on nanostructured Au electrode QCMs for Hg sensing and the author was the first to propose them. Furthermore, there has been no reports of the sensor operating conditions (i.e. optimum operating temperature of ~90℃ based on the temperature profile experiments) which may be used for enhanced Hg sorption and desorption.

Additionally, to the best of the author's knowledge, this is the first time QCM sensors were used to differentiate between sorption and adsorption of Hg vapour on Au films. Significant contributions have also been made by the author investigating the sorption/desorption rate, Hg sticking probability and the Hg interaction with various metals and surface morphologies. Surface response curves were analysed to better understand Hg sorption on Au substrates

deposited on QCMs to function as the transducer electrodes and Hg selective layers. The Hg vapour sensors developed were found to be operating temperature and interferent gases resistant while being selective towards elemental Hg vapour over long-term testing periods.

The developed nanostructures grown directly on the QCM Au electrodes were nano-islands, nanospikes or nanoprisms. These nanostructures showed QCM response magnitude enhancements of more than 800% compared to the non-modified QCMs while coping with temperature fluctuations, interferent gas species and still maintaining high selectivity and sensitivity over long testing periods. To test the long-term performance of the sensors, unmodified and nanospikes modified QCMs were simultaneously exposed to different Hg concentrations at 89℃ for 70 days. Remarkably, the modified QCM sensor with nanospikes showed only 6.0 % degradation in their response magnitude in comparison to the unmodified sensor, which degraded by 20.8 % over the long testing period. The modified sensor was also found to be little effected by ammonia and humidity interferent gases being highly selective and capable of sensing Hg vapour in such harsh environments.

The Author successfully fulfilled the objective of developing highly sensitive and selective QCM based Hg vapour sensor which can potentially be used as an online Hg sensor in the harsh industrial gaseous effluent environments. The developed sensors offer great commercialization opportunities due to their highly selective surfaces, long term stability and suitability to sensing Hg in the concentration range applicable to many industrial situations. The results presented in this thesis have lead to the project having at least one year extension with the full financial support by the industrial partners to undergo industrial trial testing of the developed sensors. The project now involves sensor exposure to Hg with the presence of other interfering gases present in the Alumina refinery gaseous effluents.

The author's achievements include

- Co-author of one provisional patent regarding the nanospikes structures for Hg vapour sensing applications
- 7 journal article publications
- 3 refereed conference proceedings,
- 2 conference proceedings,
- 2 national and 2 international – Conference abstracts, posters or oral presentations.
- 2 AINSE grants totalling over A$30,000 awards for the author to use SIMS at ANSTO, Sydney, Australia,
- 1 AINSE student travel grant for the author to present SIMS data in international conference in Ohio, USA,

- Over 15 media citations of the research work in major scientific websites and news papers and radio interviews and
- The author received the Particle and Surface Science award in two consecutive years during his PhD in 2007 and 2008 at RMIT University,

A full list of publications by the author can be found in Appendix A.

1.1.4 Thesis Organisation

This thesis is structured to provide a logical progression of the research conducted by the author. It shows the advancement from investigating Hg-Au interactions to applying the new knowledge gained in the development of an elegant, robust and inexpensive on-line mercury vapour sensor. These QCM based Hg sensors are then shown to withstand the harsh industrial effluents environment duplicated in the laboratory over long testing periods. To communicate this investigation, this thesis contains eight chapters and seven appendices.

It commences with this chapter, in which the author's motivation for undertaking research in the field of Hg vapour sensing is addressed. It outlines the objectives and provides a summary of the contributions pertained as a direct result of this PhD research program. Furthermore, literature related to this work is discussed in an ordered manner that justifies the author's proposed systematic experiments throughout this dissertation.

Chapter 2 describes the sensor calibration system which was specially designed and built to operate at conditions imposed by the industry partners. These conditions included various operating temperatures and Hg vapour concentration in the presence of various levels of ammonia and humidity interferent gases. The operating conditions, surface characterization techniques and the Hg exposure test patterns conducted are also discussed.

In chapter 3, the influence of Hg sorption and desorption on several metal layers is presented. Optically polished and mechanically roughened quartz substrates with Ti, Ni, Ag or Au thin films were investigated. Mechanically rough quartz was used due to their increased surface area compared to the polished quartz substrates. Due to the roughened Au QCM's excellent performance towards Hg vapour, Au-rough sensor was further tested towards Hg with and without the presence of interferent gases (ammonia and humidity at various levels). This sensor was found to degrade significantly with time and the presence of interferent gases was found to have detrimental effects on the sensor response.

Chapter 4 investigates the influence of Hg sorption and desorption on Au thin films of various thickness 40 – 200 nm range. Au QCM electrode film thicknesses that produced most

enhanced sensor signal to noise ratio were selected for further studies. The optimum operating temperature for Hg vapour sensing was also determined to be approximately 90°C based on the high desorption/sorption ratio and the QCM response dynamic range between the Hg vapour concentrations. This temperature was found to be similar to that used by industries when capturing Hg vapour as reported in literature.

In chapter 5, the QCM with Au electrode thickness of 150 nm was further modified for the investigation of diffusion of Hg in Au substrates. The novel idea of using QCM with layered Ti/Au/SiO_2/Au electrodes to differentiate Hg sorption/amalgamation from that of adsorption is reported for the first time. Characterisation of the surfaces using SIMS depth profiling in order to observe the diffusion behaviour of Hg in the upper most ultra-thin (10 – 40 nm) Au layer is also presented. These studies provided an insight into how Hg vapour interacts with Au films. The potential of using either thin galvanically replaced Ni-Au hybrid or thick electrodeposited Au films as Hg selective surfaces directly on QCM electrodes was realised.

In chapter 6, the surfaces modified using a novel avenue of galvanic replacement reactions directly on the QCM electrodes is presented. This procedure produced highly active and rigidly adhered nanostructured Au-Ni hybrid surfaces (nano-islands) for the detection of high concentrations of Hg vapour with and without the presence of interferent gases (NH_3 and H_2O). As postulated, these sensors were found to have excellent regeneration properties. The author provides experimental data from SIMS depth profiling to show the reasons for the high Hg regeneration properties of these sensors.

Chapter 7 presents the surfaces modified using the simple, rapid, template-less and surfactant-free electrodeposition method. The Au nanospikes produced for the first time were tightly packed and highly [111] oriented while rigidly adhered directly to the 100 nm QCM Au electrodes. These sensors were exposed to Hg vapour with and without the presence of additional interferent gases under long term testing periods duplicating Alumina industrial effluent stream conditions. The data presented showed outstanding performance illustrating sensitive, selective, robust, long life and stable Hg vapour sensor under the tested conditions.

Finally chapter 8 summarizes the thesis, providing conclusions, and presents some possible future research directions.

1.2 Literature Review

Section 1.2 covers the literature related to this research program.

1.2.1 Hg and the Environment

This subsection reviews the ill effects mercury has on the environment and human health. It also covers some of the Hg sources and the emissions data worldwide.

1.2.1.1 Impacts of Hg

According to USEPA, more than 60,000 babies are born in the US alone each year with mercury related diseases because pregnant mothers either inhale volatile mercury compounds or eat mercury contaminated fish.[21,22] Mercury is poisonous and can damage the brain, kidneys and the central nervous system with fetuses being particularly vulnerable.[23,24]

Mercury occurs in three forms, namely, metallic or elemental, organic, and inorganic.[25] Organic mercury compounds include ethylmercury, methylmercury phenylmercury, thimerosal (Merthiolate), and merbromin (mercurochrome) and are the most dangerous forms of mercury. Some of the inorganic compounds include ammoniated mercury, mercuric chloride, mercuric oxide, mercuric sulphide, mercurous chloride, mercuric iodide and phenylmercuric salts.[26] The degree of health consequence caused by mercury depends on the form of exposure, time and its concentration. The primary route of elemental mercury exposure is through inhalation. Chronic exposure to elemental mercury vapour can cause lung damage, nausea, vomiting, diarrhea, increased blood pressure or heart rate, skin rashes, eye irritation, emotional instability, tremors, inflammation of the gums, gingivitis and anorexia among other effects.[27]

A Blood mercury level of 5.8 µg/L or more is know to result in loss of intelligence quotient (IQ) as well as other ill effects in humans. The diminished economic productivity that results from the loss of IQ in children alone due to Hg exposure is estimated to be over 15.8 and 43.8 billion dollars in the United States and world wide, respectively (Costs are in year 2000 US$).[28]

1.2.1.2 Anthropogenic Hg Emissions

Environmental contamination of Hg vapour resulted from human activities such as mining, smelting, burning fossil fuels, waste incineration, nuclear fuel and weapons production and disposal just to name a few.[29] Due to the ill effects of mercury on the environment and human health, the US EPA added metallic mercury among the toxic trace metal emissions in its 1990 Clean Air Act Amendments.[30,31] Although Hg emissions have decreased since 1990 levels,[32-36] in 1995 an estimated 5500 metric tons of mercury was added into the earth's

atmosphere[37] of which 70% was anthropogenic mercury resulting from industrial activities.[28] The 1995 estimates show Asia, America and Australia (Australia and Oceania) emitted 1074.3, 272.7 and 105.5 tonnes of mercury from major anthropogenic sources that year respectively.[38] Over 300 tons of anthropogenic mercury is added to the atmosphere each year in Europe alone as a consequence of industrial activity.[39] More recent reports show an estimated ~2400 tons of mercury per year is currently released to the atmosphere worldwide as a result of human activity.[40] Although more stringent rules are encouraging reductions in mercury emissions in some countries like the United States,[24] greater emission rates are observed in other countries like China.[37] For example the human activity based mercury emission in China is estimated to be 536 ± 236, 625 ± 284 and 765 ± 337 tonnes per year for 1999, 2002 and 2004 base years respectiviely.[37]

Australia, for example, is a leading producer of mining commodities which form a large share of its exports. The National Pollutant Inventory report indicated the Australian Alumina industry alone was responsible for about 6.6% (1.6 tonnes) of Australia's total mercury vapour emissions in the year span 2007-2008.[9] Although the Hg emission rate was much lower than the 2006-2007 estimates of approximately 2.9 tonnes of mercury vapour emission by the same industry.[41] The trace quantities of Hg that have been found in emissions from various sources in the Alumina refineries include, in particular: oxalate kiln, digestion, calciners, and other minor sources such as liquor burner and boilers.[8]

Depending on the origin of the bauxite ore as a raw material for alumina production, mercury contents of 50 mg,[42] 431 mg[43] and up to 20 – 1500 mg[13] per tonne of bauxite have been reported. Mercury emitted from the Alumina refineries (based on the Bayer process) originates mainly from the sulphide minerals such as pyrite within the bauxite.[44] Almost all the mercury emitted from the Bayer refineries is elemental mercury[13] due to the digestion process being chemically reducing.[44] During the refinery process much effort is made to capture the mercury before it is emitted into the environment, however measurable quantities of Hg are still emitted for every metric tonne of alumina produced.

The large mercury emissions around the world are due to Hg emitting industries lacking appropriate retention devices.[45] The significant reduction of released mercury with time is partly due to the use of alternative materials being used in commercial products where traditionally they contained mercury.[46] A well known example is the environmental regulations banning mercury in primary batteries as corrosion inhibitor for zinc. These type of restrictions have also made the recycling of the batteries with replaced plastic insulation easier while giving them more than twice the capacity of the same size mercury Batteries.[47]

In spite of all these efforts, the continued emission of anthropogenic mercury threatens millions of people all over the world.

Mercury has an estimated 1 – 2 years[48] and up to 5.7 years[49] of residence time in the atmosphere, which is the main pathway for its global distribution. Mercury released from anthropogenic sources enters waterways where microbes convert them into its most toxic form, methylmercury which accumulates in fish.[21,22,50,51] Once formed, methylmercury bioaccumulates up the food chain from small fish being eaten by bigger fish which are then eaten by animals and humans.[52,53] The list of adverse effects of Hg on the environment and human health is ongoing yet beyond the scope of this work. A more in depth coverage of the topic is available elsewhere.[54-58]

1.2.2 Metal Surfaces as Collection Media for Mercury

The adsorption and desorption of Hg on noble metal thin films is the basis of many current commercially available Hg vapour sensors.[59] High capacity Hg vapour sorbents such as Ag, Au, Pd, Pt, Al, Zn, Se, MnO_2, $PdCl_2$, hopcalite, and even fine dust collected by a hot gas filter have been used to collect and/or detect Hg vapour.[60-67] Among the range of these Hg sorbent materials, metallic Ag and Au are attractive collectors of Hg from ambient air. They readily adsorb and retain Hg at low temperatures but can be made to release it quantitatively upon heating.[68]

1.2.3 Hg interaction with Gold and Silver Surfaces

Because of the ready wetting of gold by mercury,[69] there has been a mistaken belief by many scientists that gold has relatively high solubility in mercury at room temperature.[70] In fact, Henry reported, in as early as 1855, that the solubility of gold in mercury at room temperature is ~0.14 at%. Others have also reported similar values.[71-77] However, the solubility of gold in mercury does increase significantly with temperature having a value of 0.25, 0.68 and 3 at% at 50, 100 and 200°C respectively.[72-74]

The ability for gold, as one of the most frequently used noble metals, to absorb and amalgamate mercury is well documented.[61,78-80] Gold is commonly used to adsorb Hg before it is released by heating and measured by spectroscopic techniques.[81]

Numerous surface science techniques including microscopy and spectroscopy have been used in the past to study the adsorption of Hg on Au and Ag surfaces.[78,82-86] Despite the numerous studies, the process of Hg-Au and Hg-Ag is still far from fully being understood leading to limitations of using the noble metals as Hg collectors to determine Hg concentrations in gaseous effluents.[87] The fundamental studies to understand Hg/Au

amalgamation process are ongoing, in order to improve the vast number of commercially available Hg vapour sensors based on such process.[88,89]

To date, there are only limited studies available concerning the diffusion of Hg into Au substrates. A comprehensive list of Hg diffusion coefficients in bulk (single crystal), grain boundary (dependent on structure) and polycrystalline gold surfaces from the available literature has been compiled by George[90]. However the diffusion coefficient for Hg in Au system has also been reported elsewhere[91] to be 8-10 orders of magnitude higher than those listed by George. Such contradictions highlight a lack of understanding of Hg diffusion in Au thus resulting in numerous bodies of work to be undertaken in understanding Hg diffusion in Au films.[69,81,89,92]

It has been shown by Battistoni et al.[81] that low Hg vapour concentration is adsorbed by the first 5 – 6nm sub-layer of a thin gold film after only 30 minutes exposure to Hg at μg/m^3 range concentrations. This makes gold difficult to regenerate in a reproducible manner due to the swift diffusion of Hg into gold thin films.[67,89] Furthermore it has also been shown that the film morphology is critical for an optimum thin film sensor response to Hg, and that the rougher, more porous films promote diffusion of the mercury into the films' grain boundaries and into the gold bulk.[93] Although Au and silver are some of the costly metals with low regeneration ability following Hg exposure, they have been widely used in Hg vapour sensor designs due to the ability of the metals to withstand heat cycling at high temperatures, which is used to desorb the amalgamated Hg.[18,84] A full review of the use of gold and silver as collection media for elemental Hg may be found elsewhere.[68]

Hg adsorption to gold and silver surfaces occurs preferentially at grain boundaries forming small islands on the surface.[82] Prior to island formation, the Hg is believed to adsorb on the surfaces and be mobile until the atom either desorbs or is adsorbed at an edge site/defect on the surface, as a single Hg atom does not have the energy required to create an adsorption site.[93] Levlin et al.[78] proposed a place exchange process to help explain the formation of the islands on the Au and Ag films. In this model, some of the adsorbed Hg atoms replace the Au or Ag atoms on outermost surface layer. The replaced Au or Ag atoms are believed to shift and nucleate at the top of the surface creating islands.

Mercury is similar to gold in size and charge density, yet is different in valency and band structure. When Hg adsorbs on Au surface, the Au film resistance increases due to the electrical characteristics of thin Au films involve electronic scattering at grain boundaries and other surface defects as well as diffuse scattering of the conduction electrons at the surface-

bulk interface.[94] Such change in electrical characteristics is used to develop the conductimeteric Hg vapour sensors[61] mentioned in section 1.2.6.4.

Exposure of Au[78,85,86] and Ag[78,95] films to Hg vapour in μg/m^3 concentration range at only a few minutes under vacuum has been shown to result in adsorption of the latter.[87] Between 1 to 10 minutes adsorption is reported to be rapid but slowing between 15 and 20 minutes at 15 ppm Hg vapour exposure.[84] Longer exposure times are found to induce diffusion of Hg into the Au film resulting in the available adsorption site on the surface for additional Hg sorption.[83,84] Longer exposure periods or higher Hg vapour concentrations have also been observed to result in the surfaces undergoing irreversible changes due to the formation of Au-Hg or Ag-Hg alloy/amalgams.[96] Usually the film disrupts and amalgam island of various shapes and sizes are formed.[78,81,86,87] The amalgam size and shape are reported to be unstable and changes with time due to their mobility, usually on the gold surface deposited on SiO_2 substrates.[86,87] This may be due to desorption processes where morphological changes on Au surfaces have been observed upon desorption of Hg[84] using the necessary high temperatures ranging from 150 to 800°C.[18,67,97]

It has been well established[85] that molecular hydrogen, air and argon does not influence surface processes in the reaction of amalgam formation, but they solely influence the Hg diffusion in the gas phase. The rate of amalgamation was found to be the lowest in the air atmosphere. Hence the presence of various gases with Hg vapour is expected to effect the amalgam formation kinetics on the film surfaces.[85,98] This finding is a great step forward from a sensing point of view where interferent gases are also generally present in the analyte gas when sensing Hg vapour in the alumina industries.

The morphology of the Au has been repeatedly reported to greatly affect the degree of Hg sorption/amalgamation.[83,93] Similar findings were found, as part of the work in this thesis, on the effect of Ag morphology upon the degree of Hg sorption/amalgamation.[89] The rougher, more porous films have been shown to promote diffusion of the mercury into the films' grain boundaries with higher Hg sorption capacity, which is also thought to be thickness dependent.[93,99,100] The theoretical value of the mass of Hg required to make a monolayer on 1 cm^2 Au film is estimated to be 0.36 μg however the study of Levlin et. al.[78] did not find any evidence of complete monolayer formation of Hg even after extensive Hg exposures probably due to rapid diffusion of Hg into Au films.[93]

Another parameter that defines the affinity of an absorbent with that of an analyte is the sticking probability, *S,* which is defined as the ratio of the rate of adsorption to the rate at which atoms from the vapour phase strike a surface.[89] The *S* for Hg vapour on gold and

silver films is well known to be close to unity and decrease rapidly when the coverage exceeds ~0.5 to 1 monolayer at room temperature.[89,101,102] The *S* value is highly dependent on the gas partial pressure and operating temperature as well as the substrate on which adsorption occurs.[89] Therefore, the affinity of the Au-Hg system may be optimised by operating in the conditions with high *S* values.

Some operating conditions to achieve optimum Au affinity for Hg have been investigated in the past.[103] Often, In typical field sampling of trace amounts of Hg, an operating temperature of around 90℃ is used. Surprisingly, at this operating temperature no detectable gold surface change was observed upon exposure to low Hg vapour concentrations (30 μg/m^3) otherwise observed at higher Hg concentrations (130 μg/m^3) and/or lower operating temperatures.[78] Furthermore, a collection efficiency of 99% has been observed at an operating temperature of 89℃.[103,104] It was suggested that at higher temperatures Hg adsorbed only partly at step edges. Short collection time, higher operating temperatures and lower air flow rates (<350sccm) are suggested to be the better conditions for collecting or detecting mercury. These conditions are thought to optimise the Hg collection capacity of Au.

1.2.4 Non-Metal to Metal Transition of Hg

The number of atoms in close contact with another atom has a profound effect on the nature of the chemical bond between the atoms.[105] Mercury having a completely filled s-and d-shell in its atomic state would have no preference for one type of bond or another and so there will be a competition between a van der Waals (non-metallic) modification and a metallic modification.[106] Van der Waals modification is the weak attraction force that occurs between metal atoms in small clusters resulting in non-metallic properties.[107] Semi-empirical models have shown that van der Waals-modification becomes more and more favourable when going to a smaller number of atoms especially for mercury where a linear chain or even a monolayer is said to be predominantly non-metallic.[105,108] Furthermore, it has been predicted that by having a low surface energy substrate or elevated pressure or both, monolayers of mercury being non-metallic is highly possible.[108] Mercury being divalent may also behave as a semimetallic as in the solid the Fermi surface intersects the boundary of the first Brillouin zone. The Brillouin zone is the volume of the surface taken at the same distance from one element of the lattice and its neighbours. The metal – non-metal transition in mercury have been observed experimentally at elevated temperatures and pressures[109-112] and in conductivity experiments.[113] The mechanism of van der Waals modification to metallic modification is well known. Briefly, by reducing the interatomic distance of the separated divalent atoms in space, the atomic levels broaden in to band. The gaining of the energy is accomplished by lowering the average energy of the highest occupied band. This lowering of energy is caused by these highest occupied bands interacting with the lowest unoccupied

bands and so van der Waals-type bonding is achieved. By the atoms approaching in close proximity to each other, the valence s-band starts to overlap with the unoccupied p-band making the system metallic.[105] On this respect mercury bonding varies from primary van der Waals in the dimer to covalent in small clusters to metallic in the larger clusters of mercury.[114-116] Miedema and Dorleijn,[108] in 1981, proposed the number 22 being the critical number of atoms per cluster before mercury can show any signs of metallic properties. They have also suggested that a particle containing 36 atoms of Hg may be metallic with chemical properties comparable to that of the bulk with the top layer having a van der Waals modification. Bloch and Rice showed from their reflectivity and ellipsometric data that the surface layer of liquid mercury had conduction properties that deviated very strongly from those of the bulk metal yet again indicating a metal to non-metal transition behaviour.[117]

In regards to mercury binding with another metal, Hg binding is found to be stronger on the (001) surface as compared to the (111) surface. In addition, the order of the metal surface according to increasing reactivity towards Hg is suggested to be Ag<Au<Cu<Ni<Pt<Pd.[116] Furthermore, the process of amalgamation is said to follow the wetting process.[71,77] For surface wetting to occur, the mercury atom concentration needs to be high enough for it to have bulk (i.e. liquid metal) properties.[118] Decreasing Hg collection capacity with increasing operating temperature is therefore expected as calculations performed in past studies have shown that the general trend for surface tension is that it decreases with the increase of temperature, reaching zero at the critical temperature.[119-123] As discussed, Increased operating temperatures are also known to increase solubility of Hg in Au (increase Au-Hg affinity), Hg vapour pressure (tendency of Hg to stay in gas phase rather than adsorb on a surface) and preference of non-metallic modification.

1.2.5 Current Methods to Measure Hg

Two approaches to measuring mercury are currently considered acceptable. One is direct instrument method. The other is with sorbent traps.[19] These traps capture the mercury for a period of up to two weeks and is then analysed in a laboratory (ideally using spectroscopic techniques) to determine the mass of mercury captured during the period.

1.2.5.1 Spectroscopic based Hg Sensors

There exist different methods to measure Hg levels, typically employing different types of spectroscopy. Spectroscopy is the process by which an electrical current of light is introduced to a gaseous mixture containing mercury. The light structure that is re-emitted from the particles is then analysed to determine what chemical compounds are present. The mercury signature can then be calculated, and the strength of the signature indicates the concentration of Hg in the sample.

Various spectroscopic methods for the analysis of mercury exists and these include: photometry, fluorescence, and mass-spectroscopy.[124,125] These include atomic absorption spectroscopy (AAS), atomic fluorescence spectrometry (AFS), UV differential optical absorption spectroscopy (DOAS), inductively coupled plasma atomic emission spectrometry (ICP-AES) and inductively coupled plasma mass spectrometry (ICP-MS). A review of these methods have been published elsewhere.[126] The most commonly used methods for Hg vapour sensing are the AAS and AFS. The most convenient and widely used method of sample introduction of mercury is the cold vapour (CV) technique. Due to high vapour pressure of Hg (~14 mg/m^3 at 20°C) the cold vapour technique allows direct determination without an atomizer unit.[126] CV-AFS has superior sensitivity and detection limits than CV-AAS. However, due to the requirements of most industrial applications and due to the quenching of the fluorescence signal by nitrogen and oxygen being more frequent in the CV-AFS systems, the most widely used method for Hg vapour sensing applications is often the CV-AAS systems.[127]

The underlying mechanism of spectroscopic methods (i.e. CV-AAS) for measuring mercury is based on the absorption and emission of 253.7nm wavelength band by Hg atoms.[128-131] Although a number of commercially available mercury sensors (table 1.1) are based on this technique due to its superiority over other spectroscopy methods, there are several limitations associated with them some of which are discussed below.

Limitations

The limitation of using the CV-AAS based Hg vapour sensors as CEMs leaves little choice for (i.e. Alumina) industries but to contract specialists to capture and monitor Hg vapour. This is done at extremely high costs per sample basis in order to comply with the enforced environmental regulations.

Some of the major obstacles with CV-AAS measurements include: the occurrence of undesired photochemical reactions, collisional quenching and spurious scattered incident light, loss or oxidation of Hg via adsorption or catalysis on solid surfaces, and small temperature fluctuations (which cause small changes in the output intensity of the UV source, thus leading to errors).[132,133] These limitations are preventing the use of the CV-AAS based instruments currently available commercially, for continuously monitoring Hg in the alumina industries in addition to their lack of reliability, complexity, cost and precision issues that have not yet been established.[6,20] When used as CEMs, loss of mercury from dilute solutions can be a significant problem[16] specially in the alumina industries where the 1000 times higher Hg concentrations than most other industries are being emitted. These Hg

levels would require higher dilution factors in order to use the available systems for monitoring and process control applications.

Other gases present in industrial steams, such as SO_2, NO_2 and many carbonyl containing volatile organic compounds (VOCs) like benzene, toluene and acetone also absorb light at the same UV wavelength (253.7 nm) as mercury and thus act as interferents.[15,131,134,135] To overcome the effect of interferent gases, the utilization of a noble metal (i.e. gold or silver) trap to enrich the Hg sample is used in CV-AAS and many other spectrometry based systems.[68,126] Mercury vapour is amalgamated with the gold trap and later released via heating for detection. This allows ventilation of interfering substances from the gas stream before measurement. However, gold is not solely selective towards mercury; other contaminants present in industrial streams (such as thiols, sulphides, alcohols, ammonia and humidity) have also been known to readily adsorb on to gold surfaces.[136-144] Therefore the presence of such contaminants and lack of the right conditions to stop sorption of such chemicals would result in cross sensitivity issues.

During the high temperature heating/release cycle, there is also the possibility of distillation of the gold trap. This is a major limitation of the CV-AAS systems since it would lead to condensation of small amounts of Au on the cooler parts of the system, introducing unmonitored collection sites for Hg and a consequent negative systematic error.[68]

Conventionally, gold traps used for Hg collection consist of granulated sand or quartz coated with gold. The drawback of these systems are the difficulty to prepare them in a reproducible way.[104] Moreover, thermodynamic and hydrodynamic problems may occur while releasing Hg from the gold trap for analysis.[145] The use of Au or Ag traps in the alumina industry is an example where the Hg collector would saturate abruptly due to the gas streams containing high Hg vapour concentrations. This is due to such metals ability to capture only a limited amount of Hg vapour as they are constricted by their Hg collection capacity, which is defined as the amount of mercury collected before breakthrough (before any mercury passes the collector) occurs.[146] The occurrence of a breakthrough during sensing would result in severe underestimation of the Hg vapour concentrations in the gaseous effluents. The collection capacity is dependent on sampling flow rate, duration, aging time of the collector, gaseous effluent nature (i.e. other interferent gases being present), operating pressure and temperature. Experimental values for Hg collection capacity of Au vary significantly from 0.0117 to 0.7 $\mu g/cm^2$ while for silver it is reported to be ~360 $\mu g/cm^2$ decreasing significantly with aging.[89] These values equate to 1 – 1.5 monolayers of mercury.[89] Therefore, in order to overcome the memory effects (due to diffusion of Hg into the collector material) and

saturation issues (due to high concentrations of Hg), a high surface area to volume ratio collector is required.[67]

Another disadvantage of gold traps is the high pressure drop caused by the dense packing of these adsorbents making it impossible to use high flow rates during sampling procedure. To overcome this limitation, denuder techniques have been used where reactive wall coatings are used to trap mercury. However, this procedure requires laminar flow for optimum adsorption and it is also well known that the extent of Hg adsorbed on the surface is greatly dependent on the gas flow rate.[104,147]

1.2.5.2 Mercury Capture

Currently, the most common approach to measure Hg vapour from anthropogenic point sources are the wet-chemistry procedures involving EPA sampling train methods followed by analysis of the sample using one of the spectroscopic methods.[19] Some of the accepted and commonly used methods include EPA method 29, EPA method 101A, the tris buffer method, the Research Triangle Institute method and the Ontario Hydro method.[19,20,31] All these methods are impinger-based and rely on the collection of the flue gas through a variety of liquid and solid sorbents before quantification analysis.

Limitations

Although these methods have produced good results in the past with high level sensitivities (~0.5 $\mu g/m^3$), the sampling methods generally require extensive and complex analyte recovery and preparation steps due to the strongly oxidizing and acidic reagents that may introduce contamination or result in loss of mercury. EPA method 29 is commonly used by industries for the determination of Hg concentrations. This method involves having 2 impingers in series (out of the total 7) both containing 10% (v/v) H_2SO_4 with 4% (w/v) $KMnO_4$ to capture elemental mercury vapour before analyzing the solution.[20] Some of the practical limitations originate from the problems and difficulties of using complex sample trains that are composed of relatively large amounts of glassware and tubing in the field. These methods also require high level of quality assurance and quality control with well trained personnel. The methods do not provide real-time data and often in practice has a 2-week or more turnaround time for results,[19] making mercury emission variations difficult to predict.[6] Moreover, for effective measurements, the sample gas either needs to be transported to a conditioning system or conditioned at the sampling point and transported to the instrument.[20]

Other methods such as the flue gas mercury sorbent speciation (FMSS) or the Quick SEM™ (QSEM) methods use dry sorbent-based techniques like adsorption, amalgamation, diffusion and ion exchange processes to capture mercury. However, these methods only provide a time-average mercury concentration and fail to provide the real-time data often required by

research and compliance. Similarly, the dry sorbents are required to be sent to a laboratory for analysis. These limitations makes the dry sorbent methods inadequate for use in mercury emissions control loop.[20]

1.2.5.3 Commercial Mercury Sensor Systems

A number of commercially available Hg vapour sensors that are sometimes used as CEMs or in industrial laboratories to analyse captured Hg, are listed in Table 1.1. For sensor specifications such as sensitivity and detection limit as well as other limitations, the reader is referred to the sensors' vendors and respective reference listed in Table 1.1.

The CV-AAS based sensors are sometimes used as CEMs, however Hg analysis becomes very costly on per sample bases due to the purchase, installation and maintenance required thus limiting their sustainability for in-situ monitoring.[20]

Considerable effort is being put into employing Au films to monitor Hg upon changes in resistivity,[93,148-150] reflectivity[83,151-153] and surface plasmon resonance (SPR).[154] Research in development in the field of acoustic based chemical sensors are also leading to these devices potentially replacing the traditional analytical chemical instrumentations.[155] Recently, there has been a number of interests in developing microsensor based Hg vapour monitors.[156]

Table 1.1: Current commercially available Hg vapour sensors.

Vendor	Product	Analysis Method	Detection Range (μg/m^3)	Challenges to be overcome (See key for abbreviation)
Durag[4,20]	HM-1400 TR	CVAAS	0.5 – 500	LDR, HW, LD
EcoChem Analytics[16,20]	Hg-MK II	CVAAS	0 – 50	LDR, OL – low resolution
Envimetrics[20]	Argus-Hg 1000	CVAES	0.03	LDR, OL – Not made for continuous testing
Nippon Instruments Corporation[20]	DM-6	CVAAS	0.1 – 1000	LDR, HW, LD, RRM
Nippon Instruments Corporation[20]	DM-6B-MS1A	CVAAS	0.1 – 1000	LDR, HW, LD
Nippon Instruments Corporation[4]	Mercury/DM-5	CVAAS	5 – 25	LDR
Nippon Instruments Corporation	EM-5	CVAAS	0.001 – 2000	RRM, OL – Not made for continuous testing
Nippon Instruments Corporation	WA-4 and AMG-1	CVAAS	0.00001 – 1	LDR
Nippon Instruments Corporation	EMP-1A and EMP-1B	CVAAS	1 – 5000	OL – Not made for continuous monitoring and no mention of interferent gases
Ohio Lumex[4,20,135,157,158]	RA-915+	CVAAS	0.002 – 0.5	LDR, OL – Not made for continuous testing
Ohio Lumex[159,160]	RA-915	CVAAS	0 – 200	LDR, RRM, OL – Not made for continuous testing
Opsis[4]	AR602 / Z/600	DOAS*	0 – 150	LDR
Opsis AB[20]	HG200	CVAAS	0.5 – 1000	LDR, RRM,
PS Analytical[4,20]	Sir Galahad	CVAFS	0.001 – 2500	LDR, RRM, OL – Not made for continuous testing
Semtech Metallurgy AB[4,20]	HG 2010	CVAAS	0.3 – 160	LDR,
Sick UPA GmbH[4,20]	MERCEM	CVAAS	0 – 45	LDR, LD, HW, LOTR
ST2 Technologies[20]	SM-3	CVAAS	1 – 500	LDR, LOTR, LD, HW, STOIG

Tekran, Inc.[20]	3300	CVAFS	1 – 10	LDR, STOIG, LD, HW
Tekran, Inc.[4]	2537A	CVAFS	0.0001 – 10	LDR, HW, LD, OL – Large sample volumes
Seefelder Messtechnik[4]	Hg-Mat 2	CVAAS	0 – 75	LDR, LOTR, OL – requires nitrogen at high flow rates of 6 L/min
Arizona Instrument[161-164]	Jerome 431-X and Jerome 431-XE	RGFS**	1 – 990	LDR, LOTR, ABH
Arizona Instrument[163]	Jerome J405	RGFS**	0.5 – 999	LDR, LOTR, ABH
Arizona Instrument[163]	Jerome 471	CVAAS	0.03 – 250	LDR
Mercury Instruments Corporation USA[165-168]	Mercury Tracker 3000 IP and VM 3000	CVAAS	0.1 – 2000	RRM, OL – works at room temperature and based gold traps
Institute of Physics - Lithuania[169,170]	GARDIS 1A	CVAAS	0 – 0.0001	LDR, RRM, ABH
***DOAS = UV Differential Optical Absorption Spectroscopy **RGFS =** Resistive Gold Film Sensor				

LOTR = Low operating temperature range

LD = large Dimension

LDR = Low Detection Range

OL = Other Limitations

RRM = Requires regular maintenance

HW = Heavy Weight

ABH = Affected by humidity

STOIG = Sensitive to other interferent gases

1.2.6 Acoustic Based Sensors

This section introduces acoustic based sensors and provides justification of using QCM over the other available acoustic based sensors. Furthermore, a review of the literature is undertaken where acoustic based Hg vapour sensor developments have been reported.

1.2.6.1 Types of Acoustic Wave Gas Sensors

Acoustic wave gas sensors are based on high frequency mechanical vibrations. This makes them highly sensitive towards surface perturbations and exhibit good linearity with low hysteresis and so are ideal for chemical and physical sensing.[171,172] They are typically small, relatively inexpensive, and offer a simple means of analyte monitoring, with several advantages over other solid-state sensors. These include: well established fabrication processes, chemical inertness of the substrate materials and high structural rigidity.

The microelectronics industry has developed numerous piezoelectric transducer platforms, which in turn has widely encouraged the development and improvement of various acoustic based chemical sensors.[171,173] These devices have also been used for the monitoring of mass uptake,[174,175] density,[176] viscosity,[66] elasticity,[177] roughness,[178] conductivity and temperature changes[179,180] or a combination of these parameters.[181]

Acoustic wave devices come in a number of configurations, each with their own distinct acoustic and electrical characteristics. Two different groups of acoustic wave devices that are most commonly employed for gas sensing are Bulk Acoustic Wave (BAW) devices, which concern acoustic wave propagation through the bulk of the structure and as Surface Acoustic Wave (SAW) devices, utilizing acoustic waves confined to the surface of the piezoelectric material. These acoustic wave devices operate in a narrow frequency range between 10^6 – 10^9 Hz.[182] The BAW category of devices includes the QCM and Thin Film Resonators (TFRs), the latter encapsulating Thin Film Bulk Acoustic Resonator (TFBAR) and Solidly Mounted Resonator (SMR) structures. Schematic diagrams of all above mentioned devices these can be observed in Figure 1.1.

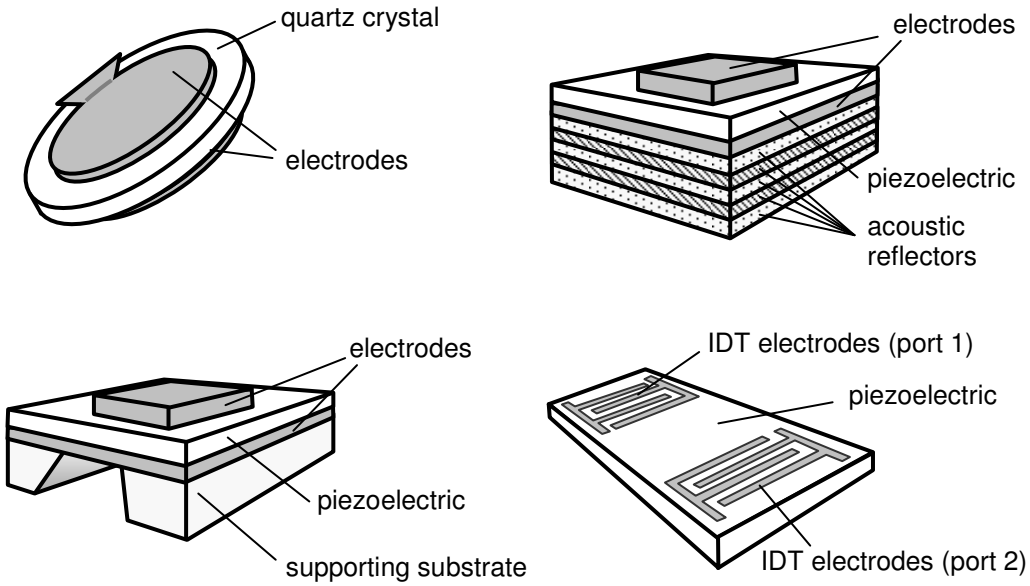

Figure 1.1: *Top left*: QCM, *bottom left*: TFBAR, *top right*: SMR, and *bottom right*: two port delay line SAW (images taken from reference 171).

Unlike the electrode structures found on QCM, TFBAR and SMR structures, SAW devices use patterned thin film interdigital transducers (IDTs) to generate and detect the acoustic waves. Both QCM and TFRs are single port devices, whereas SAW devices can be configured as two-port delay line or as one-port resonator structures. All of these devices are mass sensitive. It should be noted that there are other members of the acoustic wave device family, such as thin film Flexural-Plate-Wave (FPW) delay lines and Shear Horizontal Acoustic Plate Mode (SH-APM) devices however they are not commonly used for gas or vapour sensing applications.[171]

Some typical properties of commonly utilized acoustic wave based sensors are listed in Table 1.2 below.

Table 1.2: Typical properties of commonly utilized acoustic wave based sensors.

	QCM	TFR	SAW
Operating frequency range	5 –30MHz	500MHz – 20GHz	40MHz – 1GHz
Sensitivity towards mass	Yes	Yes	Yes
Sensitivity towards conductivity	No	No	Yes
Fractional frequency change to gas	~0.01%	~0.1%	~0.1%
Quality factor (approx.)	up to 10^5	up to 10^3	up to 10^4

In order to sense a specific gas or vapour, a sensitive layer is generally employed. The interactions between an analyte gas and the active surface of the device perturb the phase velocity of the propagating wave in a measurable way that can be correlated to the analyte concentration.[171] The most commonly measured properties of acoustic modes are resonant frequency, phase shift or attenuation.[183,184] Potential sensor response can also be achieved due to the attributions of other factors which affect or perturb the acoustic wave velocity. These factors have been listed in Table 1.3 below.

Table 1.3: Physical, electrical and thermal parameters to which acoustic waves are sensitive towards.

• T	–	temperature	• ε	–	permittivity
• E	–	Electric field	• σ	–	conductivity (electrical)
• c	–	stiffness	• η	–	viscosity
• ρ	–	Density	• p	–	pressure
• μ	–	shear elastic modulus	• m	–	mass

Variations in any of these parameters alter the mechanical and/or electrical boundary conditions producing a measurable shift in the propagating acoustic wave phase velocity, v_0. Equation 1.1 below illustrates the change in acoustic phase velocity, Δv, as a result of external perturbations, assuming that the perturbations are small and linearly combined:

$$\frac{\Delta v}{v_0} \cong \frac{1}{v_0}\left(\frac{\delta v}{\delta T}\Delta T + \frac{\delta v}{\delta \varepsilon}\Delta \varepsilon + \frac{\delta v}{\delta E}\Delta E + \frac{\delta v}{\delta \sigma}\Delta \sigma + \frac{\delta v}{\delta m}\Delta m + \frac{\delta v}{\delta \rho}\Delta \rho + \ldots\right) \qquad \text{Equation 1.1}$$

In addition, the temperature dependence of each parameter, as well as the overall temperature coefficient of the device structure must also be considered. This is because the sensor response for many gas phase sensing applications is strongly dependent on operating temperature.[185,186] In the case of gas and vapour sensors, parameters such as humidity level will typically interfere with the desired response, and therefore care must be taken to limit their effect.

1.2.6.2 Quartz Crystal Microbalance (QCM)

QCMs consist of a thin AT-cut quartz disc with electrodes deposited on both quartz surfaces. Both sides of the device are patterned with metallic pads that form the electrodes. The electrodes are used to excite and measure the acoustic bulk waves. The addition of gas sensitive layer on top of one or both of the electrode pads, as seen in Figure 1.2, is used to make the device sensitive to a target gas or vapour species interacting with the surface. The chemical or physical interaction of the analyte with the sensitive layer causes an additional

mass deposition on the quartz surface and as a result a dramatic change in resonant conditions occurs. The resulting frequency shift can be detected easily and precisely, e.g. in an oscillator circuit with the resonator as frequency determining part[173] or by using a phase lock loop system.[187,188] Additionally the frequency characteristics can be observed by using a network analyser.[189]

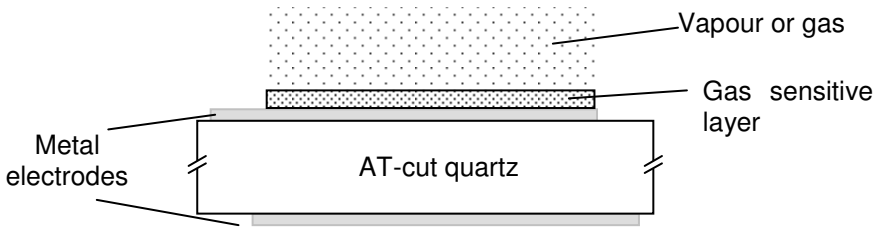

(a) Cross-section

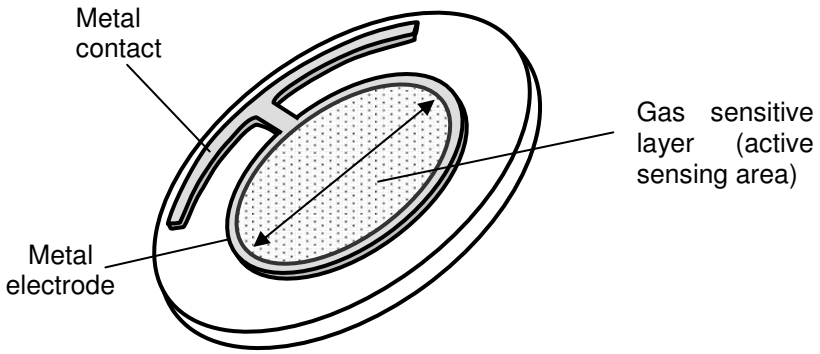

(b) Graphical projection

Figure 1.2: (a) Cross section and (b) graphical projection of a QCM, illustrating a gas sensitive layer on one electrode (images taken from reference 171).

The application of QCM devices in gas sensing is now well established and documented.[181,190-194] However, it was not until 1959 when Sauerbrey[174] determined the linear relationship between the resonance frequency (Δf) and the mass of a substance rigidly adsorbed onto the surface (Δm) of the piezoelectric QCM according to the following equation:

$$\Delta f = -\frac{2 f_0^2}{A\sqrt{\mu_q \rho_q}} \Delta m = -S_f \Delta m \qquad \text{Equation 1.2}$$

where, f_0 is the resonant frequency of the fundamental mode of the crystal, A is the active area of the electrodes in cm^{-2}, ρ_q is the quartz crystal density (2.648 $g^{-1}.cm^{-3}$), μ_q is the shear modulus of quartz (2.947×10^{11} $g.cm^{-1}.s^{-2}$) and S_f is the integral mass sensitivity or Sauerbrey constant.[180,191,195-197] The sensitivity of a QCM device is the ratio of the fractional change in output signal per fractional change in analyte concentration.

The main advantage of an increase of f_0 is that the mass sensitivity $S_f = \Delta f / \Delta m$ increases with f_0^2.[198] However, due to the relationship of f_0 with that of the bare resonator's thickness, h_s (equation below) an increased f_0 results in a thinner more fragile quartz substrate.

$$f_0 = \frac{\sqrt{\mu_q / \rho_q}}{2h_s} \qquad \text{Equation 1.3}$$

A higher mass sensitivity may also be achieved by operating the QCM at higher resonant frequencies corresponding to odd harmonics in the device, however at the cost of lower signal to noise ratio.[173] According to equation 1.3, the bare quartz resonator thickness for a 5, 10 and 30 MHz QCMs would have thicknesses of 330, 165 and 55 µm respectively.[198] Most applications utilize 5 – 10 MHz resonators. Such plate thicknesses provide a sufficient mechanical stability as well as high mass sensitivity.[199-201]

A measure for the quality of the quartz resonator is the Q-factor, which is defined as ratio of stored energy to that of the dissipated energy. The maximum value for Q is given by material constants. For the relation to the frequency the following equation applies[198]:

$$f_0 = -1.6 \times 10^{13} \frac{1}{f} s^{-1} \qquad \text{Equation 1.4}$$

The *Q*-factor of quartz resonators is influenced by factors like impurities, mobility of impurities, dislocations, hydrogen content of the quartz material, the diameter/thickness ratio and parallelity of the quartz surfaces.[202] Due to additional losses, the value calculated from equation above is, therefore, not reached in practice. The *Q*-factor can be calculated on the base of a modified Butterworth-van-Dyke (BVD) circuit[203-205] simplified to the following equation

$$Q = 2\pi f_0 \frac{Energy\ stored}{\text{Power}\ loss} \qquad \text{or} \qquad Q = \frac{f_0}{\Delta f_{3dB}} \qquad \text{Equation 1.5}$$

Where f_{3dB} is the 3 dB bandwidth that can be determined from the resonance behaviour of the resonators using network analyser.[206]

Some methods to increase the Q-factor include reducing the diameters of the deposited electrodes and/or bevelling of the quartz edges (energy trapping method).[207] A detailed description of these concepts is beyond the scope of this thesis and may be found

elsewhere.[198,208] The fluid mediums as well as the sensitive layer both act as acoustic load on the quartz resonator when using it as chemical sensor. This results in increased damping and as a consequence the excitation with an oscillator will be more difficult. The quality of QCM resonator used as gas sensor strongly depends on the characteristic properties of the layer (density, viscoelaticity, thickness, etc.).[198,209]

It is well known that the Sauerbrey's equation is linear and accurate only up to total electrode mass loads of ~2% of the mass of quartz substrate[204,210] or a frequency change of 2-5% of the fundamental frequency[207,211]. The quartz shear modulus and density are 2.947 x 10^{11} $g.cm^{-1}.s$ and 2.648 g/cm^{-3} respectively. The quartz wafers considered in this study are 7.5 mm in diameter with a calculated ~167 µm thickness for a 10MHz crystal.[198] Considering the mass loading limitation imposed by Sauerbrey, the maximum total allowable deposited mass is between 391 to 977 µg given the crystal weighs 19.3 mg.

1.2.6.3 Advantages of QCM over Other Transducers

By far, the most commonly used microsensor is the QCM having an extensive history of use for quantification of physical and chemical adsorption in both commercial and fundamental research applications.[171] Extensive research has been undertaken examining the prospect of the QCM as a chemical and gravimetric sensor in different areas, and several commercial chemical sensing applications of QCMs have been developed, especially for gaseous species.[171,181,212] The QCM is an ideal choice as a transducer in the application of high concentration Hg vapour sensing since

- They possess relatively high mass sensitivities[195]
- It has a linear response over a wide range of mass load[213]
- Stable having zero temperature coefficient around room temperature [214]
- Unlike SAW and FPW devices, QCMs are less sensitive to a high mass load, density and viscosity of the medium making it more robust and suitable for harsh environments[181] and less prone to damping [198]
- Unlike TFRs, higher quality factors can be achieved with QCMs increasing the signal to noise ratio of the device[171]

Details regarding the comparison of acoustic devices as chemical sensors are given elsewhere.[215-218]

In summary, QCMs and their respective electronics are much cheaper than the other acoustic based sensors mentioned. They attain excellent signal to noise ratio, have excellent temperature stability specially around room temperature, can be made less fragile while maintaining high enough sensitivity and are relatively easy to fabricate.[198] QCMs are widely used as on-line thickness monitors in metallic films' deposition processes.[205] Therefore, Hg

being a metal itself, it is most practical to use QCMs as the sensor transducer for Hg vapour sensing.

1.2.6.4 State of the Art Acoustic Based Hg Sensors

CEMs are one of the proposed tools that the EPA sanctions for the analysis of Hg concentrations in flue gases[219] as they offer benefits like[20]

- Real- or near real-time measure of pollutants' emission data
- Evaluation and feedback for mercury control strategies
- Greater understanding of process variability and operation
- Potential to be less costly than the current chemical methods, as they require minimal operator input
- Availability of complete history of data collection
- Greater public assurance

Currently, there are at least nine different CEM models that have been verified by the EPA to be utilized for monitoring emission of Hg into the air. Many of these are spectroscopy based and these measurement and monitoring technologies are not entirely accurate or complete.[219] Studies[132,220-223] are being undertaken worldwide to overcome the limitations of CV-AAS and other spectroscopic based Hg sensors and so the quest to develop a robust, cheap and accurate Hg vapour sensor based on techniques other than CV-AAS is ongoing.

The Jerome analyser, for example, determines the concentration of mercury based on the resistivity change of the Au electrode upon Hg adsorption/amalgamation.[93,94,104,224] This change in resistance is said to be due to an increase in scattering of conduction electrons at the Au film when mercury is adsorbed on the surface.[61,93,94,225] The Au resistive based (conductometric) Jerome analyzer is small, easily transported and is useful for indoor spills.[159] It is widely used in some industrial applications.[226] However, it is reported to be incompatible with ammonia and acetylene along with many other interferent chemicals thus limiting its use in the alumina industries.

Ryan et al.[156,227-229] showed an array of conductometric sensors could detect Hg vapour in humid air. However the sensor was made for the detection of low levels of Hg vapour (ppb range) and was therefore not suitable for alumina refinery gaseous effluents streams. Furthermore, the gold film could not be regenerated on the transducer and so $PdCl_2$ was used as the Hg selective layer. $PdCl_2$ is well known to be incompatible with some VOCs, acids, nitrates, moisture and ammonia and so this sensor would not be compatible with the harsh alumina gaseous streams.[230,231]

The Differential Absorption Lidar (DIAL) technique using dye laser systems[232] has been used by various chlor-alkali plants in the past to measure elemental Hg vapour, especially in Europe.[233] They have the disadvantage of needing frequent service due to its fast degrading gain medium.[39] Past attempts overcome the technique's numerous challenges have continuously failed. These attempts and the resulting disadvantages is thoroughly covered by Svanberg et al.[39]

Toth et al.[234] in 2007 reported their ability to identify and measure mercury by prompt gamma emission, generated by bombardment with neutrons. The method is typically used to sense in part per billion concentration range of mercury in the gaseous phase. Other methods with low detection limits also include systems based on laser Induced Fluorescence (LIF) detection, acoustic and magnetoelastic based sensor that utilise gold thin films. In the case of the LIF detection, a quantitative determination of gaseous elemental mercury in several gas matrixes was invented by D'Ottone *et al.* in 2006.[235] In this case Hg is monitored by exciting either via 1-photon LIF or 2-photon LIF and subsequently detecting the fluorescent light with an appropriate photomultiplier tube. However, the presence of nitrogen and some other gases can decrease the signal to noise ratio.

Shao et al.[14] used a mercury vapour dosimeter based on a gold-coated magnetoelastic sensor. Detection of mercury vapour is achieved by monitoring the shift in the sensor's acoustic resonant frequency, which changes due to the absorption of mercury on the gold coating. However, the study of such sensors did not include the effect of interferent gases while sensing Hg.

In 2005 Thundat et al.[236] used the adsorption induced bending method of a piezoelectric microcantilever to detect 50 ppb mercury concentration in N_2 gas. This was a follow up and improved work done by the same group in 1995.[237] Upon Hg vapour exposure, Au coated microcantilevers, such as those used in atomic force microscopy (AFM), undergo bending due to the differential stress produced during adsorption, between the microcantilever and its sensitive layer. This bending reduces the resonating frequency of the resonating microcantilever. Both the variation of the resonant frequency resulting from the mass modification of the system or the bending variation may be correlated with the Hg vapour concentration.[238] In Thundat's case the rate of change of the oscillation frequency was correlated with the mercury vapour concentration.[237,239] These systems however, have also been shown to detect other chemicals using the same Au sensitive layer[240,241], making it prone to cross sensitivity issues.

Butler et al.[153] reported a novel device to detect Hg vapour based on the principle that Hg adsorption to thin Au films causes increase in reflectivity. The reflectivity of the film as a function of Hg vapour adsorption was followed by measuring the amount of light reflected back through the Au evaporated fibre. The small size of the device and the small detection limit in the ppb range were quite exceptional. However, the group later demonstrated in a separate paper that the same instrument was also sensitive to the adsorption of small molecules such as SO_2, H_2S and other species, requiring further development or a separate filtering step for accurate mercury quantifications.[242] past studies have shown however that by having a filtering stage in the sensing process, reduced Hg readings are observed due to loss in the filtering stage.[88]

Acoustic based gravimetric sensors based on Hg sorption to Au sensitive substrate have been widely studied.[80,243-247] Bristow[248] first demonstrated the use of Au electrode QCM for Hg vapour sensing in 1972. Other investigators followed demonstrating the use of these devices for Hg vapour sensing in the proceeding years due to the QCM device being so ideal for such application.[97,213,249-254] However, none of the studies have shown Hg sensing in the presence of moisture, ammonia or any other interferent gases. A highly selective layer is required on the QCM electrode surface for Hg vapour sensing in alumina refinery gaseous applications.

Vetelino's group have used ST-cut quartz to fabricate SAW based sensor for low temperature mercury vapour sensing. It was demonstrated, by studying Au film thickness on the response of the SAW mercury sensor, that the response magnitude was highest for a 75Å thick gold film. Due to its high sensitivity however, these SAW sensors were only tested against 20 – 100 ppb Hg vapour without the presence of any interferent gases.[99,255,256]

Overall, it is generally recognised that acoustic based sensors are less sensitive[143] than that of spectroscopic techniques.[67,126] This is highly due to the fact that spectroscopic techniques use gold traps between sampling and sensing steps while acoustic based sensors may be used to continuously detect mercury levels in real time. The use of acoustic based sensors in conjunction with gold trap may also lower their detection limits. Fortunately, for the development of an acoustic wave based high concentration Hg vapour sensor, such high sensitivities are not required.

Levlin et al.[146] showed that the rate of mercury adsorption on gold is large and significantly drops after the adsorption of approximately 0.4μg/cm^2. This value is just above the estimated value of 0.36μg/cm^2 referring to a monolayer of mercury on a gold surface.[67,257] For high concentrations of Hg vapour, this limit can be reached quite quickly, making the sensor

device incapable of differentiating between Hg concentrations. At this stage an acoustic based sensors' Au surface needs to be annealed and regenerated. The annealing temperatures required are reported to range from 150 – 700℃.[18,97] Problems are known to occur at such high annealing temperatures.[61,258]

The most critical disadvantage of acoustic based sensors arises from the selectivity of the gold film to collect mercury in the presence of other interferents including hydrogen sulphide (H_2S). Commercially available H_2S sensors are available from Jerome based on the same principle of resistance change of the gold film upon H_2S exposure indistinguishable from that of mercury adsorption.[61,259,260] Fortunately, due to the differences in their chemical structures the response due to H_2S is optimum for flatter films having uniform crystallites and compact grain boundaries. On the other hand, mercury responds optimally on porous polycrystalline films that contain wide grain boundaries[90]. This indicates that differentiation may be possible by using the right selective surface morphology and sensor platform.

Finklea et al.[261] investigated the blocking effect of alkanethiol-formed self assembled monolayers (SAM) on the electrochemical oxidation of gold. Mirsky et al.[143] further developed this concept for Hg vapour sensing in the presence of volatile organic compounds (VOCs). The conductometric sensor was based on the decreasing lateral electrical conductivity of thin Au films upon sorption of Hg vapour. Hexadecanethiol SAM was deposited on the gold film before exposure to Hg in the presence of interferents. It was found that the SAM layers blocked the effects of humidity as well as some volatile sulphuric compounds but not of Hg. However, other studies have shown that Hg adsorption on Au substrates with alkanethiol SAMs induces reorientation and reorganisation of the alkanethiols both on complete and incomplete monolayers[262,263] creating Hg nanoparticles.[264] These SAMs layer containing Hg sensors are therefore non-stable when exposed to Hg containing environments and needs further development.

There exists a need for development of acoustic based sensors to overcome the limitations of, for example spectroscopic techniques for Hg vapour sensing in industrial environment applications. However, acoustic based sensors themselves are associated with their own limitations. These limitations are encouraged to be overcome with research and development since advantages such as their overall small size, ease of use, ability to be used as continuous online sensors, low cost and low power consumption far outweigh their limitations. The low cost is the result of their easy fabrication in batch quantities making them thousands of dollars less than their competing spectroscopic techniques.[155,265]

1.3 Conclusions

Over 90% of Hg emissions occur from anthropogenic sources. The ill effects of Hg on health and environment are well documented yet there is lack of any reliable, robust and accurate online Hg vapour sensor for monitoring and control of anthropogenic Hg vapour emissions. The current commercially available Hg vapour sensors all have drawbacks such as sensitivity (i.e. high Hg concentrations saturating the sorbent material resulting in breakthrough of the metal and underestimation of the concentrations) and cross contamination due to other interferent gases present in the effluent streams. This is the reason for various groups investigating new collectors and methods for Hg vapour sensing. These collection and analysis methods themselves are found to have limitations.

Literature on the interaction of Hg with that of Au suggests lack of full understanding of the process. Therefore further investigation is required before the development of highly stable, sensitive and selective Hg vapour sensors. For such sensors, high surface area of the sensitive layer as well as low Hg exposure times is prescribed. QCM sensors are thought to be the optimal choice of transducers. Among all else, their electrode surfaces may be modified to produce a sensitive and selective Hg sensor. A good balance between sensitivity, signal to noise ratio and fragility is postulated to be the choice of a 10 MHz crystal. Being less fragile, their electrode surfaces may be modified for selectivity and sensitivity more efficiently.

To the best of the Author's knowledge, no work exists regarding the surface modification of Au for Hg vapour sensing in industrial effluents. Further investigation is required to study to interaction of Hg with that of Au in order to decide on the optimum surface modification technique(s) for Hg vapour sensor development. The development of a mercury sensor suited to alumina refineries will be a significant breakthrough in controlling anthropogenic mercury emissions from many industries.

1.4 References

(1) Goldman, R. L.; Shannon, M. W. *Pediatrics* **2001**, *108*, 197-205.
(2) Rong, Y.; David Tee, L.; Joo Hwa, T. *Environmental Science and Pollution Research International* **2003**, *10*, 399-407.
(3) Palomares, E.; Vilar, R.; Durrant, J. R. *Chem. Commun.* **2004**, 362-363.
(4) Laudal, D. L.; French, N. B. In *Conference On Air Quality II: Mercury* 2000; Vol. 2, p 1-16.
(5) Lockley, I. *Emission Reduction program*, 2007.
(6) Sabri, Y. M.; Ippolito, S. J.; Bhargava, S. K. *Light Metals 2009* **2009**, 37-42.
(7) Government, A.; Department of the Environment, W., Heritage and the Arts, Ed.; National Pullutant Inventory: 2009; Vol. 2007-2008.
(8) Morency, J. *Filtration & Separation* **2002**, *39*, 24-26.
(9) Germani, M. S.; Zollert, W. H. *Environmental Science & Technology* **1988**, *22*, 1079-1085.
(10) Fthenakis, V. M.; Lipfert, F. W.; Moskowitz, P. D.; Saroff, L. *Journal of Hazardous Materials* **1995**, *44*, 267-283.
(11) Dobbs, C.; Armanios, C.; McGuiness, L.; Bauer, G.; Ticehurst, P.; Lochore, J.; Irons, R.; Ryan, R.; Adamek, G. In *7th International Alumina Quality Workshop* Perth, Western Australia, 2005, p 199-204.
(12) Shao, R.; Tan, E. L.; Grimes, C. A.; Ong, K. G. *Sensors Letters* **2007**, *5*, 6.
(13) Windham, R. L. *Analytical Chemistry* **1972**, *44*, 1334-1336.
(14) Sabri, Y. M.; Ippolito, S. J.; Tardio, J.; Sood, D. K.; Bhargava, S. K.; Mullett, M.; Harrison, I.; Rosenberg, S. In *8th International Alumina Quality Workshop* Darwin, Australia, 2008, p 260-266.
(15) Caron, J. J. *Surface Acoustic Wave Continuous Emissions Monitor for Total Mercury*, Sensor Research and Development Corporation, 2001.
(16) Schweyer, M. G.; Andle, J. C.; McAllister, D. J.; Vetelino, J. F. *Sensors and Actuators B: Chemical* **1996**, *35*, 170-175.
(17) Laudal, D. L.; Thompson, J. S.; Pavlish, J. H.; Brickett, L. A.; Chu, P. *Fuel Processing Technology* **2004**, *85*, 501-511.
(18) Holmes, M.; Pavlish, J.; EERC, Ed. North Dakota, 2004; Vol. 2009.
(19) Canstein, H. V.; Kelly, S.; Li, Y.; Wagner-Dobler, I. *Applied and Environmental Microbiology* **2002**, *68*, 2829-2837.
(20) Schrope, M. *Nature news* **2001**, *409*, 124-124.
(21) Smith, R. P. *Nature* **2005**, *436*, 779-779.
(22) Stokstad, E. *Science* **2004**, *303*, 34-.
(23) Boyd, A. S.; Seger, D.; Vannucci, S.; Langley, M.; Abraham, J. L.; King, L. E. J. *Journal of the American Academy of Dermatology* **2000**, *43*, 81-90.
(24) Graeme, K. A.; Pollack, C. V. *The Journal of emergency medicine* **1998**, *16*, 45-56.
(25) Baughman, T. A. *Environmental Health Perspectives* **2006**, *114*, 147-152.
(26) Trasande, L.; Landrigan, P. J.; Schechter, C. *Environmental Health Perspectives* **2005**, *113*, 590-596.
(27) LaMontagne, A. D.; Steenland, N. K.; Kelsey, K. *Ethylene oxide*; fourth ed.; Lippincott & Wilkins: Philadelphia, 2007.
(28) Morris, T. A. PhD by Research, The University of Alabama, 2004.
(29) Laudal, D. L.; Brown, T. D.; Nott, B. R. *Fuel Processing Technology* **2000**, *65-66*, 157-165.
(30) Bergan, T.; Gallardo, L.; Rodhe, H. *Atmospheric Environment* **1999**, *33*, 1575-1585.
(31) Pacyna, E. G.; Pacyna, J. M.; Pirrone, N. *Atmospheric Environment* **2001**, *35*, 2987-2996.
(32) Kalac, P.; Niznanská, M.; Bevilaqua, D.; Stasková, I. *Science of The Total Environment* **1996**, *177*, 251-258.
(33) Mukherjee, A. B.; Melanen, M.; Ekqvist, M.; Verta, M. *The Science of The Total Environment* **2000**, *259*, 73-83.
(34) Slemr, F.; Scheel, H. E. *Atmospheric Environment* **1998**, *32*, 845-853.
(35) Shetty, S. K.; Lin, C.-J.; Streets, D. G.; Jang, C. *Atmospheric Environment* **2008**, *42*, 8674-8685.
(36) Pacyna, E. G.; Pacyna, J. M. *Water, Air, & Soil Pollution* **2002**, *137*, 149-165.
(37) Sjöholm, M.; Weibring, P.; Edner, H.; Svanberg, S. *Opt. Express* **2004**, *12*, 551-556.
(38) Swain, E. B.; Jakus, P. M.; Rice, G.; Lupi, F.; Maxson, P. A.; Pacyna, J. M.; Penn, A.; Spiegel, S. J.; Veiga, M. M. *AMBIO: A Journal of the Human Environment* **2007**, *36*, 45-61.
(39) Government, A. *Mercury & compounds Emissions - All sources: Australia*, National Pollutant Inventory, 2006-2007.
(40) Alcoa *Environmental Review and Management Program*, Alcoa, 2005.

(41) Kockman, D.; Horvat, M.; Jacimovic, R.; Gibicar, D. *RMZ - Materials and Geoenvironment* **2005**, *52*, 71-74.
(42) Mullett, M.; Tardio, J.; Bhargava, S.; Dobbs, C. *Journal of Hazardous Materials* **2007**, *144*, 274-282.
(43) Lacerda, L. D. *Water, Air, & Soil Pollution* **1997**, *97*, 247-255.
(44) Johnson, J. *Chemical and Engineering News* **2001**, *79*, 18-19.
(45) Powers, R. A. *Proceedings of the IEEE* **1995**, *83*, 687-693.
(46) Pavlish, J. H.; Sondreal, E. A.; Mann, M. D.; Olson, E. S.; Galbreath, K. C.; Laudal, D. L.; Benson, S. A. *Fuel Processing Technology* **2003**, *82*, 89-165.
(47) Camargo, J. A. *Nature* **1993**, *365*, 302-302.
(48) Hirokatsu Akagi, Y. F., Eigo Takabatake, *Photochemistry and Photobiology* **1977**, *26*, 363-370.
(49) Pak, K.-R.; Bartha, R. *Appl. Environ. Microbiol.* **1998**, *64*, 1987-1990.
(50) Bidone, E. D.; Castilhos, Z. C.; Cid de Souza, T. M.; Lacerda, L. D. *Bulletin of Environmental Contamination and Toxicology* **1997**, *59*, 194-201.
(51) Carpi, A. *Water, Air, & Soil Pollution* **1997**, *98*, 241-254.
(52) Vallee, B. L.; Ulmer, D. D. *Annual Review of Biochemistry* **1972**, *41*, 91-128.
(53) Gillis, A. A.; Miller, D. R. *The Science of The Total Environment* **2000**, *260*, 191-200.
(54) Schroeder, W. H.; Munthe, J. *Atmospheric Environment* **1998**, *32*, 809-822.
(55) Hacon, S.; Rochedo, E. R.; Campos, R.; Rosales, G.; Lacerda, L. D. *Water, Air, & Soil Pollution* **1997**, *97*, 91-105.
(56) Scallan, K. F., University of California, 2007.
(57) Levlin, M.; Ikävalko, E.; Laitinen, T. *Fresenius' Journal of Analytical Chemistry* **1999**, *365*, 577-586.
(58) Guminski, C. *Journal of the Less Common Metals* **1991**, *168*, 329-334.
(59) McNerney, J. J.; Buseck, P. R.; Hanson, R. C. *Science* **1972**, *178*, 611-612.
(60) Granite, E. J.; Pennline, H. W.; Hargis, R. A. *Industrial & Engineering Chemistry Research* **2000**, *39*, 1020-1029.
(61) Braman, R. S.; Johnson, D. L. *Environmental Science & Technology* **1974**, *8*, 996-1003.
(62) Yan, T. Y. *Industrial & Engineering Chemistry Research* **1994**, *33*, 3010-3014.
(63) Diggs, T. H.; Ledbetter, J. O. *American Industrial Hygiene Association Journal* **1983**, *44*, 606 - 608.
(64) Reed, C. E.; Kanazawa, K. K.; Kaufman, J. H. *Journal of Applied Physics* **1990**, *68*, 1993-2001.
(65) Dumarey, R.; Dams, R.; Hoste, J. *Analytical Chemistry* **1985**, *57*, 2638-2643.
(66) Schroeder, W. H.; Hamilton, M. C.; Stobart, S. R. *REV. ANALYT. CHEM.* **1985**, *8*, 179-209.
(67) Be'er, A.; Lereah, Y.; Frydman, A.; Taitelbaum, H. *Physica A: Statistical Mechanics and its Applications* **2002**, *314*, 325-330.
(68) Guminski, C.; Galus, A.; Hirayama, C. In *Solubility Data Series: Metals in Mercury*; Warsaw, U. O., Ed.; Pergamon Press: Warsaw, Poland, 1986; Vol. 25, p 258-384.
(69) Strachan, J. F.; Harris, N. L. *Journal of the Institute of Metals* **1956**, *85*, 17-24.
(70) Sunier, A. A.; Gramkee, B. E. *Journal of the American Chemical Society* **1929**, *51*, 1703-1708.
(71) Sunier, A. A.; Weiner, L. G. *Journal of the American Chemical Society* **1931**, *53*, 1714-1721.
(72) Sunier, A. A.; White, C. M. *Journal of American Chemical Society* **1930**, *52*, 1842-1850.
(73) Mees, G. *Journal of the American Chemical Society* **1938**, *60*, 870-871.
(74) Anderson, J. T. *The Journal of Physical Chemistry* **1932**, *36*, 2145-2165.
(75) Brown, J. B. *Journal of Chemical Education* **1960**, *37*, 415.
(76) Levlin, M.; Ikavalko, E.; Laitinen, T. *Fresenius Journal of Analytical Chemistry* **1999**, *365*, 577-586.
(77) Rex, M.; Hernandez, F. E.; Campiglia, A. D. *Analytical Chemistry* **2006**, *78*, 445-451.
(78) Ruys, D. P.; Andrade, J. F.; Guimaraes, O. M. *Analytica Chimica Acta* **2000**, *404*, 95-100.
(79) Battistoni, C.; Bemporad, E.; Galdikas, A.; Kaciulis, S.; Mattogno, G.; Mickevicius, S.; Olevano, V. *Applied Surface Science* **1996**, *103*, 107-111.
(80) Morris, T.; Szulczewski, G. *Langmuir* **2002**, *18*, 5823-5829.
(81) Morris, T.; Szulczewski, G. *Langmuir* **2002**, *18*, 2260-2264.
(82) Morris, T.; Sun, J.; Szulczewski, G. *Analytica Chimica Acta* **2003**, *496*, 279-287.
(83) Kobiela, T.; Nowakowski, B.; Dus, R. *Applied Surface Science* **2003**, *206*, 78-89.
(84) Nowakowski, R.; Kobiela, T.; Wolfram, Z.; Dus, R. *Applied Surface Science* **1997**, *115*, 217-231.
(85) Fialkowski, M.; Grzeszczak, P.; Nowakowski, R.; Holyst, R. *The Journal of Physical Chemistry B* **2004**, *108*, 5026-5030.
(86) Brosset, C.; Iverfeldt, Å. *Water, Air, & Soil Pollution* **1989**, *43*, 147-168.

(87) Sabri, Y. M.; Ippolito, S. J.; Tardio, J.; Atanacio, A. J.; Sood, D. K.; Bhargava, S. K. *Sensors and Actuators B: Chemical* **2009**, *137*, 246-252.
(88) George, M. A. PhD by research, Arizona State University, 1991.
(89) Aiyer, H. N.; Kawazoe, T.; Lim, J.; Echigo, Y.; Ohtsu, M. *Nanotechnology* **2001**, *12*, 368-371.
(90) Be'er, A.; Hecht, I.; Taitelbaum, H. *Physical Review E* **2005**, *72*, 031606.
(91) George, M. A.; Glaunsinger, W. S. *Thin Solid Films* **1994**, *245*, 215-224.
(92) George, M. A.; Glaunsinger, W. S.; Thundat, T.; Lindsay, S. M. *Thin Solid Films* **1990**, *189*, 59-72.
(93) Nowakowski, R.; Pielaszek, J.; Dus, R. *Applied Surface Science* **2002**, *199*, 40-51.
(94) Yang, X. M.; Tonami, K.; Nagahara, L. A.; Hashimoto, K.; Wei, Y.; Fujishima, A. *Surface Science* **1994**, *319*, L17-L22.
(95) Scheide, E. P.; Taylor, J. K. *American Industrial Hygiene Association Journal* **1975**, *36*, 897 - 901.
(96) Stobinski, L.; Dus, R. *Surface Science* **1993**, *298*, 101-106.
(97) Haskell, R. L. B.; Caron, J. J.; Duptisea, M. A.; Ouellette, J. J.; Vetelino, J. F. In *Ultrasonics Symposium, 1999. Proceedings*; IEEE: Orono, ME, 1999; Vol. 1, p 429-434 vol.1.
(98) Chaurasia, H. K.; Huizinga, A.; Voss, W. A. G. *Journal of Physics D: Applied Physics* **1975**, *8*, 214-218.
(99) Drelich, J.; White, C. L.; Xu, Z. *Environ. Sci. Technol.* **2008**, *42*, 2072-2078.
(100) Kalb, G. W. *Atomic Absorption Newsletter* **1970**, *9*, 4.
(101) Larjava, K.; Laitinen, T.; Vahlman, T.; Artmann, S.; Siemens, V.; Broekaert, J. A. C.; Klockow, D. *International journal of environmental analytical chemistry* **1992**, *49*, 73 - 85.
(102) Larjava, K.; Laitinen, T.; Kiviranta, T.; Siemens, V.; Klockow, D. *International journal of environmental analytical chemistry* **1993**, *52*, 65-73.
(103) Jansen, H. J. F.; Freeman, A. J.; Weinert, M.; Wimmer, E. *Physical Review B* **1983**, *28*, 593.
(104) Mott, N. F. *Philosophical Magazine* **1961**, *6*, 287 - 309.
(105) Dowben, P. A. *Surface Science Reports* **2000**, *40*, 151-247.
(106) Miedema, A. R.; Dorleijn, J. W. F. *Philosophical Magazine Part B: Physics of Condensed matter: Statistical Mechanics, Electronics, Optical and Magnetic Properties* **1981**, *43*, 251-272.
(107) Schmutzler, R. W.; Hensel, F. *Journal of Non-Crystalline Solids* **1972**, *8-10*, 718-721.
(108) El-Hanany, U.; Warren, W. W. *Physical Review Letters* **1975**, *34*, 1276.
(109) Even, U.; Jortner, J. *Physical Review Letters* **1972**, *28*, 31.
(110) Hensel, F. *Berichte der Bunsengesellschaft fur Physikalische Chemie* **1976**, *80*, 786-789.
(111) Cheshnovski, O.; Even, U.; Jortner, J. *Solid State Communications* **1977**, *22*, 745-748.
(112) Gaston, N.; Schwerdtfeger, P. *Physical Review B (Condensed Matter and Materials Physics)* **2006**, *74*, 024105-12.
(113) Ballone, P.; Galli, G. *Physical Review B* **1989**, *40*, 8563.
(114) Steckel, J. A. *Physical Review B (Condensed Matter and Materials Physics)* **2008**, *77*, 115412.
(115) Bloch, A. N.; Rice, S. A. *Physical Review* **1969**, *185*, 933.
(116) Kutana, A.; Giapis, K. P. *Nano Lett.* **2006**, *6*, 656-661.
(117) Chandra, S.; Di Marzo, M.; Qiao, Y. M.; Tartarini, P. *Fire Safety Journal* **1996**, *27*, 141-158.
(118) Henn, A. R. *Biophysical Chemistry* **2003**, *105*, 533-543.
(119) Lennard-Jones, J. E.; Corner, J. *Transactions of the Faraday Society* **1940**, *36*, 1156-1162.
(120) Joseph McGuire, E. L., Robert D. Sproull, *Surface and Interface Analysis* **1990**, *15*, 603-608.
(121) Rhee, S. K. *Journal of the American Ceramic Society* **1970**, *53*, 386-389.
(122) Granite, E. J. In *Annual International Pittsburgh Coal Conference* Pittsburgh, 2003; Vol. 20, p 983-1010.
(123) Abollino, O.; Giacomino, A.; Malandrino, M.; Piscionieri, G.; Mentasti, E. *Electroanalysis* **2008**, *20*, 75-83.
(124) Clevenger, W. L.; Smith, B. W.; Winefordner, J. D. *Critical Reviews in Analytical Chemistry* **1997**, *27*, 1-26.
(125) Temmerman, E.; Vandecasteele, C.; Vermeir, G.; Leyman, R.; Dams, R. *Analytica Chimica Acta* **1990**, *236*, 371-376.
(126) Sánchez Uría, J. E.; Sanz-Medel, A. *Talanta* **1998**, *47*, 509-524.
(127) Blanco, R. M.; Villanueva, M. T.; Uría, J. E. S.; Sanz-Medel, A. *Analytica Chimica Acta* **2000**, *419*, 137-144.
(128) Das, A. K.; de la Guardia, M.; Cervera, M. L. *Talanta* **2001**, *55*, 1-28.
(129) Logar, M.; Horvat, M.; Akagi, H.; Pihlar, B. *Analytical and Bioanalytical Chemistry* **2002**, *374*, 1015-1021.
(130) Tong, X.; Barat, R. B.; Poulos, A. T. *Review of Scientific Instruments* **2002**, *73*, 2392-2397.
(131) Granite, E. J.; Pennline, H. W. *Industrial & Engineering Chemistry Research* **2002**, *41*, 5470-5476.

(132) Weissberg, B. G. *Economic Geology* **1971**, *66*, 1042-1047.
(133) Sholupov, S.; Pogarev, S.; Ryzhov, V.; Mashyanov, N.; Stroganov, A. *Fuel Processing Technology* **2004**, *85*, 473-485.
(134) Rocha, T. A. P.; Gomes, M. T. S. R.; Duarte, A. C.; Oliveira, J. A. B. P. *Analytical Communication* **1998**, *35*, 415-416.
(135) Richton, R. E.; Farrow, L. A. *The Journal of Physical Chemistry* **2002**, *85*, 3577-3581.
(136) Bilic, A.; Reimers, J. R.; Hush, N. S.; Hafner, J. *The Journal of Chemical Physics* **2002**, *116*, 8981-8987.
(137) Kay, B. D.; Lykke, K. R.; Creighton, J. R.; Ward, S. J. *The Journal of Chemical Physics* **1989**, *91*, 5120-5121.
(138) Surplice, N. A.; Brearley, W. *Surface Science* **1975**, *52*, 62-74.
(139) Nuss, H.; Jansen, M. *ChemInform* **2006**, *37*.
(140) de Vooys, A. C. A.; Mrozek, M. F.; Koper, M. T. M.; van Santen, R. A.; van Veen, J. A. R.; Weaver, M. J. *Electrochemistry Communications* **2001**, *3*, 293-298.
(141) Mirsky, V. M.; Vasjari, M.; Novotny, I.; Rehacek, V.; Tvarozek, V.; Wolfbeis, O. S. *Nanotechnology* **2002**, *13*, 175-178.
(142) Meyer, R.; Lemire, C.; Shaikhutdinov, S. K.; Freund, H. *Gold Bulletin* **2004**, *37*, 72-124.
(143) Caron, J. J. O., ME), Haskell, Reichl B. (Veazie, ME), Freeman, Carl J. (Rockville, MD), Vetelino, John F. (Orono, ME); Sensor Research and Development Corp. (Orono, ME): United States, 1999.
(144) Levlin, M.; Niemi, H. E. M.; Hautojärvi, P.; Ikävalko, E.; Laitinen, T. *Fresenius' Journal of Analytical Chemistry* **1996**, *355*, 2-9.
(145) Kvietkus, K.; Xiao, Z.; Lindqvist, O. *Water, Air, & Soil Pollution* **1995**, *80*, 1209-1216.
(146) RA-915+, l.
(147) Lumex 2008.
(148) Gochfeld, M. *Ecotoxicology and Environmental Safety* **2003**, *56*, 174-179.
(149) Holland, K. New York, 2005; Vol. 2009.
(150) Ritchie, K. A.; Burke, F. J. T.; Gilmour, W. H.; Macdonald, E. B.; Dale, I. M.; Hamilton, R. M.; McGowan, D. A.; Binnie, V.; Collington, D.; Hammersley, R. *British Dental Journal* **2004**, *197*, 625-632.
(151) Kramer, C. 2001; Vol. 2008.
(152) Arizona Instruments LLC Arizona, 2007; Vol. 2009, p mercury sensors.
(153) Wu, J. M.; Huang, H. S.; Livengood, C. D. *Development of a sorbent-based technology for control of mercury in flue gas*, 1996.
(154) Loredo, J.; Soto, J.; Álvarez, R.; Ordóñez, A. *Environmental Monitoring and Assessment* **2007**, *130*, 201-214.
(155) Monitor, T. V. M. V. 2006, p Mercury sensor.
(156) Choi, H. K.; Lee, S. H.; Kim, S. S. *Fuel Processing Technology* **2009**, *90*, 107-112.
(157) Mercury Instruments USA 2009; Vol. 2009.
(158) Wängberg, I.; Edner, H.; Ferrara, R.; Lanzillotta, E.; Munthe, J.; Sommar, J.; Sjöholm, M.; Svanberg, S.; Weibring, P. *The Science of The Total Environment* **2003**, *304*, 29-41.
(159) Ferrara, R.; Mazzolai, B. *The Science of The Total Environment* **1998**, *215*, 51-57.
(160) Skreblin, M.; Byrne, A. R. *Vestnik Slovenskega Kemijskega Drustva* **1991**, *38*, 16.
(161) Mazzolai, B.; Mattoli, V.; Raffa, V.; Tripoli, G.; Accoto, D.; Menciassi, A.; Dario, P. *Sensors and Actuators A: Physical* **2004**, *113*, 282-287.
(162) Mazzolai, B.; Mattoli, V.; Raffa, V.; Tripoli, G.; Accoto, D.; Menciassi, A.; Dario, P. In *Sensors and Microsystems, Proceedings of the Italian Conference*; 8 ed. *Trento, Italy,*, 2003; Vol. 8, p 369-375.
(163) Morris, T.; Kloepper, K.; Wilson, S.; Szulczewski, G. *Journal of Colloid and Interface Science* **2002**, *254*, 49-55.
(164) Dimasi, E.; Tostmann, H.; Ocko, B. M.; Huber, P.; Shpyrko, O. G.; Pershan, P. S.; Deutsch, M.; Berman, L. E. In *Materials Research Society Symposium Proceedings* 2000; Vol. 590, p 183-188.
(165) Butler, M. A.; Ricco, A. J.; Baughman, R. J. *Journal of Applied Physics* **1990**, *67*, 4320-4326.
(166) Chah, S.; Yi, J.; Zare, R. N. *Sensors and Actuators B: Chemical* **2004**, *99*, 216-222.
(167) Hughes, R. C.; Ricco, A. J.; Butler, M. A.; Martin, S. J. *Science* **1991**, *254*, 74-80.
(168) Ryan, M. A.; Homer, M. L.; Shevade, A. V.; Lara, L. M.; Yen, S.-P. S.; Kisor, A. K.; Manatt, K. S. *ECS Meeting Abstracts* **2008**, *16*, 431-439.
(169) Ippolito, S. J.; Trinchi, A.; Powell, D. A.; Wlodarski, W. *Solid State Gas Sensing*; Springer Science+Business Media, LLC: Brescia, Italy, 2009; Vol. 1.
(170) Ballantine, D. S.; Wohltjen, H. *Analytical Chemistry* **1989**, *61*, 704A-715A.
(171) Ward, M. D.; Buttry, D. A. *Science* **1990**, *249*, 1000-1007.
(172) Sauerbrey, G. *Zeitschrift für Physik A Hadrons and Nuclei* **1959**, *155*, 206-222.

(173) Martin, S. J.; Granstaff, V. E.; Frye, G. C. *Analytical Chemistry* **1991**, *63*, 2272-2281.
(174) Kanazawa, K. K.; Gordon, J. G. *Analytical Chemistry* **1985**, *57*, 1770-1771.
(175) Martin, S. J.; Frye, G. C.; Ricco, A. J.; Senturia, S. D. *Analytical Chemistry* **1993**, *65*, 2910-2922.
(176) Dong, Y. *Sensors and Actuators B: Chemical* **2005**, *108*, 622-626.
(177) Smith, A. L.; Shirazi, H. M. *Thermochimica Acta* **2005**, *432*, 202-211.
(178) Smith, A. L.; Shirazi, H. M.; Mulligan, S. R. *Biochimica et Biophysica Acta (BBA) - Protein Structure and Molecular Enzymology* **2002**, *1594*, 150-159.
(179) Al Kobaisi, M. Doctor of Philosophy, Royal Melbourne Institue of Technology University, 2008.
(180) Janshoff, A.; Galla, H.-J.; Steinem, C. *Angewandte Chemie* **2000**, *39*, 4004-4032.
(181) Beil, F. W.; Blick, R. H.; Wixforth, A. *Physica E: Low-dimensional Systems and Nanostructures* **2004**, *21*, 1106-1110.
(182) Schweyer, M. G.; Weaver, J. T.; Andle, J. C.; McAllister, D. J.; French, L.; Vetelino, J.; Height, J. J. In *Frequency Control Symposium, 1997., Proceedings of the 1997 IEEE International* 1997, p 147-155.
(183) Venema, A.; Nieuwkoop, E.; Vellekoop, M. J.; Ghijsen, W. J.; Barendsz, A. W.; Nieuwenhuizen, M. S. *IEEE Transactions on Ultrasonics, Ferroelectrics and Frequency Control* **1987**, *34*, 148-155.
(184) Thiele, J. A.; da Cunha, M. P. *Sensors and Actuators B: Chemical* **2006**, *113*, 816-822.
(185) Arnau, A.; Ferrari, V.; Soares, D.; Perrot, H. In *Piezoelectric Transducers and Applications*; Springer Berlin Heidelberg: 2008, p 117-186.
(186) Arnau, A. *Sensors* **2008**, *8*, 370-411.
(187) O'Sullivan, C. K.; Guilbault, G. G. *Biosensors and Bioelectronics* **1999**, *14*, 663-670.
(188) James, D.; Scott, S. M.; Ali, Z.; O'Hare, W. T. *Microchimica Acta* **2005**, *149*, 1-17.
(189) Cheeke, J. D. N.; Wang, Z. *Sensors and Actuators B: Chemical* **1999**, *59*, 146-153.
(190) Khlebarov, Z. P.; Stoyanova, A. I.; Topalova, D. I. *Sensors and Actuators B: Chemical* **1992**, *8*, 33-40.
(191) Fox, C. G.; Alderm, J. F. *Analyst* **1989**, *114*, 997-1004.
(192) Ali, Z. *Journal of thermal analysis and calorimetry* **1999**, *55*, 397-412.
(193) Tsionsky, V.; Gileadi, E. *Langmuir* **1994**, *10*, 2830-2835.
(194) Flitti, F.; Far, A.; Guo, B.; Bermak, A. *Journal of Sensors* **2008**, *2008*, 1-6.
(195) Buck, R. P.; Lindner, E.; Kutner, W.; Inzelt, G. *Pure & Applied Chemistry* **2004**, *76*, 1139-1160.
(196) Zimmermann, B.; Lucklum, R.; Hauptmann, P.; Rabe, J.; Büttgenbach, S. *Sensors and Actuators B: Chemical* **2001**, *76*, 47-57.
(197) Sagmeister, B. P.; Graz, I. M.; Schwödiauer, R.; Gruber, H.; Bauer, S. *Biosensors and Bioelectronics* **2009**, *24*, 2643-2648.
(198) Bender, J. W.; Krim, J. In *Microscale Diagnostic Techniques* 2005, p 227-259.
(199) Herrmann, F.; Jakoby, B.; Rabe, J.; Büttgenbach, S. *Sensors Update* **2001**, *9*, 105-160.
(200) Ballato, A.; Gualtieri, J. G. *Ultrasonics, Ferroelectrics and Frequency Control, IEEE Transactions on* **1994**, *41*, 834-844.
(201) Lakin, K. M.; Wang, J. S. *Applied Physics Letters* **1981**, *38*, 125-127.
(202) Granstaff, V. E.; Martin, S. J. *Journal of Applied Physics* **1994**, *75*, 1319-1329.
(203) Behling, C.; Lucklum, R.; Hauptmann, P. *Sensors and Actuators A: Physical* **1997**, *61*, 260-266.
(204) Thanner, H.; Krempl, P.; Selic, R.; Wallnöfer, W.; Worsch, P. *Journal of Thermal Analysis and Calorimetry* **2003**, *71*, 53-59.
(205) Bechmann, R. *Journal of Scientific Instruments* **1952**, *29*, 73-76.
(206) Shockley, W.; Curran, D. R.; Koneval, D. J. *The Journal of the Acoustical Society of America* **1967**, *41*, 981-993.
(207) Behling, C.; Lucklum, R.; Hauptmann, P. *Sensors and Actuators A: Physical* **1998**, *68*, 388-398.
(208) Mecea, V. M. *Sensors and Actuators A: Physical* **1994**, *40*, 1-27.
(209) Lu, C.-S.; Lewis, O. *Journal of Applied Physics* **1972**, *43*, 4385-4390.
(210) Ippolito, S. J. PhD by research, RMIT university, 2006.
(211) Ho, M. H.; Guilbault, G. G.; Scheide, E. P. *Analytica Chimica Acta* **1981**, *130*, 141-147.
(212) Konash, P. L.; Bastiaans, G. J. *Analytical Chemistry* **1980**, *52*, 1929-1931.
(213) Grate, J. W.; Martin, S. J.; White, R. M. *Analytical Chemistry* **1993**, *65*, 987A-996A.
(214) Benes, E.; Gröschl, M.; Burger, W.; Schmid, M. *Sensors and Actuators A: Physical* **1995**, *48*, 1-21.
(215) Auge, J., University of Magdeburg, 1995.
(216) Janata, J.; Josowicz, M.; DeVaney, D. M. *Analytical Chemistry* **1994**, *66*, 207-228.
(217) Bethea, T.; Cady-Sawyer, K.; Ettenson, L.; Harris, K.; Mandl, D.; Martynowicz, K.; Raeisghasem, A.; Westman, D. Columbia, USA, 2005.

(218) Fox, B. S.; Mason, K. J.; McElroy, F. C. *Journal of ASTM International (JAI)* **2005**, *2*, 11.
(219) Meischen, S. J.; VanPelt, V. J.; Zarate, E. A. In *95th Proceedings of the Air & Waste Management Association's Annual Conference & Exhibition* 2002, p 1364-1378.
(220) Magnuson, J. K.; Anderson, T. N.; Lucht, R. P.; Vijayasarathy, U. A.; Kalyan, A. In *23rd Proceedings - Annual International Pittsburgh Coal Conference (2006)* Pittsburgh, 2006; Vol. 14, p 1-14.
(221) Appel, D.; Grassi, J. H.; Kita, D.; Socha, J. United States, 2008.
(222) Raffa, V.; Mazzolai, B.; Mattoli, V.; Mondini, A.; Dario, P. *Sensors and Actuators B: Chemical* **2006**, *114*, 513-521.
(223) McNerney, J. J.; Buseck, P. R. *Gold Bulletin* **1973**, *6*, 106-107.
(224) Jerome411X.
(225) Shevade, A.; Blanco, M.; Goddard, W.; Ryan, M.; Homer, M.; Taylor, C.; Jewell, A.; Kisor, A.; Yen, S.-P.; Manatt, K.; Zhou, H.; Pelletier, C.; Lewis, C. *ECS Meeting Abstracts* **2006**, *601*, 1243-1243.
(226) Ryan, M. A.; Homer, M. L.; Zhou, H.; Mannat, K.; Manfreda, A.; Kisor, A. K.; Shevade, A. V.; Yen, S.-P. S. In *International Conference on Environmental Systems*; Jet Propulsion Laboratory, National Aeronautics and Space Administration: Rome, Italy, 2005, p 1-8.
(227) Ryan, M. A.; Shevade, A. V.; Zhou, H.; Homer, M. L. *MRS Bulletin* **2004**, *29*, 714.
(228) Huang, S. W.; Neoh, K. G.; Shih, C. W.; Lim, D. S.; Kang, E. T.; Han, H. S.; Tan, K. L. *Synthetic Metals* **1998**, *96*, 117-122.
(229) Choudary, B. M.; Madhi, S.; Chowdari, N. S.; Kantam, M. L.; Sreedhar, B. *Journal of the American Chemical Society* **2002**, *124*, 14127-14136.
(230) Weibring, P.; Andersson, M.; Edner, H.; Svanberg, S. *Applied Physics B: Lasers and Optics* **1998**, *66*, 383-388.
(231) Edner, H.; Ragnarson, P.; Wallinder, E. *Environmental Science & Technology* **2002**, *29*, 330-337.
(232) Toth, J. J.; Wittman, R.; Schenter, R. E.; Cooper, J. A. *Nuclear Instruments and Methods in Physics Research Section A: Accelerators, Spectrometers, Detectors and Associated Equipment* **2007**, *572*, 1102-1105.
(233) D'ottone, L. K. B., FL, US) United States, 2006.
(234) Adams, J. D.; Rogers, B.; Manning, L.; Hu, Z.; Thundat, T.; Cavazos, H.; Minne, S. C. *Sensors and Actuators A: Physical* **2005**, *121*, 457-461.
(235) Thundat, T.; Wachter, E. A.; Sharp, S. L.; Warmack, R. J. *Applied Physics Letters* **1995**, *66*, 1695-1697.
(236) Fadel, L.; Dufour, I.; Lochon, F.; Francais, O. *Sensors and Actuators B: Chemical* **2004**, *102*, 73-77.
(237) Hu, Z.; Thundat, T.; Warmack, R. J. *Journal of Applied Physics* **2001**, *90*, 427-431.
(238) Berger, R.; Delamarche, E.; Lang, H. P.; Gerber, C.; Gimzewski, J. K.; Meyer, E.; Güntherodt, H. J. *Applied Physics A: Materials Science & Processing* **1998**, *66*, S55-S59.
(239) Marie, R.; Jensenius, H.; Thaysen, J.; Christensen, C. B.; Boisen, A. *Ultramicroscopy* **2002**, *91*, 29-36.
(240) Butler, M. A.; Ricco, A. J. *Applied Physics Letters* **1988**, *53*, 1471-1473.
(241) Manganiello, L.; Rios, A.; Valcarcel, M. *Analytical Chemistry* **2002**, *74*, 921-925.
(242) Yao, S.; Tan, S.; Nie, L. *Fenxi Huaxue* **1986**, *14*, 6.
(243) Casilli, S.; Malitesta, C.; Conoci, S.; Petralia, S.; Sortino, S.; Valli, L. *Biosensors and Bioelectronics* **2004**, *20*, 1190-1195.
(244) Rogers, B.; Bauer, C. A.; Adams, J. D. *Micro-Electro-Mechanical Systems* **2003**, *5*, 663-666.
(245) Gomes, M. T. S. R.; Oliveira, M. O.; Oliveira, J. A. B. P. *Langmuir* **1999**, *15*, 8780-8782.
(246) Bristow, Q. *Journal of Geochemical Exploration* **1972**, *1*, 55-76.
(247) Scheide, E. P.; Taylor, J. K. *Environ. Sci. Technol.* **1974**, *8*, 1097-1099.
(248) Scheide, E. P. *Physics Teacher* **1977**, *15*, 47-51.
(249) McCammon, C. S. J.; Woodfin, J. W. *American Industrial Hygiene Association Journal* **1977**, *38*, 378-386.
(250) Scheide, E. P.; Warnar, R. B. *American Industrial Hygiene Association Journal* **1978**, *39*, 745-749.
(251) Mogilevski, A. N.; Mayorov, A. D.; Stroganova, N. S.; Stavrovski, D. B.; Galkina, I. P.; Spassov, L.; Mihailov, D.; Zaharieva, R. *Sensors and Actuators A: Physical* **1991**, *28*, 35-39.
(252) Spassov, L.; Yankov, D. Y.; Mogilevski, A. N.; Mayorov, A. D. *Review of Scientific Instruments* **1993**, *64*, 225-227.
(253) Caron, J. J.; Haskell, R. B.; Benoit, P.; Vetelino, J. F. *IEEE transactions on ultrasonics, ferroelectrics, and frequency control* **1998**, *45*, 1393-1398.
(254) Haskell, R. B. Masters, University of Maine, 2003.
(255) Mercer, T. T. *Analytical Chemistry* **1979**, *51*, 5.

(256) Hirvonen, J. K.; Weisenberger, W. H.; Westmoreland, J. E.; Meussner, R. A. *Applied Physics Letters* **1972**, *21*, 37-39.
(257) Cox, H. H. J.; Deshusses, M. A. *Chemical Engineering Journal* **2002**, *87*, 101-110.
(258) McNamara, J. D.; Wagner, N. J. *Gas Separation & Purification* **1996**, *10*, 137-140.
(259) Finklea, H. O.; Avery, S.; Lynch, M.; Furtsch, T. *Langmuir* **2002**, *3*, 409-413.
(260) Himmelhaus, M.; Buck, M.; Grunze, M. *Applied Physics B: Lasers and Optics* **1999**, *68*, 595-598.
(261) Thome, J.; Himmelhaus, M.; Zharnikov, M.; Grunze, M. *Langmuir* **1998**, *14*, 7435-7449.
(262) Aliganga, A. K. A.; Wang, Z.; Mittler, S. *The Journal of Physical Chemistry B* **2004**, *108*, 10949-10954.
(263) Li, D.; Ma, M. *Sensors and Actuators B: Chemical* **2000**, *69*, 75-84.

Chapter II

Experimental Setup

Experimental setup, sensor fabrication, instrumentation and literature considerations during the course of the present work are discussed in this chapter.

2.1 Overview

The development and testing of QCM sensors for mercury vapour requires many considerations. There are numerous physical and electrical components that make up the mercury vapour calibration system and the instrumentation used to characterize the sensors' material properties and performance. In this chapter, the chemicals, list of characterization techniques, sensor fabrication methods and Hg sensing system as well as their theoretical considerations will be listed and discussed.

2.1.1 Mercury Delivery and Sampling System

A mercury vapour delivery and data acquisition system was designed and constructed, the schematic of which is shown in Figure 2.1. One mass flow power supply (**A**, 647C Four-channel Mass Flow and Pressure Programmer/Display) controlling four mass flow meters (**A1-A4**, Mass-Flo® M100B), were purchased from MKS, USA. **A1** was connected to 3388 ppm ammonia cylinder balanced by nitrogen gas (CORGAS, Australia). **A2**-**A4** were all connected to dry nitrogen gas supplies. **A2** was used as the nitrogen dilution gas in the system while **A3** and **A4** were connected to the humidity (**B**) and Hg vapour (**C**) generators respectively. The lines consisted of 1/8" SS tubing (SS25-T2-S-035-BA), electronic-no-space 3-way gas ball valve switches (**D**, 51SC – electrical part and SS-41GXS2 – ball valve switch), 10 psi check valves for one way gas flow only (**E**, SS-2C-10), Pressure gauges (**F**, PGI-63B-PG20_CAQ1), Vernier meter for pressure control (**G**, SS-SS2-VH), and back pressure regulators (**H**, KBP1D0D4A5A20000) all purchased from Swagelok, Australia. The sulfur impregnated carbon traps (**I**) SS parts were built from Swagelok products. The sensors' housing/testing chamber (**J**) was made from Teflon and SS parts that were custom machined (also referred to as laboratory chamber. The baratron (**K**, 628D Baratron® Heated Absolute Capacitance Manometer (0-2,000 Torr) Temperature Controlled to 100℃) at the chamber exit was also purchased from MKS, USA and used to measure and log the online pressure in the chamber. The flow meters at the end of the lines (**L**) were used to confirm gas flow out of the system. The temperature of the chamber was controlled with a high current power supply (**M**, 6033A – Agilent Technologies, Australia) while the heating tapes (**HT**, EW-36050-55, Cole Parmer, Australia) were controlled with the temperature controller (**N**, TCCOBOXU – Temperature Controls) and was able to be monitored through the system temperature logger (**O**, USB TC-08, Pico Technology, USA) and control and acquisition computers (**P**). The issues of contamination, Hg or humidity condensation in the system, temperature fluctuations or pressure fluctuations were all dealt with by controlling the temperature of each section of the system and installation of various parts listed above. The Hg trap bottles (**Q**) containing potassium permanganate and sulfuric acid solutions (Sigma Aldrich, Australia) were placed just before the gas stream entered the sensors' chamber. The water trap (**Q2**) was place to ensure flow of the NH_3 gas while bleeding the cylinder before directing the flow to the testing

chamber. The gas stream containing Hg may also be redirected to the Hg trap solutions which may be analyzed using ICPMS for calibration purposes.

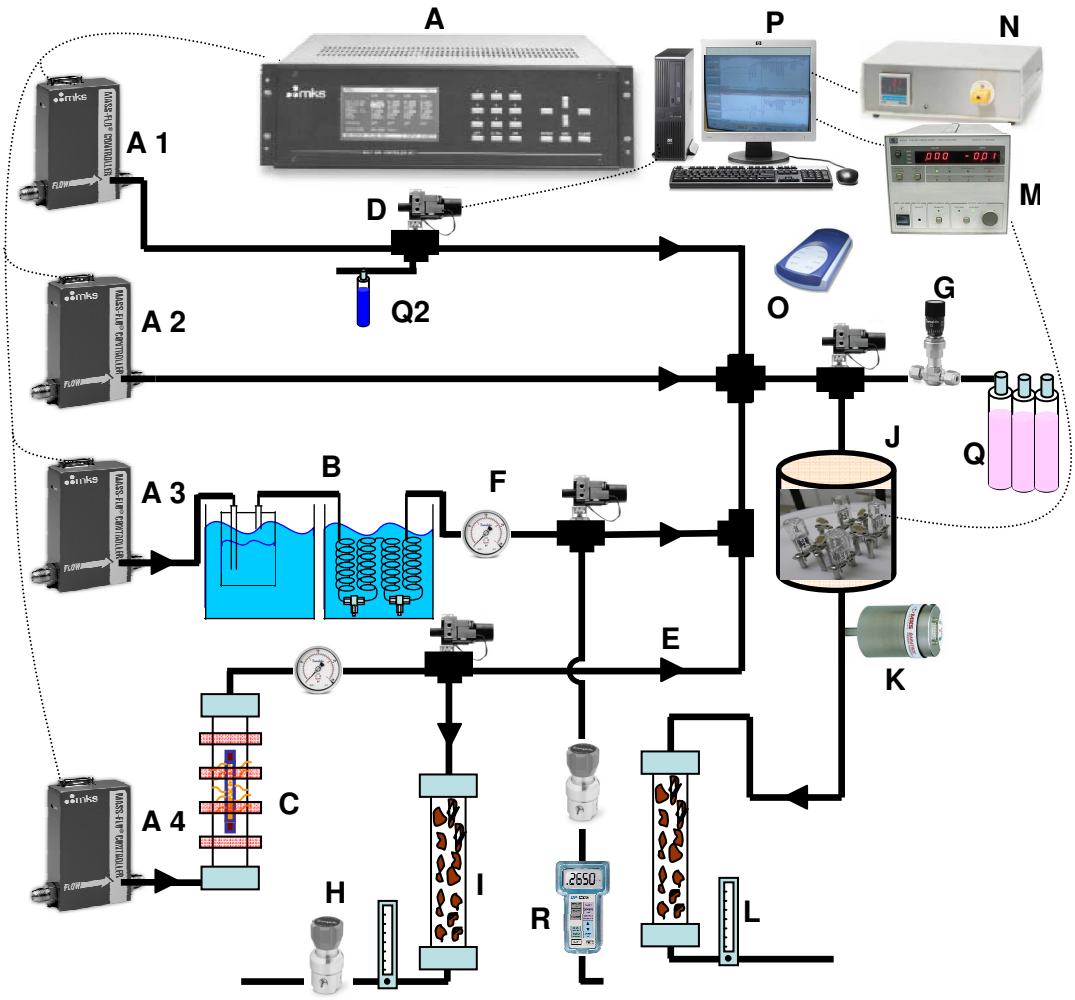

Figure 2.1: Diagram illustrating the mercury delivery and sampling system

The chamber, which housed four QCM sensors at a time, had an internal volume of 0.5L. The total gas flow was kept constant at 200 sccm in accordance with the literature[61] where optimal collection efficiency of Hg with Au substrates had been achieved at this flow rate.

The backpressure in the system due to the various components mentioned above (i.e. check valves, carbon traps etc.) reached a value of ~1220 ± 10 Torr. Therefore the entire system, including the Hg and humidity generators, was maintained at ~1220 Torr at all times. This exempted pressure fluctuations in the system upon the introduction of various gases into the chamber housing the QCM sensors and also produced repeatable Hg vapour and humidity concentrations. The operating pressure of 1220 Torr was much higher than the pressures used by others[87,95,266] for exposing Hg to metal surfaces. This was postulated to be an advantage due to the resulting higher number of collisions of the gas molecules with the sensor surfaces[267] as a result of the higher pressure and so no vacuum pump was installed at the gas outlets of the system to reduce pressures.

The humidity sensor (**R**, DP-CALC, Kenetec), by which the 100 percent relative humidity (%RH) at 25℃ was confirmed, is shown in Figure 2.1. Photographic images of some of the system parts are shown in Figure 2.2. The frequency counters (Agilent 53131A frequency counter with resolution of ±0.1 Hz over an integration period of 4 seconds and a Maxtek PLO_{10} RQCM (10MHz) phase locked oscillator, USA) were used to monitor the change in the fundamental frequency of any four QCM sensors during Hg vapour testing.

Due to Industry partners' HAZOP (hazard and operability studies) specifications, another testing/housing chamber for the QCM sensors was designed and fabricated (also referred to as industrial chamber) as shown in Figure 2.3. The purpose of this chamber was to test the best Hg vapour sensor from this research project in an industrial onsite Hg vapour monitoring program (phase 2 of this project). Preliminary results of the QCMs tested in the industrial chamber is only discussed in chapter 7, all other tests were performed in the laboratory chamber presented in Figure 2.2. The industrial chamber was fabricated in order to attain a small volume of 0.1 L as compared to 0.5 L for the laboratory chamber. Furthermore, the industrial chamber was designed in a rectangular shape as compared to circular shape for the laboratory chamber. The heating element of the industrial chamber was designed to be external and three thermocouples were fixed inside the chamber in order to monitor the internal temperature. For safety reasons, a safety cage was also built around the industrial chamber in order to keep users from heat or electrical shock. All wires were grounded for extra safety precaution.

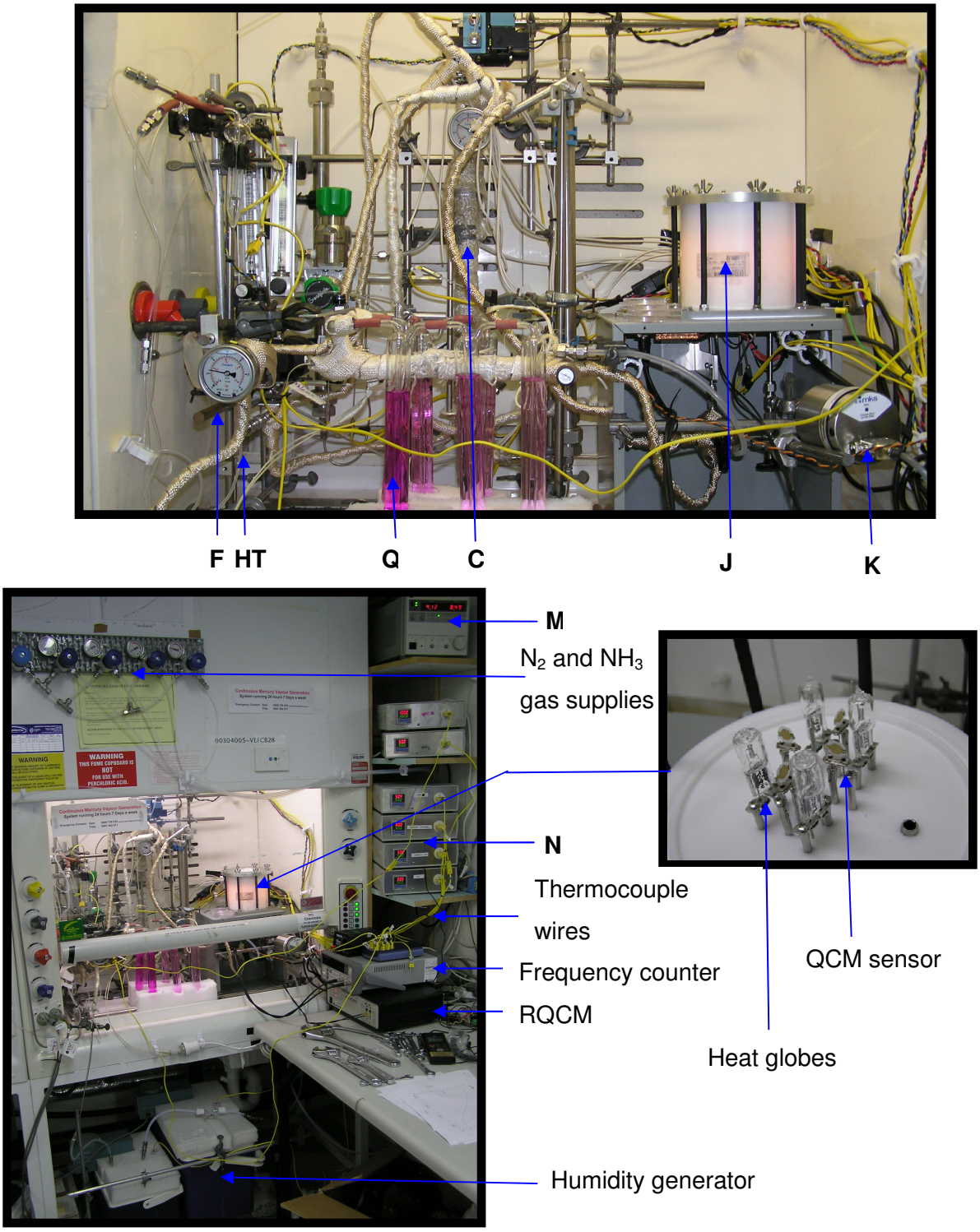

Figure 2.2: Photographic images of the mercury sensor system

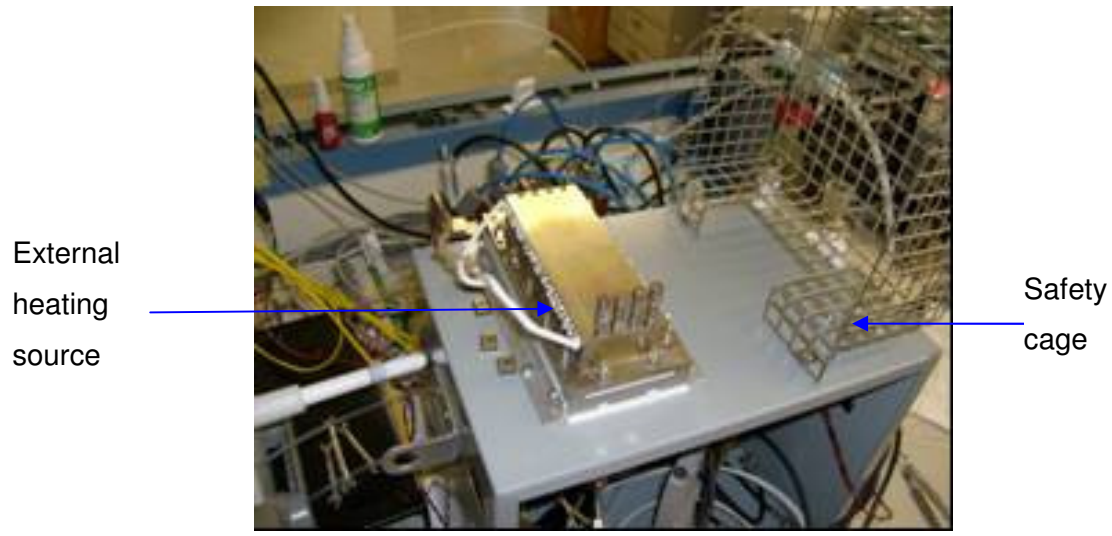

Figure 2.3: photographic images of the industrial chamber

2.1.2 Hg Vapour Generator and Calibration

The mercury vapour delivery system (Figure 2.4) was designed and constructed using stainless steel (SS) parts (Swagelok – Fluid Systems Technologies, Australia). The Hg generator worked as follows. Dry preheated (50°C) N_2 gas enters (**S**) at 50 standard cubic centimeters per minute (sccm) at all times during testing and non-testing periods. The glass beads (**T**) transfer heat to the entering gas in order for N_2 to reach the Hg generator temperature. The Hg concentration in the 50 sccm is dependent on the generator temperature which is controlled by the heating tape (**U**) and SS thermocouple (Ø = 1/16" OD) (**V**) both attached to the temperature controller. The N_2 then passes the beads and stainless steel mesh (**W**) holding the three Hg permeation tubes (**X**, P/N 137-100-0030-S56-C90, - VICI Metronics Inc., Texas, USA) upright and steady.

The Hg permeation tube is designed to release various amounts of Hg depending on the set heating tape temperature. The top and bottom of the tubes are sealed (**X1**) where the Hg gas phase (**X2**) moves towards saturation with the Hg liquid phase (**X3**) during which process Hg moves through the permeable membrane (**X4**) and into the gas stream. Prior to carrying Hg, the carrier gas (N_2) first passes the internal thermocouple (**Y**) which is connected to the temperature data logger (**Z**). The gas mixture is then either directed left towards a carbon trap or right towards the chamber housing the sensors.

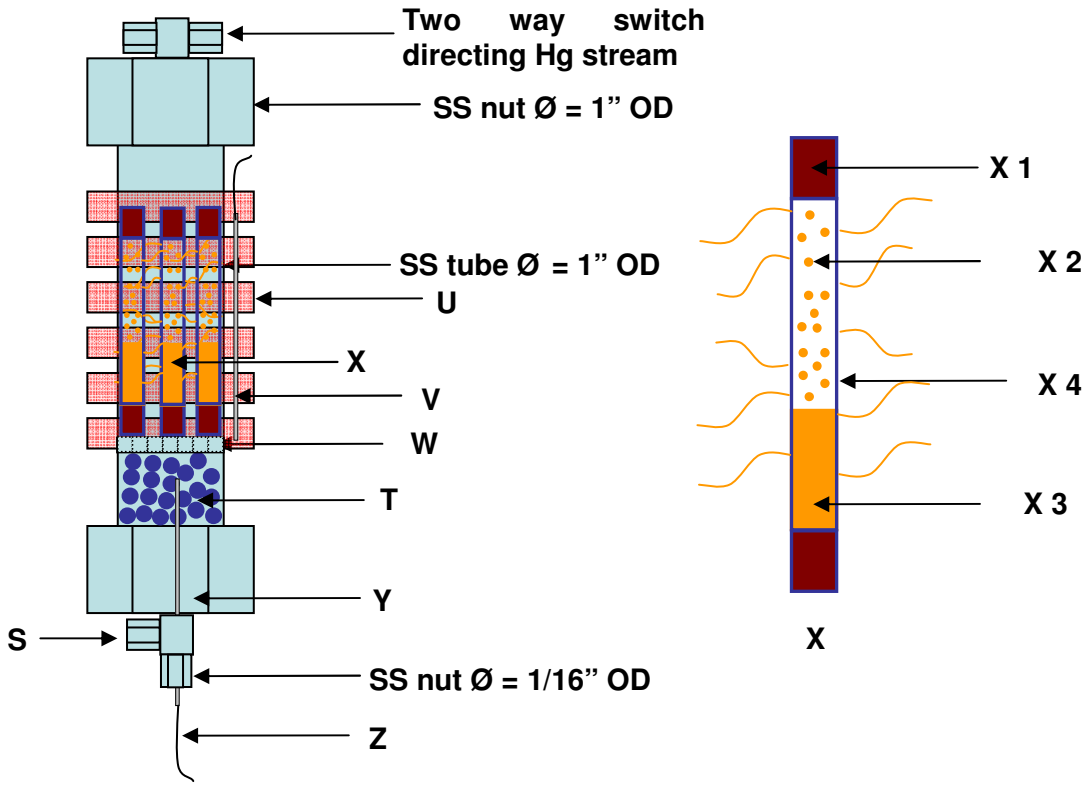

Figure 2.4: Hg vapour generator and permeation tube

Calibration

The Hg permeation tubes were verified by calibrating them in line with the system using a method similar to that of EPA method 101A.[268] This involved preparing the trap solution which was made of 10% (v/v) sulfuric acid and 4% (m/v) potassium permanganate balanced by milli-Q water (resistivity of 18.2 MΩ.cm, purified by use of a milli-Q reagent deionizer, Millipore). A train of 3 dreschel bottles was then connected in series, each bottle containing the trap solution and was connected to the system close to the point where Hg vapour enters the chamber. The gas stream was redirected isokinetically (200 sccm with 50sccm from Hg generator and 150 sccm N_2 gas through 1/8" SS tubes from the chamber towards the Hg trap train for 100 minutes, repeated three times at each of the five Hg vapour concentrations tested. The solution from each bottle was then diluted and analysed by ICPMS (as described in section 2.5.6), the overall results over the course of the work are shown in Figure 2.5. The mercury vapour generated was found to be repeatable within ±0.05 mg/m^3 over the 100 minute calibration period. The temperature inside the Hg generator was data logged to monitor the Hg generation stability at all times. The pressure of the generator was constant whether the gas was directed towards the carbon trap, the chamber or the Hg traps for calibration. The calibration graph shows the Hg concentration in the final 200 sccm gas entering the chamber. This means the 50 sccm flow through the Hg generator consists of 4 times the Hg concentration. The 50℃ temperature of the tubes (controlled by heating tapes

and controllers) was sufficient to hold the Hg vapour in the gas phase and stop it condensing through out the system. Once diluted with other gases to a total flow of 200 sccm, it was possible to test the sensors at a lower operating temperature than 50℃ (i.e. down to ~15℃ based on vapour pressure of Hg in air at saturation) without the Hg condensing in the system.

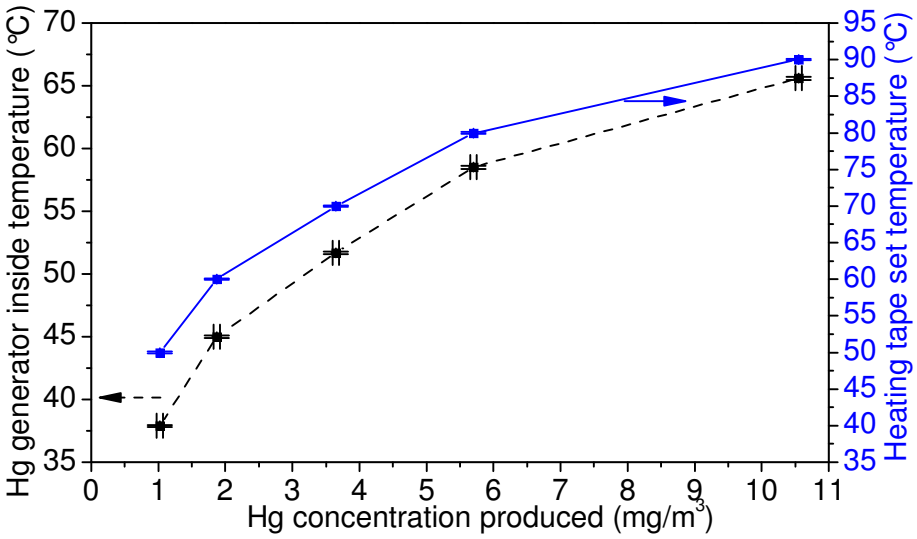

Figure 2.5: ICPMS Hg generator calibration data

2.1.3 Calibration data of the Humidity Generator

The humidity generator Figure 2.6 was built from Swagelok parts and custom-made glassware. By operating two baths at 30℃ and 25℃ respectively, it was postulated that near 100 %RH at 25℃ may be achieved at the generator outlet. The condensed water at the base of the coils was emptied regularly by unscrewing the bottom Swagelok caps.

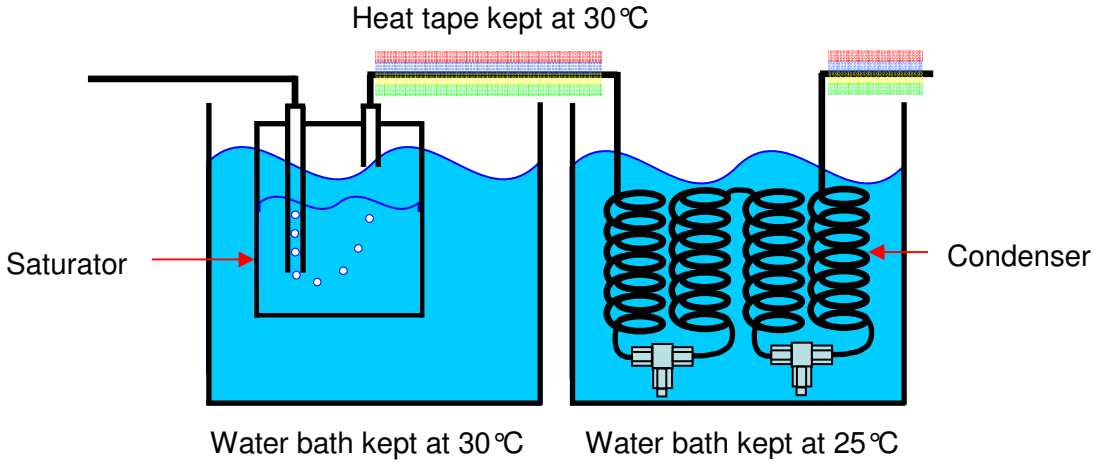

Figure 2.6: Schematic of the humidity generator producing ~100 %RH at 25℃

Calibration

The generator was run at three different flow rates, namely, 50, 100 and 150 sccm producing humidity concentrations of 4.2, 7.6 and 10.4 g/m^3 (±0.2 g/m^3) as tested with the humidity sensor (**R**) shown in Figure 2.1.

2.1.4 Testing Chamber Operating Temperatures

The operating temperatures in the testing chamber were altered by changing the current on the power supply that controlled the heat globes' heat intensity in the laboratory chamber. The outside temperature was set to achieve a stable operating temperature inside the industrial chamber. Figure 2.7 shows the current and outside temperature to achieve the operating temperatures inside the laboratory and industrial chambers, respectively.

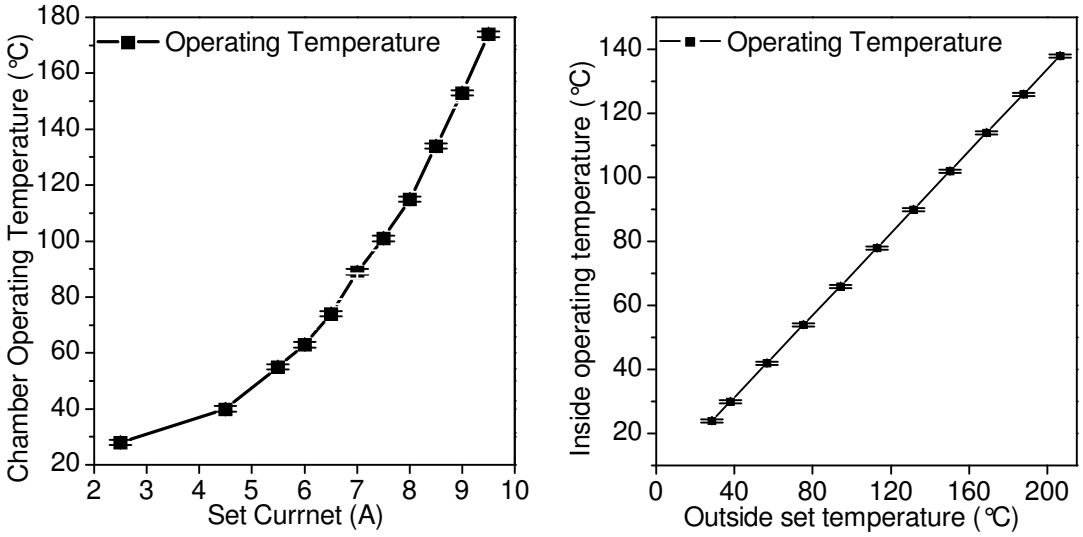

a) Laboratory chamber **b)** Industrial chamber

Figure 2.7: laboratory and industrial chamber operating temperature calibration.

The chambers were always fully pressurized with constant gas flow of 200 sccm during testing. The error bars show the fluctuations over the period of this PhD program.

2.2 QCM Fabrication

2.2.1 Metal Deposition

Optically polished AT-cut QCM substrates (7.5 mm diameter, 10 MHz resonant frequency, Hy-Q Crystals, Australia) were deposited with a 10 ± 0.01 nm Ti adhesion layer on both sides. A titanium adhesion layer was used rather than chromium because titanium has better adhesion and inertness than chromium.[269-271] Au is well known to adhere weakly to quartz and is the reason for many past studies using Cr as the adhesion layer between Au and SiO_2. However Cr is also well known to diffuse through gold and form chromium oxide on

the surface layer at even low temperatures.[272,273] Chromium oxide on the Au surface has also been observed to reduce the Au sorption capacity for Hg vapour.[94]

The additional deposition of metal types and their thickness following the Ti adhesion layer depended on the studies being undertaken. For investigations presented in chapter 4, Au layer deposition followed the Ti layer. The thicknesses of the Au layers varied from 40 to 200 nm. For the studies presented in chapter 5, an Au layer of 150 nm followed by 20 nm SiO_2 were deposited for all QCMs. Additional layers of Au were then deposited and their thicknesses ranged from 10 to 40 nm, and they were identical on both faces of the quartz substrate.

The metal depositions were performed by a Balzers^{TM} e-beam (BAK 600) at room temperature (~22℃) and typical base pressure of 2 x 10^{-7} mbar. The Ti, Au and Ni layers were deposited at 0.1, 0.2 and 0.2 nm/s deposition rates, respectively. The electron beam evaporator was set at an electron beam voltage of 6 keV for SiO_2, Ti and Ni or 11 keV for Au.

2.2.2 Surface Modification

Two novel surface modification techniques were performed in the research project, namely, galvanic replacement (Ni replaced with Au system) and electrodeposition (Au deposited on Au electrodes). The metal deposition of the QCM electrodes prior to their modification in each technique is described below.

2.2.2.1 Galvanic Replacement

A 300 nm Ni layer was deposited on QCM crystals with a 10 nm Ti adhesion layer. This was performed on several QCM crystals in the same batch to study the growth of Au on the Ni substrates over time during the galvanic replacement of Ni with Au. The procedure for the technique is described in chapter 6.

2.2.2.2 Electrodeposition

The QCMs with 100 and 150 nm thick Au layers on the 10 nm Ti adhesion layer were used for surface modifications (via electrodeposition) due to their high Q-factors. The surface modification procedures are thoroughly explained in chapter 7.

2.3 QCM Characterization

To determine the quality at each QCM fabrication step, an Agilent E5100A universal counter (network analyzer) was used throughout the fabrication processes to measure the impedance of each crystal as a series of Q-factor measurements.

For electrical characterisation, the resonators were mounted on a circuit board. The electrodes were wire bonded. All impedance data were calibrated and test fixture compensated. All the impedance measurements, to U/45 crystal bases, were carried out at room temperature (22°C). A PI network test fixture containing a coupler and power splitter was used to study the QCM resonator coating properties in the sensor development process.[181] All the circuit connections were BNC and all the leads RG 58 coaxial cables.

One of the characteristic features of quartz resonators are the frequencies of the harmonic vibration modes where the surface movement is in phase and the same direction. Beside these harmonic modes, inharmonic vibration modes are generated, which are often called spurious modes. These are characterised by the movement of particles in several regions of the quartz surface in antiphase. One of the most important requirements for operating a quartz resonator as a chemical sensor is the frequency stability. If the frequency separation between the harmonic and inharmonic modes is not sufficient, neighbouring frequencies may cross each other. This could cause effects such as mode coupling and frequency jumps. All these effects would impede a reliable frequency measurement, which commonly serves as output signal. One of the main goals in the design of the resonators is a sufficient separation of the harmonic from the inharmonic vibration modes.[198]

For this reason a relatively wide frequency band width had to be scanned in order to examine the separation of the inharmonic and the harmonic fundamental modes. For the measurement of the broad band characteristics, the bandwidths ranged from 9 to 11 MHz depending on the frequency position of the inharmonics relative to the fundamental mode. For a detailed characterisation and the determination of the equivalent circuit values at the fundamental resonant frequency, the bandwidth was reduced to 1-2 kHz. The data for the 10 MHz optically polished Au (Ti/Au = 10/100 nm) at spans of 20 kHz and 2 kHz is shown in Figures 2.8a and 2.8b, respectively.

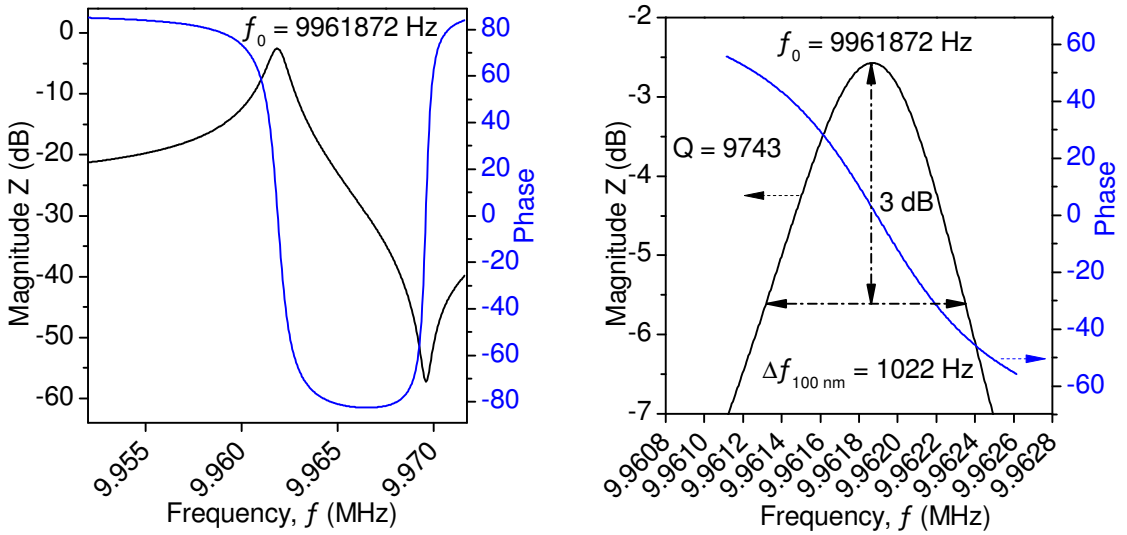

a) 20 kHz range **b)** 2 kHz range

Figure 2.8: Network analyser data of magnitude and phase of a 10 MHz QCM resonator with deposited 100 nm Au thin electrodes at spans of 20 kHz and 2 kHz frequency range.

Figure 2.9a shows the drop in Q factor when 50 rather than 100 nm Au is deposited on the QCM electrodes. Figure 2.9b shows the Q-factor of the same crystal as in Figure 2.8 decreasing when Au structures are deposited on the surface (as described in chapter 7).

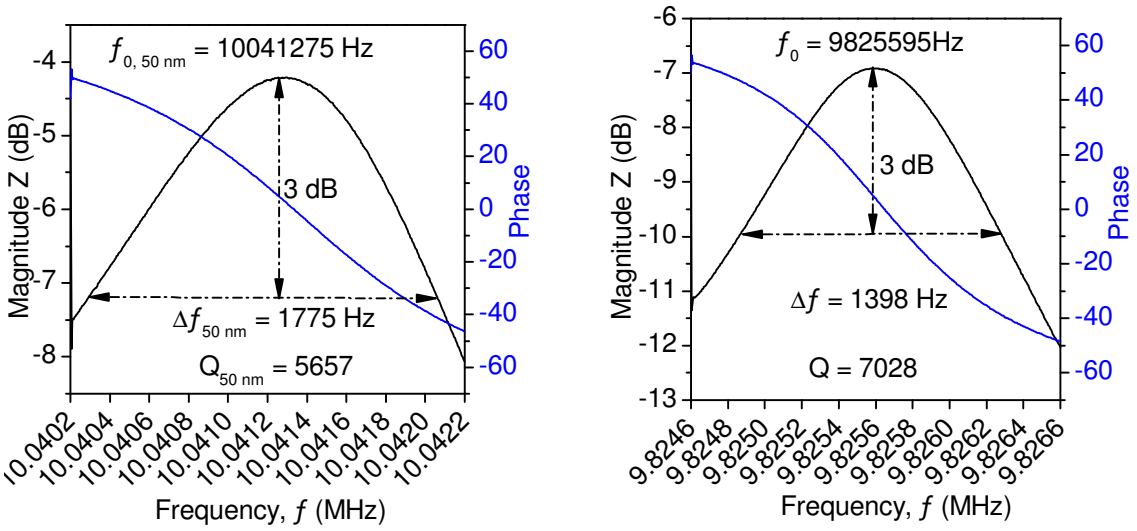

a) Non-modified Thin Au film **b)** Modified QCM following electrodeposition

Figure 2.9: Network analyser data of magnitude and phase of 10 MHz QCM resonator (a) deposited with 50 nm Au thin film and (b) 100 nm film after electrodeposition of Au.

2.4 Surface Characterization

2.4.1 Scanning Electron Microscope (SEM)

SEM characterization was performed on a FEI Nova SEM (Nova 200) instrument with an AMETEK energy dispersive X-ray (EDX) system operated at an accelerating voltage of 10 and 30 kV for imaging and EDX analysis respectively.

2.4.2 X-Ray Diffraction (XRD)

XRD data were obtained with a Bruker D8: Discover with fitted General Area Detector Diffraction System (GADDS). The system was fitted with a copper tube (Cu Ka radiation). Diffraction patterns were run using a 0.5mm colorimeter operating at 40kV and 40mA. The detector data collection range was ±15° and so the set detector 2θ values (25°, 55° and 70°) at omega values (12.5°, 27.5° and 35°) were ran for a total of 30 minutes (10 minutes at each position) to collect the diffraction peaks for each sample analysed.

2.4.3 X-ray Photoelectron Spectroscopy (XPS)

XPS measurements of the relevant surfaces were carried out on a VG MicroTech ESCA 310F instrument at a pressure better than 1 x 10^{-9} Torr. The general scan and C 1s, Au 4f, Pb 4f and Ni 2P core level spectra for the respective samples were recorded with un-monochromatized Mg Ka radiation (photon energy = 1253.6 eV) at a pass energy of 20 eV and electron takeoff angle of 90°. The core level binding energies (BEs) were aligned with the adventitious carbon binding energy of 285 eV.

2.4.4 Atomic Force Microscopy (AFM)

AFM tapping mode measurements were performed on the relevant films using a NanoScope IIIa Multimode AFM (Vecco, USA) under air-ambient conditions (20℃ and 40 %RH). MikroMasch Ultrasharp (NSC15/Al BS) silicon etched SPM probes with a backside reflective Al coating, a spring constant of 40 N m^{-1}, a radius of curvature of tip <10 nm, a resonant frequency of approximately 325 kHz, and cantilever dimensions of 125 µm x 35 µm x 4 µm were used. Minor scan line errors were removed using AFM software. More than 5 AFM scans were carried out on different locations for each sample, and the results presented within this thesis are typical examples. The AFM scan analysis software provided by Vecco Co. (USA) with the AFM instrument was used for surface analysis.

2.4.5 Secondary Ion Mass Spectrometry (SIMS)

Several days after the controlled Hg vapour exposure, SIMS (Cameca IMS 5f) depth profiles were performed using a cesium ions (Cs^+) primary ion beam of 3 keV net impact energy, 1.5 nA beam current and a raster area of 500 µm x 500 µm. To eliminate potential edge effects,

a combination of lens setting was used to restrict the secondary ion yield to a 100 μm diameter region within the centre of the rastered area. The SIMS measurements were conducted at the Australian Nuclear Science and Technology Organisation (ANSTO) facility in NSW, Australia through several Australian Institute of Nuclear Science and Engineering (AINSE) grants.

2.4.6 Inductively Coupled Plasma Mass Spectrometry (ICPMS)

ICPMS measurements were performed using a HP4500 series 300, ShieldTorch System ICPMS instrument. The samples analysed by ICPMS include the Hg calibration trapping solutions (discussed in section 2.2.1.1) as well as the solution containing the digested Au or silver electrodes exposed to Hg (discussed in chapter 3). The solutions were then diluted such that the final solution for analysis contained no more than 5 ppb Hg and had a clear colour (no potassium permanganate's purple colour could be visible); in order to avoid detector memory effects and blockage of sampling tubes on the HP4500. All solutions were spiked with 100 ppb terbium (Tb) as the internal standard and 100 ppb Au to keep Hg solution stable and draw all the Hg out of the sampling tubes on the HP4500. All solutions contained 5% HNO_3 with less than 0.02% of HCl for more accurate results. The sampling tubes of the ICPMS were washed with 5% HNO_3 solution as well as milli-Q water before each sample solution was analysed for better accuracy. The control software was set to analysed each sample three times before an average Hg concentration was displayed and recorded.

2.4.7 Electrochemical Surface Area Analysis

Electrochemical surface areas of the selected layers were determined in order to distinguish whether the improved sensing capability of the modified sensors was solely due to their higher surface area or whether their surface morphology, crystallographic orientation and other surface factors also played some role in improving their performance. The surface area of the samples was electrochemically determined by calculating the charge required for reducing the monolayer oxide as described by Rand and Woods.[274] The geometrical surface area of all the surfaces was 0.32 cm^2 as determined from the mask dimensions used to e-beam deposit the metal electrodes on the quartz substrates. The linear sweep voltammetry curves are shown where required throughout this thesis.

Voltametric experiments were conducted at 20 ± 2°C with a CH Instruments (CHI 760C) electrochemical analyser in an electrochemical cell that allowed reproducible positioning of the working, reference and auxiliary electrodes and a nitrogen inlet tube. An e-beam evaporated Au film was used as the working electrode (i.e. the QCM electrode), which was washed in acetone and methanol followed by drying in a stream of dry nitrogen gas prior to

use. When a 1.6 mm diameter gold electrode (BAS) was used as the working electrode it was polished with an aqueous 0.3 μm alumina slurry on a polishing cloth (Microcloth, Buehler), sonicated in deionized water for 5 min, and dried with a flow of nitrogen gas prior to use. The reference electrode was Ag/AgCl (aqueous 3 M KCl). For voltammetric studies the counter electrode was a Pt wire. Before any electrochemical experiment commenced, the electrolyte solutions were degassed with dry nitrogen for at least 10 min prior to any measurement.

2.5 Hg Testing Patterns

This section explains some general test patterns that were applied to the sensors. The various investigations in chapters 3 to 7 specify each time a test pattern was used.

2.5.1 Pre-treatment

Before commencing long-term testing, preliminary results showed the necessity to pre-treat the sensors to stabilize them. This procedure involved Hg exposure of the sensors at high temperatures for several days before testing at lower operating temperatures. The pre-treatment procedure is illustrated in Figure 2.10 below.

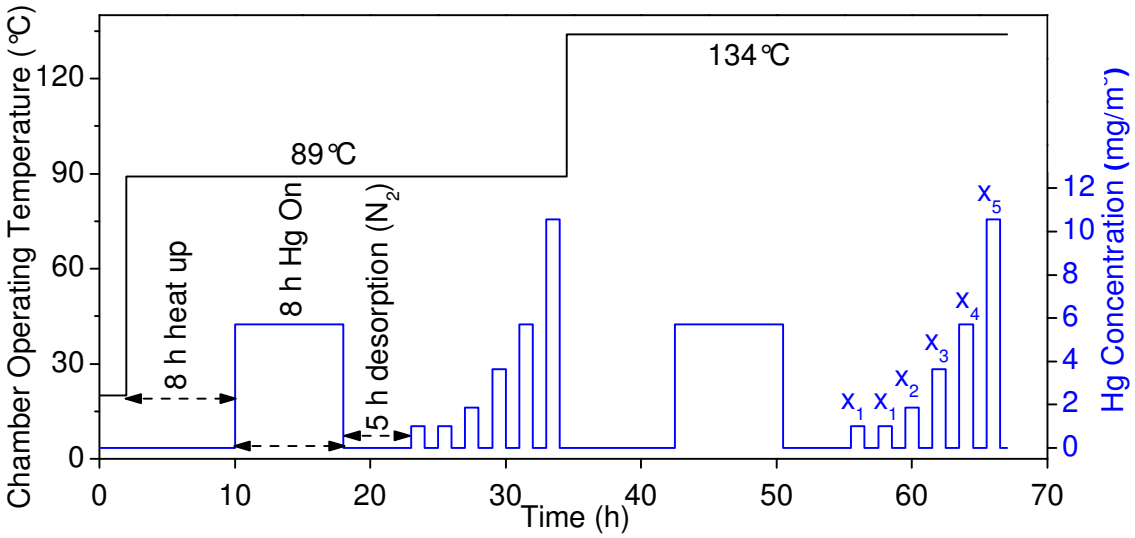

Figure 2.10: Test pattern for sensors pre-treatment procedure

The pattern shown was found to achieve the optimum stability over the shortest time period. The prefix x_n where n = 1, 2, 3, 4 and 5 refer to Hg concentrations of 1.02, 1.87, 3.65, 5.70 and 10.55 ± 0.05 mg/m^3, respectively.

2.5.2 Temperature Profile

Following pretreatment, all of the sensors were tested towards the five Hg concentrations at the nine operating temperatures as shown in Figure 2.11, except where specified. The tests were performed from high to low operating temperatures. This was advantageous as it was

thought that most of the Hg from a previous test would be desorbed because of the higher operating temperature, thus reducing their effect in the next lower operating temperature. Each concentration of Hg was exposed for 1 hour, thereafter sensors were regenerated by N_2 flow alone for the next hour while holding them at the same operating temperature and pressure. This is referred to as a single pulse. Five pulses, starting from low and finished with the highest Hg vapour concentration in sequence is referred to as a 'set'. A 1-hour desorption period was chosen in order for the Hg generator to have enough time to re-equillibrate for the next Hg concentration being exposed.

The short – 1 hour adsorption time was used to reduce amalgamation effects while still obtaining a large QCM response magnitude. The 1 hour period was also sufficient for the Hg generator to re-equilibrate for the next pulse having a different Hg vapour concentration.

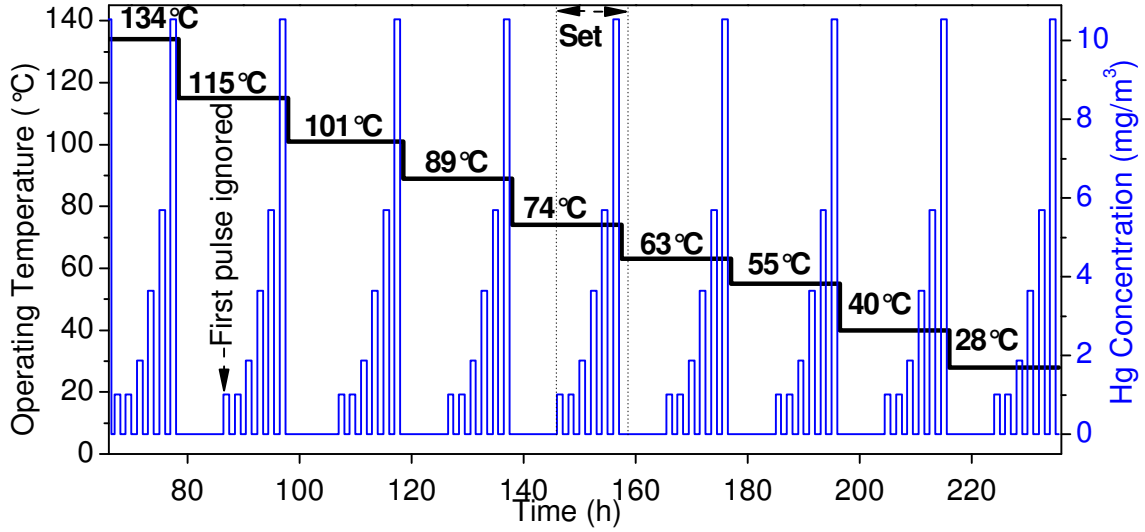

Figure 2.11: Test pattern for sensor temperature profile

The first pulse of 1.02 mg/m^3 Hg concentration from the set at each operating temperature was ignored (Figure 2.11) in order to remove ambiguities resulting from longer recovery periods during the operating temperature change over.

The same rough Au electrodes QCM was used throughout the 8 temperature increments. The reason new QCMs were not used for each operating temperatures was because each QCM would have a different mass sensitivity in relation to its fundamental frequency. For example, from Sauerbrey's equation (equation 1.2 in chapter 1) a 1% change in f_0 (from 10MHz to 10.1MHz) would result in more than 2% change in the mass sensitivity of the QCM, resulting in a slightly different response magnitude for the same concentration of Hg vapour. Furthermore, it is known to be next to impossible to fabricate two QCMs with exactly the same characteristics[198]. Fortunately the error involved in using the same QCM sensor for multiple pulses of Hg vapour was found to be minimal.[16] Therefore considering time

restrictions, the use of new sensors for each tested Hg vapour concentration and operating temperature was deemed impractical, the process of which would result in 45 QCM sensors being tested. Furthermore, previously published data from this thesis has shown pre-treatment of the sensor electrodes with mercury (amalgam surface) is necessary in order to stabilise the sensors and obtain a representative and repeatable response[16].

2.5.3 Hg Sensing in the Presence of Interferent Gases

Following temperature profile experiments, the sensors with the best potential to be used as Hg vapour sensor were further tested towards interferent gases with a test pattern shown in Figure 2.12 below. This test pattern is referred to as 'set U'.

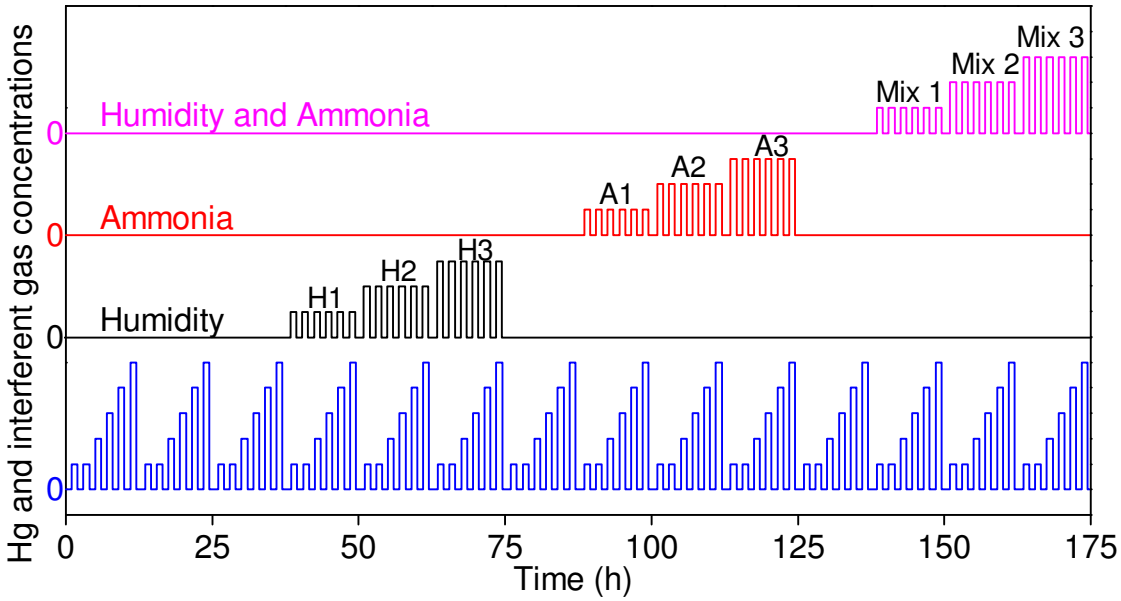

Figure 2.12: Test pattern for exposure towards Hg in the presence of interferent gases.

This test pattern and the test patterns shown in sections 2.6.4 and 2.6.5 were generally performed at an operating temperature of 89°C, except where specified. The humidity levels H1, H2 and H3 refer to 4.2, 7.6 and 10.4 mg/m^3 H_2O concentrations respectively. The ammonia levels A1, A2 and A3 refer to 847, 1694 and 2541ppm respectively and are achieved by varying the flow of ammonia from the gas cylinder (3388ppm). The mixed interferent gases' mix 1, 2 and 3 refer to H1+A1, H2+A1 and H1+A2 respectively. No interferent gases were exposed to the sensors during the 1 hour Hg desorption periods between Hg exposures, in order to duplicate real world sensing and regeneration events. Five sets of Hg pulses are run while testing for the affect of presence of interferent gases. Three sets were run before the introduction of humidity, one set before the introduction of ammonia and one set before the introduction of mixed interferent gases were performed.

2.5.4 Memory Effect – Hg Concentration Fluctuations

The test pattern shown in Figure 2.13 was used to study the effect of the previous Hg concentration on the next Hg concentration pulse. This test pattern was run at 89°C for the sensors presented in chapter 7. This tested the sensors for any memory effect on response magnitude and is referred to as 'set V_a' where a =1, 2 or 3 for the first, second and third repeat of the test pattern on a particular sensor. The test pattern was used to determine if the previously tested concentration of Hg influences the subsequent sensor response (i.e. testing for memory effects). For example, the 1.02 mg/m^3 pulse was tested at least 5 times, where it was tested after a pulse of each of the other concentrations (1.87, 3.65, 5.7 and 10.5 mg/m^3).

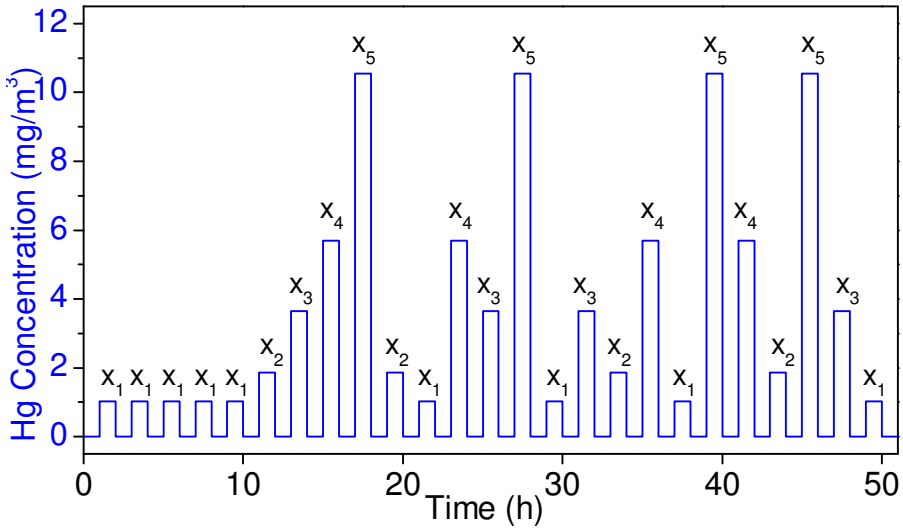

Figure 2.13: Test pattern to observe the memory effect of preceding pulse of varying Hg vapour concentrations.

This test pattern was also used in the presence mix 2 and mix 3 interferent gases levels during the mercury exposure period of the pulse and are referred to as 'set V2' and 'set V3' respectively. This was conducted to simulate interference, which meant that dry N_2 was only used for regeneration for all pulses (as would most likely be used in a plant trial situation).

2.5.5 Hg Sensing – Interferent Gases Concentration Fluctuations

The purpose of the test pattern shown in Figure 2.14 was to determine the effect of varying the interference levels on the sensors at a constant Hg vapour concentration. This test pattern, referred to as 'x_n set W', was performed at an operating temperature of 89°C towards all the five Hg vapour concentrations. No other combination of interferent gases levels were tested due to time constraints. This test pattern was employed only for the sensors presented in chapter 7 due to their high prospect of being used as online sensors in the future, based on their stability and high affinity towards Hg vapour. The test pattern was used to determine the effect of variable NH_3 and H_2O on consecutive pulse of Hg at a fixed concentration. Again, dry N_2 was only used during the regeneration phase of each pulse, and NH_3 and H_2O

were exposed to the sensor during the Hg exposure period. As well as ammonia and humidity, the sensors presented in chapter 7 were also exposed to other interferent gases (acetone, MEK, Acetaldehyde, and dimethyl disulphide) in a similar test pattern which is described therein.

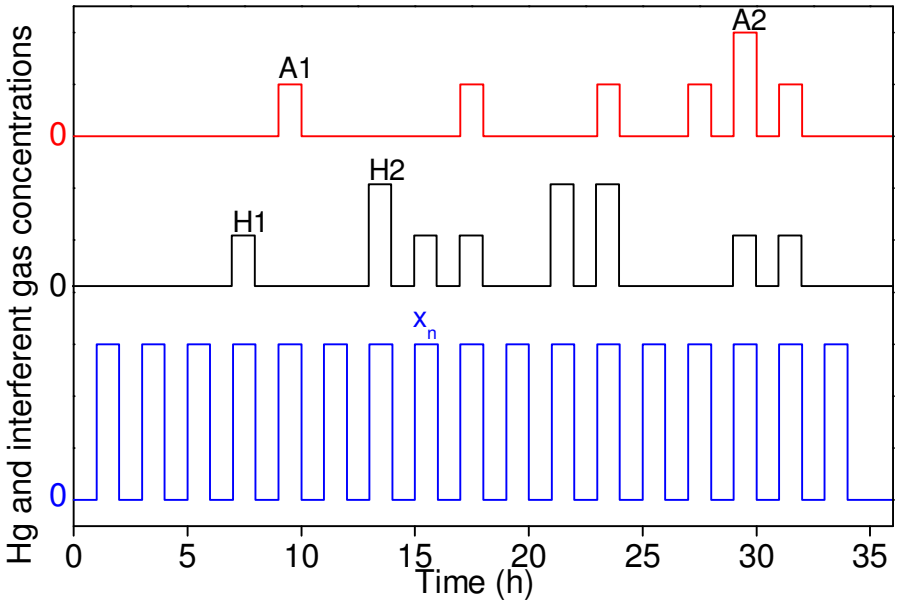

Figure 2.14: Test pattern to determine the effect of varying levels of interferent gases at constant Hg concentration. The symbol x_n (where n=1 to 5 referring to 1.02 to 10.55 mg/m^3 Hg) refers to the Hg vapour concentrations tested.

2.5.6 Mercury Saturation of Au Thin and Ultra-thin Films

The test pattern shown in Figure 2.15 was used to study Hg sorption and desorption on Au thin and ultra-thin films.

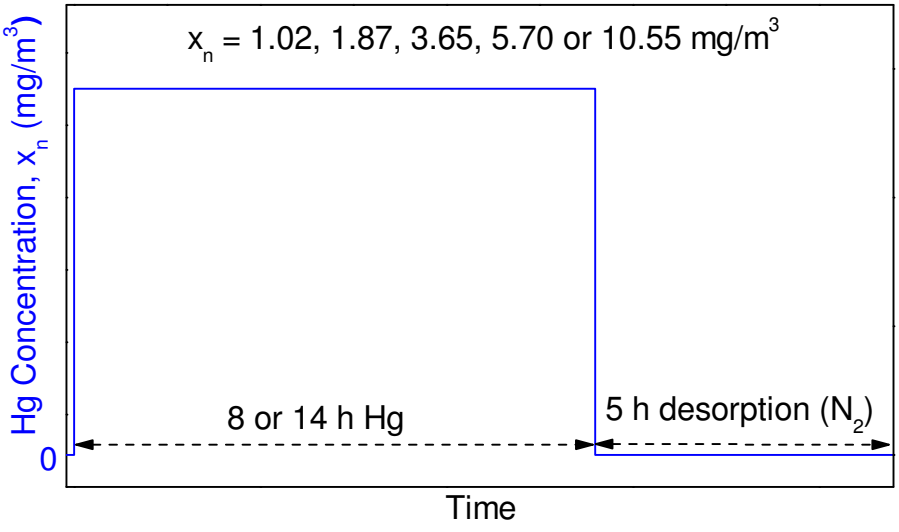

Figure 2.15: Hg sorption and desorption test pattern used for Au thin films (8 h Hg exposure for Au films between 50 and 200 nm) and Au ultra-thin films (14 h Hg exposure for Au films between 10 to 40 nm).

A Hg exposure period of either 8 hours (Au thin films) or 14 hours (Au ultra-thin films) was used at various Hg vapour concentrations and operating temperatures. Thereafter, a recovery period (using dry nitrogen) of 5 hours was used. The increased exposure time of 14 hours for the Au ultra-thin films (chapter 5) rather than 8 hour periods used for Au thin films (chapter 4) was due to the high dependency of the experimental outcomes on the saturation (or near saturation in the case of Hg-Au system) of Au with Hg vapour.

In summary, the experimental setup, sensor fabrication, instrumentation and literature considerations during the course of the present work are presented. The test patterns described in this chapter will be refered to in the proceeding results chapters throughout this thesis.

2.6 References

(1) McNerney, J. J.; Buseck, P. R.; Hanson, R. C. *Science* **1972**, *178*, 611-612.
(2) Joyner, R. W.; Roberts, M. W. *Journal of the Chemical Society Faraday Transactions 1* **1973**, *69*, 1242-1250.
(3) Nowakowski, R.; Pielaszek, J.; Dus, R. *Applied Surface Science* **2002**, *199*, 40-51.
(4) Fialkowski, M.; Grzeszczak, P.; Nowakowski, R.; Holyst, R. *The Journal of Physical Chemistry B* **2004**, *108*, 5026-5030.
(5) Atkins, P. W. *Physical Chemistry*; 2nd ed.; Oxford University Press: Oxford, Great Britain, 1982.
(6) Nott, B. R. *Water, Air, & Soil Pollution* **1995**, *80*, 1311-1314.
(7) Nilsson, S.; Klett, O.; Svedberg, M.; Amirkhani, A.; Nyholm, L. *Rapid Communications in Mass Spectrometry* **2003**, *17*, 1535-1540.
(8) Hoogvliet, J. C.; van Bennekom, W. P. *Electrochimica Acta* **2001**, *47*, 599-611.
(9) Sexton, B. A.; Feltis, B. N.; Davis, T. J. *Sensors and Actuators A: Physical* **2008**, *141*, 471-475.
(10) Ali, M. B.; Bessueille, F.; Chovelon, J. M.; Abdelghani, A.; Jaffrezic-Renault, N.; Maaref, M. A.; Martelet, C. *Materials Science and Engineering: C* **2008**, *28*, 628-632.
(11) Moody, N. R.; Adams, D. P.; Medlin, D.; Headley, T.; Yang, N.; Volinsky, A. *International Journal of Fracture* **2003**, *120*, 407-419.
(12) George, M. A.; Glaunsinger, W. S.; Thundat, T.; Lindsay, S. M. *Thin Solid Films* **1990**, *189*, 59-72.
(13) Al Kobaisi, M. Doctor of Philosophy, Royal Melbourne Institue of Technology University, 2008.
(14) Zimmermann, B.; Lucklum, R.; Hauptmann, P.; Rabe, J.; Büttgenbach, S. *Sensors and Actuators B: Chemical* **2001**, *76*, 47-57.
(15) Rand, D. A. J.; Woods, R. *Journal of Electroanalytical Chemistry* **1971**, *31*, 29-38.
(16) Sabri, Y. M.; Ippolito, S. J.; Tardio, J.; Sood, D. K.; Bhargava, S. K.; Mullett, M.; Harrison, I.; Rosenberg, S. In *8th International Alumina Quality Workshop* Darwin, Australia, 2008, p 260-266.

Chapter III

Investigation of Hg Interaction with Various Thin Metal Films and Surface Morphologies

The influence of Hg sorption and desorption characteristics on Au and Ag thin films which have been e-beam deposited on optically polished or mechanically roughened quartz substrates are presented in this chapter. Additionally, QCMs with Ni and Ti thin film electrodes are shown to undergo minimal Hg vapour sorption thus confirming the correlation between metal solubility in Hg and metal affinity for Hg vapour during sensing. The Au and Ag QCMs were exposed to Hg vapour and the sensors' dynamic response is used to calculate t_{90} and sticking probability of Hg to the thin metal films. The thin films were then characterized using AFM, SEM and SIMS depth profiling. Thereafter they were acid digested and analysed using ICP-MS. Hg distribution was found to follow an asymptotic function through the depth of each thin metal film investigated. Furthermore, the optimal thin film (in terms of Hg sorption and desorption kinetics as well as high Hg affinity) is tested towards Hg vapour in the presence of interferent gases (ammonia and humidity).

Part of the work presented in this chapter has been published:
Sabri, Y.M; Ippolito, S.J; Tardio, J; Atanacio, A. J; Sood, D. K and Bhargava, S. K; "Mercury diffusion in gold and silver thin film electrodes on quartz crystal microbalance sensors" *Sensors and Actuators B: Chemical*, **2009,** 137(1), pp. 246 – 252.

3.1 Introduction

QCM based sensors are highly sensitive towards surface perturbations and can be used to monitor mass uptake, density, elasticity and temperature changes, to name only a few parameters. With regards to monitoring Hg vapour on an Au or Ag thin film based QCM, a combination of phenomena may occur on the thin metal film surface. These include Hg sorption (adsorption and absorption), amalgamation, diffusion and desorption.[61,78,79,89] Understanding these phenomena in the gas-solid system is a key element in analyzing QCM based Hg vapour sensing events.

The affinity of Au and Ag towards mercury is well known[159,275] but not very well understood[276] as it is difficult to study due to the ease with which the amalgamation process takes place.[277] Only one study[93] was found concerning the effect of Hg sorption behavior correlated with the substrate morphology of the Hg-Au system. It was found that rougher Au films promote Hg diffusion into the films' grain boundaries. No studies concerning the influence of morphology on Hg sorption and desorption for the Hg-Ag system were found. Therefore the influence of morphology on the sorption, amalgamation, diffusion, and desorption behavior of Hg on Au and Ag thin films deposited on either mechanically roughened or optically polished quartz substrates was investigated as part of this research program.

Data extracted from Guminski et al.[70] (and references within) and presented in Figure 3.1 shows the solubility of Au, Ag, Ni and Ti in mercury at various temperatures. It is thought that the high affinity of Au and Ag films towards Hg vapour may be correlated with the metals' high solubility in mercury.

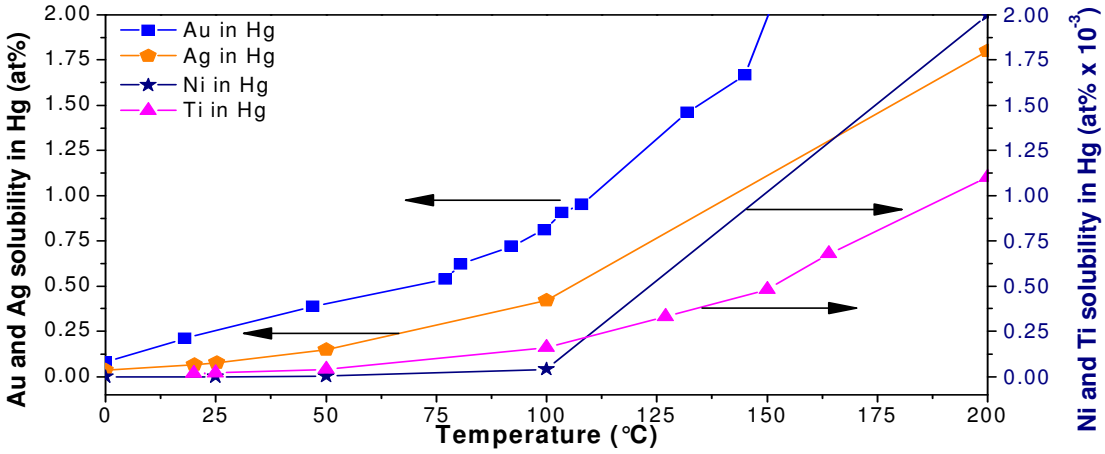

Figure 3.1: Solubility of gold, silver, nickel and titanium in mercury

Ni and Ti, on the other hand, are observed to have 3-6 orders of magnitude lower solubility in mercury than that of Au and Ag over the temperature range 0-200°C. Thus, these metals are

expected to show low affinity towards Hg vapour thus confirming the correlation of metal solubility in Hg with that of metal affinity towards Hg vapour. Furthermore, the lack of affinity of Ti with Hg vapour would suggest that the Hg diffused into the Au layer during sensing experiments may not pass beyond the Ti adhesion layer (this adhesion layer was used for all fabricated sensors throughout this research program). Furthermore, the low affinity of Ni towards Hg would justify its use as the control film during one of the Au surface modification experiments (presented in chapter 6).

3.2 Hg Sorption/Desorption of Surfaces Investigated

3.2.1 Metals Types Investigated

Thin films of Au and Ag each with thickness of 115 nm were e-beam deposited on quartz substrates (as described in chapter 2) to serve as the QCM electrodes as well as the Hg sensitive layers. Ti and Ni QCMs were fabricated by depositing 300 nm thick electrodes at room temperature. Thicker films were chosen for the Ni and Ti to ensure high Q-factors for the fabricated QCM sensors.

3.2.2 Surface Types Investigated

Optically polished and mechanically roughened quartz substrates were used to control the surface morphology of the metal surfaces. The deposition of the chosen metals on these substrates (bottom up approach) ensured having two different types of morphologies of the same metal type.

3.2.3 Surface Morphology – SEM

The SEM micrographs of the Au-polished, Ag-polished, Au-rough, Ag-rough, Ni-polished and Ti-polished are shown in Figures 3.2a to f, respectively. The various film type and morphology produced are expected to have different Hg sorption behaviours. Although deposited at similar conditions (i.e. deposition rate, temperature etc.), the Au-polished (Figure 3.2a) is observed to contain grains of smaller size than that of the Ag-polished (Figure 3.2b). Similar trend is observed for their respective mechanically roughened surfaces (Figures 3.2c and 3.2d). Ni-polished (Figure 3.2e) and Ti-polished (Figure 3.2f) are also observed to produce different surface morphology when deposited on optically polished quartz substrates.

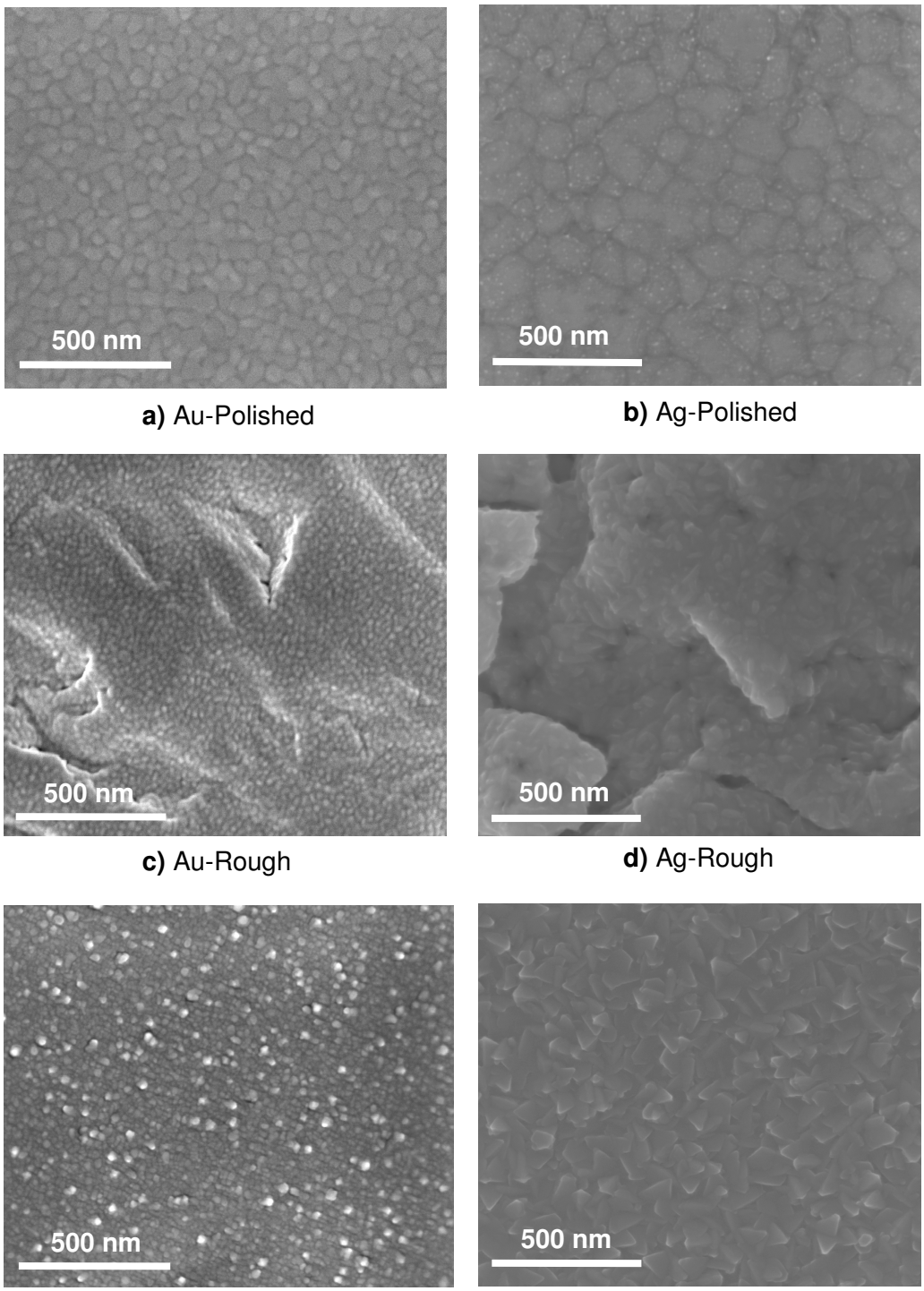

a) Au-Polished **b)** Ag-Polished

c) Au-Rough **d)** Ag-Rough

e) Ni-Polished **f)** Ti-Polished

Figure 3.2: SEM images of QCM electrode surfaces

3.2.4 Determination of Equilibrium Time

Preliminary tests were conducted in order to determine the time required for the Au surface to reach saturation level under a constant Hg concentration exposure. Saturation is usually described as the point where the adsorption rate becomes equal to that of the desorption rate.[267] However, for the case of Hg sorption on Au surface, saturation occurs when a decrease in the adsorption rate is observed due to gradual diffusion of Hg in the Au

films.[78,278] Following saturation, the thin film surfaces were exposed to dry nitrogen in order to observe the fraction of Hg that may be desorbed off the surface.

As an initial step, the Au-rough QCM was exposed to Hg followed by dry nitrogen for extended periods of time in order to estimate the time required to saturate and regenerate the gold surface, respectively. The QCM response from the Hg and dry nitrogen exposure at Hg vapour concentration of 3.65 mg/m^3 and an operating temperature of 55℃ is shown in Figure 3.3. It can be seen that due to the Hg present on the gold surface from the first 8-hour Hg vapour exposure, a second pulse of 8-hour Hg exposure results in the sensor saturating around the same Δf value (~530 Hz) as the first exposure. Although the signal from the second 8-hour Hg exposure is observed to drop by ~150 Hz than the first 8-hour Hg exposure pulse, the total Hg (or total Δf from when t=0) adsorbed on the surface following saturation is found to be similar.

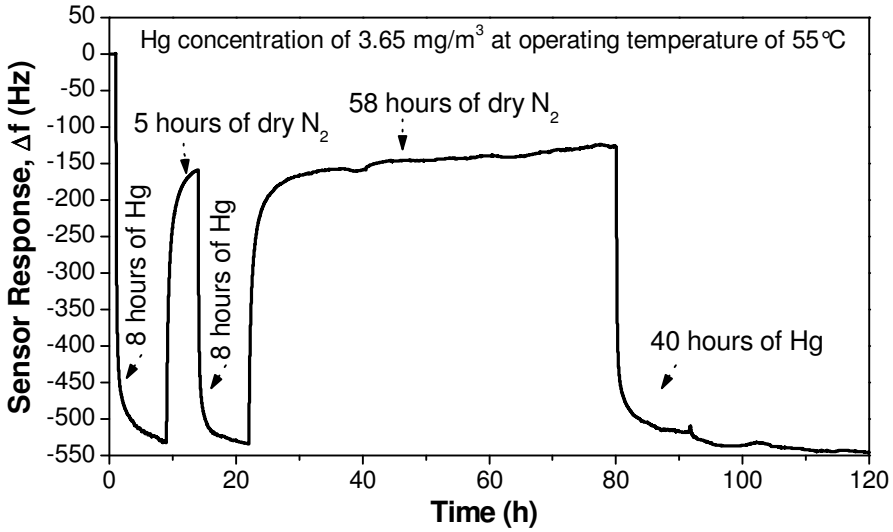

Figure 3.3: Sorption and desorption behaviour of Hg exposed to Au-rough QCM. The influence of long Hg exposure as well as long desorption times may be observed.

A similar observation was made for the 40-hour Hg exposure period where the total Hg on the Au surface is observed to be similar to that of the first 8-hour Hg exposure period before saturation level has been reached. The slow increase in response magnitude during the 40 hour Hg exposure indicates a small accumulation of Hg on the sensor electrode surface. In addition, following the first 8-hour Hg sorption and 5-hour desorption period, the pre-exposed surface is observed to undergo a similar amount of Hg sorption thereon to reach saturation. It then follows that an 8-hour Hg exposure pulse is sufficient to reach saturation point. Coincidentally, a maximum 8 hour mercury exposure period is also the time-weighted average (TWA) recommended by the National Institute for Occupational Safety and Health (NIOSH) at Hg concentration of 0.05 mg/m^3.[14]

The 150 Hz drop in response observed in the second 8-hour compared to the first 8-hour Hg exposure pulse is equivalent to 658.7 ng/cm^2, which is the amount of Hg that has amalgamated with Au and is not desorbed even after extended periods of exposure to dry nitrogen. It then follows that Hg amalgamation is relatively higher on a fresh unexposed Au surface than that of the Hg exposed Au surface. In addition, it is observed that better repeatability in response magnitude may also be obtained with the pre-exposed Au surface.

Approximately 100% recovery (compared to the initial contaminated state) is reached when the Au surface is exposed to dry nitrogen following the 8-hour Hg exposure period. The desorption of Hg beyond the initial 5 hour period was found to be minimal as shown in Figure 3.3, thus justifying the chosen 5 hour desorption time used in the experiments following the saturation of the films with Hg. That is, the amount of Hg desorbing off the Au film is observed to be similar whether a 5-hour or 58-hour recovery time is used.

Based on these findings, the QCM sensors were exposed to Hg vapour for 8 hours followed by exposure to dry N_2 for a further 5 hours. No prior pre-treatment of the surfaces was performed. In order to estimate the remaining amalgamated/adsorbed Hg content on the Au and Ag electrode surfaces, the QCM devices were made and tested in duplicates before being digested in aqua regia (1:3 concentrated HNO_3:HCl) directly following their removal from the chamber. The solution was then analysed by ICP-MS with the procedure detailed in Chapter 2. The duplicate samples were characterized by AFM, FE-SEM and SIMS. QCM results revealed good repeatability of around ±0.6% of the mean response magnitude between duplicate tests and of similar substrates.

3.2.5 Morphology Influence on Hg Sorption and Desorption Characteristics

The dynamic response of the six QCM devices, namely, Ti-polished, Ni-polished, Ag-polished, Au-polished, Ag-rough and Au-rough electrode QCMs towards 3.65 and 1.02 mg/m^3 of Hg vapour are shown in Figures 3.4a and b, respectively. No detectable Hg vapour sorption occurred on the Ni or Ti QCM electrodes and so no further characterization was deemed necessary for these two samples.

The AFM images of the Au-polished, Ag-polished, Au-rough and Ag-rough AFM images prior to Hg exposure are shown in Figure 3.5. The average roughness (Ra) and root-mean-square roughness (Rq) over a 500 x 500 nm scan size are also shown for the respective thin films. The AFM measurements revealed the Au-Polished QCM electrodes have a 4.75% larger surface area than its projected surface area. Similarly Au-rough, Ag-polished and Ag-rough were found to have 18.9, 7.7 and 41.8% higher surface areas than their projected surface areas.

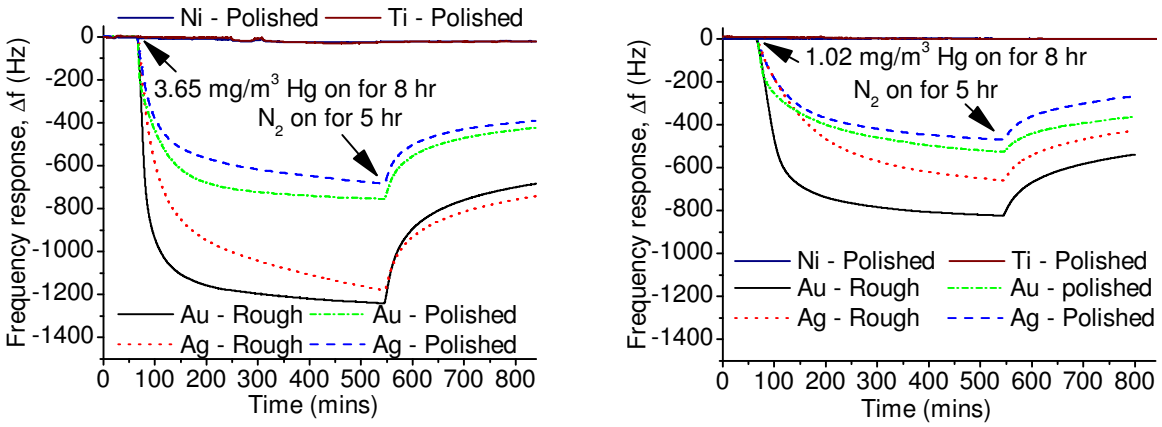

a) 3.65 mg/m^3 Hg **b)** 1.02 mg/m^3 Hg

Figure 3.4: Sensor response of the Au-/ Ag-/ Ni-/ Ti-polished and Au-/ Ag-rough thin film QCMs exposed to Hg for 8 h followed by dry N_2 for 5 h at 40℃.

The smaller grain size of the Au-rough, as confirmed by SEM images, is not apparent in AFM characterization due to the much roughened substrates. It may be observed that the much larger features of the roughened substrate are formed of many smaller gold grains that follow the topology of the underlying roughened quartz.

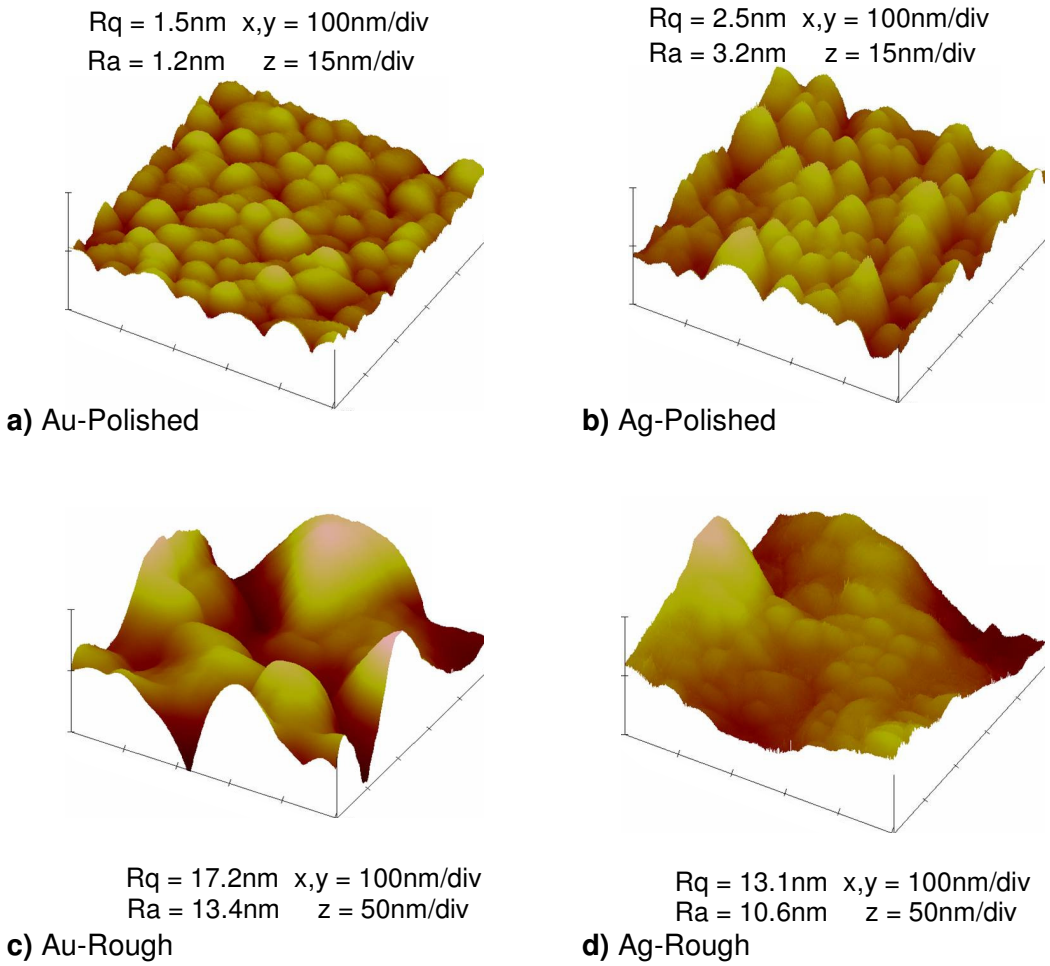

a) Au-Polished **b)** Ag-Polished

c) Au-Rough **d)** Ag-Rough

Figure 3.5: AFM images of QCM electrode surfaces

The roughened QCM crystals are expected to have a higher response towards Hg vapour than their polished counterparts mainly due to their higher surface areas and smaller grain size which would result in many more grain boundaries and possibly more defect sites. The QCM responses towards Hg vapour (Figure 3.4) show the Au-rough to exhibit the highest response magnitude even though the Ag-rough has a 19.3% higher surface area than the Au-rough QCM. Similarly, Au-polished QCM is found to have a larger response magnitude than the Ag-polished substrate, although having lower surface area than its Ag-polished counterpart.

The ICP-MS and QCM results obtained for the Au and Ag samples shown in Figure 3.4a are summarized in Table 3.1. The adsorption and desorption rates for the initial two minutes are reported. The initial rate of adsorption is observed to be largest for the Au-polished. However, during the desorption phase (time >550 min in Figure 3.4a), the Au-rough is found to dominate having the highest desorption rate of the four samples (Table 3.1). It is worth noting that at the end of the desorption period, some of the adsorbed Hg is not desorbed from the surfaces, indicating amalgamation of Hg with the Au thin films. This is evident from the QCM baseline shift between t = 0 and t = 800 minutes in Figure 3.4a.

At the end of the 8 hour Hg exposure period, the Ag-rough and Au-rough were observed to adsorb a larger quantity of Hg than their respective polished counterparts, with Au-rough sample having adsorbed 5% more Hg then the Ag-rough. The highest desorption rate occurred on the Au-rough and Ag-rough substrates with the Au desorbing at more than double the rate of Ag in the initial two minute desorption time following the 8 hour Hg exposure period (see **bold** values in Table 3.1).

Table 3.1: QCM adsorption/desorption data of Hg on Au-/ Ag-rough and Au-/ Ag-polished thin films.

Sample	Adsorption Rate ($\mu g.cm^{-2}.min^{-2}$)	Total Adsorbed ($\mu g.cm^{-2}$)	Desorption rate ($\mu g.cm^{-2}.min^{-2}$)	Total Desorbed ($\mu g.cm^{-2}$)	ICP-MS ($\mu g.cm^{-2}$)
Ag-Polished	0.079	3.000	0.016	1.290	0.775
Au-Polished	0.213	3.320	0.020	1.460	0.706
Ag-Rough	0.087	5.190	**0.024**	1.940	**1.380**
Au-Rough	0.160	5.450	**0.050**	2.440	**1.190**

The higher desorbing property of gold was confirmed when the samples were immediately digested in aqua regia solution following the 5 hour desorption period, and the solution was analyzed by ICP-MS. The total Hg content in the Ag-rough films was found to be 16% by mass more in comparison to the Au-rough film based QCM (Table 3.1), indicating Ag retained more Hg than the gold surfaces even after the 5 hour desorption period. The results show that Hg desorption occurs faster from both the Au-polished and Au-rough QCMs than the Ag counterparts. The high desorption ability indicates that gold is the better candidate for Hg sensing applications.

3.2.6 Morphology Influence on Sensor Response Time

Regarding sensor design, the response time of the QCM based sensors is also an important parameter. For most applications a short response time indicates a higher affinity towards the analyte. The required times for an analyte to adsorb or desorb from the substrate have been reported to depend on the diffusion coefficient of the analyte in the substrate.[279] The t_{90} parameter is used within the sensor community to define the time required to obtain 90% of the intensity of the equilibrium value for a given adsorption or desorption phase of a sensing process. The t_{90} was found to be the fastest for the Hg adsorption phase on the Au-rough QCM (Figure 3.4a), having reached 90% of the surface saturation within 93 minutes after exposure to a Hg vapour concentration of 3.65 mg/m^3. Similarly, the t_{90} for Au-polished, Ag-rough and Ag-polished were found to be 134, 263 and 230 minutes, respectively. Surprisingly all four samples had equal desorption t_{90} of 191.5 ±1 minutes indicating similar desorption kinetics for all 4 substrates. For the lower Hg concentration of 1.02 mg/m^3 (Figure 3.4b), the adsorption t_{90} for Au-rough and Au-polished had increased by 50% and 100%, respectively. However, the adsorption t_{90} for Ag-rough and Ag-polished had increased by around 5% each. Although the t_{90} response times are known to be dependent on the analyte concentration, the data provides an insight into the practicality of employing Ag and Au thin films as sensitive layers for Hg sensor applications. It is well known that with higher analyte concentrations much lower t_{90} are obtainable.[280]

3.2.7 Morphology Influence on Hg Diffusion Behaviour

The QCM samples that were set aside for SIMS characterization were analyzed 40 days after their exposure to Hg due to the lack of instrument availability. The samples were stored in air at room temperature during the 40 day period. The SIMS depth profiles shown in Figure 3.6 and Figure 3.7 are for the samples which were exposed to 3.65 mg/m^3 Hg at 40°C (Figure 3.4a). Each sample had undergone an 8-hour Hg exposure and 5-hour dry nitrogen recovery period.

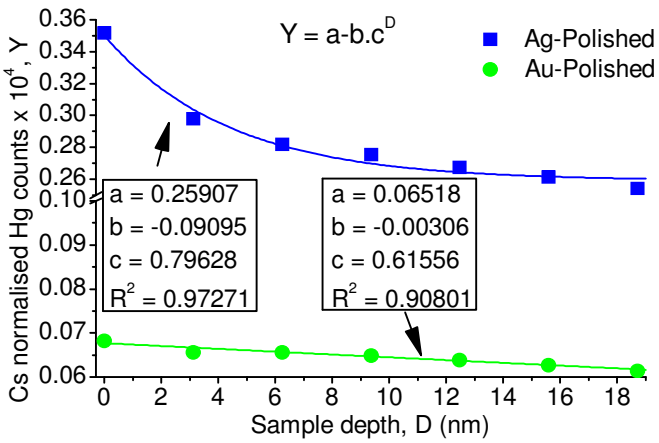

Figure 3.6: SIMS depth profile for Au-/Ag-polished thin film QCM electrodes.

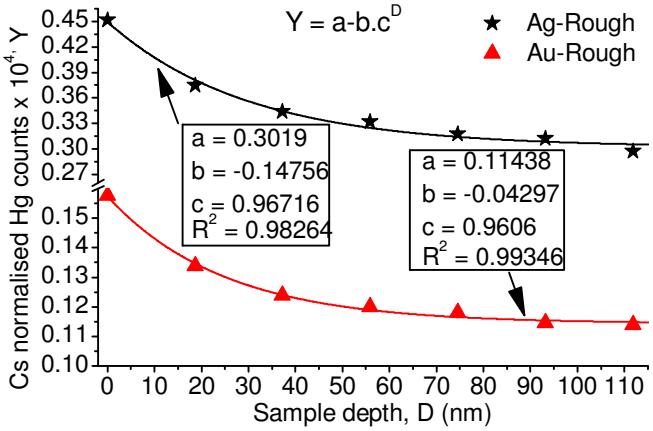

Figure 3.7: SIMS depth profile for Au-/Ag-rough thin film QCM electrodes.

The SIMS data clearly shows that Hg diffuses deeper into the Au-rough over the Au-polished substrate. Diffusion is the process by which matter is transferred from a region of higher to lower concentration in the system as a result of random molecular motions.[281] The depth to which Hg has diffused through the Au or Ag thin film is dependent on the difference between the total amount of Hg adsorbed during the initial exposure and the desorbed quantity during the controlled 5 hour desorption period. This difference has been obtained from the QCM data and confirmed with ICP-MS as shown in the last column of Table 3.1.

It was observed that ICP-MS repeatedly showed lower Hg content in each sample as compared to the QCM data derived from the Sauerbrey equation. This discrepancy may be due to some further uncontrollable desorption of Hg content while placing the device in the digestion solution directly after the 5h desorption phase of the experiment. That is, some of the adsorbed elemental Hg is expected to not digest/oxidize well in aqua regia,[282-284] as opposed to Au, and may evaporate during the digestion process. Acidic permanganate solutions and Hopcalite based catalyst adsorbent tubes are widely used and have been adopted as official assessment methods for oxidizing elemental Hg vapour that may be

desorbed off the sample surface.[285-287] These methods have not been used in this case due to the additional need to dissolve the Au film for the analysis of amalgamated Hg. It has been reported earlier that all the Hg may not be dissolved off the Au surface by acid dissolution alone[84] and so digestion of the sorbent metal film was also necessary in order to detect the amalgamated as well as the adsorbed Hg. In any case, with the current digestion method used, the ICP-MS results conclusively confirm the lower mercury content in Au samples as compared to Ag substrates with similar surface morphology.

The Hg depth profile in Au film presented in Figures 3.6 and 3.7 correspond to the conclusions made by George et al.[93] indicating that Hg vapour nucleates and diffuses better at surfaces with more surface defects and grain boundaries, thus showing that the rough surfaces do indeed provide a higher concentration of adsorption sites. Therefore the extent of roughness of the material used as the sensing layer for Hg sorption is suggested as the dominant factor in the extent of diffusion/amalgamation that occurs as the rougher surfaces are expected to have higher density of surface defects and grain boundaries.

The depth profiles show that from the 4 different surface configurations, the least amount of Hg diffusion occurred through the Au-polished sample. This further supports the mass change calculated from the Sauerbrey equation and the ICP-MS results (Table 3.1), showing that the Ag samples retain the larger proportion of the adsorbed Hg content when compared to the Au QCMs.

The trend lines (Figures 3.6 and 3.7) were fitted to the data points using best line of fit method. These fitted lines are found to best follow the asymptotic equation (equation 3.1):

$$Y = a - b.c^{D} \quad , \qquad \text{Equation 3.1}$$

where Y is the normalized Hg count, parameters a, b and c are constants, and D is the surface depth to which Hg has diffused.[89] Due to a lack of SIMS Au-Hg reference materials, the normalized Hg counts were not quantified. The parameters a, b and c for the three different Hg concentrations on the 4 different substrate configurations are shown in Table 3.2. The product of ($b.c^{D}$) in Equation 3.1 is indicative of the extent of diffusion occurring in a substrate while the parameter a indicates the flux/counts of Hg in the substrate where no further diffusion occurs. A high a value indicates the lower ability of Hg diffusion in the substrate.

Table 3.2: Parameters a, b and c (to three decimal places) for Equation 3.1.

	1.02 mg/m^3 Hg			1.86 mg/m^3 Hg			3.65 mg/m^3 Hg		
Sample	a	b	c	a	b	c	a	b	c
Ag-Polished	0.041	0.000	0.000	0.057	0.000	0.000	0.259	-0.091	0.796
Au-Polished	0.041	0.000	0.000	0.058	0.000	0.000	0.065	-0.003	0.616
Ag-Rough	0.274	-0.191	0.970	0.224	-0.163	0.971	0.302	-0.148	0.967
Au-Rough	0.085	-0.029	0.972	0.068	-0.041	0.985	0.114	-0.043	0.961

Due to the low QCM response for Ag-polished films and the high Hg diffusion observed in Figure 3.6, it is clear that Ag retains more of the adsorbed Hg than the Au films. The lower t_{90} and higher desorption rate observed for Au-polished than the Ag-polished may be due to lower Hg diffusion in the gold substrate observed in Figure 3.6. This may in turn be due to the initial lower Hg concentration on the Au surfaces before the substrates were left for 40 days prior to SIMS analysis. The higher a values observed for Ag substrates over the Au is a clear indication that diffusion is limited to within a few nanometres at the surface of the substrate even though high Hg counts are observed. This inconsistency maybe explained by further analysing parameters b and c in Equation 3.1.

It is observed from Equation 3.1 that the constant b is indicative of the amount of Hg diffusing into the bulk, while c is indicative of the kinetics revealing how much diffusion occurs within the depth. That is, a lower c value indicates less diffusion into the depth, while a higher b magnitude is an indicative for a greater drive for Hg to diffuse.

It is consistently observed that the a and b values for the Ag substrates are always higher than the Au substrates. The constant b for Ag-polished and Au-polished is observed to be zero (to three decimal places) and increases with a higher concentration of Hg in the gas stream. This is an indication of the Hg atoms' inability to diffuse through the optically polished metal surfaces at low flux; however this is not the case with Ag and Au-rough substrates where Hg is shown to diffuse into the bulk. At the higher concentration of 3.65 mg/m^3 of Hg, where diffusion conditions are more favoured in the polished substrates, Hg is observed to diffuse deeper into the Ag surface and is represented by the higher b magnitudes in Table 3.2. It is worth mentioning that it is the product of the constants b and c that determine the overall diffusion in the substrate and that the Hg diffusion in a given substrate may not be determined by each parameter separately.

The constant c for the rough surfaces is observed to be similar in magnitude for all concentrations of Hg vapour; however, the increase in constant c for the Ag film is more defined when comparing the polished substrates at the higher Hg concentration of 3.65mg/m^3. These higher c values are further evidence that Hg diffusion is more favoured in the silver substrates compared to their Au counterparts.

3.2.8 Surface Provoked Hg Affinity (Sticking Probability)

It is often argued when comparing substrates that high surface area to volume ratios are the reasons for high sorption capacity. In order to illustrate the domination of active adsorption sites on the roughened Au substrates, the sticking probability, S, was calculated. Sticking probability is defined as the ratio of the rate of adsorption (K_{ads}) to the rate at which atoms from the vapour phase strike a surface (Z_W). The S for Hg vapour on gold film is well known to be close to unity and decrease rapidly when the coverage exceeds ~0.5 to 1 monolayer at room temperature.[61,78,101,102,257] Sticking probability is also well known to depend on the Hg partial pressure (P, mmHg), the temperature (T, K) and the atomic mass of Hg (m, u)[101,267] as well as the adsorbate (which is Hg in this case) and the substrate (Au or Ag), as shown in Equations 3.2 and 3.3 where k is the Boltzmann constant:

$$S = K_{ads} \Big/ Z_W \qquad \text{Equation 3.2}$$

$$Z_W = P \times (2\pi mkT)^{-1/2} \qquad \text{Equation 3.3}$$

By calculating K_{ads} from the rate of the QCM response, and defining a monolayer, the affect of surface area may be diminished. However, some discrepancies appear in the literature defining one monolayer of Hg. The number of sites on a gold surface is reported to be ~1.4 x 10^{15} sites.cm^{-2}.[195] Assuming each site could support one Hg atom, one monolayer of Hg would consist of ~470 ng.cm^{-2}. By assuming that the mercury atoms are stacked side by side on the surface of a flat gold film with no surface morphology, Haskell et. al.[256] calculated a monolayer of Hg to be 285 ng.cm^{-2}. Other reports have indicated that one monolayer of mercury on a gold surface contains 360 ng.cm^{-2}.[146] Mercer[257] estimated the absorptive capacity of gold films to be 700 ng.cm^{-2}, while for Ag it was reported to vary significantly with aging (time) ranging from 2/3 to one and a half monolayers of Hg or approximately 360 ng/cm^2. Morris et al.[84] used X-ray photoelectron spectroscopy to estimate 1/70th of a monolayer of Hg on polycrystalline gold having ~2x10^{13} atoms/cm^2, which converts to a monolayer having 469 ng.cm^{-2}. For the purpose of this work, it is thought that the experimental value of 469 ng.cm^{-2} is a good representation for the mass of Hg monolayer. By differentiating the sensor response in Figure 3.4a with respect to time, to calculate K_{ads} and then using K_{ads} in conjunction with Equations 3.2 and 3.3 a plot of S versus the number of

monolayers of Hg can be obtained. However, the response time of the chamber housing the QCM sensors must be taken into account to determine the initial Hg vapour concentration being exposed to the QCM surfaces during the initial stages of each experiment; until equilibrium is reached. The increase in Hg concentration, and therefore Z_W, is estimated by assuming that Hg vapour entering the chamber is instantly dispersed throughout the chamber before exiting through the exhaust port. Based on this assumption, the change in Z_W was derived using Equation (3.4):

$$Z_W(t) = Z_\infty\left(1 - e^{-kt}\right) \quad \text{Equation 3.4}$$

where Z_∞ is the Z_W at equilibrium and estimated from Equation 3.3, t is the time (s) from which Hg enters the chamber and k is the system constant, which is dependent on the inlet/outlet gas flow rates as well as the chamber volume and the Hg concentration. From Equation 3.4 it is determined that in order to reach 99% equilibrium in the chamber (0.99 of Z_W), a time of ~11.5 minutes is required for each of the tested Hg concentrations. Taking this into account, the sticking probability of all four surface configurations, based on Equation 3.4 is shown in Figure 3.8a and 3.8b for Hg concentrations of 3.65 and 1.02 mg/m^3, respectively.

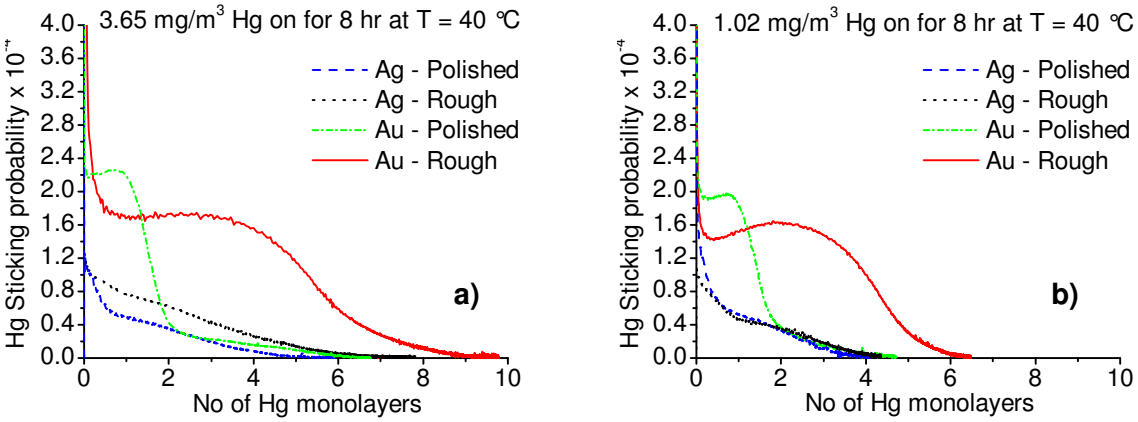

a) 3.65 mg/m^3 Hg **b)** 1.02 mg/m^3 Hg

Figure 3.8: Sticking probability of Hg-Au and Hg-Ag on rough and polished substrates against Hg coverage when exposed to Hg at 40℃.

The Z_W value at equilibrium, in the current investigation, was calculated to be around 24-87 monolayers per second of Hg striking the surface, depending on Hg vapour concentration being tested. The elevated temperature of 40℃ and the relatively high Hg concentrations used in this study may be the reason for the sharp drop in S values observed over the first 0-0.5 monolayer formation.

As early as 1971, Ford et al.[288] reported a low sticking probability of 0.01 for Hg on Au surfaces at room temperature. Later in 1973, Joyner et al.[266] observed that sticking probability of Hg vapour on Au surface was unity up to nearly one monolayer coverage, however rapidly declined thereafter, explaining that the decrease in sticking probability may be due to reactions beyond the monolayer, which may also be the reason in the current case where S is observed to reduce with increasing Hg sorption. Figure 3.8a shows that S decreases rapidly to an intermediate affinity of ~1.8 x 10^{-4} for the Au-rough substrate, and then proceeds to decrease towards zero after the equivalent of approximately 4 monolayers of Hg coverage. The Au-rough surface is observed to maintain higher intermediate affinity of Hg for higher Hg coverage than the Au-polished, Ag-polished and Ag-rough substrates. Figure 3.8b shows the change in S for the lower Hg concentration of 1.02 mg/m^3. However, it should be noted that the lower Hg concentration of 1.02 mg/m^3 is much higher (~1000 times) than the μg/m^3 range usually used in other studies.[81,101,143]

The decrease in S observed for all four sample configurations can be explained by the work of Mazzolai et al.[149] Briefly, the group explains that for low Hg concentrations, Hg sorption proceeds faster than the rate at which mercury is supplied at the interface, by the process of diffusion. The sorption process would therefore be limited by diffusion and an increase in the QCM response proportional to Hg concentration is expected. Therefore, the high S observed initially in this study may be the result of the high rate at which Hg is adsorbed onto the fresh Au and Ag surfaces due to the low availability of Hg in the vapour phase. Once Hg concentration in the vapour phase is high enough, the rate-limiting step becomes the surface absorption[149]. That is, all the Hg supplied at the surface cannot be consumed / diffused into the surface fast enough and so reduced Hg sorption (flattening of the response curve in Figure 3.4) is observed. This therefore explains the decreasing sticking probability with increasing Hg exposure time and/or Hg coverage and demonstrates the lower t_{90} observed for higher Hg concentrations. Furthermore, the results indicate that high S can be maintained for longer periods of time given Hg sorption rate on a surface is reduced to zero at a slow rate. Therefore, in order to achieve high Hg sorption and hence high QCM response magnitude towards Hg vapour, the development of a surface with a morphology such that the Hg sorption rate is initially high and reduces to zero slowly is critical.

Figures 3.9a and 3.9b show the sticking probability and surface monolayer coverage versus time for Hg concentration of 1.02 mg/m^3. The arrows indicate the data's respective Y-axis scale. Although Figure 3.9a shows that both the Au-rough and Au-polished have comparable S values, the affinity of the rough surface towards Hg is shown not to decrease as rapidly as the polished surface. However, the trend for the Ag-rough and Ag-polished surfaces (Figure 3.9b) is shown to decrease in the same manner with time. The in-situ S data, presented for

the first time, clearly agrees with the experiments of George et al.[93] and the model offered by Levlin et al.[78] Morris et. al.[84] have also shown that the Hg that diffuses into the films' bulk releasing the surface adsorption sites, thus promoting further Hg adsorption to occur. This phenomenon explains the gradual increase in response magnitude obtained during the 40 hour Hg vapour exposure to the Au electrode QCM (Figure 3.3). With regards to the gold surfaces, this may be the reason for the observations of high sticking probability for longer periods of time on rough surfaces over that of Au-polished. Additionally the same trend is shown with the increase of nominal monolayers (i.e. a layer of Hg atoms having the same surface atom density as a gold (111) surface[78]).

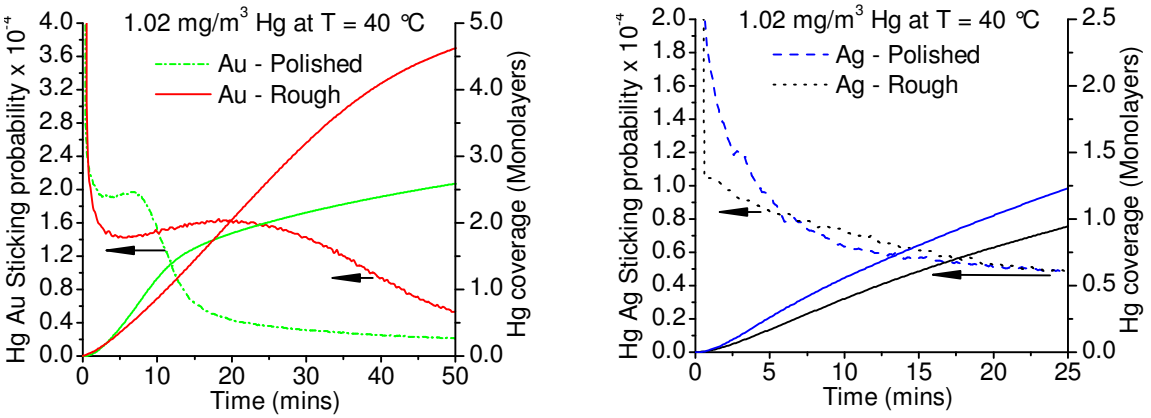

a) Hg-Au system **b)** Hg-Ag system

Figure 3.9: Sticking probability and Hg coverage on metal-rough and metal-polished substrates with time when exposed to 1.02 mg/m^3 of Hg at 40℃

3.2.9 Outperformance of Au-Rough over Other Surfaces

The optically polished electrodes have so far been found to underperform in terms of Hg sorption and desorption rates as well as have low affinity towards Hg (i.e. low sticking probability). However, much work in the past[100,289,290] has used smooth thin films of Au when studying Hg-Au interaction. This is because the morphological changes on these surfaces following Hg sorption and desorption may easily be monitored as opposed to the mechanically roughened films.

The non-viability of the silver surfaces is demonstrated in Figure 3.10 where Ag-rough QCM is compared with that of the stable Au-rough substrate towards continuous pulses of constant Hg vapour concentration. The graph clearly demonstrates that the Au-rough QCM has better Hg sorption and desorption capabilities resulting in a stable response throughout the testing period as opposed to Ag-rough QCM where a large drift is shown. The average response magnitude of all the pulses shown in Figure 3.10 for Ag-rough was found to be 165.1 Hz with a standard deviation of 2.77 Hz. Similarly, the Au-rough had an average response magnitude of 165.7 Hz and a standard deviation of 3.01 Hz. Although the Au-rough response magnitude

is similar to that of the Au-rough, the drift from the silver QCM may be due to Hg accumulation. That is, the Au-rough and Ag-rough are observed to desorb ~95% and ~85% of their adsorbed/amalgamated Hg at the conclusion of each pulse. This finding is inline with the suggestion made by Dumarey et al.[67] and Mercer[257], who stated that as well as silver retaining its mercury content, the metal also has diminishing aging effects associated with it relative to gold. Furthermore the high sticking probability (shown in Figures 3.8 and 3.9) of the Au-rough QCM for higher numbers of nominal monolayer of mercury relative to the Ag-rough makes the Au-rough the ideal substrate to test further towards Hg vapour at various concentrations and operating temperatures. Therefore it was also decided not to pursue Ag-rough substrate as a possible Hg vapour sensor. The results presented from here on in this chapter are those related to the Au-rough electrode QCMs.

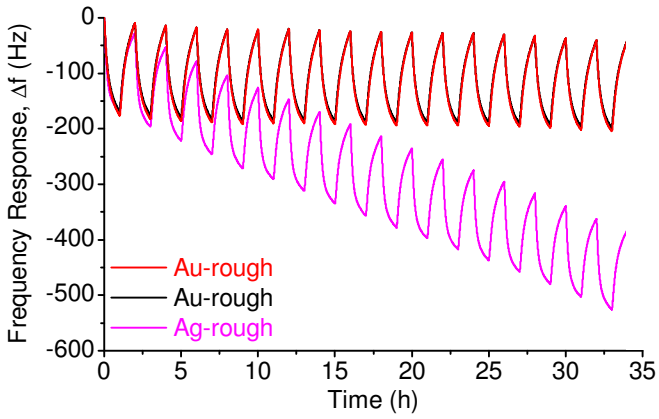

Figure 3.10: Au-rough stability as compared to Ag-rough when exposed to continuous Hg pulses of constant concentration

3.3 Feasibility of Au-rough as a Hg Vapour Sensor

3.3.1 Temperature Profile and Adsorption Isotherms

The Au-rough QCM was further investigated as a potential Hg vapour sensor by exposing Hg using the temperature profile test pattern explained in Chapter 2. The response magnitude of the Au-rough QCM for the five Hg vapour concentrations and nine different operating temperatures is shown in Figure 3.11. The data in Figure 3.11 was extracted from the response curves shown in Appendix C (Figure C1).

It may be observed from Figure 3.11a that as the temperature is increased both the response magnitude and the dynamic range between the Hg vapour concentrations (ranging from 1.02 – 10.55 mg/m^3) is decreased. The highest temperature where a relatively large response magnitude and dynamic range existed was found to be at the operating temperature of 89°C (circled in Figure 3.11a).

An alternative way to observe the data in Figure 3.11a is in Figure 3.11b which represents the sorption isotherm of Hg vapour on gold film surface at various operating temperatures. The sorption isotherm was extracted from the QCM data (since Δf is proportional to the mass of Hg adsorbed/amalgamated on the Au film) over 1 hour Hg exposure time for each Hg concentration and temperature.

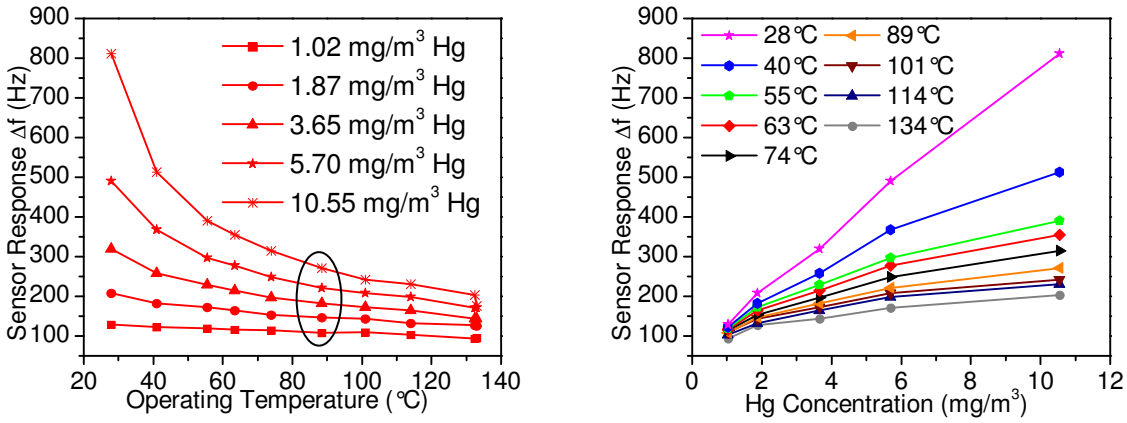

a) Temperature profile **b)** Sorption isotherm

Figure 3.11: QCM response magnitudes at various operating temperature and Hg vapour concentrations

A number of adsorption isotherms have been experimentally observed in the past with the eight most common examples shown in Figure 3.12. Depending on the physicochemical conditions, it is possible to fit adsorption isotherms in one of the models in Figure 3.12. For a more thorough discussion of each of the adsorption type as well as some other common adsorption isotherm types, the reader is referred to the articles of Butt et al.[291] and Meghea et al.[292], respectively.

In the case of Hg vapour, several studies have been conducted in the past and sorption isotherms at various temperatures on various substrates have been reported[293-298]. Studies are scarce[257] for the case of Hg sorption isotherms on Au thin films while no reports of Hg sorption isotherms on Au thin films at various temperatures (and Hg vapour concentrations studied) may be found.

The obvious assumption for the Hg-Au system would be to fit the Hg sorption isotherms shown in Figure 3.11b with that of Langmuir type isotherm in Figure 3.12c. However, in Langmuir's model, the maximum allowable amount of adsorbed species is one monolayer after which case saturation occurs.[291] In the case of mercury adsorption on Au, it is well known that Hg is mobile on the Au surface until it reaches an adsorption site such as a defect or grain boundary[93,289] and there was an indication of the lack of monolayer formation of Hg

on the Au films. Levlin et al.[78] and Inukai et al.[290] later studied the adsorption of Hg vapour on gold surfaces and failed to observe any continuous monolayer formation. Similarly, Figure 3.9 confirms such observations that Hg vapour does not form a continuous monolayer on the Au-rough film. That is, it takes well above one nominal monolayer of Hg on the Au-rough film before the sticking probability drops to zero, hence, saturation. Although it is difficult to fit a Hg sorption isotherm to any of the pre-existing models shown in Figure 3.12, it is clear from Figure 3.11b that the Au surface's capacity to uptake Hg reduces as the temperature increases.

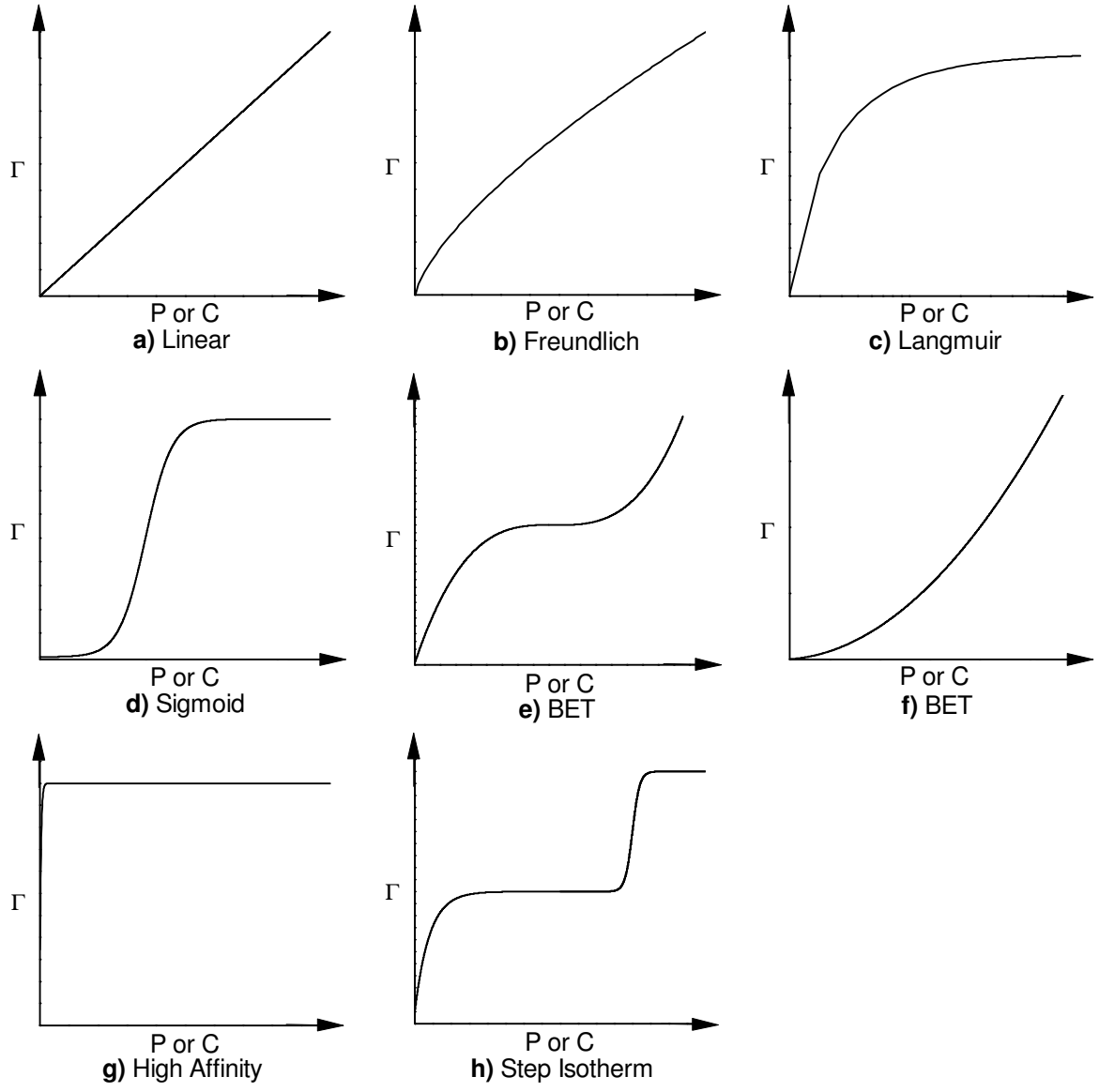

Figure 3.12: Schematic plot of eight most commonly observed adsorption isotherms. The X-axis is either pressure (P) or concentration (C) of the adsorbate while the Y-axis represents mass adsorbed or surface coverage of the adsorbate on the adsorbent (Γ). Figure taken from Butt et al.291 (page 180).

Even though only five concentrations of Hg vapour have been studied in this research program, it is quite clear from Figure 3.11b that the Hg-Au adsorption may fit a linear type adsorption isotherm at room temperature, transforms to a Freundlich type as the temperature increases towards 100℃ and progresses to a Langmuir type above 100℃. The equations describing the linear, Freundlich and Langmuir isotherms are shown in Equations 3.4, 3.5 and 3.6, respectively[291], Where Γ and Γ_{mon} are the amount of adsorbed gas and amount of one monolayer of adsorbed gas respectively. K_H, K_F and $q(q<1)$ are constants and θ is the relative coverage.

$$\Gamma = K_H P \quad \text{.....Equation 3.4}$$

$$\Gamma = K_F \cdot P^q \quad \text{.....Equation 3.5}$$

$$\theta = \frac{K_L P}{1 + K_L P} \text{ with } \theta = \frac{\Gamma}{\Gamma_{mon}} \quad \text{.....Equation 3.6}$$

The constant for the QCMs used in this study is calculated to be 227.71 Hz.cm^2.μg^{-1}. The electrochemical surface area of the Au-rough was found (using the procedure outlined in Chapter 2) to be ~1.22 cm^2. The QCM response magnitude is therefore ~88 Hz for every nominal monolayer of Hg vapour deposited (Hg sorption) on the surface. The Au-rough QCM response magnitude for Hg concentrations of 1.02 and 10.55 mg/m^3 was observed to be 93 and 202 Hz respectively at an operating temperature of 134℃. These values are observed to be higher at the lower operating temperatures (Figure 3.11), indicating that at least one nominal monolayer of Hg sorption occurs upon each Hg pulse at any concentration or operating temperature. This suggests that saturation does not occur due to the formation of Hg monolayer on the surface, as no saturation is observed at 28℃ sorption isotherm. Furthermore the Hg vapour pressure at 28 and 134℃ may be converted to the values of 25.6 and 41524mg/m^3 respectively.[299] It is clear that the tendency of Hg to stay in the vapour phase rather than adsorb on the Au surface increases three orders of magnitude with little increase in temperature. These results are a clear indication that the change in the sorption isotherms is operating temperature dependent and the tendency of Hg atoms to stay in the gas phase due to high vapour pressure of Hg at the higher temperatures enhances saturation due to reduction in the Hg sorption capacity of the Au-rough surface and not due to monolayer formation.

3.3.2 Sorption, Desorption and Their Rates

The Hg sorption, desorption and their rate curves (in Appendix C) are overlayed following their baseline to zero and shown in Figures 3.13 and 3.14 for the operating temperatures of 40℃ and 89℃, respectively. The increase in the amount of Hg sorption as well as an

increase in the maximum sorption rate onto the Au-rough surface for the tested Hg vapour concentrations may be observed in Figures 3.13a and 3.13b respectively.

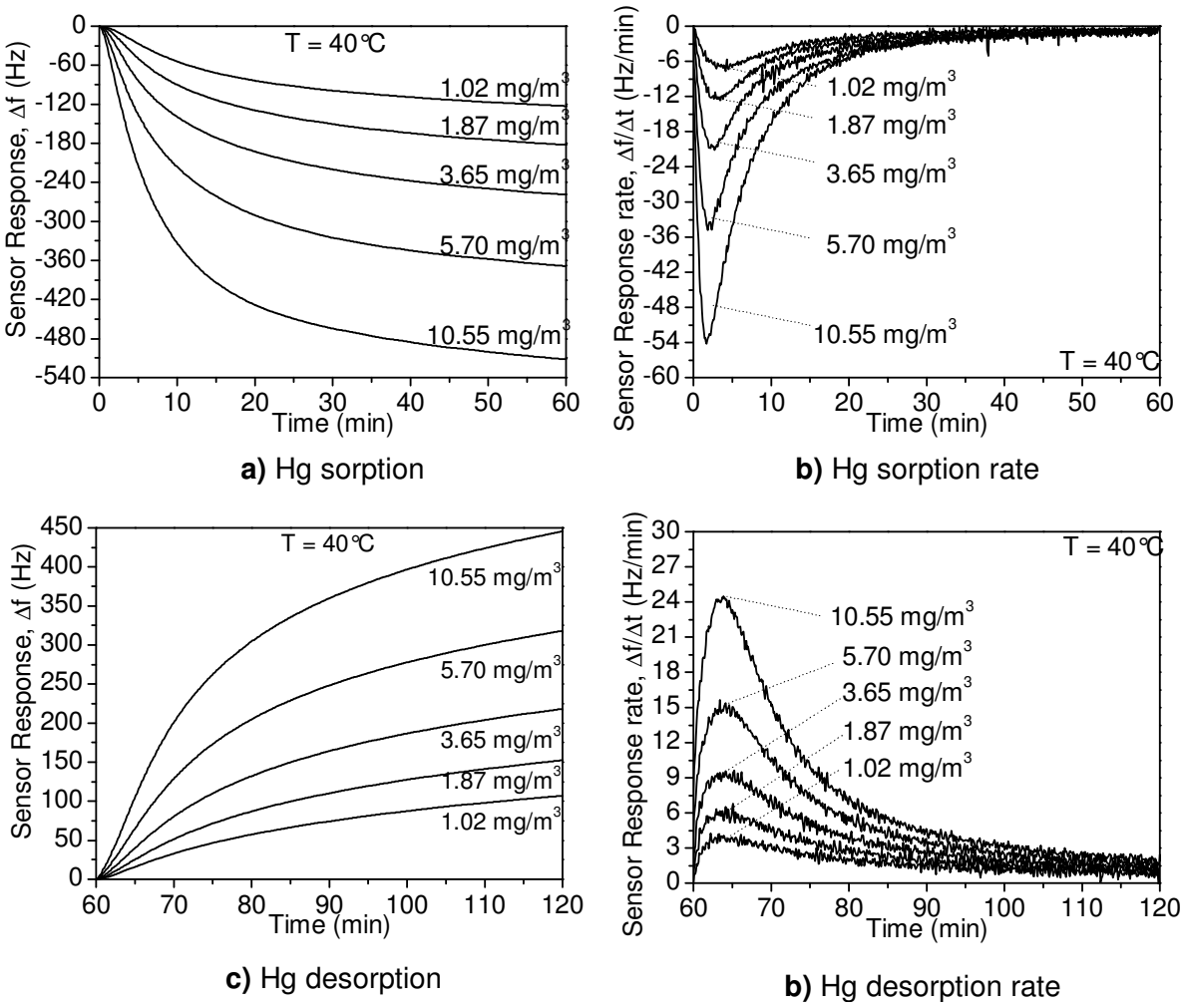

a) Hg sorption

b) Hg sorption rate

c) Hg desorption

b) Hg desorption rate

Figure 3.13: Dynamic response and sorption desorption rates of Au-rough film exposed to five Hg vapour concentrations at 40℃.

The correlation of the sensor response magnitude with that of Hg vapour concentration is already shown in Figure 3.11b. A quicker response may be obtained from the QCM sensors if the maximum response rate is correlated with that of Hg vapour concentration. It is interesting to observe from Figure 3.13b that it only takes approximately 100 seconds to reach the maximum adsorption rate at Hg vapour concentration of 10.55 mg/m^3 and an operating temperature of 40℃. This time increases slightly (~155 seconds) at Hg vapour concentration of 1.87 mg/m^3. At the higher operating temperature of 89℃ (Figure 3.14b) the times taken to reach the maximum adsorption rate for 10.55 and 1.87 mg/m^3 were observed to be ~65 and ~175 seconds respectively. The time required to reach the maximum adsorption rate varies with temperature due to their relative saturation points between the Hg in the gas phase and that adsorbed on the Au film. In general, the response time is observed to increase with decreasing Hg vapour concentration.

As expected, the maximum sorption rate is observed to increase with increasing Hg vapour concentration. Furthermore, the higher the Hg vapour concentration, the slower the rate of sorption drops back towards zero after reaching the maximum sorption rate (Figure 3.13b). This slow return back to zero sorption rate is also the reason for the higher response magnitude, hence there are larger number of Hg atoms adsorbed/amalgamated rigidly on the gold surface. But the slower return back towards zero sorption rate also implies more diffusion of mercury into the gold bulk. That is, diffusion is promoted by the higher concentrations of Hg on the surface and it is well known that diffusion of mercury releases the sorption site for more Hg to adsorb/amalgamate[89,93]. Since this phenomenon is promoted better with the higher Hg vapour concentrations, a slower decrease in the Hg sorption rate (Figure 3.13b) as well as a slow decrease in the sticking probability (comparison of Figures 3.8a and b) is observed.

Operating temperature is also observed to affect the Hg sorption rate. The sorption rate, having reached maximum, decreases faster back towards zero at 89°C as compared to 40°C, possibly due to the higher vapour pressure of Hg at the higher temperature of 89°C (Figure 3.13b as compared to Figure 3.14b). It is for this quick approach towards the zero sorption rate that caused the decreased response magnitude as well as lower Hg uptake capacity to be observed at the higher operating temperatures (Figures 3.13a and 3.14a). Similarly a higher magnitude of maximum Hg sorption rate is observed at the higher operating temperature of 89°C than that of 40°C for every Hg vapour concentration. This may be due to the increasing solubility (or affinity) of Au in Hg at the higher operating temperatures (Figure 3.1). That is, the increased surface affinity towards Hg may be a result of the tendency of the small size Au clusters on the Au-rough film to melt at lower temperatures than that of bulk Au.[300]

The comparison of desorption with the sorption response curves (Figures 3.13a with 3.13c and Figures 3.14a with 3.14c) clearly indicates that not all mercury adsorbed on the surface is fully desorbed within the 1 hour desorption period. This is a clear indication that Hg has amalgamated strongly and diffused through gold making it difficult for full desorption to occur. An increase in temperature following the Hg exposure period is required before full desorption may be observed.[67,84,97] An increase in operating temperature is impractical when using QCMs as online Hg vapour sensors due to their high sensitivity to temperature fluctuations at higher than 25°C.[301] Therefore the approach that will be discussed in Chapter 4 is to find an operating temperature where high sorption and desorption is observed.

For a given surface Jones and Perry[295] have suggested that desorption of Hg vapour maybe coverage dependent. This is evident from desorption rate curves in Figures 3.13d and 3.14d

where higher magnitudes of maximum desorption rate are observed following larger Hg vapour concentration exposures. The maximum desorption rate is far less than the sorption rates of the corresponding Hg vapour concentrations at the same operating temperature. This again agrees with the study of Jones and Perry where they suggested, based on their data, that there may be an activation energy which increases as the Hg coverage on a substrate decreases during desorption.[295]

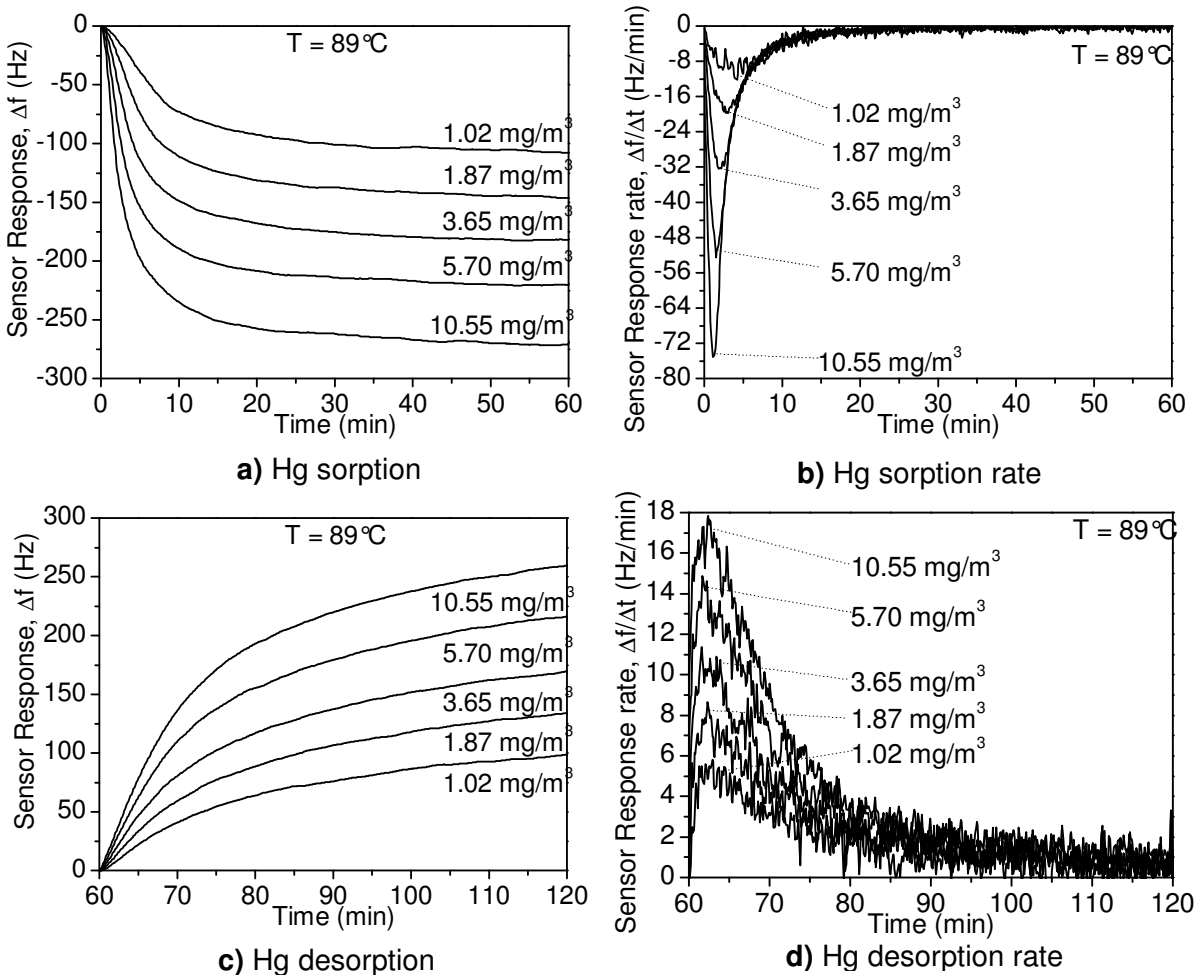

Figure 3.14: Au-rough film exposed to five Hg vapour concentrations at 89°C.

The ratio of the maximum desorption rate to the maximum sorption rate is found to be higher at 40°C as compared to that of 89°C operating temperature (0.45 as compared to 0.24 at Hg concentration of 10.55 mg/m^3). Conversely, the ratio of the total Hg desorbed to that of total mercury adsorbed/amalgamated, at the same Hg vapour concentration, on the Au-rough surface is higher at the operating temperature of 89°C than that of 40°C (0.96 as compared to 0.87). It is well known that higher temperatures enhance desorption[84] as well as increase the Hg tendency to behave in a non-metallic manner.[109-112] This means that amalgamation with the gold surface would be minimal, resulting in loosely adsorbed Hg atoms that may be sensed by the QCM sensor while also being desorbed readily during the desorption period. Although the maximum desorption rate is higher at 40°C, the reason for the observation of

the lower ratio of Hg desorbed to that adsorbed at this temperature as compared to 89℃ may be observed in Figures 3.13d and 3.14d. It can be observed that the time taken to reach maximum desorption rate at 40℃ and 89℃ is ~240 and ~145 seconds respectively. Furthermore, it takes longer for the desorption rate to approach zero for 40℃ as compared to 89℃. This results in the area under the curves in Figure 3.14d being higher than their respective curves in Figure 3.13d. A higher area under the curve indicates more mass of Hg desorbed from the Au-rough surface.

3.4 Repeatability of Au-Rough QCM

In order to test the stability and repeatability of the Au-rough QCM, four duplicate Au-rough sensors (QCM1-4) were tested towards Hg vapour at various Hg concentrations and operating temperatures, and with and without the presence of various levels of ammonia and humidity. This was a preliminary test in order to determine how the Au-rough QCM based sensors would behave towards Hg vapour in the presence of interferent gases. Additionally the performance of the Au-rough sensor with respect to medium term stability and repeatability has been studied over a 45 day testing period.

3.4.1 Repeatability and Stability

The dynamic response of the four Au-rough QCMs towards 5.70 mg/m^3 Hg vapour following the pre-treatment procedure (day 9) is shown in Figure 3.15a. The sensors' response magnitudes are shown to be in excellent agreement (within ±0.44% of their mean response magnitude). Small and gradual reductions in the mean response magnitude is observed (mean Δf are labelled on the graph) in the 3 successive pulses. The average response magnitude reduction rate for the QCMs was found to be ~1.4Hz/h proving these QCMs to be stable towards constant Hg concentrations. Due to the close resemblance in response curves of all four QCMs, only data from QCM1 and 2 will be presented for clarity reasons.

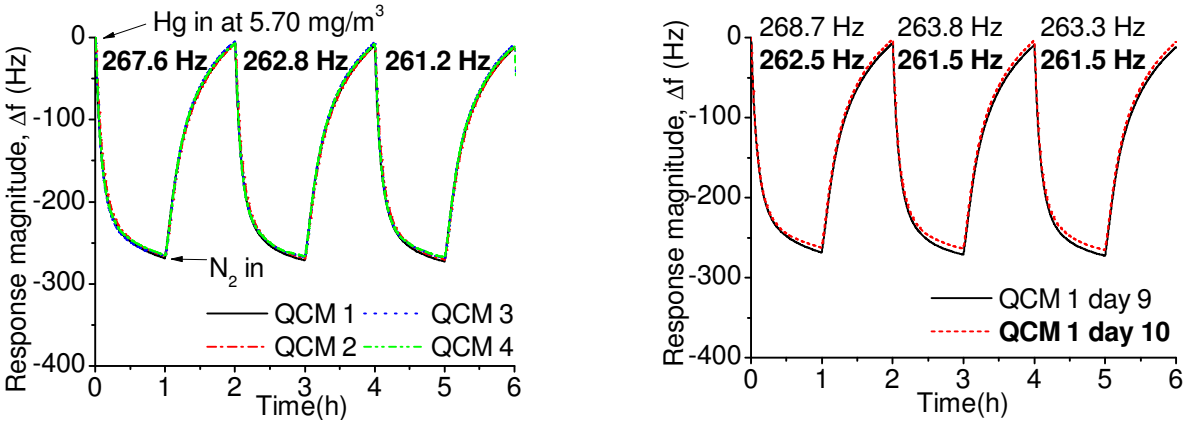

a) Repeatability between 4 QCMs

b) Repeatability between 2 days

Figure 3.15: QCM dynamic response when exposed towards Hg concentration of 5.7 mg/m^3 at an operating temperature of 55℃

By continuing Hg exposure at the same concentration of 5.70 mg/m^3, it was observed that the QCM is stabilised. This is clearly indicated by the response magnitude of the final two pulses of QCM1 at day 10 in Figure 3.15b showing a Δf of 261.5Hz in the final two pulses. The result from Figure 3.15b is a further proof that pre-treatment of Au is required indicating an Au amalgam is a better suface for continuous Hg vapour sensing as compared to a freshly unexposed Au surface (also discussed in Chapter 2). The small difference between the adsorption and desorption pulses (reduction in response magnitude between successive pulses) maybe attributed either to the sensor drift and/or the portion of adhered Hg which has not desorbed during the 1 hour desorption period.

The QCM response data during days 31-33 of the 45 day testing period is shown in Figure 3.16. The influence of increasing the 1 hour recovery period on the sensor response as well as the repeatability of the sensor towards successive pulses of 5.7 mg/m^3 Hg is observed. Arrow 1 in Figure 3.16 refers to the response magnitude towards the first 1 hour exposure of 5.7 mg/m^3 Hg following a 3 hour recovery period. The observed response magnitude of the sensor following the 3 hour recovery period was significantly larger than that obtained after a 1 hour recovery period used in the subsequent pulses. The influence of an increased recovery period was again investigated following 29 hours of Hg pulses at a concentration of 5.70mg/m^3, where the sensors underwent a 2 hour recovery period (arrow 2) before the 1 hour Hg exposure period. This again led to a significant increase in the extent of recovery, where the response obtained in the following pulse was equivalent to 96.4% of that obtained after 3 hours of recovery. The influence in response magnitude of the QCM (towards 1 hour Hg exposure period) by rising the recovery period from 2 to 3 hours is observed to be a mild increase of ~3.7%.

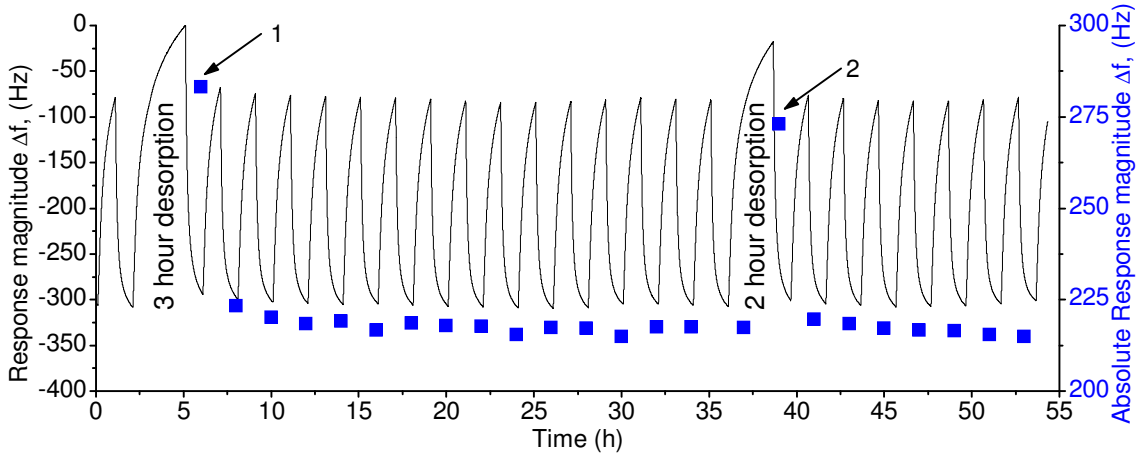

Figure 3.16: Degradation over 50 hours (Days 31-33) at constant Hg concentration of 5.70 mg/m^3 for Au-rough (QCM1). The response curves and the blue squares (response magnitude) belong to the left and right axis, respectively.

The data in Figure 3.16 demonstrates that continuous Hg pulses with 1 hour recovery and 1 hour Hg exposure produces similar sensor response magnitudes for each successive pulse. During the 55 hour testing period, the deviation in the QCM response magnitude during successive Hg pulses (I hour of each exposure and recovery periods) was found to lie within ±5.0% of the mean response magnitude.

The QCMs were also exposed to different concentrations of Hg vapour, which involved exposing the sensors to 5 concentrations of Hg (two pulses of each) in increasing sequence. The QCM response data is shown in Figure 3.17a. This pattern was run to study the behaviour of the sensors when exposed to changing Hg concentration as well as the short term repeatability of the sensors. Both QCM1 and QCM2 showed similar response magnitudes towards each Hg concentration. The reduction in response over two successive pulses of 5.70 mg/m^3 Hg is found to be 3.34% and 3.39% for QCM1 and QCM2, respectively. This magnitude of deviation did not change significantly when the test was repeated the next day (a reduction of 3.48% in response magnitude for QCM1 in Figure 3.17b at 5.7mg/m^3 Hg). However, it is evident that greater reduction in response magnitude occurs when the Au-rough sensors are exposed to variable Hg concentration within the range of 1.02 to 10.55 mg/m^3, as opposed to constant Hg pulses (Figure 3.15).

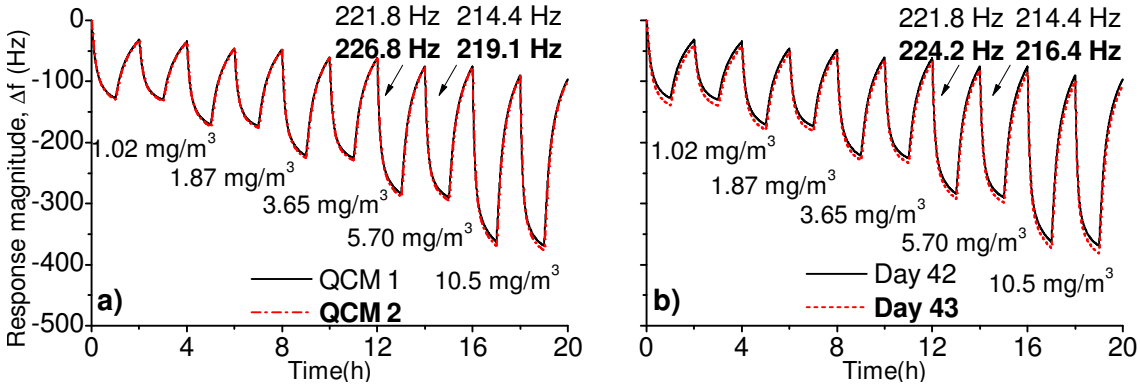

a) Repeatability between 2 QCMs **b)** Repeatability between 2 days

Figure 3.17: QCM dynamic response when exposed towards 5 different Hg concentrations at an operating temperature of 55℃.

3.4.2 Long Term Stability and the Influence of Interferent Gases

To investigate the long-term stability and influence of interferent gases (ammonia and humidity), the sensors were exposed to 1.87 and 5.7 mg/m^3 pulses of Hg at various humidity and ammonia interferent conditions over the 45 day testing period. The Au-rough response curve from the 27th day of testing when exposed to Hg concentration of 5.7 mg/m^3 in the presence of 7.6 g/m^3 H_2O is shown in Figure 3.18. By this stage of testing, it is observed that the response magnitudes of the QCMs are reduced to ~234 Hz as compared to day 9 where a response magnitude of ~263 Hz was observed (Figure 3.15). Each time a new condition

was tested, the sensors were subjected to at least three pulses (data points) of Hg exposure with/without the presence of interferent gases during the long term testing. An example of one of these conditions is shown in Figure 3.18 where no interferent gases were present.

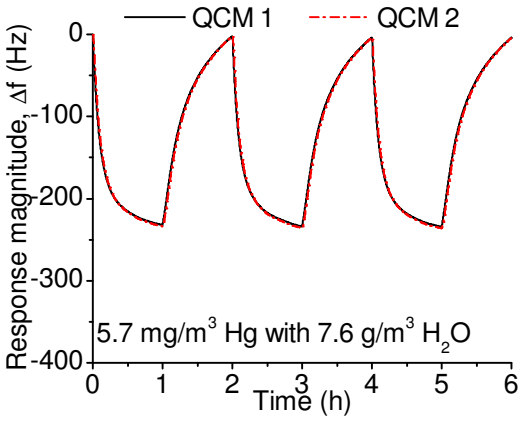

Figure 3.18: QCMs exposed to two Hg concentration of 5.70 mg/m^3 in the presence of 7.6 g/m^3 humidity at an operating temperature of 55℃.

The reduction in response is believed to be due to the aging of the sensor and not due to the presence of humidity as is evidenced from Figure 3.19. The first 35 days of data for which the QCM was tested at 55℃ is shown in Figure 3.19a. QCM2 data has been omitted for clarity; however similar trend and Δf values were observed for all Au-rough QCM sensors. The response magnitude of the Au-rough QCM is found to reduce by ~40% on the 35th day of testing when compared to the 1st day, due to aging effects. Thus, the sensor reports ~40% lower concentration if the calibration curve of the 1st day was applied to that of the 35th day.

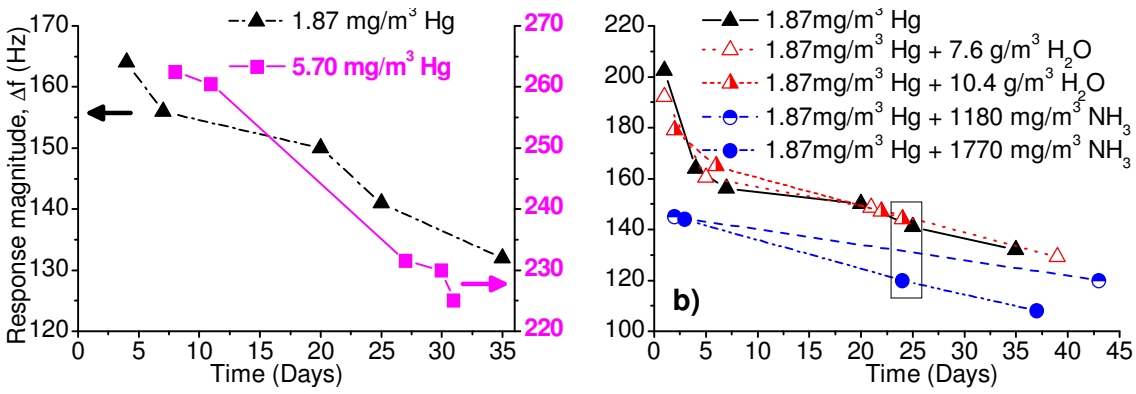

a) Influence of Hg concentration **a)** Influence of interferent gases

Figure 3.19: QCM response magnitude over a 45 day test period *Note: in a)* the Δf towards 1.87mg/m^3 and 5.7mg/m^3 Hg are shown on the left and right Y-axis, respectively.

Figure 3.19b shows the response magnitude of QCM1 towards Hg concentration of 1.87 mg/m^3 with and without the presence of humidity and ammonia interferent gases over the entire 45 day testing period. Again, it is clearly visible that the reduction in response magnitude is due to aging and the presence of ammonia. The results clearly suggest that

humidity did not significantly affect the response of the sensor, as for any given day during the 45 day testing period the response magnitude towards Hg is observed to be similar to that of Hg in the presence of humidity. This is presumed to be due to the elevated operating temperature of 55℃. However, ammonia interference is shown to reduce the Hg response magnitude as a function of NH_3 concentration.

The data within the box in Figure 3.19b, taken on day 25 of the test, clearly shows the effect of both humidity and ammonia interference. Without humidity and ammonia, a response magnitude of ~141Hz towards Hg vapour concentration of 1.87 mg/m^3 was recorded. However, in the presence of 7.6 mg/m^3 or 10.4mg/m^3 humidity, an overestimation of ~2% (w.r.t response magnitude) would occur (Figure 3.19b). It may also be observed that an underestimation of ~6.8% and ~14.9% (w.r.t response magnitude) of the Hg vapour concentration would occur when ammonia is present at 1180 mg/m^3 and 1770 mg/m^3, respectively. It appears that the effect of ammonia interference is also observed to increase with the sensors' age. For example, on the 4th and 36th day, the increase in response error is calculated to be 12.2% and 18.2% respectively in the presence of 1170 mg/m^3 ammonia.

3.4.3 Au-rough Surface Morphology Change Following Hg Exposure

At the end of the 45 day testing period, the Au-rough electrodes were characterized via SEM and AFM, shown in Figures 3.20 and 3.21, respectively. The small Au islands observed in Figure 3.20a of a Au-rough QCM electrode, are observed to be approximately 20-27 nm in size before the 45 day testing was conducted. These islands are observed to agglomerate and grow into bigger island structures of size ~23-40 nm following the testing period.

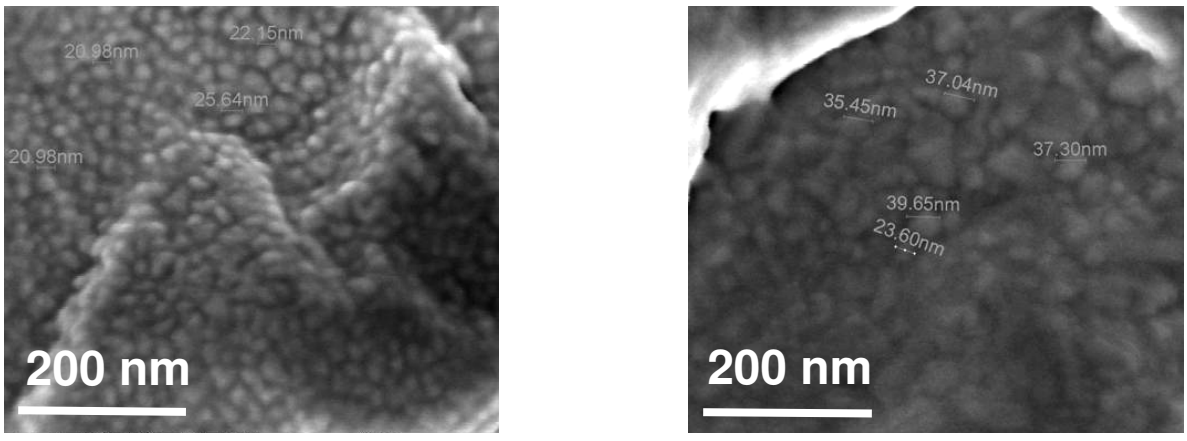

a) Before **b)** After the 45 day testing period

Figure 3.20: SEM characterization of Au-rough electrodes

The observation of island growth following Hg exposure of Au films is inline with that of literature.[146,289,302]

In this work, the AFM characterization of QCM1 (Figure 3.21) before and after the 45 day testing period showed that the roughness of the gold electrode surface had reduced significantly. The average island heights were observed to reduce from ~ 90 nm to ~40nm – a reduction of over 50%. This observation is found to contradict that of Kobiela e al.[85] where they observed, using AFM characterisation, an increase in some of the Au island heights to over 800nm and several μm in island size following Hg exposure. This contradiction may be due to the difference in their experimental procedure compared to this work. That is, their work was conducted under different experimental conditions like using Au films deposited on glass substrates, testing conducted under vacuum and using lower Hg concentration of ~0.11 mg/m^3. It is the Author's opinion that the reduction in roughness could be a 'melting' effect of Au due to the higher Hg concentrations used in this study.

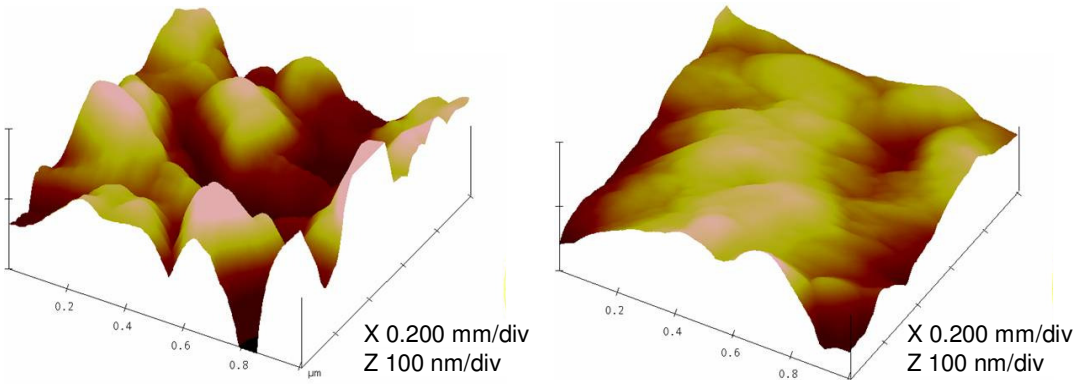

a) Before **b)** After the 45 day testing period

Figure 3.21: AFM characterization of Au-rough electrodes

Nevertheless, the morphology of the sensitive Au-rough substrate has changed substantially which may explain why the sensors' response magnitude dropped significantly during the early stages of the long term Hg vapour exposures. Furthermore, the largest reduction rate in response magnitude of the Au-rough QCM sensor was observed to occur during the pre-treatment process (first 8 days of the 45 day test). This may be due to most of the morphological changes and the stabilisation of the Au-rough QCM having occurred during the pre-treatment period (see Figure 3.19b). If one assumes that the QCM response magnitude reduction occurs mostly due to the changes in the Au surface morphology as a result of Hg exposure, the need for a highly roughened yet stable sensor becomes important for Hg vapour sensing. Such film fabrication is attempted directly on the QCM electrodes and tested towards Hg in the presence of ammonia and humidity, the results of which are presented in Chapters 6 and 7.

3.5 Summary

The ability of Au to adsorb/amalgamate and desorb Hg at higher rates than those over Ag has been shown, thus indicating that Au surfaces have the distinct advantage of being able to desorb Hg with a higher efficiency. The t_{90} analysis of the QCM responses was used to confirm the higher ability of Au to adsorb Hg within the tested concentration range. It was found that the Au and Ag surfaces desorbed up to 90% of their equilibrium value within a similar time frame of 191.5 ± 1 minutes following an 8 hour Hg exposure period. The presented model, based on SIMS data was used to estimate the depth at which Hg diffused in the Au and Ag films based on the initial Hg vapour concentration. The sticking probability, S, of Hg-Au and Hg-Ag were calculated to gain a further insight into the behaviour of Hg vapour with thin metal films at different Hg vapour concentrations. This showed that the Au-rough surface not only has higher affinity for Hg but retained its affinity for longer periods of time and a large number of Hg monolayer coverage. The S calculations also demonstrated that the amount of active sites for Hg adsorption/amalgamation was not solely due to higher surface area when compared to the Au-polished surface. Other factors such as the type of metal film and the morphology of the film surfaces also affect Hg sorption kinetics.

Based on these results, four Au-rough substrates were tested for a 45 day period in the presence of humidity and ammonia in order to observe their behaviours in terms of interferent gases, long term stability, repeatability and their decline in response magnitude output with time. Overall, the repeatability of the non-modified sensors was shown to be within ±5% towards mercury over the 2 to 4 day period. The sensors were found to produce up to 40% lower response magnitude towards Hg vapour in the 35th day when compared to the first day of testing, thus, leading to an approximately 40% lower concentration if the calibration curve of the first day was applied to the 35th day. Furthermore, NH_3 was found to reduce the sensor's response magnitude by over 18% when tested towards 5.70 mg/m^3 Hg in the presence of 1770 mg/m^3 NH_3 as opposed to dry or humid conditions.

Results indicate that some of the criteria for modifying Au surfaces for Hg vapour sensing may be having an Au surface that is highly stable, has rough morphology and a high surface area for high selectivity and sensitivity towards Hg vapour. Such a surface is postulated to optimise adsorption/desorption kinetics, have a high sensitivity towards Hg vapour and induce the least reduction in response magnitude. Testing these sensors in high operating temperatures not only simplifies desorption (no further heating required during testing) but also increases the desorption kinetics and is postulated to reduce interferent effects from the presence of other gases such as ammonia and humidity.

3.6 References

(1) McNerney, J. J.; Buseck, P. R.; Hanson, R. C. *Science* **1972**, *178*, 611-612.
(2) Levlin, M.; Ikavalko, E.; Laitinen, T. *Fresenius Journal of Analytical Chemistry* **1999**, *365*, 577-586.
(3) Rex, M.; Hernandez, F. E.; Campiglia, A. D. *Analytical Chemistry* **2006**, *78*, 445-451.
(4) Sabri, Y. M.; Ippolito, S. J.; Tardio, J.; Atanacio, A. J.; Sood, D. K.; Bhargava, S. K. *Sensors and Actuators B: Chemical* **2009**, *137*, 246-252.
(5) García-Sánchez, A.; Contreras, F.; Adams, M.; Santos, F. *Environmental Geochemistry and Health* **2006**, *28*, 529-540.
(6) Gochfeld, M. *Ecotoxicology and Environmental Safety* **2003**, *56*, 174-179.
(7) Li, J.; Herrero, E.; Abruña, H. D. *Colloids and Surfaces A: Physicochemical and Engineering Aspects* **1998**, *134*, 113-131.
(8) George, M. A.; Glaunsinger, W. S. *Thin Solid Films* **1994**, *245*, 215-224.
(9) Guminski, C.; Galus, A.; Hirayama, C. In *Solubility Data Series: Metals in Mercury*; Warsaw, U. O., Ed.; Pergamon Press: Warsaw, Poland, 1986; Vol. 25, p 258-384.
(10) Atkins, P. W. *Physical Chemistry*; 2nd ed.; Oxford University Press: Oxford, Great Britain, 1982.
(11) Scott, J. E.; Ottaway, J. M. *Analyst* **1981**, *106*, 1076-1081.
(12) Shao, R.; Tan, E. L.; Grimes, C. A.; Ong, K. G. *Sensors Letters* **2007**, *5*, 6.
(13) McDonagh, C.; Bowe, P.; Mongey, K.; MacCraith, B. D. *Journal of Non-Crystalline Solids* **2002**, *306*, 138-148.
(14) Bohets, H.; Vanhoutte, K.; De Maesschalck, R.; Cockaerts, P.; Vissers, B.; Nagels, L. J. *Analytica Chimica Acta* **2007**, *581*, 181-191.
(15) Crank, J. *The Mathematics of Diffusion*; Oxford University Press, London, England, 1975; Vol. 2nd edition.
(16) Richaud, R.; Lachas, H.; Healey, A. E.; Reed, G. P.; Haines, J.; Jarvis, K. E.; Herod, A. A.; Dugwell, D. R.; Kandiyoti, R. *Fuel* **2000**, *79*, 1077-1087.
(17) Krata, A.; Bulska, E. *Spectrochimica Acta Part B: Atomic Spectroscopy* **2005**, *60*, 345-350.
(18) Ping, L.; Dasgupta, P. K. *Analytical Chemistry* **1989**, *61*, 1230-1235.
(19) Takaya, M.; Joeng, J. Y.; Ishihara, N.; Serita, F.; Kohyama, N. *Industrial Health* **2006**, *44*, 287-290.
(20) Marins, R. V.; de Andrade, J. B.; Pereira, P. A. d. P.; Paiva, E. C.; Paraquetti, H. H. M. *Journal of Environmental Monitoring* **2000**, *2*, 325-328.
(21) Moreno, F. N.; Anderson, C. W. N.; Stewart, R. B.; Robinson, B. H. *Environmental and Experimental Botany* **2008**, *62*, 78-85.
(22) Morris, T.; Sun, J.; Szulczewski, G. *Analytica Chimica Acta* **2003**, *496*, 279-287.
(23) Kalb, G. W. *Atomic Absorption Newsletter* **1970**, *9*, 4.
(24) Drelich, J.; White, C. L.; Xu, Z. *Environ. Sci. Technol.* **2008**, *42*, 2072-2078.
(25) Mercer, T. T. *Analytical Chemistry* **1979**, *51*, 5.
(26) Tsionsky, V.; Gileadi, E. *Langmuir* **1994**, *10*, 2830-2835.
(27) Haskell, R. B. Masters, University of Maine, 2003.
(28) Levlin, M.; Niemi, H. E. M.; Hautojärvi, P.; Ikävalko, E.; Laitinen, T. *Fresenius' Journal of Analytical Chemistry* **1996**, *355*, 2-9.
(29) Ford, R. R.; Pritchard, J. *Transactions of the Faraday Society* **1971**, *67*, 216-221.
(30) Joyner, R. W.; Roberts, M. W. *Journal of the Chemical Society Faraday Transactions 1* **1973**, *69*, 1242-1250.
(31) Battistoni, C.; Bemporad, E.; Galdikas, A.; Kaciulis, S.; Mattogno, G.; Mickevicius, S.; Olevano, V. *Applied Surface Science* **1996**, *103*, 107-111.
(32) Mirsky, V. M.; Vasjari, M.; Novotny, I.; Rehacek, V.; Tvarozek, V.; Wolfbeis, O. S. *Nanotechnology* **2002**, *13*, 175-178.
(33) Mazzolai, B.; Mattoli, V.; Raffa, V.; Tripoli, G.; Accoto, D.; Menciassi, A.; Dario, P. *Sensors and Actuators A: Physical* **2004**, *113*, 282-287.
(34) George, M. A.; Glaunsinger, W. S.; Thundat, T.; Lindsay, S. M. *Journal of Microscopy* **1988**, *152*, 703-713.
(35) Chaurasia, H. K.; Huizinga, A.; Voss, W. A. G. *Journal of Physics D: Applied Physics* **1975**, *8*, 214-218.
(36) Inukai, J.; Sugita, S.; Itaya, K. *Journal of Electroanalytical Chemistry* **1996**, *403*, 159-168.
(37) Dumarey, R.; Dams, R.; Hoste, J. *Analytical Chemistry* **1985**, *57*, 2638-2643.
(38) Butt, H.-J.; Graf, K.; Kappl, M. In *Physics and Chemistry of Interfaces* 2004, p 177-205.

(39) Meghea, A.; Rehner, H.; Peleanu, I.; Mihalache, R. *Journal of Radioanalytical and Nuclear Chemistry* **1998**, *229*, 105-110.
(40) Jones, R. G.; Perry, D. L. *Surface Science* **1978**, *71*, 59-74.
(41) Jones, R. G.; Perry, D. L. *Surface Science* **1979**, *82*, 540-548.
(42) Jones, R. G.; Perry, D. L. *Vacuum* **1981**, *31*, 493-498.
(43) Singh, N. K.; Jones, R. G. *Surface Science* **1990**, *232*, 229-242.
(44) Levine, H. S.; MacCallum, C. J. *Journal of Applied Physics* **1960**, *31*, 595-599.
(45) Yoshida, Z. *Bulletin of the Chemical Society of Japan* **1981**, *54*, 562-567.
(46) Aylward, G. H.; Findlay, T. J. V. *SI Chemical Data*; John Wiley & Sons, 2002; Vol. 5.
(47) Buffat, P.; Borel, J. P. *Physical Review A* **1976**, *13*, 2287.
(48) Scheide, E. P.; Taylor, J. K. *American Industrial Hygiene Association Journal* **1975**, *36*, 897 - 901.
(49) Lucklum, R.; Eichelbaum, F. In *Piezoelectric Sensors* 2007, p 3-47.
(50) Schmutzler, R. W.; Hensel, F. *Journal of Non-Crystalline Solids* **1972**, *8-10*, 718-721.
(51) El-Hanany, U.; Warren, W. W. *Physical Review Letters* **1975**, *34*, 1276.
(52) Even, U.; Jortner, J. *Physical Review Letters* **1972**, *28*, 31.
(53) Hensel, F. *Berichte der Bunsengesellschaft fur Physikalische Chemie* **1976**, *80*, 786-789.
(54) Yang, X.; Tonami, K.; Nagahara, L. A.; Hashimoto, K.; Wei, Y.; Fujishima, A. *Chemistry Letters* **1994**, *11*, 2059-2062.
(55) Kobiela, T.; Nowakowski, B.; Dus, R. *Applied Surface Science* **2003**, *206*, 78-89.

Chapter IV

Study of Hg Interaction kinetics on Au Thin Films

The effect of Hg sorption and desorption on thin Au-polished films of different thickness deposited on QCM crystals is investigated and the results are presented in this chapter. An investigation to determine the optimum Au film thickness and operating temperature for Hg vapour sensing is also carried out. The trend of increasing sorption capacity with decreasing Au film thicknesses is shown not to follow for all Au thicknesses and is found to depend on parameters such as Hg vapour concentration and operating temperature. In choosing the optimum operating temperature, a trade off between maintaining a large dynamic range of the sensor response and the ratio of desorbed to adsorbed and/or amalgamated Hg is considered. A comparison of Hg sorption and desorption kinetics is also made between the Au-rough and Au-polished films.

Part of the work presented in this chapter has been published:

1) Sawant, P.D; Sabri, Y.M; Ippolito, S.J; Bansal, V and Bhargava, S.K. “In-depth nano-scale analysis of complex interactions of Hg with gold nanostructures using AFM based power spectrum density method” *Physical Chemistry Chemical Physics*, **2009,** 11(14), pp. 2374 – 2378.

4.1 Introduction

The development of selective and sensitive chemical sensors cannot simply rely on empirical observations, but requires a more fundamental understanding of the involved interaction phenomena of the target chemical (adsorbate) on the sensitive layer's (adsorbent) surface. The key parameters usually investigated to understand analyte sorption capacity of a sensitive layer are the variations in film thickness,[303-305] operating temperature[306-308] and analyte concentration.[309-311]

Film thickness studies have been performed for Au based Hg sensors in order to study Hg-Au interaction phenomenon[61]. The thickness of Hg layer on Au films is assumed to be fixed at saturation under a constant Hg vapour concentration and operating temperature conditions.[99] Therefore, from Sauerbrey's equation (Equation 1.2), a larger surface area should result in proportionally larger Hg sorption and hence greater frequency change. Studies have shown that the optimum Au film thickness for Hg sorption is between 7.5 – 10 nm, above which, is postulated to reduce sensitivity.[99] This is because at thicknesses above 7.5 nm the Au film is believed to undergo transition from small Au islands into a continuous film due to coalescence of the islands and therefore reduction in the available surface area resulting in reduced Hg sorption.[61,99,100,256]

The influence of parameters such as Hg partial pressure (concentration), Hg exposure time, operating temperature and Au film thickness on Hg sorption capacity, to the best of the Author's knowledge, has so far not been described in literature. It was therefore deemed necessary to investigate the influence of the above mentioned parameters for Au film thickness between 40 and 200 nm deposited on QCM crystals.

4.2 Experimental Setup

Studies[198,301] have shown that a 10 MHz QCM crystal with 4mm diameter Au electrodes (As used in this study) must consist of Au film thickness of approximately 100 nm in order to obtain high Q factors. It has also been established that at least 80 nm thick Au film is required to be deposited on the 10 MHz quartz crystal of even the largest electrode diameter in order for the sensor to oscillate and maintain good electrical properties of the QCM electrodes. However, as discussed above, thinner Au films are said to increase sensitivity when monitoring Hg vapour[100]. Furthermore, previous studies have shown that thin film properties become highly dependent on film thickness for thickness below 150 nm.[312]

To study the influence of Au film thickness on Hg sorption and desorption kinetics, Au films of 40, 50, 100, 150 and 200 nm were deposited on both AT-cut quartz crystals' faces following

10 nm Ti adhesion layers using e-beam evaporation. The Au films were deposited to form the QCM electrodes and to function as the sensitive layers. Au film thicknesses ≥ 100 nm were selected based on the work of Zimmermann et al.[198] while the work of Chaurasia et al.[100] was the motivation for film thicknesses < 100 nm.

The sensors were exposed to two different Hg vapour concentrations (5.70 and 10.55 ± 0.05 mg/m^3) at operating temperatures of 28 and 89°C. The sensors were first exposed to dry N_2 for 100 minutes in order to observe the sensor signal drift and noise. This was followed by Hg exposure for 8 hours and dry N_2 for a further 5 hours. Hg sorption and desorption kinetics at different operating temperatures was studied based on QCM response data, in order to determine the optimal operating temperature. The temperature profile test pattern described in chapter two was run to determine the optimal operating temperature.

The drift, noise and Q-factor before Hg exposure for each QCM with different Au electrode thicknesses are shown in Table 4.1 below. It is observed that as the electrode film thickness increases, the drift of the sensors increase while the noise is decreased over a 100 minute period. The decrease in noise is probably due to the increasing Q-factors with Au film thickness. The Q-factors (averaged for 10 samples of each film thickness) are observed to increase with Au thickness up to 150 nm and reduced for the 200 nm Au thickness. For this reason no testing was performed for Au thicknesses above 200 nm. It was also observed that the 40 and 50 nm Au thicknesses do not oscillate well due to their low Q-factors.

Table 4.1: Drift and noise of the five QCM optically polished Au electrodes thicknesses at operating temperatures of 28 and 89°C.

	Operating Temperature (°C)				
	28		89		
Sample	Drift (Hz/hr)	Noise (Hz)	Drift (Hz/hr)	Noise (Hz)	Q-factor
40 nm	0.41	± 0.63	0.45	± 2.59	5124
50 nm	0.62	± 0.45	0.71	± 1.83	5720
100 nm	1.57	± 0.14	1.07	± 0.3	7387
150 nm	1.63	± 0.02	1.28	± 0.14	7732
200 nm	1.74	± 0.02	3.2	± 0.05	7100

4.3 Parameters Influencing Hg Sorption and Desorption Characteristics

The influence of Hg exposure time, Hg coverage on Au surface (surface coverage, atoms/cm^{-2}), operating temperature and Hg vapour concentration on Hg sorption and desorption capacity of thin Au films (listed in Table 4.1) is presented in this section.

4.3.1 Influence of Hg Exposure Period and Surface Coverage

Figure 4.1a shows the dynamic response graph of a set of samples each with Au film thicknesses listed in Table 4.1 exposed to Hg vapour concentration of 10.55mg/m^3. An 8 hour Hg exposure and a 5 hour recovery period in dry nitrogen at an operating temperature of 28℃ was used.

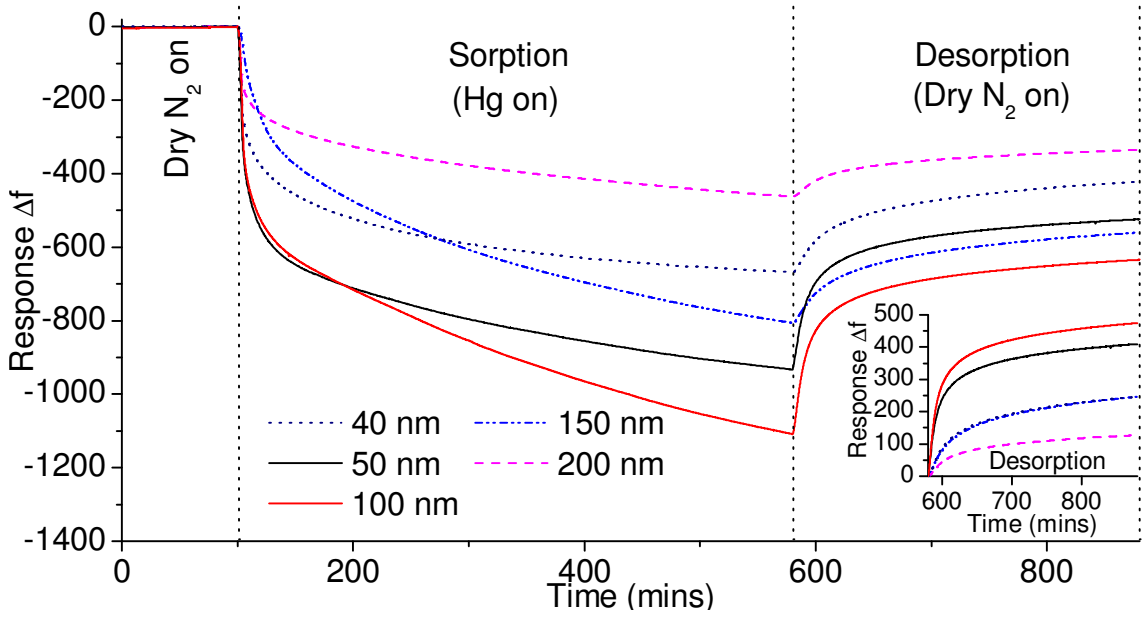

a) Dynamic response for 8 hour Hg exposure and 5 hour recovery periods using dry N_2 gas (Inset: zero-shifted QCM response during desorption period).

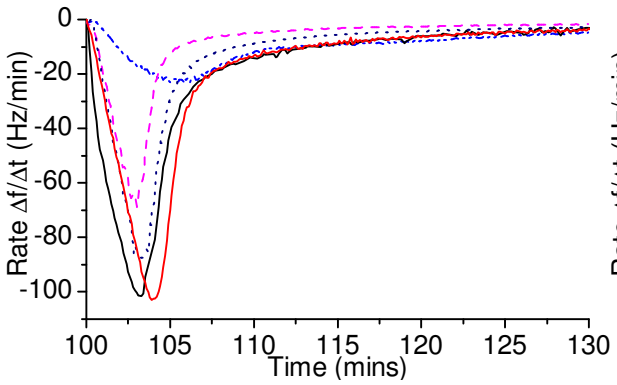

b) Hg sorption rate

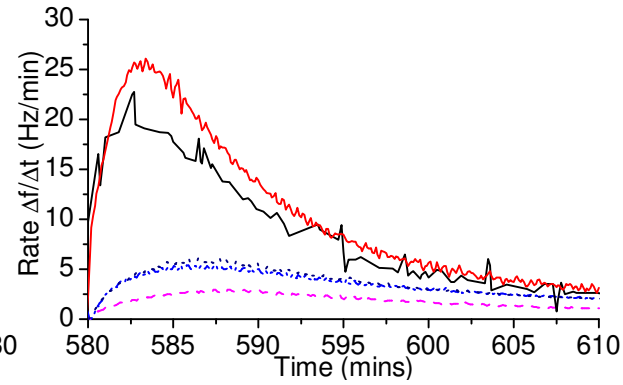

c) Hg desorption rate

Figure 4.1: Dynamic response, Hg sorption and desorption rate profiles of QCM sensors with electrode film thicknesses of 40, 50, 100, 150 and 200 nm when exposed towards 10.55 mg/m^3 Hg at an operating temperature of 28℃.

The influence of Au film thickness on Hg sorption capacity was realized by calculating the electrochemical surface area of each Au thin film and comparing with that of the geometrical surface area of each electrode (i.e. ~0.32 cm^2 given each of the two QCM electrodes are 4.5 mm in diameter). The electrochemical surface area of the Au electrodes were determined by calculating the charge required for reducing the monolayer of oxide as described by Rand

and Woods[274] (i.e. by integrating the cyclic voltammetric region shown in Appendix D, Figure D5). The electrochemical/geometrical surface area ratio of each Au film was evaluated to be ~1.5 cm^2/cm^2 ± 2% variation between the various Au film thicknesses. From Sauerbrey's equation (Equation 1.2), it is expected that such close proximity in surface area should result in similar dynamic response magnitudes between each of the QCMs. However, the large difference in the various Au film based QCM response magnitudes indicates that the Au thin film Hg sorption capacity is influenced by their thicknesses rather than surface area. The postulation of thickness dependence would also be inline with Haskell's[256] observation that beyond 10 nm, the Au forms continuous film and expected to have similar surface areas thereon resulting in similar sensor response magnitude towards Hg vapour.

The QCM response during Hg desorption using dry nitrogen at constant operating temperature of 28℃ is shown as an inset in Figure 4.1a. The dynamic response from each QCM has been shifted to initialize from zero hertz (zero-shifted) in order to observe the desorption trend from each of the Au thin films. The amount of Hg desorbed is found to follow the same trend throughout the 5 hour desorption period.

The sorption rate for the first 60 minutes of Hg exposure is shown in Figure 4.1b. Similarly, desorption rate during the first 60 minute exposure of dry nitrogen is shown in Figure 4.1c. It is observed that both Hg sorption and desorption rates are Hg surface coverage dependent. Hg surface coverage is defined as the mass of Hg per surface area of Au film. Since the QCMs used in this work have a sensitivity of 4.39 $ng/cm^{-2}Hz^{-1}$, the product of QCM sensitivity with response magnitude (Δf in Hz) indicates how much mercury is on the Au sensitive layer. An increase in Δf indicates an increase in the amount of Hg adsorbed/amalgamated on the Au surface (increase in Hg surface coverage) and vice versa.

Hg sorption rate is observed to increase initially and reach a maximum within the first 4 minutes of exposure time (at time of ~104 minutes in Figure 4.1b) due to initial lack of Hg on the Au substrate. As Hg builds on the Au surface, the sorption rate is observed to reduce and approach zero. Similarly Hg desorption rate is observed to increase initially reaching a maximum within the first 4 minutes of recovery time (at time of ~584 minutes in Figure 4.1c)due to initial high surface coverage of Hg on the Au surface. As Hg is depleted from the Au surface, Hg desorption rate is observed to reduce and approach zero. This observation is in line with that of Jones and Perry[295] where they also observed that the desorption rate was initially large, but rapidly dropped as Hg surface coverage decreased indicating that Hg desorption rate is Hg surface coverage dependent. The observations made from Figure 4.1 refer to Hg-Au interaction, however the observations of Jones and Perry were made for Hg-

Fe and assumed for all metal surfaces interacting with Hg. The results presented in Figure 4.1 confirm such assumption for Hg-Au system.

The Hg sorption capacity is also found to be affected by Hg exposure time on the different Au film thicknesses. The trend in Hg sorption capacity for each Au film thickness is observed to change at exposure times of ~20 and ~200 minutes as observed from Figure 4.1a. The response magnitude of the various Au film thicknesses at times of 10, 100 and end of the exposure period (480 minutes) is shown in Figure 4.2. It is apparent that the Hg exposure time influences the trend of Hg sorption capacity of the various Au films and is a critical parameter to be considered when using Au films for Hg vapour sensing.

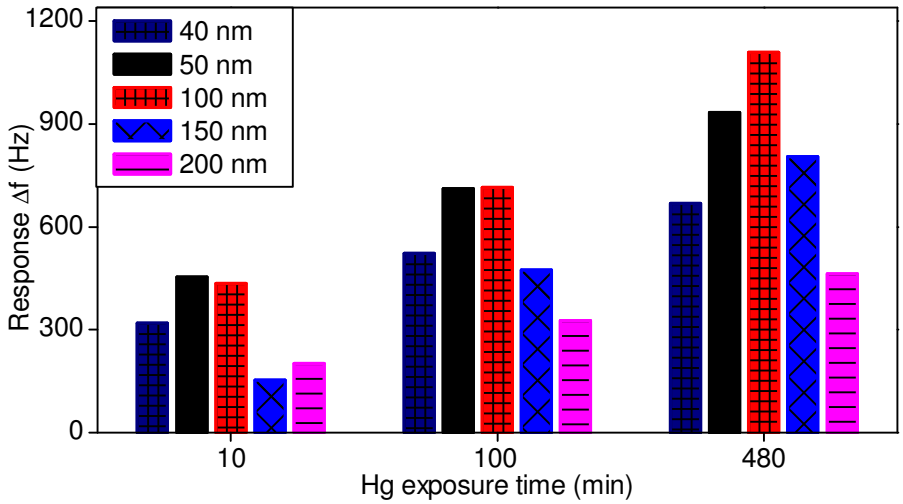

Figure 4.2: Effect of Hg exposure time on dynamic response of Au films with film thicknesses from 40 to 200 nm.

4.3.2 Influence of Operating Temperature

In order to determine the influence of operating temperature on Au film Hg sorption capacity, a set of new QCMs with various Au film thicknesses were tested towards Hg vapour concentration of 10.55 mg/m^3 at an operating temperature of 89℃. The 40 nm thick Au film was excluded from any further testing as it was found to be noisy and not able to oscillate at the higher operating temperature of 89℃. The response curves for the QCMs are shown in Figure 4.3.

Comparing Figure 4.1a with that of 4.3a, it can be clearly observed that the Hg sorption capacity of the different Au film thicknesses is greatly affected by the operating temperature. Hg sorption capacity is observed to increase with increasing Au thickness following 8 hours of Hg exposure at 89℃ (Figure 4.3a) as opposed to 28℃ (Figure 4.1a). Exposure time is again observed to affect the sorption trend of the different Au thicknesses. For example, at exposure times less than 7 hours, the 150 nm Au QCM is observed to undergo the largest

Hg sorption. However, by the end of the 8 hour Hg exposure period, the 200 nm Au QCM is observed to produce the highest Hg sorption capacity at an operating temperature of 89℃. Furthermore, the 100 nm Au QCM was observed to produce the highest response magnitude towards an 8 hour Hg exposure period at an operating temperature of 28℃. However the 200 nm Au QCM produced the highest response magnitude at the operating temperature of 89℃ demonstrating that operating temperature influences Hg sorption capacity of the Au thin films.

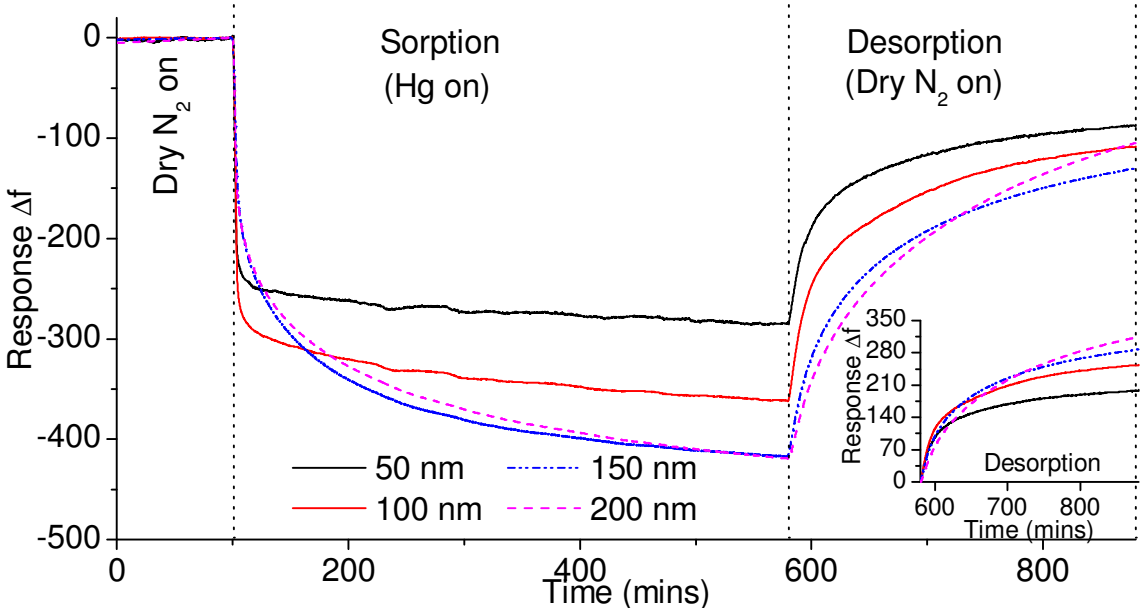

a) Dynamic response for 8 hour Hg exposure and 5 hour recovery periods using dry N_2 gas (Inset: initialized QCM response during desorption)

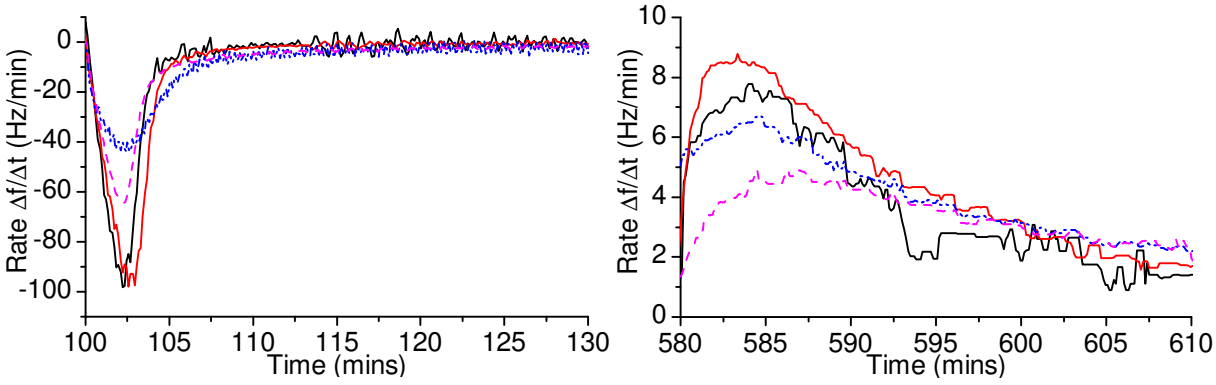

b) Hg sorption rate

c) Hg desorption rate (smoothed)

Figure 4.3: Dynamic response, Hg sorption and desorption rate profiles of QCM sensors with electrode film thicknesses of 50, 100, 150 and 200 nm when exposed towards 10.55 mg/m^3 Hg at an operating temperature of 89℃.

It is further observed that the thinner Au films (50 and 100 nm) approach saturation following 10 mins of Hg exposure period (at time of 110 minutes on the X-axis in Figure 4.3a).

However saturation is not reached even following 8 hours of Hg exposure period indicating Hg diffusion through the Au thin film. The thicker films (150 and 200nm) on the other hand show little sign of saturation indicating diffusion is more predominant in the thicker Au samples. The diffusion behaviour of Hg in Au substrates will be further investigated in Chapter 5.

Similar to sorption, the desorption behaviour of the Au QCMs with various film thicknesses following 5 hours of desorption period is also observed to follow the trend of increasing desorption with increasing film thickness as shown in the inset of Figure 4.3a. The trend may also be attributed to the surface coverage, where the thicker samples that adsorbed/amalgamated a larger amount of Hg were observed to have desorbed larger amount of Hg upon exposure of dry N_2 during the 5 hour recovery period. The desorption curves, however, don't follow the same trend throughout the 5 hour desorption period. This behaviour is attributed to the mobility of the amalgam islands at high temperatures[86] as more Hg contaminated surface would be exposed to dry N_2 environment due to the mobility of the granules resulting in enhanced desorption.

The sorption/desorption rate of the QCMs are also shown in Figure 4.3 with the adsorption rate in the first 60 minutes of Hg exposure in Figure 4.3b and the desorption rate of the first 60 minute period in Figure 4.3c. The order of maximum sorption and desorption rate magnitude with that of Au film thickness is observed to be 150 nm < 200 nm < 100 nm ~ 50 nm. Four Duplicate QCMs with the various Au film thicknesses were characterized using SEM, the images of which are shown in appendix D (Figure D.4). Minor changes in surface morphology were observed between the various Au thicknesses (namely the 50, 100, 150 and 200 nm thick Au films) indicating that the order of sorption and desorption rate was not morphology dependent. The order of maximum sorption and desorption rate magnitudes for each of the Au film thickness is observed to vary at 89℃ (Figure 4.1b and 4.1C) as compared to that observed at 28℃ (Figures 4.3b and 4.3c) indicating they are highly influenced by operating temperature.

4.3.3 Influence of Hg Vapour Concentration

Figure 4.4 shows the response and response rate curves for the four QCMs of different Au thicknesses exposed to Hg vapour concentration of 5.70 mg/m^3 at 89℃ (same operating temperature but lower Hg vapour concentration from Figure 4.3).

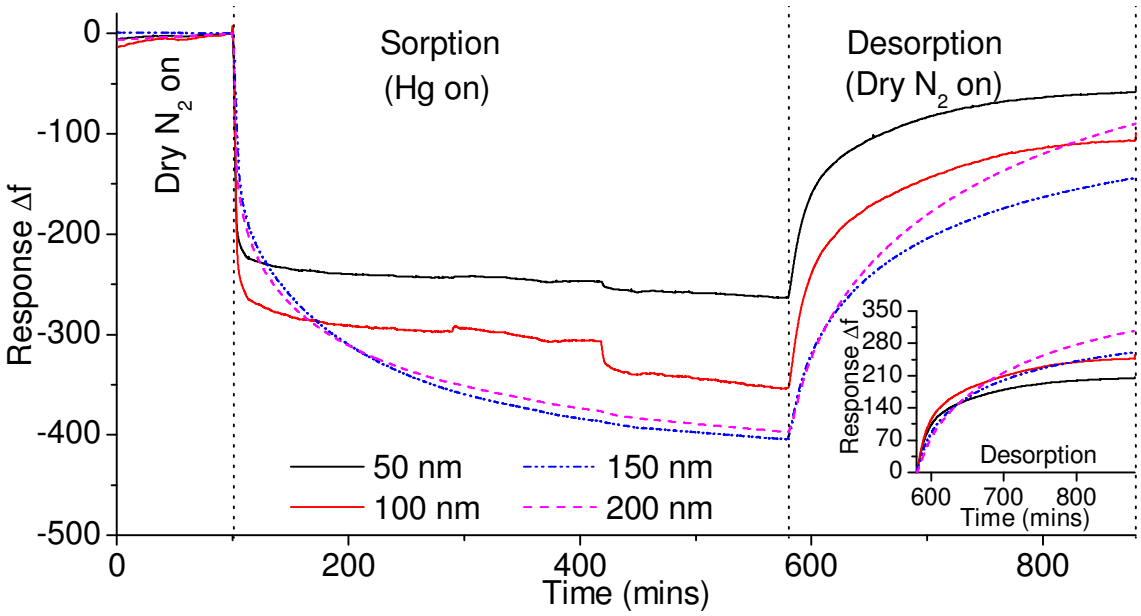

b) Dynamic response for 8 hour Hg exposure and 5 hour recovery periods using dry N_2 gas (Inset: initialized QCM response during desorption)

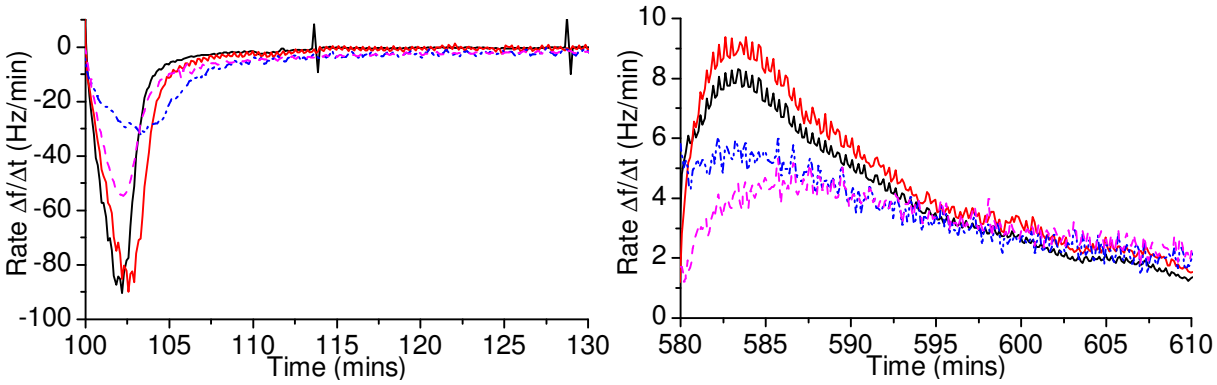

b) Hg sorption rate

c) Hg desorption rate

Figure 4.4: Dynamic response, Hg sorption and desorption rate profiles of QCM sensors with electrode film thicknesses of 50, 100, 150 and 200 nm when exposed towards 5.70 mg/m^3 Hg at an operating temperature of 89℃.

Comparing Figure 4.4a with that of 4.3a, the Hg sorption and desorption trends for the various Au film thicknesses are quite similar. This indicates that the trend of Hg sorption capacity with respect to thickness is similar at the operating temperature of 89℃ and that the trend is not affected by a decrease in Hg vapour concentration. The sorption and desorption rates are also found to follow similar trends as indicated by Figures 4.4b and c respectively. The 100 nm sample is found to show some instability in the response curve in Figure 4.4a. This may be due to surface changes resulting from amalgamation or simply the instability of the QCM at the higher operating temperature during the 8 hour Hg exposure period.

4.4 Temperature Profile of Au Thin Film Based QCM Sensors

The response magnitude of thin Au film based QCMs (100, 150 and 200 nm) towards various Hg concentrations (1.02 to 10.55 mg/m^3) at different operating temperatures (28 to 173℃) is studied. The analysis of the response magnitude shape against operating temperature at every Hg vapour concentration is attempted to be explained using Hg-Au solubility data obtained from literature. The optimum Au film from the investigation in chapter 3 (Au-rough) is also compared with the 100 nm optically polished Au thin film. A comparison of Au thin film surface area on Hg sorption capacity, Au film morphology on the resultant Hg sorption isotherms at various temperatures and influence of Au film morphology on their Hg sorption and desorption kinetics is made.

4.4.1 Test Pattern

The temperature profile test pattern was started following a pre-treatment procedure as described in chapter 2. As well as the 100, 150 and 200 nm optically polished Au QCMs, a duplicate 100 nm thick Au QCM was also placed in the test chamber in order to observe the repeatability of the response curves. A period of 60 minutes of each sorption and desorption times were chosen at all Hg vapour concentrations and operating temperatures. As the Hg concentration in this study is in the mg/m^3 range rather than µg/m^3 range normally used in other studies[143,252], it is thought that the short exposure times of 60 minutes may reduce the possibility of Hg breakthrough from the Au film[88,146] as well as restrict the exposure time dependent amalgamation process.[78,127]

From the 11 operating temperatures tested, the response curve for 55℃ is shown in Figure 4.5.

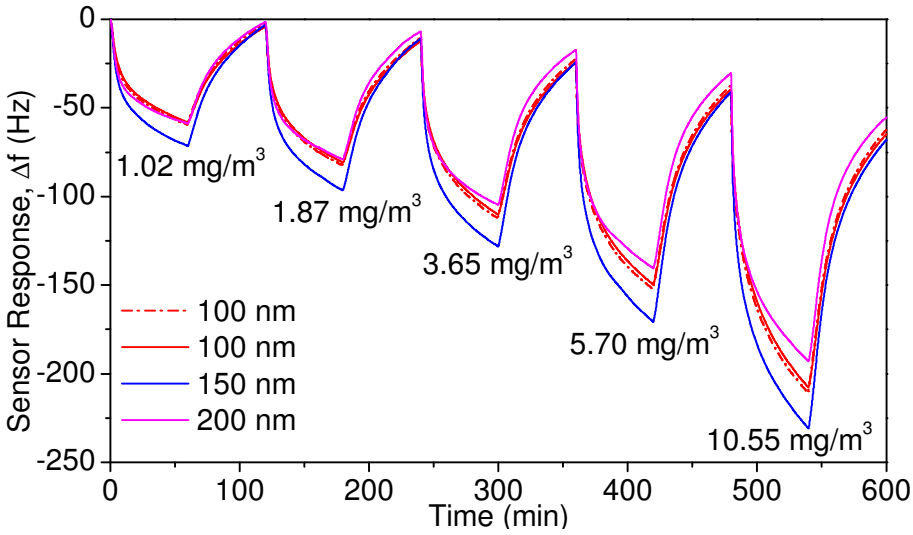

Figure 4.5: Four QCMs exposed to Hg concentrations of 1.02, 1.87, 3.65, 5.70 and 10.55 mg/m^3 at an operating temperature of 55℃

It may be observed that the two 100 nm thick Au QCMs have similar response curves and so the repeatability between QCMs of same Au electrode thicknesses is confirmed. It is also observed that sensor recovery during the dry nitrogen exposure periods are not fully complete as gradual drift is observed between Hg sorption and desorption stages. That is, for the 150 nm thick Au QCM at the operating temperature of 55°C and Hg concentration of 3.65 mg/m^3, the difference in response magnitude between Hg sorption and desorption was found to be 13.35Hz. The drift in the QCM signal at this operating temperature is calculated to be 1.36Hz/h. Therefore the reduced Hg sorption is calculated to be ~12Hz. Since the Sauerbrey equation sensitivity of the QCMs used in this study are ~4.39 $ng.cm^{-2}.Hz^{-1}$, the amalgamated/diffused Hg following desorption period is estimated to be ~52.6 $ng.cm^{-2}$. From a Hg vapour sensor point of view, at the optimum operating temperature, the extent of amalgamated/diffused Hg needs to be at its lowest (or acquire high Hg desorption to sorption ratio) while producing high enough response magnitude towards Hg vapour.

4.4.2 Temperature Profile Studies

The response curves for the 100 nm thick optically polished Au QCM at the tested Hg vapour concentrations and operating temperatures is presented in Appendices D, Figure D1. Similar curves were used to produce Figure 4.6 which shows the response magnitude of each sensor towards different Hg vapour concentrations and various operating temperatures.

Figure 4.6a shows the response-temperature curve for the 100 nm Au and duplicate 100 nm (overlayed black lines) Au QCMs. It is observed that the response magnitudes of the two identical QCMs are repeatable at all temperatures and Hg vapour concentrations. More significantly, the sensor response of the 150 and 200 nm thick Au QCMs are also observed to produce similar magnitudes to that of the 100 nm thick Au QCM as observed in Figures 4.6b and c, respectively. This similarity in response magnitudes are presented in the overlayed data (Hg concentration of $10.55mg/m^3$) of all sensors in Figure 4.6d. The same trend in the response-temperature behaviour was observed for all Hg vapour concentrations tested. The response magnitudes of the 150 and 200 nm thin Au films are observed to be similar for the first 1 hour Hg exposure period for the data presented in Figure 4.1. Since the response-temperature curves in Figure 4.6 are obtained from the 1 hour Hg pulse tests, it is no surprise to observe all three different Au thick QCMs follow similar trend of a cubic type curve. It follows then that Hg sorption may be occurring in a similar fashion on all the QCMs as the Au thickness in these thin films are quite large and therefore will have similar properties. A better understanding may be obtained by investigating Hg sorption in ultra thin (10 – 40 nm) films which is the subject of chapter 5. At this stage, it is worth investigating the reason for the cubic type shape of the curves observed for all the three Au films of different thicknesses shown in Figure 4.6.

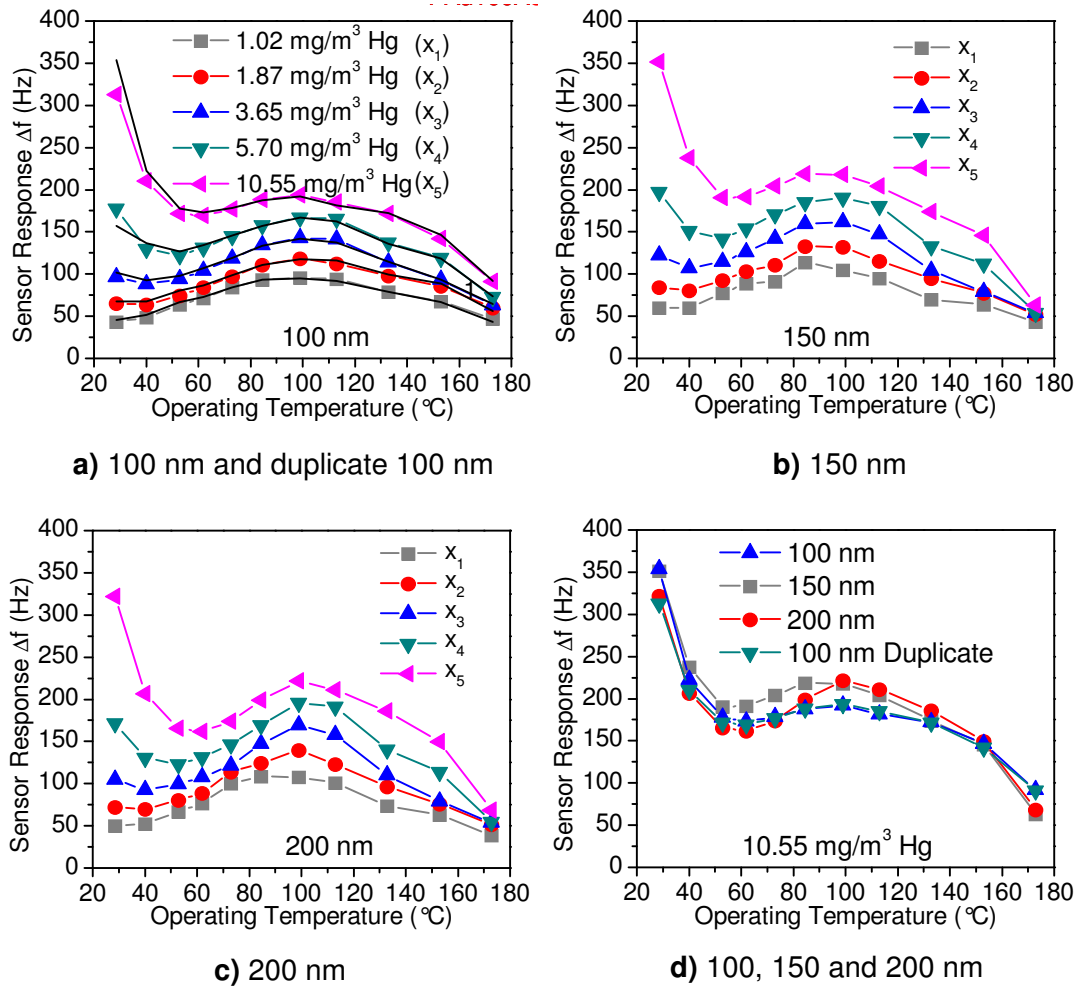

Figure 4.6: Temperature profile of QCMs with thin Au film electrodes

4.4.3 Analysis of Temperature Profile Shape

As discussed in chapter 3, the extent of diffusion of Hg in Au is dependent on the amount of Hg sorption on the surface. The four main factors that gas sorption are the collision rate of the gaseous atoms with the solid surface, the probability of finding a suitable site, probability of being in correct orientation and probability of overcoming the adsorption barrier.[78,267] One of the major factors affecting Hg sorption on Au surfaces, which takes the factors mentioned above into account, is the affinity of Au for Hg at different temperatures. A parameter that may be related to affinity is the solubility of Au in Hg. An increase in solubility is postulated to increase the affinity between the two metals. The other parameter is the change in the vapour pressure of Hg with temperature. That is, at increasing operating temperatures, the amount of Hg that can be saturated in air increases, reducing Hg atoms tendency to adsorb on the Au surface. This parameter (vapour pressure) therefore reduces rather than increase Hg affinity towards Au films when operating temperatures are increased.

The curve shown in Figure 4.7 illustrates the change in Au solubility in Hg as well as the Hg vapour pressure with temperature. It is observed that both the Affinity factor (solubility) as

well as the repulsive factor (vapour pressure) of Hg sorption increase with increasing temperature. The cubic shape observed in Figure 4.6 may be the result of the balance between these two factors.

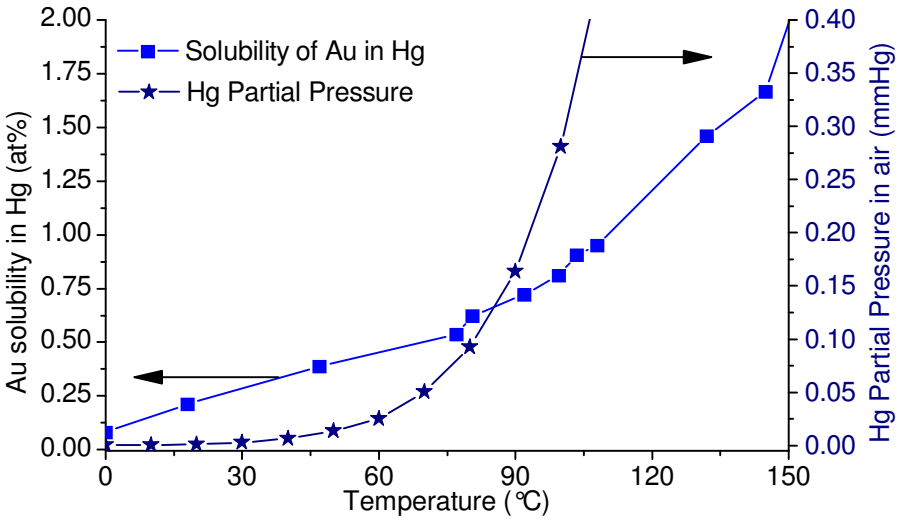

Figure 4.7: Influence of Operating temperature on the change in solubility of Au in Hg and vapour pressure of Hg in air

At low temperatures for example, the solubility of Au in Hg as well as the vapour pressure are both low in magnitude. This produces high Hg sorption on the gold surface as there is low tendency for Hg to stay in the vapour phase specially when it collides with the Au substrate. At temperatures between 40 – 60°C the vapour pressure is increased. Although the solubility of Au in Hg is also increased, the influence of vapour pressure is higher and so Hg sorption is observed to decrease. Between 60 – 90°C the increase in solubility is found to dominate again and so Hg sorption is found to increase once again. Thereon, an increase in the operating temperature results in Hg vapour pressure increasing rapidly reducing the likeliness of the Hg atoms to leave the gas phase and adsorb/amalgamate on the now hot surface.

It is worth noting that the increase in temperature also increases the gas atoms' kinetic energy, which inturn reduces their tendency to adsorb/amalgamate on the surface. That is, surfaces with large number of kinks, edges and other defects are required at higher temperatures in order for the Hg vapour atoms to collide and lose their kinetic energy prior to adsorption/amalgamation.[267] The fact that the Au-rough surface contains high concentration of surface defects per surface area[313] may be the reason for the absence of such cubic curve behaviour for the Au-rough film in chapter 3, Figure 3.11a although the Au-rough QCM was exposed to the same Hg concentrations, temperatures and exposure times as the optically polished surfaces presented in this chapter. It is postulated that the kinks and other defects are able to overcome the Hg atoms' kinetic energy encouraging sorption. The presence of

such surface defects may alter the kinetics of Hg sorption on the Au-rough surface and therefore the cubic curve type shape is not observed in the response-temperature curve.

4.4.4 Influence of Operating Temperature and Surface Morphology

The temperature profile of Au-rough film was presented in chapter 3 (Figure 3.11a) while that of the Au-polished film (100 nm Au thin film) is shown in Figure 4.6a. In this section, Hg sorption isotherm at various operating temperatures, Hg sorption capacity, Hg sorption/desorption kinetics and Hg desorption/sorption ratio a comparison is made (using the temperature profile response curves of both Au-rough and Au-polished films) between the two surfaces in terms of Hg sorption isotherm and capacity.

4.4.4.1 Hg Sorption Isotherm

A comparison of the Hg sorption isotherms at various operating temperatures for the 100 nm thick Au QCM is presented in Figure 4.8. The Hg sorption isotherms for the duplicate 100nm as well as the 150 and 200 nm Au QCMs were observed to be similar and shown in Appendix D (Figure D2). Needless to say, these curves are plotted from the data observed in Figure 4.6a above.

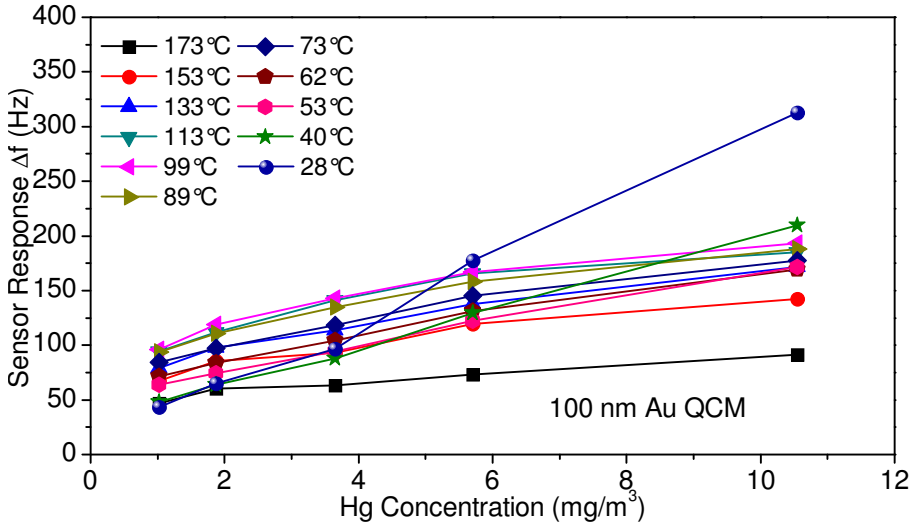

Figure 4.8: Hg sorption Isotherm for the 100 nm Au QCM at various operating temperatures.

The adsorption isotherms in Figure 4.8 for the optically polished Au film may be compared with that of the mechanically roughened Au film presented in chapter 3 Figure 3.11b. It may be observed that the Hg sorption capacity follows a more ordered trend on the mechanically roughened Au than the optically polished thin Au films. The general trend for Hg sorption on the Au-rough film is that it increases with increasing Hg concentration or decreasing operating temperature. However for an optically polished film, no such trend is observed. The postulation made in chapter 3 that roughened surface morphology may be the optimum sensitive films to be used as a potential online Hg vapour sensor, is now becoming more evident. The lack of order in the trend for the optically polished Au film indicates that if used

as an online Hg vapour sensor, small temperature fluctuations and Hg vapour concentration fluctuations may largely affect the sensor leading to large errors in Hg vapour concentration estimations.

4.4.4.2 Effect of Morphology on Detection Limit and Sensitivity

The detection limit (DL) and sensitivity of the Au-rough and Au-polished (100 nm Au thin film) QCMs when exposed towards Hg vapour at different concentrations and operating temperatures are calculated and compared using the method described by Miller et al.[314] Briefly, the sensitivity [Hz/(mg/m^3)] is calculated by the slope of the calibration graph (or sorption isotherms) provided the plots are linear. The detection limit is calculated with the aid of the section of the plot close to the origin utilizing both the slope and the intercept. Interestingly, the slopes for the Au-polished and Au-rough films (observing their Hg sorption isotherms) were found to be linear with coefficient of determination (R^2) values of 0.990 and 0.997, respectively, only at an operating temperature of 28℃. At operating temperatures > 28℃, the sorption isotherms were found to be linear when the sensor response magnitude is plotted against the logarithm of Hg vapour concentration resulting in the modified linear plots having the following relationships:

$$\Delta f = a\ln(x) + b \qquad \text{(For T > 28℃)} \qquad \text{Equation 4.1}$$

$$\Delta f = ax + b \qquad \text{(For T = 28℃)} \qquad \text{Equation 4.2}$$

The parameters a and b are the slope and intercept of the linear curves, Δf is the sensor response magnitude (Hz) and *x* represents the Hg vapour concentration (mg/m^3) tested. The lines of best fit for both Au-polished and Au-rough at 28 and 89℃ is shown in Figure 4.9.

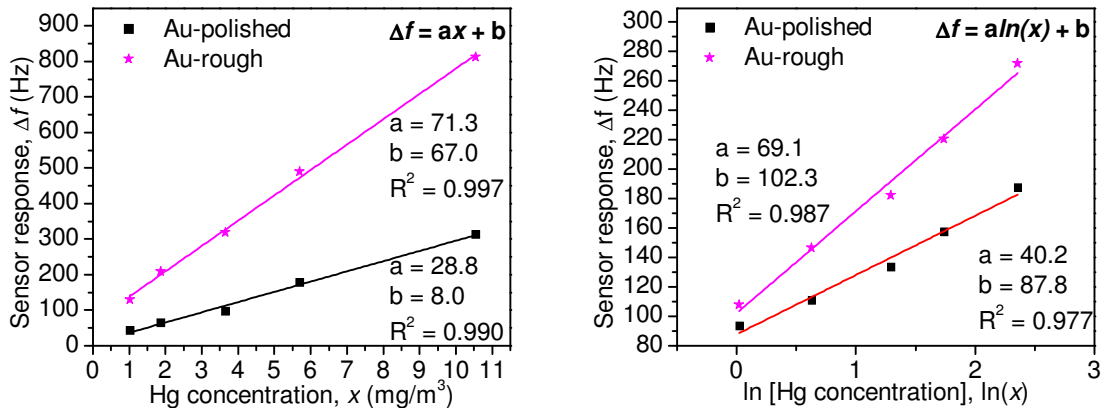

a) 28℃ **b)** 89℃

Figure 4.9: Linear plots of Hg sorption isotherms at 28 and 89℃. The linear plots are used to calculate sensitivity and detection limit of QCM based Hg vapour sensors.

It is observed that the Au-rough sensitivity towards Hg vapour is ~2.5 times that of the Au-polished QCM at 28℃ [slope = a = sensitivity of 71.3 vs 28.8 Hz/(mg/m^3)]. At operating temperatures above 28℃, sensitivity is observed to be Hg concentration dependent since

the slope represents $\partial(\Delta f)/\partial(\ln x)$ rather than $\partial(\Delta f)/\partial(x)$. However using the chain rule for differentiation of Equation 4.1, it is observed that $\partial(\Delta f)/\partial(x) = \frac{a}{x}$ indicating sensitivity is inversely proportional to Hg concentration at operating temperature $28°C < T \leq 173°C$. Therefore the Au-rough is observed to have higher sensitivity towards Hg vapour at 89℃ than the Au-polished QCM due to its higher a value as depicted in Figure 4.9b.

The sensors' limit of detection (LOD) was calculated for both Au-rough and Au-polished film based QCMs and compared at 89℃ using Equation 4.3.

$$LOD = 3\times\left(\frac{\sum(\Delta f_i - \Delta f_e)^2}{n-2}\right)^{\frac{1}{2}} \qquad \text{Equation 4.3}$$

Δf_i and Δf_e represent the sensor response magnitude determined by experiment and extracted from the fitted linear plot, respectively. the number of data points, n, is five being the number different Hg vapour concentrations tested during the experiments. Once obtained, the LOD value is substituted into the respective linear equations and the unit of sensor response (Hz) is converted to Hg concentrations (mg/m^3). It was found that the 100 nm Au-polished based QCM had a better detection limit (0.171 mg/m^3) than the Au-rough based QCM (0.311 mg/m^3) at an operating temperature of 89℃. Due to the high temperature stability of AT-cut based QCMs at around room temperature, the detection limit of both the Au-rough and Au-polished were observed to be 0.012 and 0.035 mg/m^3, respectively.

Overall, the Au-rough was observed to have higher sensitivity towards Hg vapour than Au-polished film based QCM at operating temperatures of 28 as well as 89℃. On the other hand, the DL for Au-rough was observed to be lower then the Au-polished film based QCM at 28℃ and vice versa at 89℃. Similarly, the QCM sensitivity and detection limit was calculated for each of the fabricated sensors in this research project and are presented in chapter 8 (Table 8.1).

4.4.4.3 Effects of Surface Area on Hg Sorption Capacity

The relative electrochemical surface area of rough to the optically polished Au film was found to be 2.542 using the method described in section 4.3.1. However, in comparing the response magnitudes of the Au-rough to the optically polished surface based QCMs (Figure 3.11 in chapter 3 with that of Figure 4.6 above) the ratios are observed to be different at various Hg concentrations and operating temperatures as can be observed from Figure 4.10. It is observed that the amount of Hg sorption is not dependent only on the available Au surface area but also the surface morphology as well as the operating temperature and Hg

vapour concentration. That is, the ratio of Hg adsorbed/amalgamated on the Au-rough to that on the Au-polished film is not fixed (as it would be if it were purely surface area effect) and changes depending on the experimental conditions (i.e. operating temperature and Hg vapour concentration).

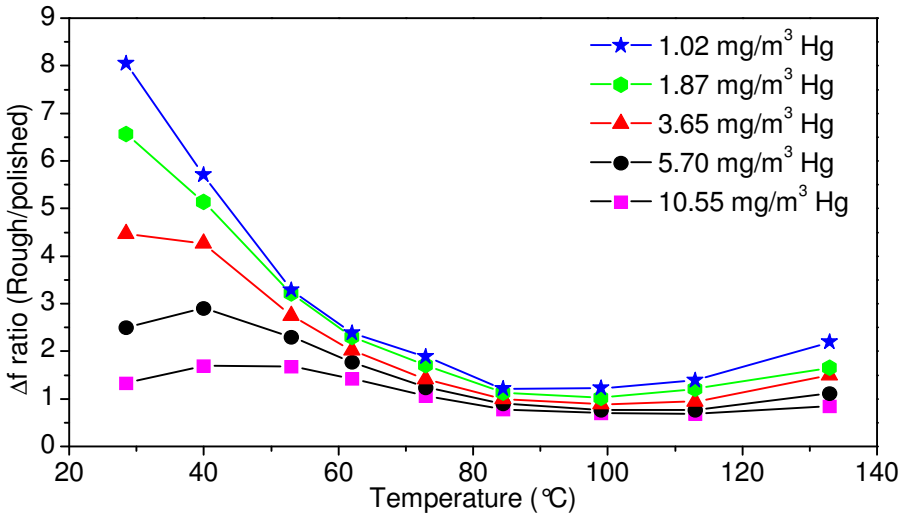

Figure 4.10: Hg sorption capacity ratio of rough/polished Au QCMs at various operating temperatures and Hg vapour concentrations

4.4.4.4 Effects of Surface Morphology on Hg Sorption/Desorption Kinetics

Figure 4.11 illustrates the adsorption response curve for the 100 nm optically polished and mechanically roughened Au QCMs for the first 2 minutes of Hg exposure at a concentration of 5.70 mg/m^3. It may be clearly observed that the adsorption kinetics vary with surface morphology.

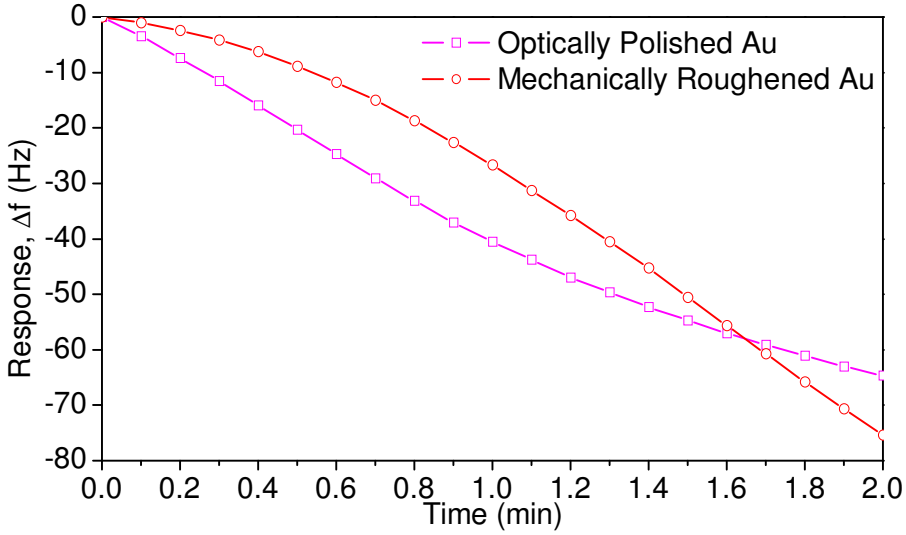

Figure 4.11: Hg sorption in the first two minutes for both optically polished and mechanically roughened Au QCMs

It was observed that the initial rate of Hg sorption was higher for the optically polished Au film based QCM in the first 1.5 – 2 minutes. The same trend was observed at all Hg vapour concentrations and operating temperatures tested. Following the 1.5 – 2 minutes of Hg exposure, the rate of Hg sorption then increased for the mechanically roughened Au thereon and may be observed from the sorption rate figures presented in Appendix D (Figure D3). From Figure D3 it may also be observed that the mechanically roughened Au based QCM maintains higher Hg sorption rate for longer period than the optically polished Au film for all Hg vapour concentrations and operating temperatures. This may be attributed to the high sticking probability of the Au-rough as compared to the optically polished Au film as was observed in chapter 3. It is also observed that the maximum rate of Hg sorption, in general, increases with increasing temperature (Figure D.3). However, the rate of sorption approaches zero from its maximum value faster at the higher temperatures. The maximum desorption rates are observed to increase with decreasing temperatures which may be correlated to larger Hg sorption at the lower operating temperatures (Figure 4.6) and the dependence of Hg desorption rate on the Hg surface coverage.[295]

4.4.4.5 Effects of Surface Morphology on Hg Desorption/Sorption Ratio

The ratio of Hg desorption to that of sorption (adsorbed/amalgamated) at Hg concentration of 10.55 mg/m^3 is presented in Figure 4.12 for both the 100 nm optically polished and mechanically roughened Au QCMs. Similar trends were also observed for the lower Hg vapour concentrations tested.

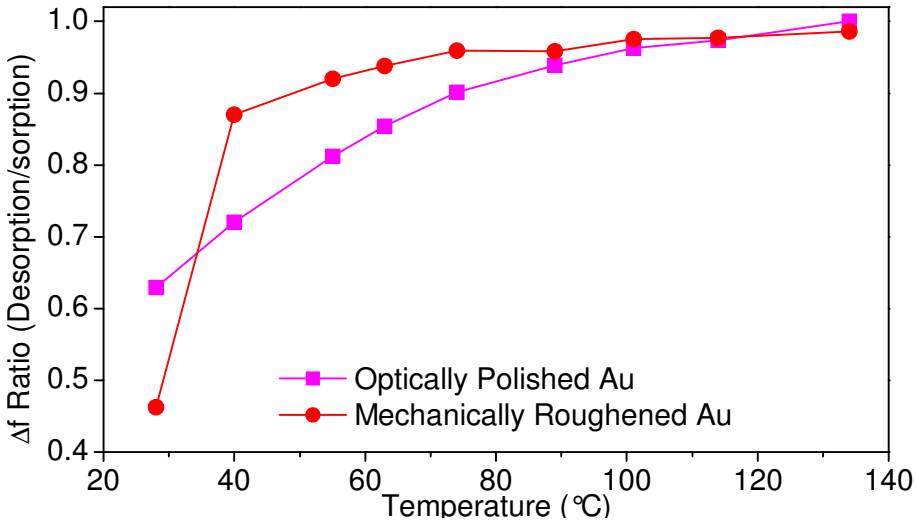

Figure 4.12: Desorption/sorption ratios for optically polished and mechanically roughened Au QCMs at Hg vapour concentration of 10.55 mg/m^3 and various operating temperatures.

It may be observed that the ratio of the Hg desorbed to that adsorbed/amalgamated increases with increasing operating temperatures reaching 1 and 0.986 (100 and 98.6% desorption) for the rough and polished Au surfaces respectively at an operating temperature of 134℃. However, at the higher operating temperatures, it is observed that the dynamic

range between the Hg concentrations is reduced (Figure 4.8). The optimum temperature at which a high Hg desorption/sorption ratio, high sensor response magnitude as will as large dynamic range was reached was found to be ~90°C. This result was in line with those of Larjava et al[103,104] whom performed experiments in order to determine the collection efficiency of gold diffusion screens (Hg traps, similar to those used in CVAAS techniques for Hg sensing). They have also found that Hg collection efficiencies above 99% may be achieved at operating temperatures of ~90°C.

The combination of high Hg collection efficiency of Au found in past studies and the high desorption/sorption ratio found in this work at ~90°C is encouraging. It is envisaged to use an operating temperature of ~90°C for Hg sensing tests with/without the presence of ammonia and humidity interferents when undergoing medium and long term testing of the modified sensors (presented in chapters 6 and 7). The relatively high operating temperature of ~90°C is expected to produce high sensitivity towards Hg vapour as well as low cross sensitivity issues from the interferent gases.

4.5 Summary

In this chapter, it was shown that the optimum Au film thickness for QCM based Hg vapour sensors were the 100 and 150 nm thick Au films. To the best of the author's knowledge, this is the first time it is observed that the dependence of increasing sorption capacity of Au films did not follow a simple trend with film thickness. It was found that Hg sorption capacity also depended on other parameters such as Hg vapour concentrations, Hg exposure time and operating temperatures. A change in one of these parameters results in either film having the largest sorption capacity depending on which parameter is altered.

Interestingly, the 100, 150 and 200 nm thin Au film based QCMs were observed to produce similar response magnitudes at all Hg vapour concentrations and operating temperatures provided 1 hour pulses were used. The temperature profiles for the various thin Au films were observed to be cubic type and was proposed to be due the competition between increasing Au solubility in mercury (affinity factor of Au for Hg) and increasing Hg vapour pressure (repulsive factor).

Hg sorption and desorption kinetics data obtained using QCM sensors showed maximum Hg sorption rate increased with increasing operating temperature. However, the rate of Hg sorption approaches zero from its maximum value faster at the higher temperatures resulting in relatively low response magnitudes. Desorption rate is found to follow an opposite trend where increased maximum desorption rate was observed with decreasing temperature. This is inline with literature where it was reported that desorption rate is Hg surface coverage

dependent. That is, it was observed from the data presented in this chapter that decreased temperatures results in increased Hg sorption and therefore Hg surface coverage.

The optimum operating temperature was found to be ~90℃ based on desorption/sorption ratios and the dynamic range of the sensors' response towards various Hg vapour concentrations. A comparison of Hg sorption and desorption kinetics is also made between the mechanically roughened and optically polished Au films. The findings lead the author to believe that modification for Hg vapour sensing requires being of roughened morphology for optimum sorption and desorption properties. These morphologies will be incorporated during the surface modification procedures and will be presented chapters 6 and 7. Prior to surface modification of the 100 and 150 nm thick Au films for optimum Hg vapour sorption and desorption, it is necessary to understand the diffusion of Hg through ultra thin Au films. The diffusion of Hg through ultra thin Au films is presented in the next chapter.

4.6 References

(1) Sakai, G.; Baik, N. S.; Miura, N.; Yamazoe, N. *Sensors and Actuators B: Chemical* **2001**, *77*, 116-121.
(2) Hsieh, J. C.; Liu, C. J.; Ju, Y. H. *Thin Solid Films* **1998**, *322*, 98-103.
(3) Lucklum, R.; Behling, C.; Hauptmann, P. *Analytical Chemistry* **1999**, *71*, 2488-2496.
(4) Schramm, U.; Roesky, C. E. O.; Winter, S.; Rechenbach, T.; Boeker, P.; Schulze Lammers, P.; Weber, E.; Bargon, J. *Sensors and Actuators B: Chemical* **1999**, *57*, 233-237.
(5) Cavicchi, R. E.; Suehle, J. S.; Kreider, K. G.; Gaitan, M.; Chaparala, P. *Sensors and Actuators B: Chemical* **1996**, *33*, 142-146.
(6) Sakai, G.; Matsunaga, N.; Shimanoe, K.; Yamazoe, N. *Sensors and Actuators B: Chemical* **2001**, *80*, 125-131.
(7) Bakker, E.; Pretsch, E.; Buhlmann, P. *Analytical Chemistry* **2000**, *72*, 1127-1133.
(8) Hahm, J.-i.; Lieber, C. M. *Nano Lett.* **2003**, *4*, 51-54.
(9) Zheng, G.; Patolsky, F.; Cui, Y.; Wang, W. U.; Lieber, C. M. *Nat Biotech* **2005**, *23*, 1294-1301.
(10) McNerney, J. J.; Buseck, P. R.; Hanson, R. C. *Science* **1972**, *178*, 611-612.
(11) Haskell, R. L. B.; Caron, J. J.; Duptisea, M. A.; Ouellette, J. J.; Vetelino, J. F. In *Ultrasonics Symposium, 1999. Proceedings*; IEEE: Orono, ME, 1999; Vol. 1, p 429-434 vol.1.
(12) Haskell, R. B. Masters, University of Maine, 2003.
(13) Chaurasia, H. K.; Huizinga, A.; Voss, W. A. G. *Journal of Physics D: Applied Physics* **1975**, *8*, 214-218.
(14) Zimmermann, B.; Lucklum, R.; Hauptmann, P.; Rabe, J.; Büttgenbach, S. *Sensors and Actuators B: Chemical* **2001**, *76*, 47-57.
(15) Lucklum, R.; Eichelbaum, F. In *Piezoelectric Sensors* 2007, p 3-47.
(16) Dryzek, J.; Czapla, A. *Journal of Materials Science Letters* **1986**, *5*, 1269-1270.
(17) Rand, D. A. J.; Woods, R. *Journal of Electroanalytical Chemistry* **1971**, *31*, 29-38.
(18) Jones, R. G.; Perry, D. L. *Vacuum* **1981**, *31*, 493-498.
(19) Nowakowski, R.; Kobiela, T.; Wolfram, Z.; Dus, R. *Applied Surface Science* **1997**, *115*, 217-231.
(20) Mirsky, V. M.; Vasjari, M.; Novotny, I.; Rehacek, V.; Tvarozek, V.; Wolfbeis, O. S. *Nanotechnology* **2002**, *13*, 175-178.
(21) Scheide, E. P.; Warnar, R. B. *American Industrial Hygiene Association Journal* **1978**, *39*, 745-749.
(22) Levlin, M.; Niemi, H. E. M.; Hautojärvi, P.; Ikävalko, E.; Laitinen, T. *Fresenius' Journal of Analytical Chemistry* **1996**, *355*, 2-9.
(23) Brosset, C.; Iverfeldt, Å. *Water, Air, & Soil Pollution* **1989**, *43*, 147-168.
(24) Temmerman, E.; Vandecasteele, C.; Vermeir, G.; Leyman, R.; Dams, R. *Analytica Chimica Acta* **1990**, *236*, 371-376.
(25) Levlin, M.; Ikavalko, E.; Laitinen, T. *Fresenius Journal of Analytical Chemistry* **1999**, *365*, 577-586.
(26) Atkins, P. W. *Physical Chemistry*; 2nd ed.; Oxford University Press: Oxford, Great Britain, 1982.
(27) Green, T. A. *Gold Bulletin* **2007**, *40*, 105-114.
(28) Miller, J. C.; Miller, J. N. *Statistics for Analytical Chemistry*; 3rd ed.; Ellis Horwood Limited: West Sussex, 1993.
(29) Larjava, K.; Laitinen, T.; Vahlman, T.; Artmann, S.; Siemens, V.; Broekaert, J. A. C.; Klockow, D. *International journal of environmental analytical chemistry* **1992**, *49*, 73 - 85.
(30) Larjava, K.; Laitinen, T.; Kiviranta, T.; Siemens, V.; Klockow, D. *International journal of environmental analytical chemistry* **1993**, *52*, 65-73.

Chapter V

Investigation of Hg Sorption and Diffusion Behaviour on Ultra-thin Films of Gold

The contribution of Hg adsorption and absorption on response magnitude by studying the dynamic response curve and diffusion profile of Hg in QCM sensors that employ ultra-thin films (10 – 40 nm) of Au electrodes is presented in this chapter. In order to differentiate the two sorption processes for Hg-Au system the response magnitudes of the QCMs were studied under different operating conditions. The response magnitudes of the Au ultra-thin film based QCMs were then extrapolated to zero thickness (ETZT) in an attempt to determine the contribution of adsorbed Hg in the sensor response. The effect of Hg concentration and operating temperature on the adsorbed-to-absorbed ratio is also presented. Finally, the QCMs were characterised using SIMS depth profiling in order to study the diffusion behaviour of Hg in the Au films and correlate with the diffusion rates calculated using the QCM data.

5.1 Introduction

A number of investigations have been performed to study Hg-Au interaction[78,81,86,89,90,93,289] however the interaction between the two metals is still not fully understood[315] and needs to be further investigated. It was shown in the previous chapters that QCM response magnitude depends on the operating conditions and sensor design. In this chapter, an attempt to differentiate between Hg sorption processes (adsorption and absorption) as well as study of Hg diffusion in Au ultra-thin films of 10, 20, 30 and 40 nm thicknesses is presented.

In order to differentiate between Hg sorption and adsorption processes, the method of extrapolating the response magnitudes of the Au ultra-thin film based QCMs to zero film thickness under different operating conditions is used. It is thought that by defining zero thickness of Au, no Hg sorption may occur and therefore the extrapolated response magnitude should refer to adsorbed Hg alone. To the best of the Author's knowledge, this is the first attempt to extrapolate the response magnitudes of the Au ultra-thin film based QCMs in order to differentiate between the adsorbed and absorbed Hg vapour. By understanding the contribution, the Hg sorption and desorption processes on Au ultra-thin films may be further understood.

In addition to the study of adsorbed to absorbed Hg, the diffusion of Hg into Au ultra-thin films by SIMS depth profiling characterisation is presented. Diffusion is the process of atoms being randomly mobile from a point of higher concentration to lower concentration, and the mobility is proportional to this concentration gradient.[281,316] The Hg on the thicker samples is therefore expected to migrate deeper within the bulk of the thicker films (where the Hg concentration gradient is higher relative to thinner films) in order for Hg distribution in the film to reach equilibrium. Furthermore, a larger number of amalgams may result on the thicker Au films because as the film thickness grows during Au deposition, the kink and step defects propagate themselves throughout the growing phase[267] which could act as Hg sorption sites. The thicker the Au film, the larger the QCM response magnitude expected due to a larger amount of Hg diffusion into the thicker film's depth,[317] thus releasing the Hg sorption sites on the Au surface for more Hg sorption to occur.[93]

In this chapter, firstly the method of extrapolating the Au ultra-thin film based QCM response magnitudes to zero thickness (ETZT) is used to differentiate between the two Hg sorption processes (i.e. adsorption and absorption). Then, SIMS depth profiling is employed on the same samples to study the Hg diffusion processes in the ultra-thin films of Au that occurred during the sensing experiments. It is envisaged that these studies will provide insight into the

type of Au surface modification techniques required to develop selective QCM based Hg vapour sensors.

5.2 Experimental Setup

In order to study the Hg interaction with ultra-thin films of Au using SIMS depth profiling and ETZT method, Au ultra-thin films of thicknesses between 10-40 nm were evaporated on to specially prepared QCM sensors. It has been previously reported[99] that at Au film thicknesses above 7.5 nm, a transition from non-continuous to a continuous form occurs. Therefore a minimum Au film thickness of 10 nm is chosen in order to ensure the thinnest continuous film possible for extrapolation to zero Au film thickness. Thereon Au film thicknesses of increments of 10 nm up to 40 nm are chosen to achieve different response magnitude data points for extrapolation purposes.

Prior to depositing the Au ultra-thin films, QCMs with high Q-factors were prepared. In accordance with the results presented in Chapter 4, 150 nm optically polished Au films were used as these were found to have highest Q-factors. Therefore QCMs with 150 nm Au film on 10 nm Ti adhesion layer were deposited on each side of the quartz substrate. This was followed by a 20 nm SiO_2 layer (barrier layer) to stop any mercury from diffusing into the 150 nm Au film below it. After this critical layer, an ultra-thin film of Au with thicknesses of 10, 20, 30 or 40nm was deposited over both electrode faces. A set of 10 QCMs was prepared for each thickness of the Au ultra-thin films. Of the total of 40 QCMs, 36 QCMs were exposed to Hg vapour and 4 were kept aside as experimental controls. Each thickness was exposed to Hg vapour concentrations of 1.02, 3.65 or 10.55 mg/m^3 at operating temperatures of 28, 55 or 89°C. The time of Hg exposure was 14 hours followed by 5 hours of recovery period under dry nitrogen atmosphere (as explained in Chapter 2 Section 2.6.6). The 40 Au ultra-thin films were then characterised using SIMS depth profiling. Due to the lack of availability of SIMS, the Au films of all 40 QCMs were characterised within a 3 day period, 8 weeks after being exposed to Hg vapour.

5.3 Differentiation of Hg Vapour Sorption Processes on Gold

It was realised in Chapter 4, Section 4.3 that Hg sorption capacity of Au is dependent on the Au film thicknesses, Hg concentration, operating temperature and Hg exposure period. Therefore, QCMs with different Au film thicknesses are postulated to produce different signal outputs (Δf values) for each film thickness when exposed to identical Hg vapour concentration, operating temperature and Hg exposure period (see Figure 5.1). The extrapolation of Δf values to zero Au film thickness corresponds to Hg adsorption alone thus enabling the response magnitude contribution due to adsorption to be determined at zero thickness from the combined response of adsorption and absorption. It is well known[84] that

the higher the temperature, the more Hg may be desorbed from the Au surface; however, there is no data is available to show the ratio of the desorbed Hg to that of absorbed/amalgamated Hg.

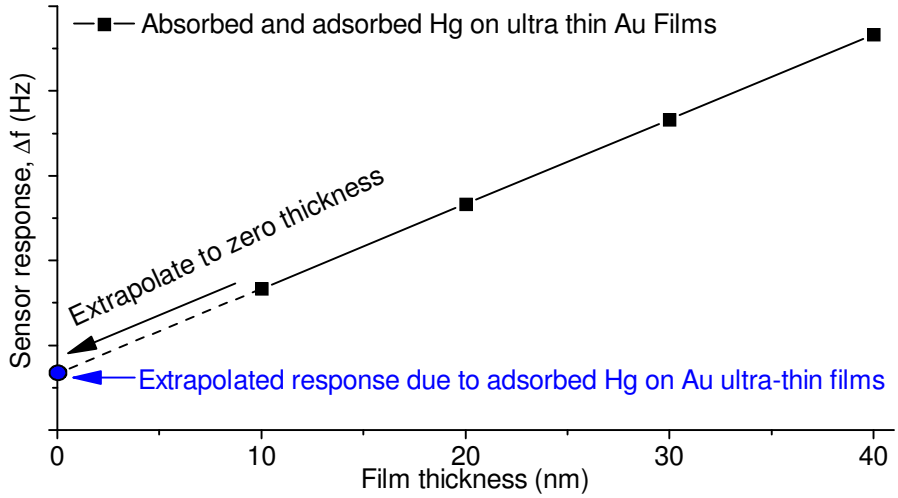

Figure 5.1: Expected Δf of four QCMs with film thicknesses of 10, 20, 30 and 40 nm Au electrode exposed to constant Hg vapour and operating temperature – data extrapolation to zero thickness (ETZT) method.

The extrapolation to zero thickness (ETZT) is the key point to this method of separating such signals. That is, by defining a zero film thickness of Au, it is proposed that the Au surface maintains its adsorption properties, hence Δf value at zero thickness. Inevitably, the Δf value at the Y-axis intercept cannot contain a contribution from Hg amalgamation or diffusion processes, since no such process is possible at zero Au thickness.

5.3.1 Influence of Hg Concentration on Hg Sorption Processes on Gold

The influence of Hg concentration on the amount of Hg adsorbed to absorbed at an operating temperature of 28℃ is presented in the following subsections. Au ultra-thin films (Au electrode thicknesses of 10, 20, 30 and 40 nm) based QCMs were exposed to Hg vapour concentrations of 1.02, 3.65 or 10.55 mg/m^3 at an operating temperature of 28℃. The calculated amount of Hg adsorbed using the ETZT method as well as the influence of Hg concentration at an operating temperature 28℃ on the total Hg adsorbed/absorbed is presented in the following subsections.

5.3.1.1 Hg Concentration of 10.55 mg/m^3

Figure 5.2 shows the Au ultra-thin films based QCMs response behaviour towards Hg vapour concentration of 10.55 mg/m^3 at an operating temperature of 28℃. It may be observed that the 10 and 20 nm Au QCMs reach saturation within the 14 hour Hg exposure period (Figure 5.2a). However the 30 and 40 nm QCMs are observed to have a substantial drift and do not show signs of reaching saturation. This is attributed to Hg diffusionin the ultra-thin films. That

is, Hg is well known to nucleate and diffuse at surface defects[93] (i.e grain boundaries and kinks), thus releasing the adsorption sites and therefore promoting further Hg sorption to occur at the surface of the film.[78,84,89,93] Figures 5.2a confirms the phenomenon, showing the thicker the gold film, the more Hg diffusion occurs and hence an increase in QCM response magnitude relative to the thinner Au films. As the Hg diffuses in the gold substrate, more Hg is adsorbed on the surface, hence the observed continual drift in response magnitude with time.

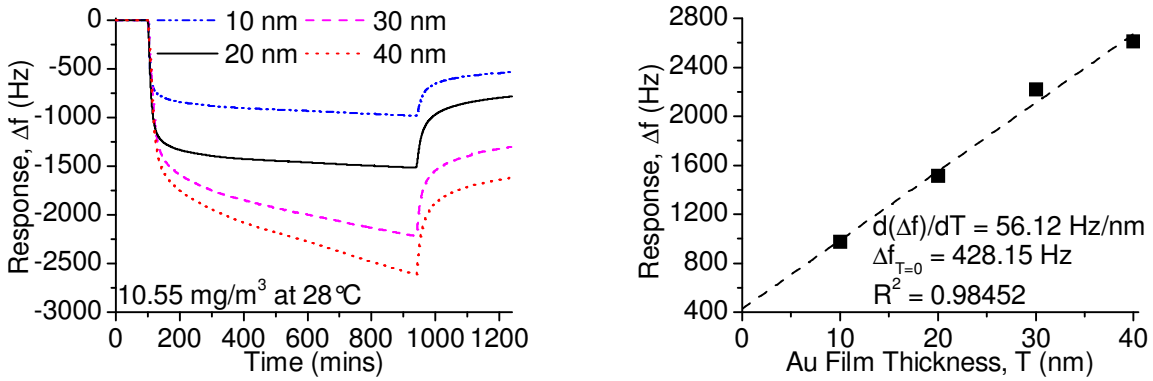

a) Dynamic response for 14 hour Hg exposure and 5 hour recovery period

b) ETZT method applied following 14 hour of Hg exposure

Figure 5.2: Dynamic response and ETZT graphic representation of QCM sensors with electrode film thicknesses of 10, 20, 30, and 40 nm when exposed towards 10.55 mg/m^3 Hg at 28℃.

Although the 30 and 40 nm QCMs did not reach saturation after 14 hours of Hg vapour exposure at 10.55 mg/m^3 and 28℃, the linear relationship in the ETZT method observed in Figure 5.2b is encouraging due to its resemblance to the predicted relationship shown in Figure 5.1. From the ETZT method, it is estimated that the extrapolated y-intercept of 428Hz ($\Delta f_{T=0}$) in Figure 5.2b is due to Hg vapour adsorbing on each of the Au film at the conclusion of the 14 hours of Hg exposure. The slow downward drift or increase in the response signal following the first 300 mins (time > 400 mins in the X-axis of Figure 5.2a) of Hg exposure period is attributed to slow Hg migration in the bulk of the Au films and releasing of the Hg sorption sites on the Au surface promoting more Hg vapour to adsorb/amalgamate.

Some observations can be made from these results. Firstly, the thinner the gold film the lower the observed ratio of the absorbed to adsorbed Hg. The increase in response magnitude per nm of deposited Au film towards 10.55 mg/m^3 Hg vapour concentration at 28℃ is estimated by observation based upon the slope/gradient ($d(\Delta f)/\Delta T$) of the extrapolated curve in Figure 5.2b which has a value of 56.12 Hz/nm. As previously mentioned in Chapter 4, Section 4.3 the sensitivity of the QCMs used for this study was

estimated at ~4.39 ng.Hz^{-1}.cm^{-2} using the Sauerbrey equation[97,174,182]. By using the geometrical surface area of the QCM electrodes, the d(Δf)/ΔT value equates to ~78.9 ng/nm. This value is an indication of the relationship between increased film thickness and Hg sorption capacity characteristics of Au ultra-thin films.

During the 14 hour exposure period, the total response magnitude from the 40 nm thick Au electrode QCM was observed to be 2613.5 Hz. However, as observed in Figure 5.2a, most of the sorption occurred in the first 300 minutes of Hg exposure time (between 100 and 400 mins on the X-axis of Figure 5.2a) at which stage the sensor response was recorded to be 2078.8 Hz. This potentially means ~535 Hz or 2347 ng.cm^{-2} of Hg had diffused in the subsequent 540 minutes of Hg exposure resulting in the average diffusion rate of ~72.4 pg.cm^{-2}.s^{-1}. The adsorbed Hg (428Hz) on any of the Au surfaces at these conditions equates to 1880 ng.cm^{-2}. Since one nominal monolayer of Hg on gold is equivalent to 469 ng.cm^{-2} [84] and using the electrochemical surface area of Au-polished films in the calculations (Chapter 3, Section 3.3.1) this value may be converted to 2.67 nominal monolayers of Hg (or 4 monolayers if the mechanical surface area was used)[89]. These values are in line with the literature (presented in Chapter 1, Section 1.2.3) where Hg has been reported to not make a full monolayer on the Au surface and that several nominal Hg monolayers are required before amalgamation may take place.[78,105,108] In the current Hg exposure conditions, it may be that amalgamation initiates following ~2.67 nominal monolayers of adsorbed Hg where the number of Hg atoms to Au atoms is satisfied.[302]

Previous work conducted by Haskell[256] using sputter deposited thin films of Au with thicknesses ranging from 2.5-50 nm showed that Au film with a thickness of 7.5 nm underwent the highest Hg sorption. However, Hg sorption was observed to reduce with increased Au film thickness. It should be noted however that Haskell conducted his experiments using SAW sensors with ~10 times less Hg concentration than the study presented here. Additionally far lower exposure times (of 30 minutes) and a fixed operating temperature of 50°C were used. In an attempt to explain his results, Haskell postulated that the thinner Au films were not continuous, and thus attained a high surface to volume ratio that resulted in relatively larger response magnitudes than sensors with continuous, thicker Au films. It is interesting to note that the opposing trend of increasing Hg sorption with increasing Au film thickness is observed in the current study by using different operating conditions compared to that of Haskell's work. This confirms that Hg sorption capacity of Au is not just dependent on Au film thicknesses but, as stated earlier, also on other operating conditions such as Hg vapour concentration, operating temperature and Hg exposure period.

Analysis of QCM Response Rate

The resonant frequency of acoustic based sensors such as the QCM is not just affected by the mass of the adsorbed gas, but also the density, viscosity and elasticity changes of the deposited film.[318] In the case of the Hg-Au system, the morphology of the Au substrate is well known to undergo slight changes upon sorption and desorption of elemental Hg.[78,81,86,96,146,289,302,319] Figures 5.3a and 5.3b show the first 60 minutes of Hg sorption and desorption rates, respectively, which were both derived from the data presented in Figure 5.2a. The 'shoulder' observed in Figure 5.3a for the thicker Au electrodes (30 and 40 nm) is attributed to the morphology change of the Au surface during Hg exposure, as all the operating parameters that affect the QCM response were constant.

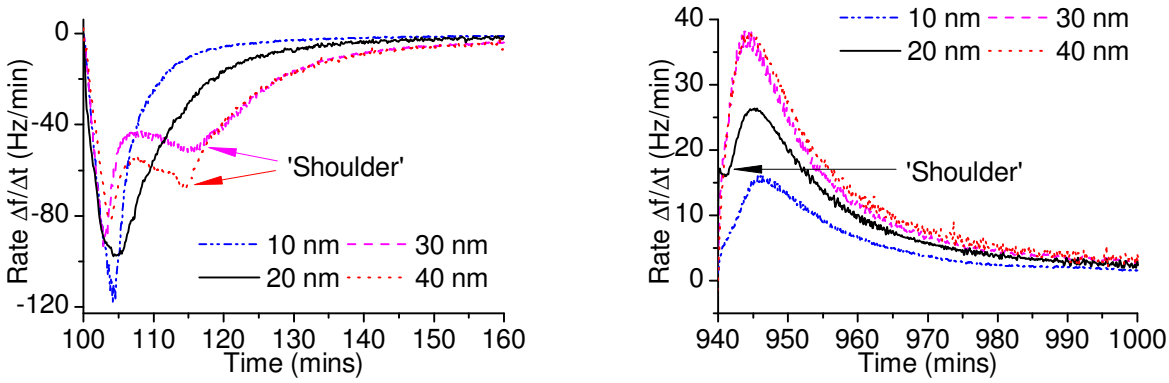

a) Sorption rate (First hour) **b)** Desorption rate (First hour)

Figure 5.3: Hg sorption and desorption rates of QCM sensors with electrode film thicknesses of 10, 20, 30, and 40 nm when exposed to 10.55 mg/m^3 Hg at 28°C.

In an effort to observe if morphology changes of the Au surfaces occurred during Hg vapour exposure, SEM images of the 10 and 40 nm Au ultra-thin film surfaces before and after Hg exposure were conducted, as shown in Figure 5.4. It may be observed that, following the relatively short Hg exposure period of 14 hours, the defined island type grains on the 10 nm ultra-thin film have coagulated and transformed to more continuous type islands with thinner widths. The Au clusters on the 40 nm ultra-thin film is also observed to have coagulated into bigger islands with less defined grain boundaries following Hg exposure. It should be noted that larger, more prominent changes in morphology become more apparent when longer Hg exposure times are conducted as will be shown in Chapter 7, Figure 7.32.

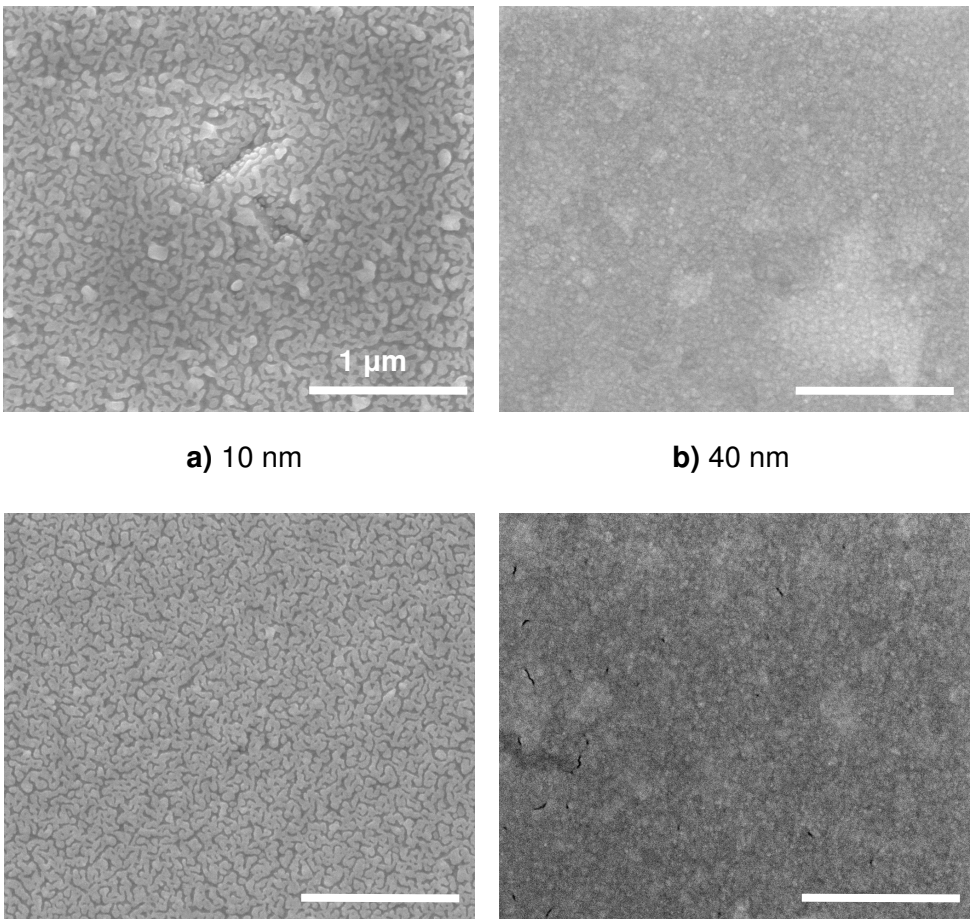

a) 10 nm **b)** 40 nm

c) 10 nm with Hg **d)** 40 nm with Hg

Figure 5.4: SEM images of ultra thin Au films before (a and b) and after (c and d) Hg exposure at a concentration of 10.55 mg/m^3 and 28℃.

Influence of Hg Exposure Time on Hg Sorption Capacity of Au Ultra-thin Films

As observed from the first 60 minutes of Hg exposure period presented in Figure 5.5, Hg exposure time is observed to alter the trend in the amount of adsorbed/amalgamated Hg between the different Au ultra-thin films based QCMs. Interestingly, the transition in trend between the four different Au films thickness occurs in the same time frame where the 'shoulders' in the Hg sorption rates occur in Figure 5.3a. This indicates that the Hg sorption rate is potentially affected by the morphological changes that occur on the Au films. The increasing Δf with increasing Au film thicknesses trend is observed to continue between the different thicknesses only beyond ~30 minutes of Hg exposure. However, for the thin Au films (50-200 nm) studied in Chapter 4, a 200 minute period was required before a trend in Hg sorption capacity between the different films was observed. The lower time required to reach this Hg sorption trend between to Au ultra-thin films (10-40 nm) may be due their thinner nature when compared to the Au thin films (50-200 nm) studied in Chapter 4. Furthermore, the thinner nature of the Au ultra-thin films may have made them more susceptible to morphological changes at the surface.

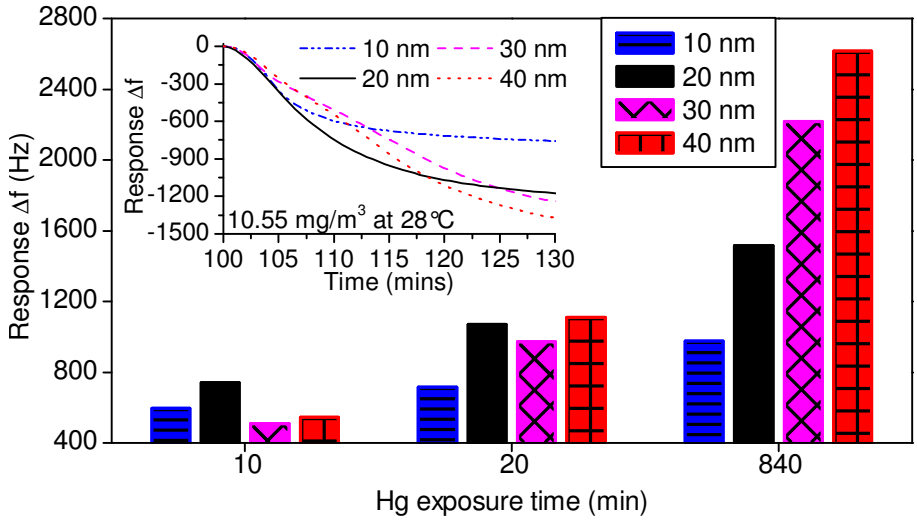

Figure 5.5: Au ultra-thin film based QCM response magnitude towards Hg vapour concentration of 10.55 mg/m3 at 28℃ at various Hg exposure times. Inset shows the QCMs' response curve in the first 60 minutes of Hg exposure period.

5.3.1.2 Hg Concentration of 3.65 mg/m^3

By reducing the Hg concentration, it is expected that less Hg sorption occurs on the Au ultra-thin films, thus either increasing or decreasing the ratio of Hg adsorption to absorption depending on the amount of adsorbed Hg on each Au surface. The dynamic response of each QCM exposed to Hg concentration of 3.65 mg/m^3 at 28℃ is shown in Figure 5.6.

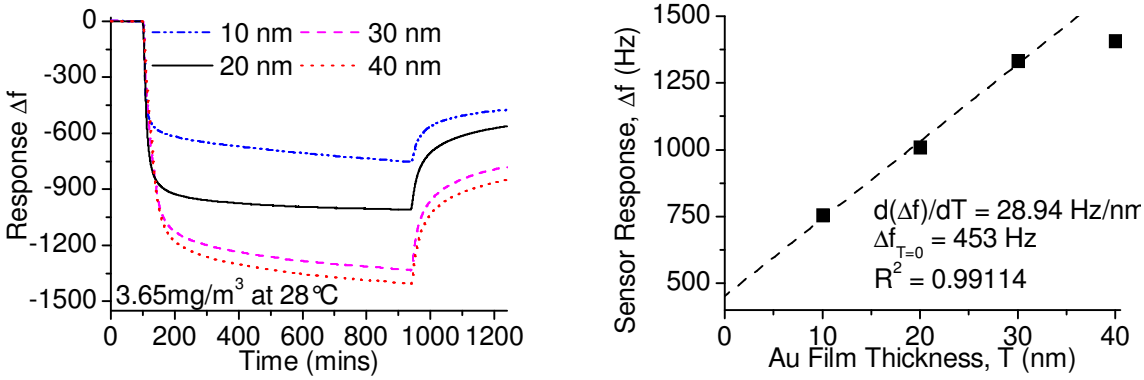

a) Dynamic response for 14 hour Hg exposure and 5 hour recovery period

b) ETZT method applied following 14 hour Hg exposure

Figure 5.6: Dynamic response and ETZT graphic representation of QCM sensors with electrode film thicknesses of 10, 20, 30, and 40 nm when exposed towards 3.65 mg/m^3 Hg at 28℃.

As expected, the comparison of Figure 5.6a with that of 5.2a shows a lower response magnitude with the lower mercury concentration due to the lower saturated Hg thickness on the Au film. The trend of increased Hg sorption with increasing Au film thickness is also observed to hold following the 14 hour Hg exposure period. However, the difference between

the 30 and 40 nm thick gold electrode QCM response magnitudes is found to be closer following Hg exposure (1332.5 and 1405.5 Hz, respectively) as compared to the response magnitude from the higher (10.55 mg/m^3) Hg vapour concentration (2218.8 and 2613.5 Hz, respectively). On analysis of the data presented in Figure 5.6b and Figure 5.2b it can be determined that a higher ratio of adsorbed to absorbed Hg occurred when exposed to Hg concentration of 3.65 than 10.55 mg/m^3. That is, using the ETZT method the adsorbed Hg on the Au films at 3.65 mg/m^3 exposure was found to be 453 Hz ($\Delta f_{T=0}$) as compared to 428 Hz for a Hg exposure of 10.55mg/m^3. Since the total Hg sorption is found to be larger for the higher Hg concentration (Figure 5.2a), the ratio of adsorbed to absorbed Hg is found to be much less at the lower Hg concentration. In addition, the gradient ($d(\Delta f)/\Delta T$ values) of the extrapolated line from the ETZT method in Figures 5.2b and 5.6b were also calculated and found to be 28.94 Hz/nm at 3.65 mg/m^3 compared to 56.12 Hz/nm at 10.55 mg/m^3. This indicates a lower response magnitude increase per nm of deposited Au at the Hg concentration of 3.65, as expected. It is worth noting that the 40 nm response magnitude following the 14 hour Hg exposure period was not included in the ETZT method in Figure 5.6b, as a similar amount of Hg sorption was observed to occur on the 30 nm Au film. The similarity in response magnitude may be due to the lower Hg concentration in the vapour phase restricting the amount of adsorbed Hg on the Au surfaces. This would result in a similar amount of diffused Hg in the 30 and 40 nm Au ultra-thin films, and thus in similar response magnitudes following 14 hours of Hg exposure.

The zero-shifted QCM response during the 5 hour sensor recovery period is shown in Figure 5.7 (data extracted from Figures 5.2 and 5.6). From the zero-shifted desorption curves presented in Figure 5.7a it may be observed that the 30 nm and 40 nm QCMs had similar levels of Hg desorption capacity. This similarity in desorption response magnitude from both the 30 and 40 nm Au ultra-thin based QCMs were observed at Hg concentration of 3.65 (Figure 5.7a) but not at 10.55 mg/m^3 (Figure 5.7b). As discussed in Chapter 4, Section 4.3, the desorption kinetics of Hg from a surface is known to be dependent on Hg coverage on Au surface.[295] Therefore, a similar Hg desorption response observed for the 30 and 40 nm Au ultra-thin film based QCMs in Figure 5.7a confirms the similar Hg coverage on the 30 and 40 nm Au ultra-thin films when exposed to Hg concentration of 3.65 mg/m^3 at an operating temperature of 28°C.

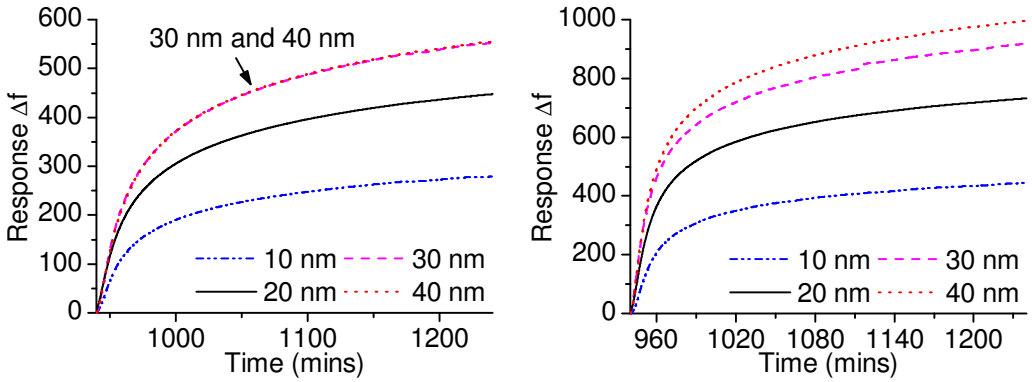

a) 3.65 mg/m^3 Hg **b)** 10.55 mg/m^3 Hg

Figure 5.7: Zero-shifted QCM response during desorption period of QCM sensors with electrode film thicknesses of 10, 20, 30, and 40 nm when exposed towards dry nitrogen for 5 hours following a 14 hour Hg exposure period at 28℃.

Most of the change in response magnitude for each sensor was observed to occur in the first 100 minutes of Hg exposure (time between 100 and 200 mins on the X-axis in Figure 5.6a), indicating that Hg sorption in the Au films is initially fast and reduces with time. This can also be observed from the sorption rate data in Figure 5.8a where the Hg sorption rate is observed to increase before slowly approaching zero (saturation). Because thinner films saturate faster, the rate at which saturation is achieved is related to Au film thickness. The surface morphology changes on the thicker Au ultra-thin films (30 and 40 nm) are evident from the shoulders observed in the response rate data shown in Figure 5.8a.

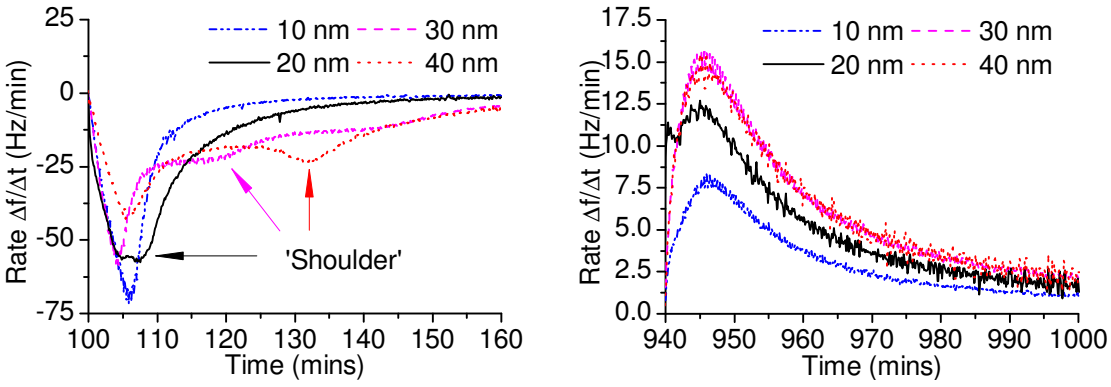

a) Sorption rate (First hour) **b)** Desorption rate (First hour)

Figure 5.8: Hg sorption and desorption rate profiles of QCM sensors with Au electrode ultra-thin film thicknesses of 10, 20, 30, and 40 nm when exposed towards 3.65 mg/m^3 Hg at 28℃.

It is interesting that changes in the sorption kinetics of the thicker gold substrates are observed during the first 60 minutes of Hg exposure as shown in Figure 5.8a. At Hg concentration of 10.55 mg/m^3 presented in Figure 5.3a, the shoulders are observed to occur

at ~15 minutes for both the 30 and 40 nm Au films. These shoulders appear at ~20 and ~30 minutes for the 30 and 40 nm Au ultra-thin films, respectively when a lower Hg concentration of 3.65 mg/m^3 is exposed to the Au films as presented in Figure 5.8a. This indicates that an increase in Hg vapour concentration reduces the period taken for the Hg sorption rate kinetic changes (attributed to changes in Au film morphology) to occur.

5.3.1.3 Hg Concentration of 1.02 mg/m^3

A further reduction in Hg vapour concentration from 3.65 to 1.02 mg/m^3 at an operating temperature of 28℃ is shown in Figure 5.9. The 30 and 40 nm thick gold electrode based QCMs are also observed to produce similar response magnitudes. Therefore, the response magnitude from the 40 nm Au ultra-thin film based QCM is not used in the ETZT method, for the same reasons discussed for the Hg concentration of 3.65 mg/m^3 in Section 5.3.1.2.

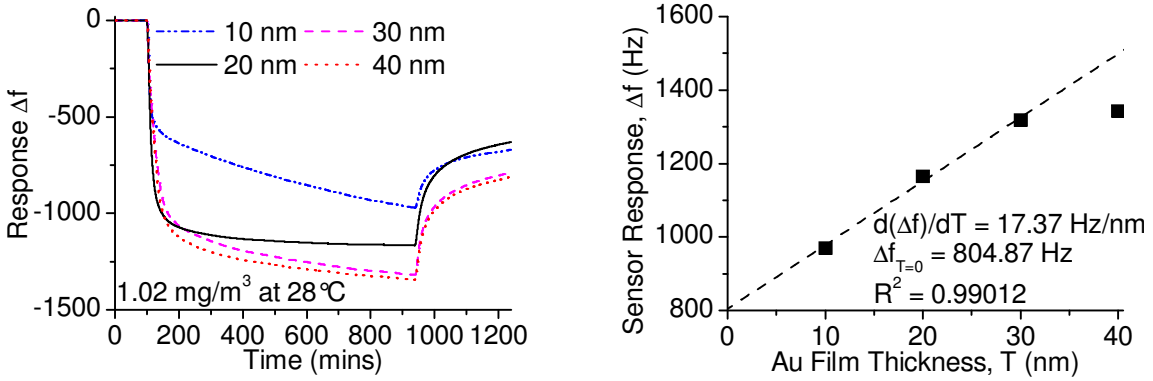

a) Dynamic response for 14 hour Hg exposure and 5 hour recovery period

b) ETZT method applied following 14 hour Hg exposure

Figure 5.9: Hg sorption and desorption rate profiles of QCM sensors with Au electrode ultra-thin film thicknesses of 10, 20, 30, and 40 nm when exposed towards 1.02 mg/m^3 Hg at 28℃.

The rate at which Hg diffuses through the Au ultra-thin films following 300 mins of Hg exposure (saturation) may be calculated, as it is assumed that the significant drifts in response curves thereon are due to slow Hg diffusion. The effect of decreasing Hg vapour concentration on Hg adsorption, absorption/amalgamation, desorption and diffusion is summarised in Table 5.1. All QCM response magnitudes are converted to mass of Hg using the QCM sensitivity of 4.39 ng.Hz^{-1}.cm^{-2}, deduced from Sauerbrey's equation for a 10 MHz QCM resonator as discussed in Chapter 4, Section 4.3.

Table 5.1: Effect of Hg concentration on the amount of Hg sorption, adsorption and diffusion in the various Au ultra-thin films at an operating temperature of 28℃.

Hg concentration (mg/m^3)	1.02				3.65				10.55			
Film thickness (nm)	**10**	**20**	**30**	**40**	**10**	**20**	**30**	**40**	**10**	**20**	**30**	**40**
Total Hg sorption ($\mu g.cm^{-2}$)	4.2	5.1	5.8	5.9	3.3	4.4	5.8	6.2	4.3	6.6	9.7	11
Total Hg desorbed ($\mu g.cm^{-2}$)	1.3	2.3	2.3	2.3	1.2	2.0	2.4	2.4	2.0	3.2	4.0	4.4
Hg diffusion rate ($pg.cm^{-2}.s^{-1}$)	29	8	17	14	11	4.8	13	14	10	12	50	72
$\Delta f_{T=0}$ (Hz or $\mu g.cm^{-2}$)	805 or 3.5				453 or 2.0				428 or 1.9			
$d(\Delta f)/\Delta T$ (Hz/nm or ng/nm)	17.4 or 24.4				28.9 or 40.6				56.1 or 78.9			

The Hg diffusion rate, following saturation, is observed to increase with increasing film thickness at all the tested Hg vapour concentrations, with the exception of the 10 nm Au film. This may be due to the nano-island type morphology of the 10 nm Au ultra-thin film (Figure 5.4a) as opposed to a continuous film resulting in different Hg diffusion behaviour. That is, the nano-island morphology of the 10 nm Au ultra-thin film may be undergoing a larger surface modification process due to the mobile nature of these nano-islands. It may be further observed that as Hg vapour concentration decreases; the amount of Hg adsorbed (extrapolated Δf values at zero film thickness) on the Au ultra-thin films is increased ($\Delta f_{T=0}$ values in Table 5.1). As expected, the total Hg sorption on each film thickness is observed to decrease with decreasing Hg concentration. However, at the Hg concentration of 3.65 mg/m^3, the 10 and 20 nm Au ultra-thin films are observed to undergo lower Hg sorption than at 1.02 mg/m^3. This higher Hg sorption may be due to the higher Hg diffusion rate observed for the 10 and 20 nm Au ultra-thin films at 1.02 mg/m^3 than at 3.65 mg/m^3. A decrease in Hg concentration also decreases the slope of the ETZT curves, indicating a lower response magnitude for every nm of Au film deposited on the QCM electrodes. Overall, the Hg sorption capacity of the thinner Au films (10 and 20 nm) is observed to be more influenced by changes in Hg vapour concentration than the thicker films (30 and 40 nm) following 14 hours of Hg exposure.

5.3.2 Influence of Operating Temperature on Hg sorption Processes on Gold

The influence of operating temperature on the ratio of Hg adsorbed to absorbed is presented in the following subsections. Au ultra-thin films (Au electrode thicknesses of 10, 20, 30 and 40 nm) based QCMs were exposed to Hg vapour concentrations of 1.02, 3.65 or 10.55 mg/m^3 at operating temperatures of 28, 55 and 89℃. The amount of Hg adsorbed, deduced by applying the ETZT method as well as the influence of Hg concentration on the total Hg adsorbed/absorbed is presented in the following subsections.

5.3.2.1 Operating Temperature of 89℃

The dynamic response of four QCMs with a 10, 20, 30 and 40 nm Au layer when exposed to Hg vapour concentration of 10.55 mg/m^3 at 89℃ is shown in Figure 5.10. An operating temperature of 89℃ was chosen as it is the typical temperature of many industrial processes that contain Hg vapour.[104,146]

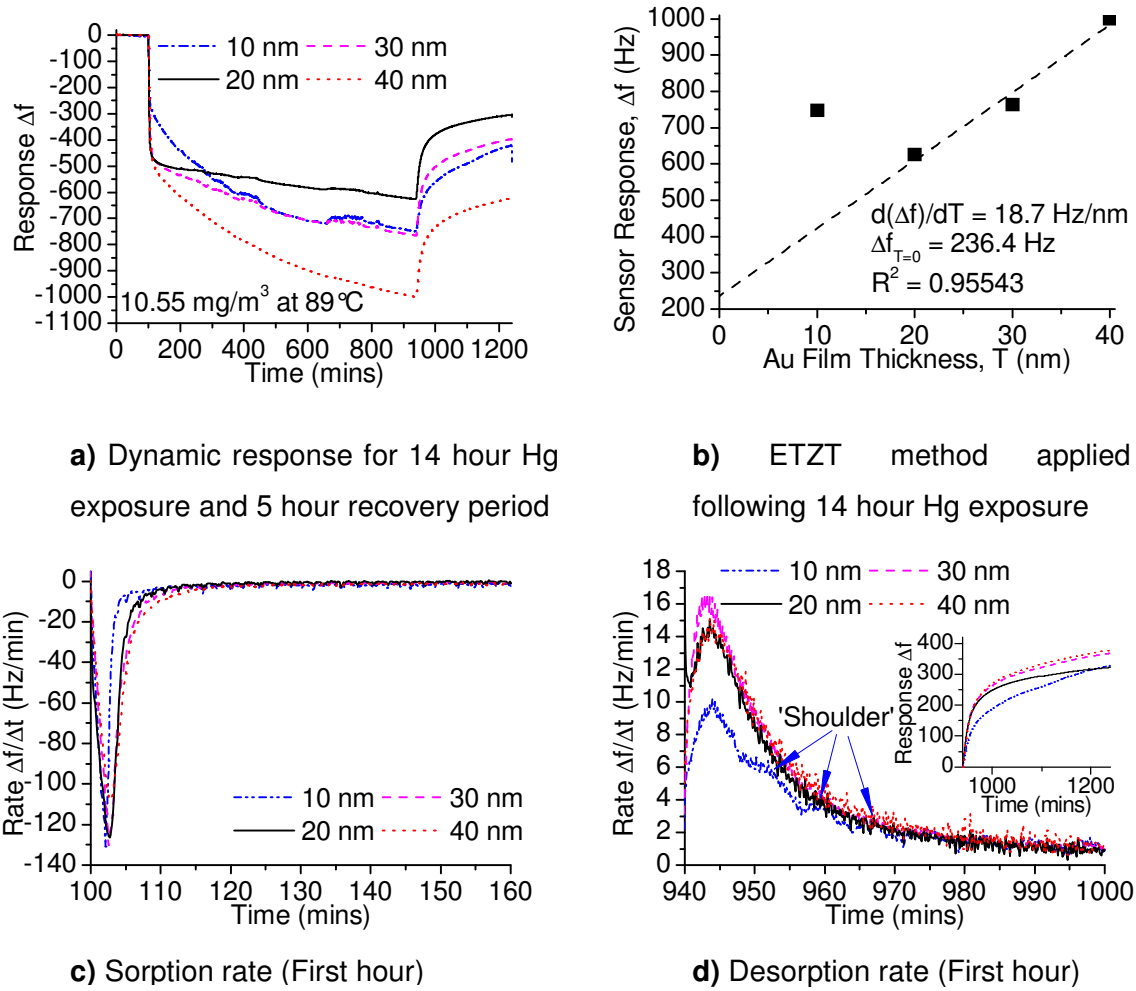

a) Dynamic response for 14 hour Hg exposure and 5 hour recovery period

b) ETZT method applied following 14 hour Hg exposure

c) Sorption rate (First hour)

d) Desorption rate (First hour)

Figure 5.10: Dynamic response, ETZT graphic representation, Hg sorption and desorption rate profiles of QCM sensors with electrode film thicknesses of 10, 20, 30, and 40 nm when exposed towards 10.55 mg/m^3 Hg at 89℃. Inset of (d) shows the zero-shifted desorption dynamic response data of the QCMs.

At these conditions, the 10 nm Au substrate QCM response magnitudes is found to be unexpectedly higher than the 20 nm Au substrate and close to the response magnitude of the 30 nm Au substrate (Figure 5.10a). This is significantly different to the trend shown in Figure 5.2a for a similar group of sensors operating at 28°C.

It is well known that upon Hg exposure, the thin Au film deposited on SiO_2 substrate 'cracks' and produces nanoislands.[85-87] Due to the ultra-thin nature of the 10 nm Au film, it is postulated that melting point depression (referring to the phenomenon of reduction of the melting point of a material with reduction of its size) have taken effect on these Au nanoislands.[300,320,321] Furthermore, the temperature at which diffusion becomes appreciable is known to be roughly proportional to the melting point of the metal.[322-325] In addition, the gold islands are very likely to be mobile on the silica barrier layer due to the weak adherence of Au on SiO_2.[269,270,326] The unstable response dynamics, as well as the relatively high response magnitude of the 10 nm Au ultra-thin film based QCM observed in Figure 5.10a may be due to the combination of both the mobile nature of the Au islands and the higher operating temperature. Additionally, the mobility of the gold islands would reveal unexposed gold resulting in more Hg sorption from the vapour phase in order for the surface Hg to reach equilibrium with the Hg vapour phase again. Subsequently, the 10 nm response magnitude does not conform well to the ETZT method as shown in Figure 5.10b, and therefore was omitted when extrapolating data to determine the contribution of adsorbed from absorbed Hg. Although it is now apparent that the ETZT method of differentiation has limitations for the Au-Hg system at some operating conditions, these limitations may be overcome by using more Au films with thicknesses in the range where a linear relationship between Hg sorption and film thickness is observed. The limitations of the ETZT method will be further discussed later in Section 5.3.2.3.

A comparison of the data in Figure 5.2b with that of 5.10b demonstrates that a higher operating temperature increases the ratio of adsorbed to absorbed Hg on each Au ultra-thin film. For example, using the ETZT method, the ratio of amalgamated to adsorbed Hg for the 40 nm Au film following 14 hours of 10.55 mg/m^3 Hg exposure was estimated at 6.10 and 4.23 at 28°C and 89°C, respectively. The slopes of the ETZT curves were also calculated and found to be only 18.7 Hz/nm at 89°C compared to 56.12 Hz/nm at 28°C. This indicates a reduced Hg sorption within the film depth. The lower Hg sorption at the higher operating temperature is potentially due to the relatively higher vapour pressure of Hg[327] and therefore its tendency to stay in the vapour phase rather than adsorb on the Au surface. The surface coverage of Hg would therefore be reduced at the higher operating temperature, thus reducing the flux of Hg through the Au film resulting in less diffused or amalgamated Hg within the bulk of the film.

Hg sorption and desorption rates for the first 60 minutes are shown in Figures 5.10c and 5.10d, respectively. It may be observed that both maximum sorption and desorption rates are reached in less time at the higher operating temperature of 89℃ than at 28℃ (Figures 5.3a and 5.3b). In Addition, a number of shoulders may be observed in the desorption rate curve of the 10 nm Au film during the first 60 minutes of the desorption period at 89℃. These shoulders are again attributed to the mobility of the amalgam islands[86] on the 10 nm Au film during the recovery period.

5.3.2.2 Operating Temperature of 55℃

In order to study the influence of reducing the operating temperature from 89 to 55℃, a new set of Au ultra-thin film based QCMs were exposed to Hg vapour concentration of 10.55 mg/m^3 at 55℃, the response dynamics of which are shown in Figure 5.11a. It is observed that at the operating temperature of 55℃, the 10 and 20 nm Au ultra-thin films had similar response magnitudes at the conclusion of the 14 hour Hg exposure period. The thicker Au films (30 and 40 nm) also had similar response magnitudes. These similarities are attributed to the influence of operating temperature and exposure time on Hg sorption capacity of Au films, as discussed in Chapter 4, Section 4.3. Therefore only the 20 and the 30 nm Au ultra-thin films were used in the ETZT method to differentiate Hg adsorption from absorption for comparison, as shown in Figure 5.11b. This is another operating condition where a limitation of the ETZT method is observed. The limitation may be overcome in future studies by using more Au film thicknesses in the range 20≤T≤30 at the operating temperature of 55℃ and Hg vapour concentration of 10.55 mg/m^3 before applying the ETZT method.

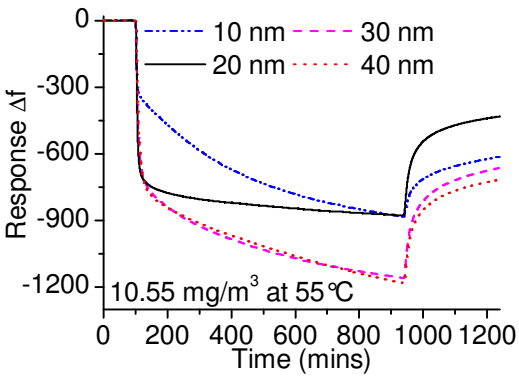

a) Dynamic response for 14 hour Hg exposure and 5 hour recovery period

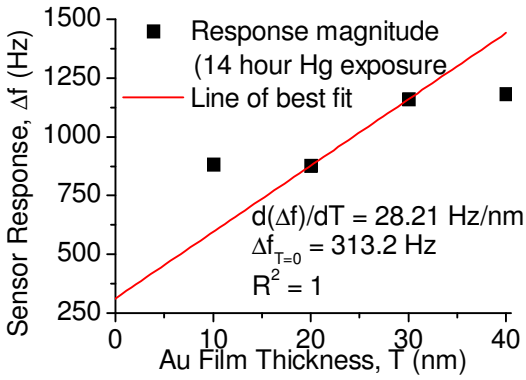

b) ETZT method applied following 14 hour Hg exposure

Figure 5.11: Dynamic response and ETZT graphic representation of QCM sensors with electrode film thicknesses of 10, 20, 30, and 40 nm when exposed towards 10.55 mg/m^3 Hg at 55℃.

An increased amount of adsorbed Hg is observed at the lower temperature of 55℃ (extrapolated Δf value of 313.2 Hz) relative to 89℃ (extrapolated response magnitude of 236.4 Hz). However, the relatively higher Δf values of the QCMs at 55℃ has resulted in a reduced ratio of adsorbed to absorbed Hg, due to the decreased operating temperature.

5.3.2.3 Operating Temperature of 28℃

In order to study the influence of reducing the operating temperature from 89 and 55℃ to 28℃, the response curves presented in Figures 5.10 and 5.11 is compared with Figure 5.2. Similar operating conditions were used in all the experiments presented in Figures 5.10, 5.11 and 5.2, with the only changed parameter being a reduction in the operating temperature from 89 or 55 to 28℃, respectively. The influence of reducing the operating temperature from 55 to 28℃ is observed to be similar to that observed when reducing the operating temperature from 89 to 55℃, as presented in Section 5.3.2.2. It is shown that there is a larger extrapolated response magnitude at 28℃ relative to the higher temperatures of 55 and 89℃, which indicates that the amount of adsorbed Hg increases with decreasing operating temperature.

The ETZT calculations (for operating conditions of 1.02 mg/m^3 Hg at 55℃, 3.65 mg/m^3 Hg at 55℃, 1.02 mg/m^3 Hg at 89℃, 3.65 mg/m^3 Hg at 89℃) as well as the zero-shifted desorption curves are presented in Appendix E (Figures E1-E5). The results of all nine operating conditions are summarised in Table 5.2 for operating temperatures of 55 and 89℃. The data for 28℃ was presented in Table 5.1. It is clear from the results presented in Tables 5.1 and 5.2 that the ETZT method of differentiation has limitations and can only be used in certain conditions for the film thicknesses used (for example, Hg concentration of 10.55 mg/m^3 at an operating temperature of 28℃). However, the method gives an insight into the influence of film thickness on Hg sorption capacity and how the ratio of adsorbed to absorbed Hg influences Hg diffusion rate on the different ultra-thin films of Au, following saturation or 300 minutes of Hg exposure. In the case of other conditions (for example, a Hg concentration of 10.55 mg/m^3 at and operating temperature of 89℃), these influences may be studied in greater detail by using more Au ultra-thin films with thicknesses of 20<T<40 nm, as observed in Figure 5.10b. In general, it is observed from Table 5.2 that the amount of Hg adsorbed ($\Delta f_{T=0}$) and Hg sorption per nm of deposited Au films (d(Δf)/ΔT values) reduces with increasing operating temperature. It is also observed that the Hg diffusion rate in the Au ultra-thin films is slow (in pg.cm^{-2}.s^{-1}) following Hg exposure beyond 300 minutes (after saturation is reached) at all operating temperatures. The ambiguities with the diffusion rate and Hg sorption capacity between the different Au ultra-thin films at the different operating conditions may be further understood by studying the Hg diffusion behaviour in these films. This is the subject of Section 5.4.

Table 5.2: Effect of Hg concentration on the amount of Hg sorption, adsorption and diffusion in the various Au ultra-thin films at an operating temperatures of 55 and 89℃.

	55℃												89℃											
Hg concentration (mg/m^3)	**1.02**				**3.65**				**10.55**				**1.02**				**3.65**				**10.55**			
Film thickness (nm)	**10**	**20**	**30**	**40**	**10**	**20**	**30**	**40**	**10**	**20**	**30**	**40**	**10**	**20**	**30**	**40**	**10**	**20**	**30**	**40**	**10**	**20**	**30**	**40**
Total Hg sorption ($\mu g.cm^{-2}$)	2.7	3.4	3.6	3.4	2.3	2.9	3.7	3.8	3.7	3.9	5.1	5.2	1.6	1.6	2.1	2.5	2.3	2.3	2.4	2.6	2.1	2.8	3.4	4.4
Total Hg desorbed ($\mu g.cm^{-2}$)	0.9	1.4	1.4	1.4	0.8	1.4	1.5	1.5	1.0	2.0	2.2	2.1	0.6	0.2	0.8	0.9	1.0	1.0	1.1	1.1	0.3	1.4	1.6	1.7
Hg diffusion rate ($pg.cm^{-2}.s^{-1}$)	17	8.7	13	8.7	14	5.0	18	17	22	7.8	24	29	6.1	0.1	1.5	4.7	18	15	17	16	17	12	19	29
$\Delta f_{T=0}$ (Hz or $\mu g.cm^{-2}$)	452 or 2.0				349 or 1.5				313 or 1.4				179 or 0.8				429.8 or 1.9				236.4 or 1.0			
$d(\Delta f)/\Delta T$ (Hz/nm or ng/nm)	16.0 or 22.5				16.0 or 22.5				28.2 or 39.6				9.9 or 13.9				4.0 or 5.6				18.7 or 26.3			

5.4 Hg Diffusion Behaviour in Ultra-thin Films of Gold

To study the diffusion behaviour of Hg vapour in ultra-thin films of Au, a total of 40 QCMs (including 4 control QCMs with no Hg exposure) were characterised using SIMS depth profiling. The response data for these QCMs was presented in Section 5.3. The SIMS depth profile experimental procedure is discussed in Chapter 2, Section 2.4.5.

5.4.1 Influence of Hg Concentration on Hg Diffusion Behaviour

The influence on Hg diffusion behaviour in Au ultra-thin films of reducing the Hg vapour concentration from 10.55 to 3.65 mg/m^3 at an operating temperature of 28℃ is presented in the following subsections.

5.4.1.1 Hg Concentration of 10.55 mg/m^3

The SIMS depth profiles for a 40 nm Au control QCM (no Hg exposure) and a 40 nm Au QCM which was exposed to Hg at 10.55 mg/m^3 for a period of 14 hours followed by 5 hours of recovery period, at an operating temperature of 28℃ are shown in Figure 5.12.

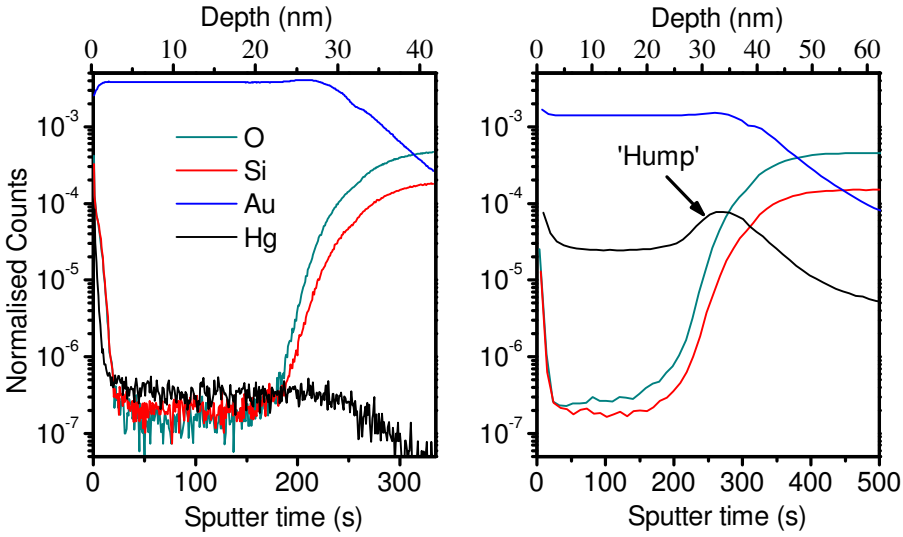

a) 40 nm Au (No Hg exposure)

b) 40 nm Au (Hg exposed)

Figure 5.12: SIMS depth profile of the Au ultra-thin films exposed to10.55 mg/m^3 Hg at an operating temperature of 28℃.

The SIMS counts for each element have been normalised with primary Cs^+ ion counts (Y-axis). The X-axis represents the sputter time (in seconds) and Au ultra-thin film depth (in nm) where depth profilometer measurements showed ~328 seconds equates to 40.7 nm of etching. Since the etching rate from the beam line was partially different from day to day, both sputter time and the conversion of it to Au film depth have been plotted in the X-axis. This method is used for all subsequent SIMS depth profiles presented in this chapter. It

should also be noted that the initial high count for Hg is due to the system stabilizing when the primary Cs^+ ion beam is introduced, and therefore the counts for Hg from the first few nanometers should be ignored.

As expected, Figure 5.12a shows no Hg is present throughout the Au depth. Furthermore, the Au counts are observed to decrease with sputter time while the Si and O counts increase substantially after 200 seconds of etching, thus confirming the existence of the SiO_2 barrier film beneath the Au ultra-thin film. The diffusion behaviour of Hg in the 40 nm Au ultra-thin film may be observed in Figure 5.12b. The presence of Hg, Si and O are observed on the 10 nm Au film surface. As the Au signal reduces with the Au film depth, the Si and O signals are observed to increase. The Hg signal is observed to closely follow the Au profile and reduce to noise level once maximum Si and O signals are reached. In addition, the SIMS depth profiles show an increase in Hg counts or 'humps' near the Au/SiO_2 interface as shown in Figure 5.12b. Similar humps are also observed for the 20 and 30 nm films, however no such obvious hump is observed for the 10 nm ultra-thin film, as shown in Figure 5.13. These humps show the lack of diffusion of Hg through the SiO_2. This behaviour was expected as the layer was purposefully deposited as a Hg barrier between the Au ultra-thin films and the 150 nm Au electrodes of the QCMs. More importantly, the increase in the Hg counts at the interface (humps) shows the accumulation of Hg at that point in the film. Be'er et al.[69] have also observed similar behaviour of liquid elemental Hg droplets, which diffuse through gold and accumulates at the Au/SiO_2 interface. The decrease in Hg counts following the hump is observed to be similar to the trend for gold indicating that the SiO_2 layer may have contained some pores containing Au which amalgamated with Hg.

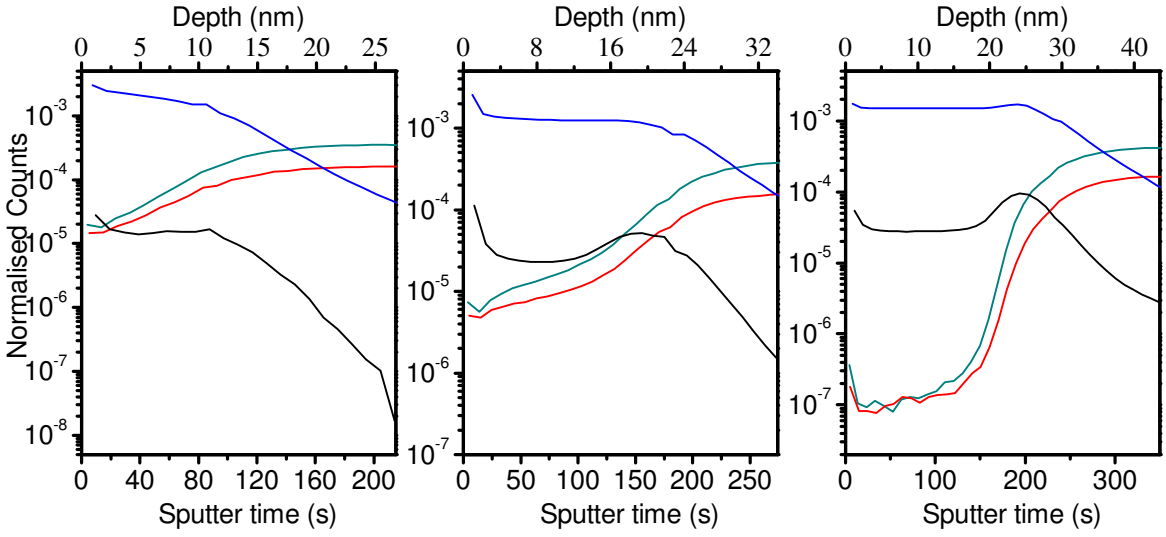

a) 10 nm Au **b)** 20 nm Au **c)** 30 nm Au

Figure 5.13: SIMS depth profiles of the Au ultra-thin films exposed to 10.55 mg/m^3 Hg at an operating temperature of 28℃.

The normalised Hg counts for each Au thickness are summarised in Figure 5.14. The position of the humps maxima in the X-axis is observed to correspond with the thickness of the Au ultra-thin films used in the analysis. It should be noted that the area under the curve is directly proportional to the amount of Hg available in the region. It can be clearly observed that the area under the humps appears to be larger as the Au thickness increases. This is attributed to more amalgamated Hg with the thicker Au electrodes, as may be observed from the QCM response curves in Figure 5.2a.

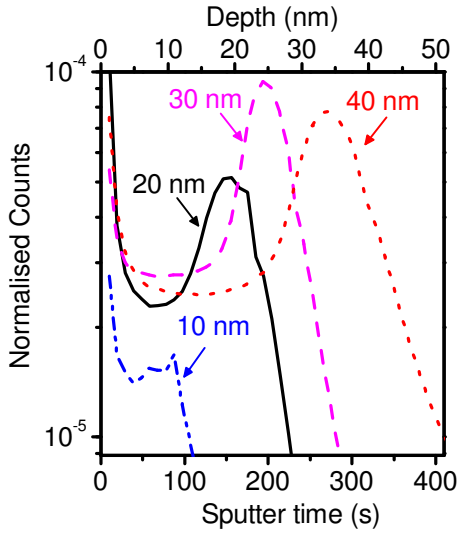

Figure 5.14: SIMS depth profile of the Au ultra-thin films exposed to a Hg concentration of 10.55 mg/m^3 at an operating temperature of 28℃.

5.4.1.2 Hg Concentration of 3.65 mg/m^3

The SIMS profile of the Au ultra-thin films exposed for 14 hours to Hg vapour with a concentration of 3.65 mg/m^3 followed by 5 hour recovery in dry nitrogen, at an operating temperature of 28℃ is presented in Figure 5.15. The accumulation of Hg at the Au/SiO_2 interface is also observed to occur at the lower Hg concentration. This behaviour was observed for all three operating temperatures and Hg concentrations tested in this study, the SIMS data of which is shown in Appendix E (Figure E6). By comparing Figure 5.15 with 5.14 (SIMS data for Hg vapour concentrations of 10.55 and 3.65 mg/m^3, respectively), it is observed that the Hg signal throughout the films which were exposed to Hg concentration of 10.55 mg/m^3 is relatively higher than the samples exposed to 3.65 mg/m^3. This indicates that Hg accumulation in the Au ultra-thin film increases with increasing Hg vapour concentration at the operating temperature of 28℃.

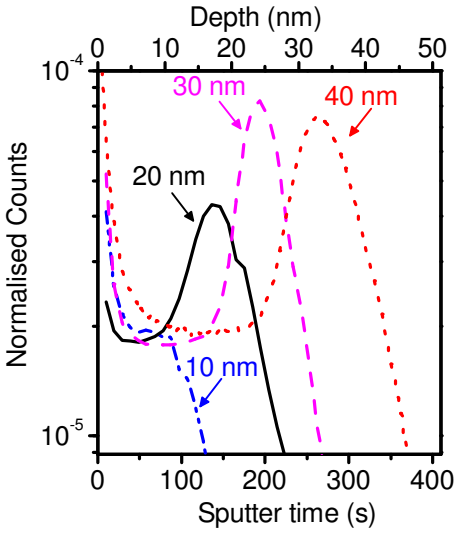

Figure 5.15: SIMS depth profile of the Au ultra-thin films exposed to a Hg concentration 3.65 mg/m^3 at an operating temperature of 28℃.

5.4.2 Influence of Operating Temperature on Hg Diffusion Behaviour

The influence of operating temperature on the diffusion behaviour of Hg in ultra-thin films of Au was also investigated. Figure 5.16 shows the SIMS profile of the Au ultra-thin films after they were exposed to Hg vapour concentration of 10.55 mg/m^3 at operating temperatures of 55℃ and 89℃.

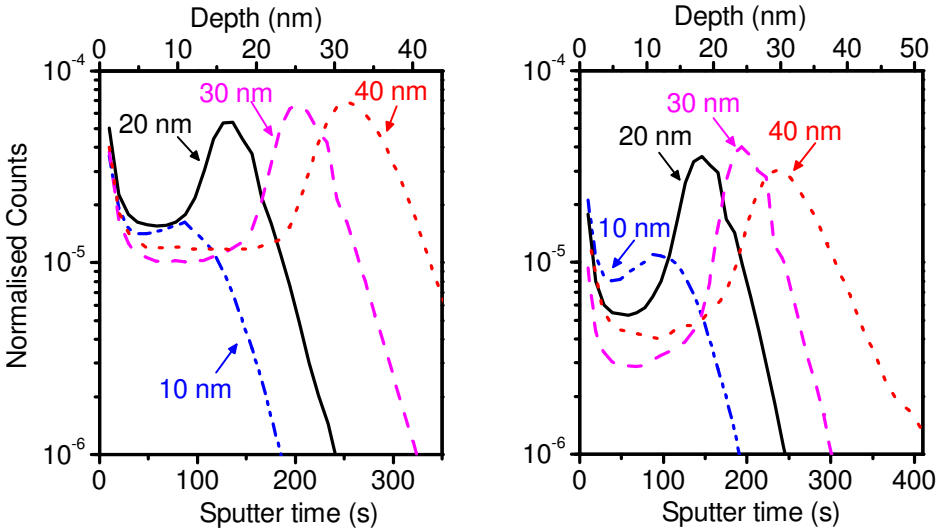

a) 55℃ **b)** 89℃

Figure 5.16: SIMS depth profile of the Au ultra-thin films exposed to 10.55 mg/m^3 Hg at an operating temperature of 55 and 89℃.

The SIMS depth profile is observed to produce humps for all Au thicknesses including the 10 nm Au ultra-thin film when exposed to high Hg vapour concentrations at operating temperatures above 28℃. The hump observed on the 10 nm thick Au QCM profile in Figure 5.16b is postulated to be due to the higher then expected Hg sorption that occurred

(Figure 5.10a). The three shoulders observed in the recovery rate data for the 10 nm thick Au film based QCM during the desorption period (Figure 5.10d) may be attributed to the rapid Au dissolution in accumulated Hg,[96] that may have taken place due to the large presence of Hg between the SiO_2 barrier layer and the 10 nm Au film.

By comparing Figures 5.14 (28℃) and 5.16 (55 and 89℃), it is observed that the Hg count is reduced throughout the Au films' depth with increasing operating temperature. Since Hg diffusion is dependent on the amount of Hg on the Au surface,[89] which is in turn influenced by the operating conditions, some differences in diffusion behaviour are observed on each Au film at each operating condition. That is, humps are observed for the 10 nm Au ultra-thin film at 89℃ but no such observation was made when the film was exposed to Hg vapour at the lower operating temperatures of 55 and 28℃. Furthermore, integration of the SIMS depth profiles of each of the 36 Au ultra-thin films exposed to Hg vapour at the 9 different operating conditions was determined by calculating the area under the curves presented in Figures 5.12 through to 5.16, and presented in Appendix E, Figure E6. The evaluated data are summarised in Figure 5.17. Due to the lack of commercially available Au-Hg amalgamated SIMS characterisation standards, the depth profile data presented may only be used qualitatively for comparison purposes and may not be converted to the actual mass of Hg accumulated. The results presented in Figure 5.17 confirm that the relative amount of accumulated Hg increases with increasing Au film thickness as well decreasing operating temperature. This is attributed to the increased Hg sorption which occurs when the operating temperature is decreased as was observed from the QCM response data in Section 5.3.2.

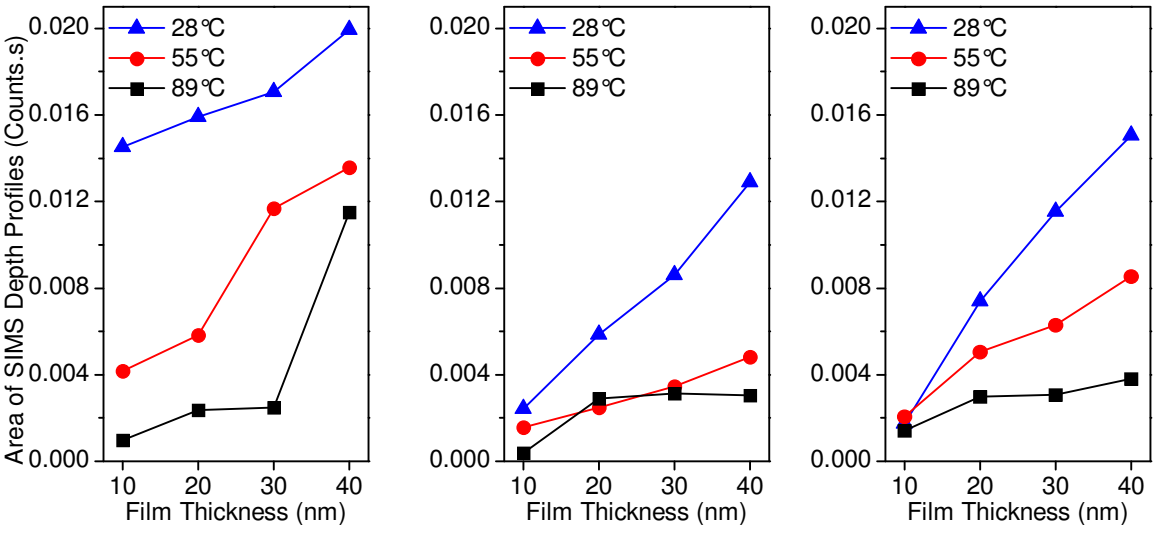

a) 1.02 mg/m^3 **b)** 3.65 mg/m^3 **c)** 10.55 mg/m^3

Figure 5.17: The area under the SIMS depth profiles (in counts.s) showing the influence of operating temperature and Hg vapour concentration on the amount of diffused and accumulated Hg in the Au ultra-thin films.

5.5 Summary

The influence of Hg vapour concentration and operating temperature on the Hg adsorption to absorption ratio as well as the Hg diffusion behaviour in Au, were studied by exposing ultra-thin films of Au towards Hg for 14 hours followed by 5 hours of recovery time at different operating conditions. A total of forty QCMs were specially fabricated. Ten sets of 4 QCMs each with either a 10, 20, 30 and 40 nm ultra-thin film of Au were used. Nine sets of QCMs (36 QCMs in total) were exposed towards Hg at nine different operating conditions (Hg vapour concentrations of 1.02, 3.65 and 10.55 mg/m^3 at operating temperatures of 28, 55 and 89°C) while the tenth set was kept as unexposed experimental controls. The electrodes of all forty QCMs were then characterized using SIMS depth profiling.

In an attempt to differentiate between Hg adsorbed and Hg absorbed, the response magnitude of each set of sensors were used to extrapolation to zero thickness (ETZT) for the 9 different operating conditions. In general, the ratio of adsorbed to absorbed Hg on Au films is found to decrease with increased Hg vapour concentration. This ratio was also found to increase with increased operating temperature. Although the ETZT method was found to have limitations at some operating conditions, when coupled with the data obtained by SIMS characterisation the method did provide insight into Hg absorption, adsorption and the diffusion behaviour of Hg in Au ultra-thin films for most of the operating conditions. It is thought, however, that by using more film thicknesses in the range 10<T<40 nm it may be possible to obtain a better understanding of the adsorbed Hg contribution in the QCM response magnitude under other operating conditions.

SIMS depth profiling of all 40 QCMs showed Hg diffusion in the films and accumulation between the Au ultra-thin film and the SiO_2 barrier layer. It was found that significant Hg accumulation occurred in the 20, 30 and 40 nm film but not the 10 nm Au ultra-thin film, at all Hg concentrations and at operating temperatures of 28 and 55°C. However, Hg accumulation was observed in all the Au ultra-thin films (including the 10 nm ultra-thin film) following Hg exposure at an operating temperature of 89°C and Hg vapour concentrations of 1.02, 3.65 and 10.55 mg/m^3.

From the results, it is deduced that in order to reduce Hg accumulation in Au, a non-continuous type film (similar to the 10 nm Au ultra-thin film morphology) may need to be fabricated and used as the Hg sensitivity layer. The Hg sensor would perform well given the film could be fabricated directly onto QCM electrodes with a high surface to volume ratio which could ensure a large response magnitude. On the other hand, a continuous type thick Au film (similar to the Au-rough QCM presented in Chapter 3) is also believed to perform well. This is because Hg diffusion and accumulation processes are known to release the

surface Hg sorption sites, therefore having little affect on the performance of QCM based Hg vapour sensors, as was observed in Chapter 3, Section 3.4.1. The fabrication of QCM based Hg vapour sensors with non-continuous thin film and continuous thick film electrodes are the subjects of Chapter 6 and Chapter 7, respectively.

5.6 References

(1) Sabri, Y. M.; Ippolito, S. J.; Tardio, J.; Atanacio, A. J.; Sood, D. K.; Bhargava, S. K. *Sensors and Actuators B: Chemical* **2009**, *137*, 246-252.
(2) George, M. A.; Glaunsinger, W. S.; Thundat, T.; Lindsay, S. M. *Journal of Microscopy* **1988**, *152*, 703-713.
(3) George, M. A. PhD by research, Arizona State University, 1991.
(4) Nowakowski, R.; Kobiela, T.; Wolfram, Z.; Dus, R. *Applied Surface Science* **1997**, *115*, 217-231.
(5) Battistoni, C.; Bemporad, E.; Galdikas, A.; Kaciulis, S.; Mattogno, G.; Mickevicius, S.; Olevano, V. *Applied Surface Science* **1996**, *103*, 107-111.
(6) Levlin, M.; Ikavalko, E.; Laitinen, T. *Fresenius Journal of Analytical Chemistry* **1999**, *365*, 577-586.
(7) George, M. A.; Glaunsinger, W. S. *Thin Solid Films* **1994**, *245*, 215-224.
(8) Li, J.; Abruna, H. D. *The Journal of Physical Chemistry B* **1997**, *101*, 2907-2916.
(9) Crank, J. *The Mathematics of Diffusion*; Oxford University Press, London, England, 1975; Vol. 2nd edition.
(10) Jain, R. K. *Cancer and Metastasis Reviews* **1990**, *9*, 253-266.
(11) Atkins, P. W. *Physical Chemistry*; 2nd ed.; Oxford University Press: Oxford, Great Britain, 1982.
(12) Wei, G. C. T.; Wuensch, B. J. *Journal of the American Ceramic Society* **1976**, *59*, 295-299.
(13) Haskell, R. L. B.; Caron, J. J.; Duptisea, M. A.; Ouellette, J. J.; Vetelino, J. F. In *Ultrasonics Symposium, 1999. Proceedings*; IEEE: Orono, ME, 1999; Vol. 1, p 429-434 vol.1.
(14) Morris, T.; Sun, J.; Szulczewski, G. *Analytica Chimica Acta* **2003**, *496*, 279-287.
(15) Sauerbrey, G. *Zeitschrift für Physik A Hadrons and Nuclei* **1959**, *155*, 206-222.
(16) Janshoff, A.; Galla, H.-J.; Steinem, C. *Angewandte Chemie* **2000**, *39*, 4004-4032.
(17) Scheide, E. P.; Taylor, J. K. *American Industrial Hygiene Association Journal* **1975**, *36*, 897 - 901.
(18) Jansen, H. J. F.; Freeman, A. J.; Weinert, M.; Wimmer, E. *Physical Review B* **1983**, *28*, 593.
(19) Miedema, A. R.; Dorleijn, J. W. F. *Philosophical Magazine Part B: Physics of Condensed matter: Statistical Mechanics, Electronics, Optical and Magnetic Properties* **1981**, *43*, 251-272.
(20) Yang, X.; Tonami, K.; Nagahara, L. A.; Hashimoto, K.; Wei, Y.; Fujishima, A. *Chemistry Letters* **1994**, *11*, 2059-2062.
(21) Haskell, R. B. Masters, University of Maine, 2003.
(22) Buttry, D. A.; Ward, M. D. *Chem. Rev.* **1992**, *92*, 1355-1379.
(23) Zierhut, A.; Leopold, K.; Harwardt, L.; Worsfold, P.; Schuster, M. *Journal of Analytical Atomic Spectrometry* **2009**, *24*, 767-774.
(24) Levlin, M.; Niemi, H. E. M.; Hautojärvi, P.; Ikävalko, E.; Laitinen, T. *Fresenius' Journal of Analytical Chemistry* **1996**, *355*, 2-9.
(25) Yang, X. M.; Tonami, K.; Nagahara, L. A.; Hashimoto, K.; Wei, Y.; Fujishima, A. *Surface Science* **1994**, *319*, L17-L22.
(26) Jones, R. G.; Perry, D. L. *Vacuum* **1981**, *31*, 493-498.
(27) Larjava, K.; Laitinen, T.; Kiviranta, T.; Siemens, V.; Klockow, D. *International journal of environmental analytical chemistry* **1993**, *52*, 65-73.
(28) Fialkowski, M.; Grzeszczak, P.; Nowakowski, R.; Holyst, R. *The Journal of Physical Chemistry B* **2004**, *108*, 5026-5030.
(29) Kobiela, T.; Nowakowski, B.; Dus, R. *Applied Surface Science* **2003**, *206*, 78-89.
(30) Buffat, P.; Borel, J. P. *Physical Review A* **1976**, *13*, 2287.
(31) Huang, D.; Liao, F.; Molesa, S.; Redinger, D.; Subramanian, V. *Journal of the Electrochemical Society* **2003**, *150*, G412-G417.
(32) Akita, T.; Okumura, M.; Tanaka, K.; Kohyama, M.; Haruta, M. *Journal of Materials Science* **2005**, *40*, 3101-3106.
(33) Akhter, J. I.; Ahmed, E.; Ahmad, M. *Materials Chemistry and Physics* **2005**, *93*, 504-507.
(34) Porter, D. A.; Easterling, K. E. *Phase Transformations in Metals and Alloys*; 2nd Edition ed.; CRC Press, 1992.
(35) Mehrer, H. *Diffusion in Solids*; 1 ed.; Springer, 2007.
(36) Avallone, E. A.; Baumeister, T.; Sadegh, A.; Marks, L. S. *Marks' Standard Handbook for Mechanical Engineers*; 11 ed.; McGraw-Hill Professional, 2006.
(37) Hoogvliet, J. C.; van Bennekom, W. P. *Electrochimica Acta* **2001**, *47*, 599-611.
(38) Caron, J.; Freeman, C. J. *Surface Acoustic Wave Mercury Vapor Sensor*, Sensor Research and Development Corporation, 1998.

(39) Nilsson, S.; Klett, O.; Svedberg, M.; Amirkhani, A.; Nyholm, L. *Rapid Communications in Mass Spectrometry* **2003**, *17*, 1535-1540.
(40) Sanemasa, I. *Bulletin of the Chemical Society of Japan* **1975**, *48*, 1795-1798.
(41) Be'er, A.; Lereah, Y.; Frydman, A.; Taitelbaum, H. *Physica A: Statistical Mechanics and its Applications* **2002**, *314*, 325-330.

Chapter VI

QCM Based Hg Vapour Sensor Enhancement by Surface Modification using Galvanic Replacement Reaction

This chapter presents the result of surface modification of Ni-Au hybrid based QCMs used to sense Hg vapour selectively in the presence of interferent gas species. The modification step was performed using the novel idea of growing well adhered Au nanostructures directly on the Ni electrodes by galvanic replacement reaction. More specifically, 300 nm thin nickel films were thermally evaporated onto QCM substrates, and subsequently reacted with $AuCl_4^-$ ions in a time-dependent controlled manner. Investigations towards the Hg-sensing capabilities of the resultant Ni-Au hybrid sensors showed Hg desorption or sensor recovery of approximately 100% following Hg exposure. Furthermore, the modified sensors are found to be highly selective towards Hg vapour in the presence of NH_3 and H_2O interferent gases.

6.1 Introduction

In this chapter, the prospect of galvanic replacement (GR) reaction is investigated as a modification technique to produce Ni-Au hybrid surfaces to enhance QCM based Hg vapour sensor response characteristics. GR reactions are single-step reactions that utilize the difference in the standard electrode potentials of the two metals leading to deposition of the more noble metal (Au) and dissolution of the less noble metal (Ni).[328] In chapter 3 it was demonstrated that Au-rough morphology with high number of surface defects was an ideal surface for optimum Hg sorption and desorption properties. In chapter 5 it was realised that reduced Hg accumulation occurs on thin non-continuous Au films when exposed to Hg vapour. It is postulated that such Au films having large number of surface defects and non-continuous nature can be fabricated using GR the technique.

GR reactions operate on the basis of differences in the standard reduction potential of the systems under investigation. Since the standard reduction potential of the Au^{3+}/Au pair (+1.4 V vs. standard hydrogen electrode[329] (SHE)) is much higher than that of the Ni^{2+}/Ni pair (–0.25 V vs. SHE)[328], the reaction between the replacement of Ni^0 with that of Au^{3+} ions (Equation 6.1) is kinetically favourable.

$$3Ni^{0}_{(s)} + 2Au^{3+}_{(aq)} \rightarrow 2Au^{0}_{(s)} + 3Ni^{2+}_{(aq)} \quad \text{Equation 6.1}$$

The oxidation of solid Ni results in its dissolution in the surrounding aqueous environment as Ni^{2+} ions while elemental gold (Au^0) is simultaneously produced (via reduction from the aqueous solution of $AuCl_4^-$) and deposited onto both QCM Ni electrodes. Therefore three atoms of Ni are expected to be replaced by two atoms of Au creating surface defects which would result in increased Hg sorption and desorption properties of the gold island nanostructures on the Ni substrate.

In the past, GR reactions have been employed for the synthesis of highly active hollow/porous metal alloy nanoparticles in aqueous and organic environments.[330-335] However recently, GR reactions have been performed on thin films in order to create surfaces with significantly larger surface area, surface defect sites and activity (i.e. SPR, catalysis etc.) relative to their unreacted counterparts[328,336-340]. The electroless nature of galvanic replacement reactions provides unique and significant advantage of simplicity.

For the Ni-Au system presented in this work, nickel was chosen as an ideal support metal because of its negligible solubility in mercury (as shown in Chapter 3, Figure 3.1). In fact, the interaction between Hg and Ni is so low that past studies have shown that Ni vessels are good for encapsulating mercury[341]. The galvanic replacement of the Ni film with gold was

chosen to form highly active sensing material because of gold metal's well-known highest affinity towards Hg. By forming well adhered nano-sized Au structures on QCM electrode surfaces using GR reaction, it is envisaged the sensor will have excellent Hg sorption and desorption properties due to the thin, well dispersed Au nanostructures. That is, the Au ultra-thin films presented in Chapter 5 (Section 5.4) were observed to accumulate Hg between the Au and SiO_2 barrier layer. In the case of the Au nanostructures formed on Ni electrode surfaces, a large number of defects and therefore Hg sorption sites will be created while at the same time hindering any unwanted Hg accumulation at the surface. It is postulated that the nano-sized Au nanostructures would promote Hg desorption from their side edges rather than Hg accumulation (due to their non-continuous film nature) resulting in optimised Hg desorption properties.

6.2 Experimental Setup

The specially prepared QCM for this work were fabricated by evaporating thin titanium and nickel layers of 10 and 300 nm thick by e-beam evaporation onto AT-cut quartz substrates. The purpose of the Ti layer was to assist with the adhesion of the Ni layer to the substrate surface. The 2 sided Quartz crystal microbalance with 10nm Ti adhesion layer and 300nm Ni film on each side (0.32 cm^2 total surface area) was placed in a dialysis bag (12 kDa cut-off) containing 10 mL of deionized water (Milli-Q, Elix 3) and dialysed against 100 mL of $HAuCl_4$ (2×10^{-4} M) under constant stirring at room temperature for various time intervals (0.5 h, 1 h, 2 h, 4 h, and 8 h). The nickel films obtained after galvanic replacement reactions were thoroughly washed with Milli-Q water and dried under nitrogen. The confinement of nickel thin film in the dialysis bag assisted in the controlled inward movement of Au^{3+} ions to react slowly with nickel film, as well as simultaneous outward movement of leached Ni^{2+} ions. The resultant Ni-Au hybrid nanostructures were characterized by using scanning electron microscopy (SEM), X-ray diffraction (XRD), X-ray photoemission spectroscopy (XPS) and secondary ion mass spectroscopy (SIMS) techniques. The QCMs from each time point were then exposed to Hg vapour using the temperature profile test sequence outlined in Chapter 2 (Section 2.5.2). Selected QCMs were then exposed to Hg vapour of various concentrations in the presence of H_2O, NH_3 and mixture of both H_2O and NH_3 at various levels.

6.3 Ni-Au hybrid Sensitive Layer Characterisations

Important information about the GR reaction can be obtained by recording the changes in the surface features of Ni-Au system during a time-dependent GR experiment. In this section the various surface characterization techniques used to analyze the modified surfaces using GR reactions is presented.

6.3.1 Surface Morphology – SEM

The morphology of the GR surfaces was characterized using SEM imaging. Figure 6.1 shows the SEM images of Ni-Au system obtained after reaction of nickel film with Au^{3+} ions before reaction (a), reaction for 0.5 h (b), 1 h (c), 2 h (d), 4 h (e) and 8 h (f), respectively.

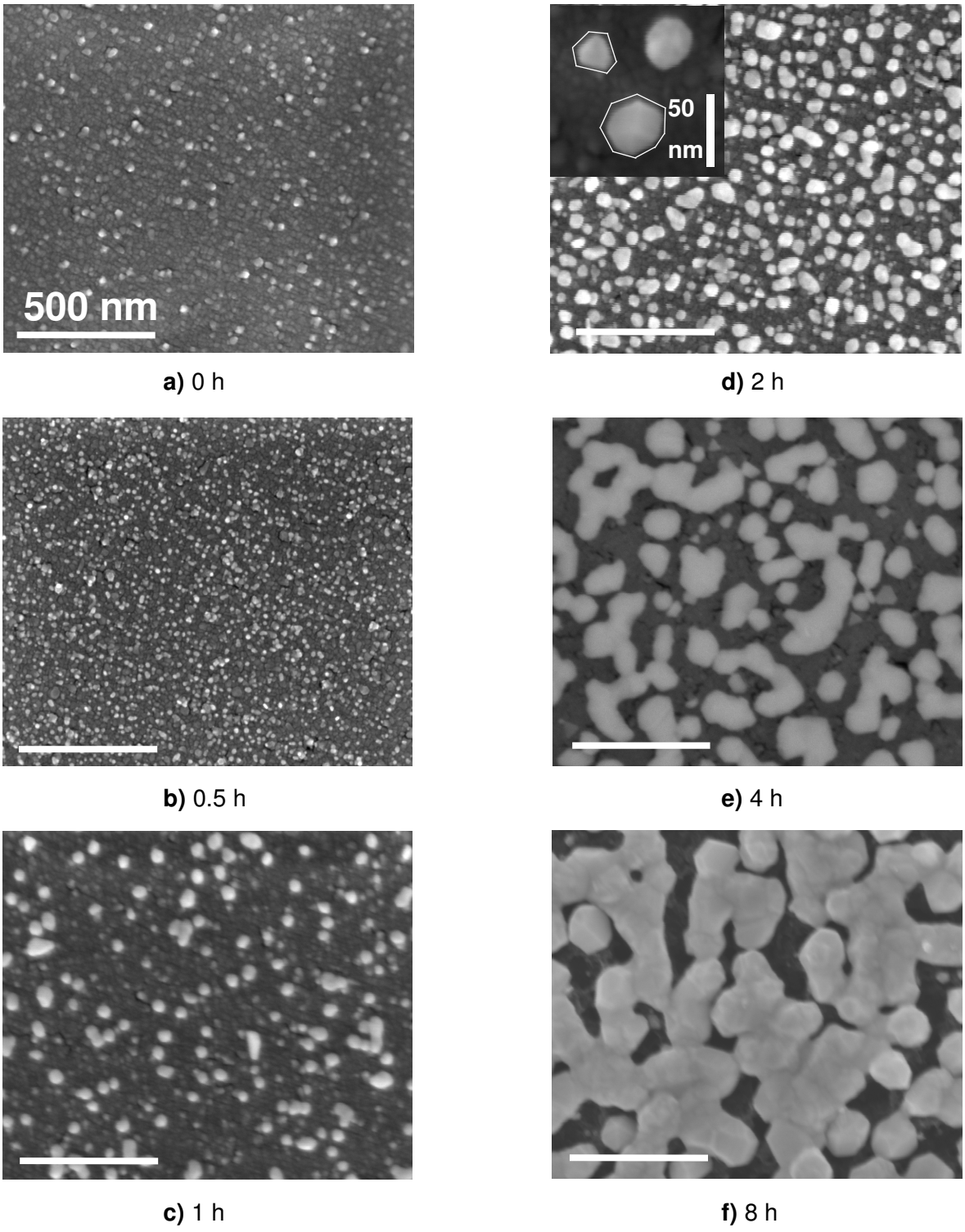

a) 0 h

d) 2 h

b) 0.5 h

e) 4 h

c) 1 h

f) 8 h

Figure 6.1: SEM images showing the Ni-Au surfaces at various GR reaction times. Inset in (B) shows some of the Au islands grown following 2 hours of reaction time.

The SEM images clearly indicate a relatively flat surface of nickel with small grains of maximum size of ~30 nm before GR reaction (Figure 6.1a). The reaction of nickel metal with Au^{3+} ions results in Au island formation which grow in a time dependent manner as a result of the GR reaction between Ni^0 and Au^{3+} (Figures 6.1b through to 6.1f). The Au islands were found to be approximately 20, 40 and 70 nm in size for the 0.5, 1 and 2 h GR QCMs, respectively. Coagulation of the Au islands is clearly evident with increasing GR reaction time to 4 and 8 hours as observed in Figures 1.1e and 1.1f, respectively.

6.3.2 Surface Roughness - AFM

AFM characterisation of the Ni-Au system were performed in order to determine the change in the surface area and surface roughness of the Au nanostructures with increasing reaction time. Figure 6.2 shows the AFM images representing the Ni film before reaction (a) and following GR reaction for 0.5 h (b), 1 h (c), 2 h (d), 4 h (e) and 8 h (f) with Au^{3+} ions, respectively. It is observed that the small grains tend to grow and coalescence into bigger nanostructures as the GR reaction time is increased beyond 2 hours, confirming the similar observations made using SEM characterization of the GR surfaces.

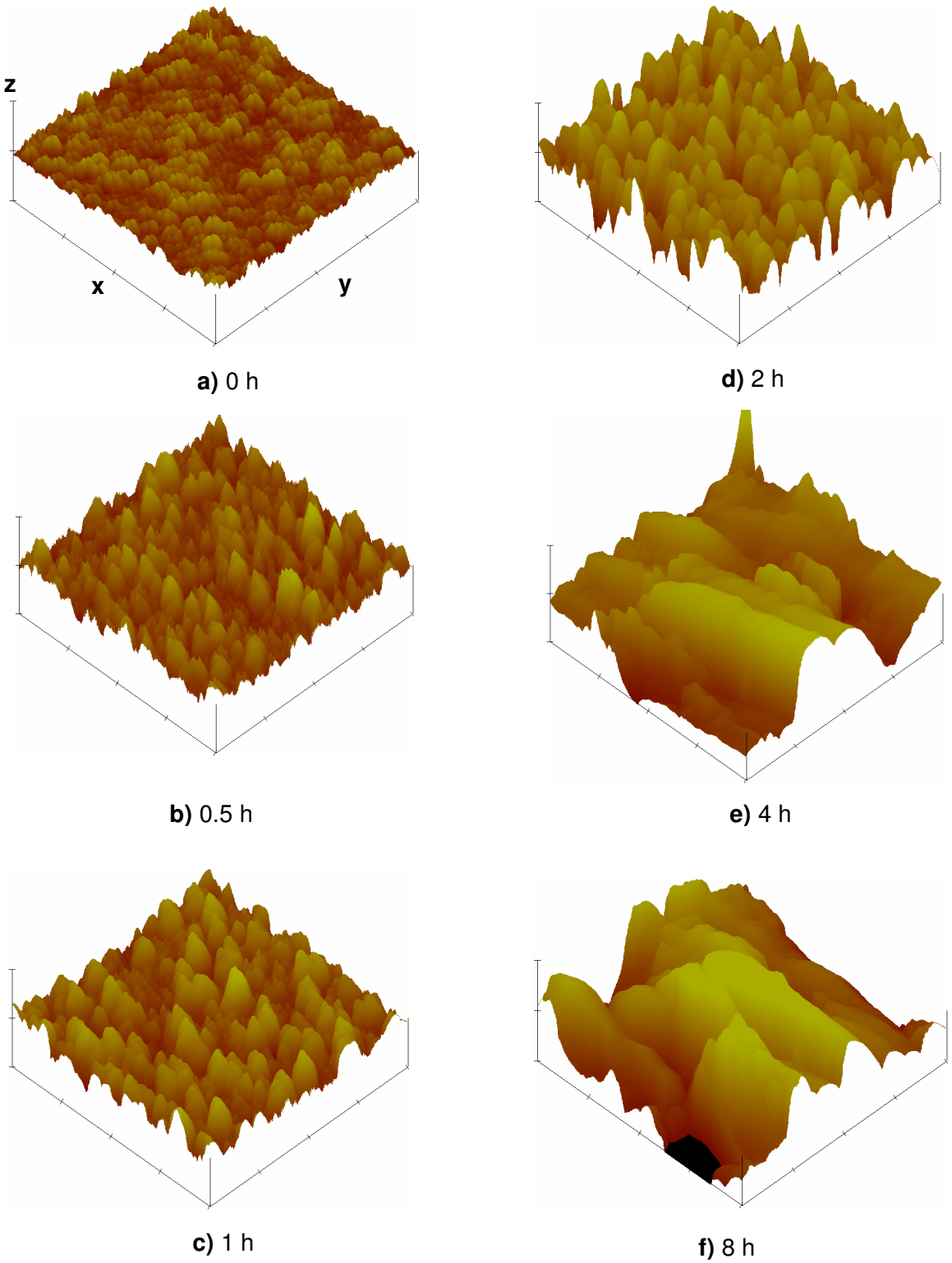

Figure 6.2: AFM images showing the Ni-Au surfaces at various GR reaction times. Scale for x, y and z axis are 500, 500 and 100 nm, respectively.

The roughness data obtained from AFM is shown in Figure 6.3. The average roughness (R_a) and the root-mean-square roughness (R_q) are observed to increase with increasing reaction time. The increased surface roughness was preferred in this case as it is well known that rougher surfaces contain larger number of defects[89,313,342] and therefore Hg adsorption

sites.[93,290] The actual surface area increase as compared to the scanned projected surface area of 4 μm^2 was observed to fluctuate between the reaction time points. Furthermore, the largest increase in surface area was observed to be at the GR reaction time of 2 hours with an increase in the projected surface area of 40.4% (within the AFM resolution limitations). The modified films' surface area was observed to resemble closely the projected surface area for the higher GR reaction times (4 and 8 hour) QCMs which indicates the approach of continuous Au film formation. The combination of large surface area and roughness is expected to increase Hg sorption during Hg vapour sensing. Therefore the 2 hour GR QCM is expected to have a larger response magnitude towards Hg vapour than the QCMs with lower GR reaction times. The 4 and 8 hour GR QCMs are also expected to undergo high Hg sorption due to their high roughness, however the total Hg sorption could be lower than the 2 h GR QCM due to their lower surface area. It is expected however that the 8 h GR QCM undergo higher Hg sorption than the 4 h GR QCM due to its relatively higher surface area and roughness.

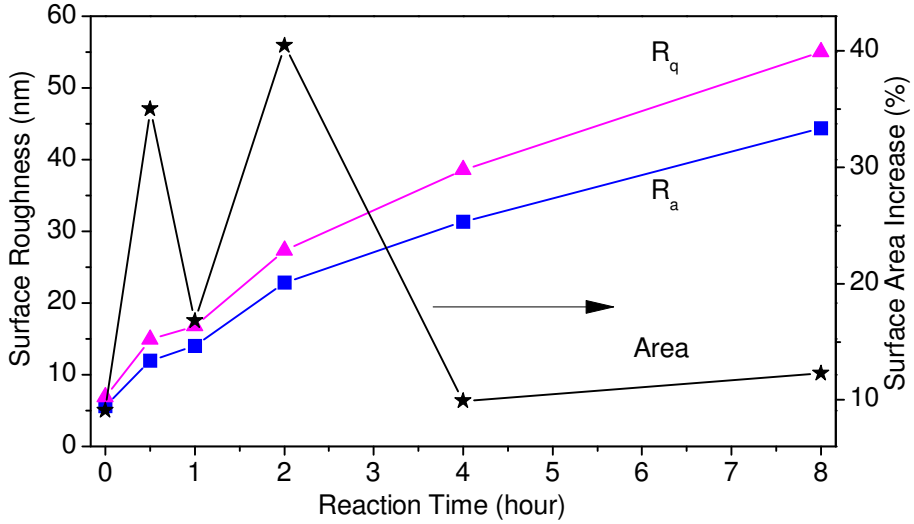

Figure 6.3: Surface roughness and surface area change with respect of GR reaction time as obtained from AFM resolution for the Ni-Au system.

6.3.3 Crystallography - XRD

XRD analysis was performed in order to determine the crystallographic orientation of the deposited Au as well as to confirm the existence of Au-Ni alloy at the Au and Ni interface. The Au nanostructures may be rigidly adhered on the Ni surface when alloying between the two metals occur resulting in strong metalic bonds between the Ni atoms on the thin film and the gold atoms in the Au nanostrucutres. Figure 6.4 below shows the XRD (with a GAADS detector) spectra of the GR reaction samples reacted for various time points with the upper most peak refering to pure Au substrate. Spectra from all Ni-Au system samples have been normalised to the Ni [200] peak. It is observed that as reaction time progresses, the Au [111] as well as the overlapped Au[200]/Ni[111] peaks increases. The inset in Figure 6.4 shows

the overlapped Au[200]/Ni[111] peaks with the upper most peak being the Au[200] obtained from pure gold substrate x-ray pattern.

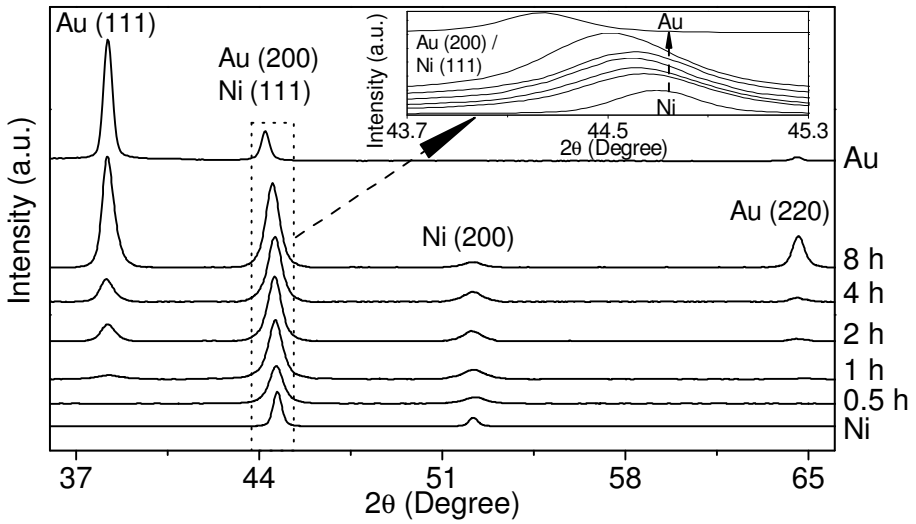

Figure 6.4: XRD spectra of Ni and Au control as well as all the GR reaction time samples. The uppermost spectrum is for Au substrate. Inset: Au [200]/Ni [111] region.

As the reaction time increases, it is observed that the overlapped Au[200]/Ni [111] peaks from the Ni-Au system substrates shift towards the Au[200] peak indicating increased amount of Au with increasing GR reaction time. The shift towards the left with increasing reaction time (as shown in the inset) indicates the possibility of alloying between the Ni and Au. This indicates the Au nanostructures' rigid adherence to the Ni substrate.

6.3.4 Surface Chemical Analysis - XPS

The chemical surface analysis of the Ni-Au surfaces used in this study was performed using XPS, which is a highly surface sensitive technique. The XPS data for the surfaces are shown in Figure 6.5. Figure 6.5a shows the Ni 2 $p_{3/2}$ core level spectra for the Ni surfaces undergoing GR reaction for various periods of time. Prior to GR reaction (Ni curve in Figure 6.5a), the Ni $2p_{3/2}$ core level spectrum shows two major $2p_{3/2}$ components at ca. 852.9 and 856.5 eV, which can be assigned to Ni^0 and NiO respectively[328,343,344]. The simultaneous presence of Ni and NiO components indicates the partial oxidation of Ni film surface on its exposure to air. Apart from these two components, a weak satellite peak[345] towards the higher binding energies was also observed in the Ni control sample (indicated by arrow marks). Upon GR reactions of the samples with Au^{3+} ions at various time points, the Ni^0 peak starts to vanish with the development of a more pronounced NiO peak. This indicates the Ni surface has oxidised to NiO during the GR reaction in the aqueous environment. Similar observation was made by Bansal et al.[328] when they galvanically replace Ni with Cu^{2+} ions. Furthermore, the shake-up satellites[343] in the Ni $2p_{3/2}$ XPS spectrum becomes more intense

following GR reactions. Shake-up refers to non-adiabatic relaxation of the electron cloud upon photoionionization where the energy is used to promote another valence electron to an unoccupied state giving rise to shake-up transition or extra peaks in the XPS spectrum. Since the shake-up satellites are mainly 3d to 4s transitions (which are forbidden in metals but present in transition metal oxides), the oxidation of Ni to NiO increases the intensity of these satellites[328].

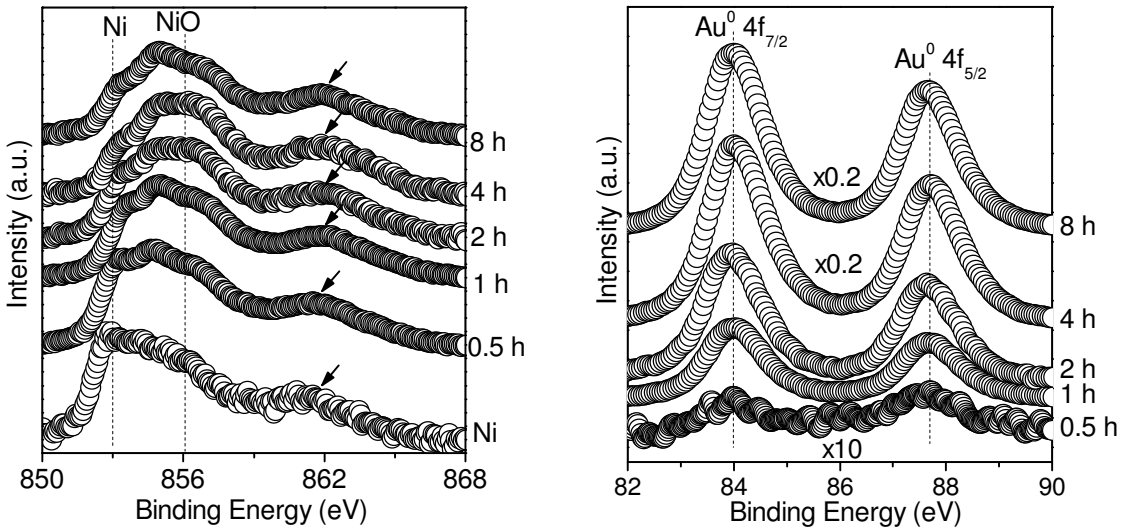

a) Ni 2p core level spectra

b) Au 4f core level spectra

Figure 6.5: XPS spectra of Ni-Au system.

Figure 6.5b shows the Au particles XPS spectra for the surfaces having undergone various GR reaction times. Two peaks at binding energies (BE) 84 and 87.7 eV resulting from Au $4f_{7/2}$ and $4f_{5/2}$, respectively, are identified with Au^0 oxidation state[346]. There are no peaks for Au^{1+} and Au^{3+} which should be present at 85.6 eV and 86.5 eV, respectively.[347] The detected Au 4f peaks did not exhibit any significant shift in the BE from those of bulk gold, indicating that the gold particles of all the samples were in metallic form.

The content of Ni and Au within the x-ray penetration depth (2-3 nm)[289,348] on the film surface is calculated from the Ni 2p and Au 4f peak areas and are presented in Figure 6.6a. It is observed that the composition of Au increases with longer reaction times as expected. However, the composition of the two metals is observed to be similar between the 4 h GR and 8 h GR QCMs. This indicates that the GR reaction slows with time due to the presence of reduced Ni on the surface which can be replaced by the gold ions from the solution. Therefore most of the darker surfaces observed in the SEM image in Figure 6.1f is believed to be NiO rather than Ni; as no GR reaction appear to occur in some regions of the Ni film. The deconvoluted XPS data for the NiO and Ni signal for each sample (0, 0.5, 1, 2, 4 and 8 h GR QCM electrodes) is presented in Appendix F (Figure F1) from which the composition of Ni and NiO is estimated and summarised in Figure 6.6b. It is observed that the

composition of NiO relative to Ni is increased up to a period of 2 h GR reaction period and is severely reduced for the 4 h GR and 8 h GR reaction times. The increase in NiO signal relative to Ni further supports the assumption that Ni is oxidised to NiO as well as replaced by Au during GR reaction. Ni is also known to diffuse into Au and oxidise to NiO in the presence of oxygen. The reduced NiO signal observed for the 4 h GR and 8 h GR QCM electrodes is attributed to the low x-ray penetration depth (near the surface region). That is, the NiO and/or Ni below the large Au nanostructures have not diffused close enough to the Au nanostructures' surface in order to be detected by XPS in the time period between GR reaction and XPS characterisation. However, the decrease in the composition of NiO observed from XPS data is not well understood and needs to be further investigated by XPS depth profiling, however is beyond the scope of this research project and is the subject of future work.

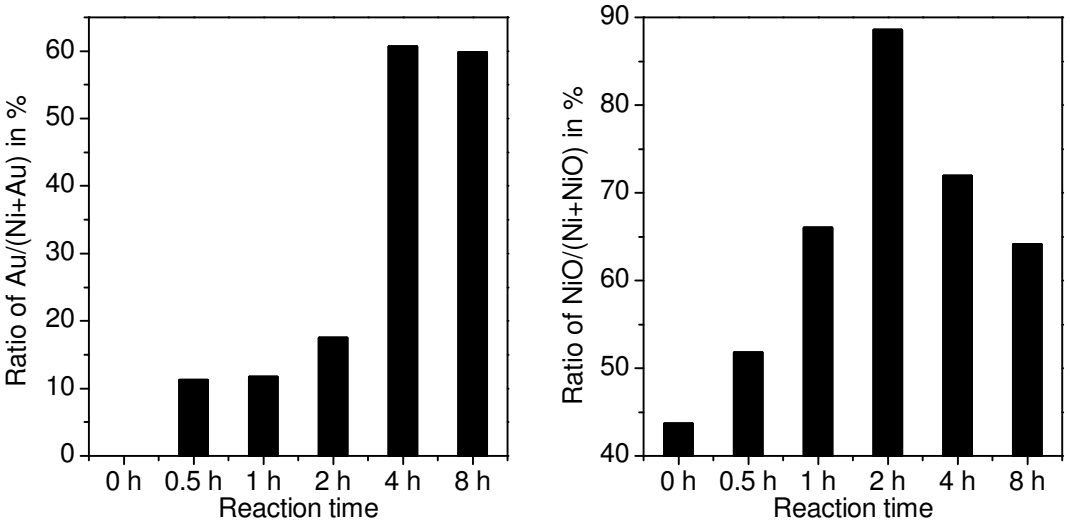

a) Ni 2p and Au 4f peak area ratios

b) Ni 2p component peak area ratios

Figure 6.6: Peak area ratios showing the ratio of Au to Ni as well as NiO to Ni as a function of GR reaction time. Peak areas for the NiO composition were obtained from deconvoluted XPS spectra shown in appendix F, Figure F1.

6.4 Hg Sensing Performance of Galvanically Replaced QCMs

The galvanically replaced Ni-Au QCMs were tested toward Hg vapour concentrations ranging from 1.02 to 10.55 mg/m^3 and operating temperatures ranging from 28 to 134℃ with and without the presence of H_2O, NH_3 and their mixtures at different levels. The temperature profile, interferent gases and mercury saturation test patterns describe in Chapter 2, Section 2.5 were performed on the developed GR QCM sensors. The influence of operating temperature, GR reaction time and presence of interferent gases on the performance of the developed GR QCMs are presented in this section.

6.4.1 Influence of Operating Temperature on Hg Sorption and Desorption Characteristics

In order to study the influence of operating temperature on Hg sorption and desorption characteristics, the galvanically replaced, nickel and gold control based QCMs were exposed to Hg vapour at operating temperatures of 28 and 89℃. The sensors were exposed to Hg concentration of 5.7 mg/m^3 for 8 hours followed by dry nitrogen for a recovery period of 5 hours. The QCMs' response magnitudes are analysed and presented in the following subsections.

6.4.1.1 Operating Temperature of 28℃

The response magnitude of the GR QCMs together with both Ni as well as 200 nm Au-polished QCMs serving as controls towards Hg vapour concentration of 5.7 mg/m^3 at an operating temperature of 28℃ is illustrated in Figure 6.7. Figures 6.7a show the sensor response during the 8 hour Hg sorption, whereas Figure 6.7b shows the zero-shifted 5 hour desorption phase of the sensor response.

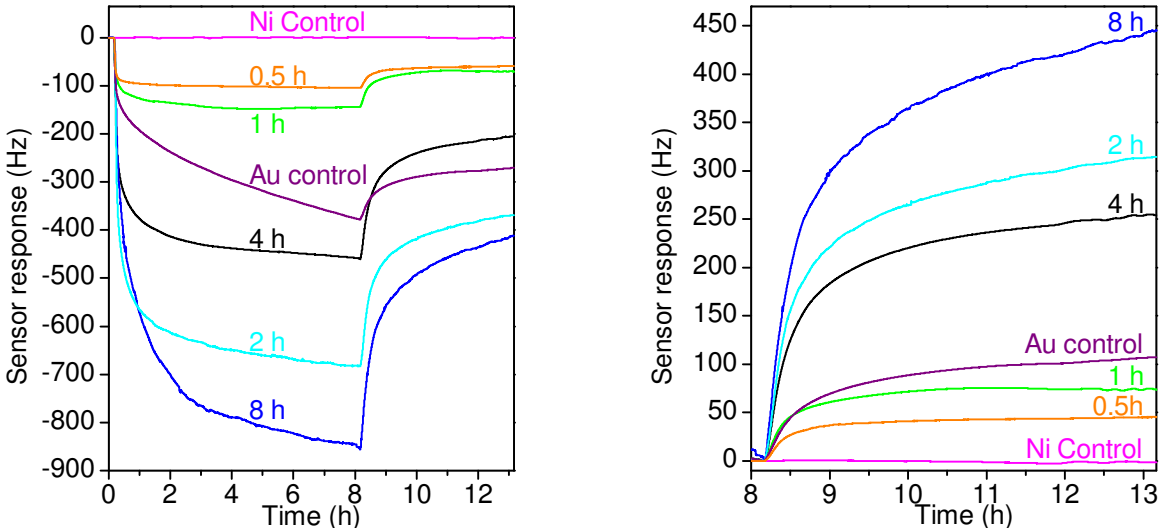

a) Hg sorption at 28℃ **b)** Hg desorption at 28℃

Figure 6.7: QCM response curves of all GR QCMs as well as the Ni and Au controls exposed to Hg concentration of 5.7 mg/m^3 for eight hours before a five hour recovery period using dry nitrogen. The desorption curves (b) have been zero-shifted for comparison purposes.

It is observed that the Hg sorption capacity of the GR QCMs increases up to a GR reaction time of 2 hours. The increasing Hg sorption capacity of the Ni-Au electrode QCMs is attributed to the high number of defect sites generated as a result of galvanic replacement reaction.[328] As the GR reaction time is increased beyond 2 hours, the Hg sorption capacity is observed to reduce (i.e. 4 h GR QCM). The reduced Hg sorption capacity for the

4 h GR QCM becomes apparent when a comparison of the SEM image of the 4 h GR electrode in Figure 6.1e is made with the 2 h GR QCM electrode surface in Figure 6.1d. The 2 hour surface contains many small nano-islands while the larger nano-islands in the 4 h GR QCM electrode are less sparely distributed. Such difference in morphology indicates that the 4 h GR electrode contains less surface area to volume ratio than that of the 2 h GR QCM electrode surface. This is clearly the case as observed from the AFM data presented in Figure 6.2. However, the AFM data also shows increased surface roughness and therefore increased number of defects resulting in increased number of Hg sorption sites on the 4 h GR QCM. Furthermore, it is also evident from the Hg sorption data that the reduction in surface area outweighs the increase in surface roughness. That is, the 8 h GR QCM was found to produce the highest response magnitude when exposed to Hg vapour. SEM image in Figure 6.1f shows large but thin nano-islands. It was observed in Chapter 5 thicker films of Au have large Hg sorption capacity. This was attributed to Hg migration into the bulk resulting in the release of Hg sorption sites for more Hg atoms to adsorb/amalgamate.[93] The 8 h GR QCM is also observed behave similar to the Au ultra-thin film having significant drift during the 8-hour Hg exposure period as observed in Figure 6.7a. The QCM electrodes with shorter GR reaction times are observed to reach close to saturation due to the smaller Au particles deposited on them. This indicates lack of Hg accumulation, which is similar to the findings observed for the 10 nm Au ultra-thin film in Chapter 5 (see Section 5.3.1.1 and the corresponding SIMS depth profile in Section 5.4.1.1 showing no Hg accumulating in the Au bulk). As expected, The Ni control QCM is observed to produce no response towards Hg vapour exposure.

During the 5 hour sensor recovery period shown in Figure 6.7b, the amount of Hg desorbed is observed to follow the trend of Hg sorption that occurred following the 8 hours of Hg exposure period. This indicates that desorption is also surface Hg coverage dependent on the galvanically replaced surfaces. Similar trends were observed in Chapter 5 for the polished Au ultra-thin film based QCMs. That is, the total amount of desorbed Hg following the 5 h sensor recovery period was observed to have the same trend as the total amount of Hg sorption on the different Au films during Hg exposure at all operating conditions.

6.4.1.2 Operating Temperature of 89°C

Figure 6.8 shows the QCM response magnitude during Hg exposure and desorption (zero shifted) of the GR QCMs as well as that of the control Ni and Au QCMs operating at 89°C. From Figure 6.8a the Au control QCM was found to attain the largest Hg sorption capacity at the operating temperature of 89°C and Hg concentration of 5.7 mg/m^3. Surprisingly, it was the 2 h GR QCM that produced the next highest sorption capacity, and having saturated with a t_{90} of only ~35 minutes compared to Au control having a t_{90} of ~250 minutes over the

8 hour Hg exposure period. The Au control is not observed to reach saturation even after 8 hours of Hg exposure period under the same operating conditions. The characteristic response which saturates is preferred for Hg vapour sensing applications as it indicates minimal diffusion of Hg through the available Au on the GR QCMs.

The trend in response magnitude between the different QCMs is observed to be the Ni, 0.5 h, 1 h, 4 h, 8 h, 2 h and Au in increasing order as observed in Figure 6.8a. A similar trend is also observed in the zero-shifted desorption response magnitudes following the 5 hour recovery period as shown in Figure 6.8b. The trends at 89℃ is observed to be in a different order to that observed for 28℃ in Figure 6.7. This indicates that the GR modified as well as the Au control QCMs have different Hg sorption and desorption capacities relative to each other depending on the operating temperature. Furthermore, it is observed that the QCM response dynamics during desorption follow similar trend to Hg sorption with the GR QCMs having smaller t_{90} during desorption than Au control QCM. That is, the Au control was observed to have a t_{90} of ~215 minutes during the 5 hour recovery period while the 0.5, 1, 2, 4 and 8 h GR QCMs had t_{90} values of approximately 124, 139, 120, 173 and 143 minutes, respectively. These values indicate that the sensor recovery rate is not necessarily decreased by the GR reaction time (or amount of deposited Au on the Ni electrodes) as GR reaction introduces surface defects which positively influence Hg desorption from Au surfaces.[89]

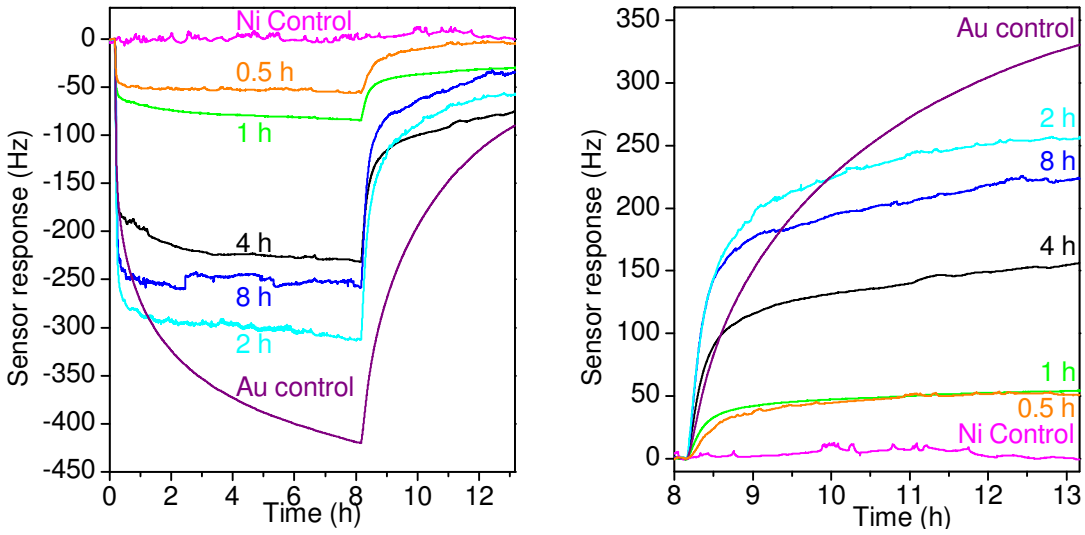

a) Hg sorption at 89℃ **b)** Hg desorption at 89℃

Figure 6.8: QCM response curves of all GR QCMs as well as the Ni and Au controls exposed to Hg concentration of 5.7 mg/m^3 for eight hours before a five hour recovery period using dry nitrogen. The desorption curves (b) have been zero-shifted for comparison purposes.

The Hg exposure time, especially at an operating temperature of 89℃, was observed to have little effect on the sorption trend of the different GR QCM electrodes. This is observed to be due to the fast saturation of the Ni-Au electrodes while having high response magnitude. This again indicates lower diffusion of Hg through the GR produced gold nano-islands. This was not observed to be the case for the Au ultra-thin film based QCM electrodes in Chapter 5 where the change in the sorption trend was attributed to the diffusion of Hg through the 30 and 40 nm thick Au films. The constant trend of the order between the different GR QCM response dynamics with Hg exposure time and their quick saturation towards Hg vapour is encouraging and shows repeatable response magnitudes is obtainable for a particular Hg concentration (especially at 89℃ operating temperature used in industries) for any exposure times above 30 minutes.

6.4.2 Influence of Operating Temperature on Hg Sensing

The galvanically replaced sensors as well as the optically polished 200 nm Au electrode QCMs were exposed to various Hg vapour concentrations and operating temperatures. The response curves for the sensors at operating temperatures of 28 and 89℃ are shown in Figures 6.9a and 6.9b, respectively. It is observed that the QCM electrode undergoing 8 hours of GR reaction produced the highest response magnitude for both operating temperatures (28 and 89℃) and for all tested Hg vapour concentrations (1.02, 1.87, 3.65, 5.70 and 10.55 mg/m^3).

It was observed that except for the 0.5 and 8 h GR QCMs, GR QCM electrodes were not saturated following a 1 hour of Hg exposure at an operating temperature of 28℃ (Figure 6.9a). However, unlike Au films, when exposed to Hg vapour at the higher operating temperature of 89℃, all GR QCMs are observed to reach saturation even at the lower Hg exposure times of 1 hour during sensing (Figure 6.8b). The fact that the modified sensors reach saturation indicates maximum sorption capacity for the particular Hg vapour concentration has been reached by the surfaces. Reaching saturation point is an advantage in Hg sensing as it indicates that Hg diffusion and accumulation through the sample is less likely to occur and therefore enhancing regeneration of the Hg sensor during the recovery period. The lack of Hg diffusion is attributed to the low availability of Hg vapour on the surface which would otherwise encourage diffusion[89] as was discussed in chapter 4, Section 4.3.2. It was also shown in chapter 5, Section 5.3.2 that Hg saturation of Au ultra-thin films was not reached even after 14 hours of Hg exposure period. The advantage of the modified Au films (GR QCMs) exhibiting such short saturation times of ~30 minutes is that an increase in exposure time beyond 30 minutes will not severely affect the final sensor output signal when compared with the non-modified Au films. The GR QCMs are therefore shown to have

quick response times with high response magnitudes towards Hg vapour which makes them ideal candidates for Hg vapour sensing applications at 89℃.

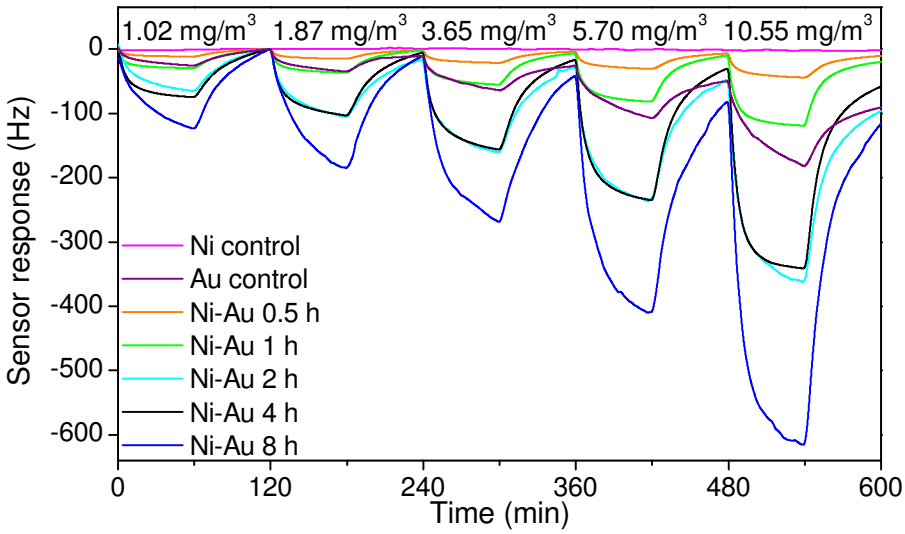

a) Operating temperature of 28℃

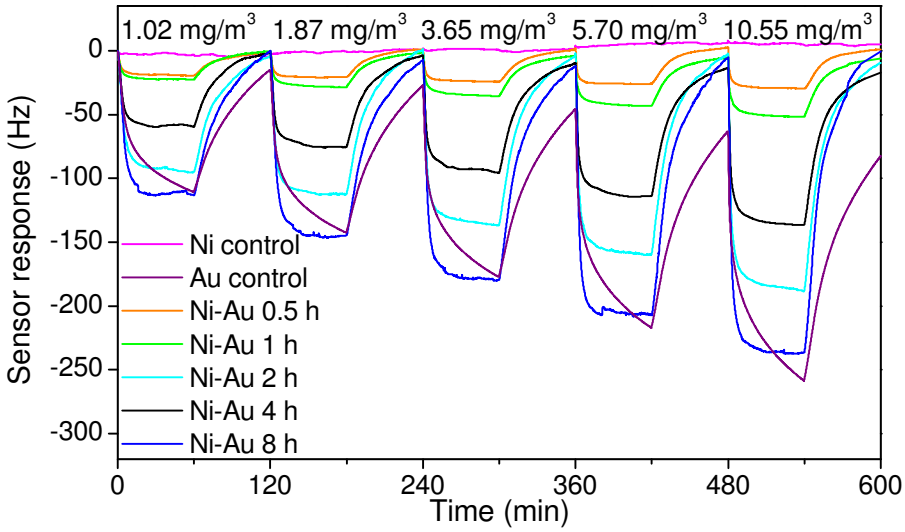

b) Operating temperature of 89℃

Figure 6.9: QCM response curves for the controls as well as the Ni-Au systems modified by GR reaction and exposed to Hg at various concentrations and operating temperatures.

6.4.3 Influence of Operating Temperature on Response Time and Response Magnitude

The response time of the Au control as well as the modified sensors was assessed by their t_{90} parameters. Figure 6.10 illustrates the influence of temperature on t_{90} (Figure 6.10a) as well as the response magnitude (Figure 6.10b) for Au control and the GR modified QCMs at various operating temperatures and Hg concentration of 1.02 mg/m^3.

In general, the t_{90} parameter of the sensors is observed to reduce with increasing operating temperature. The response time of the modified sensors is also observed to be equivalent or lower than that of the control Au QCM for all operating temperatures. The response curves as well as the response rate curves for all tested operating temperatures are shown in (appendix F, Figures F.2 through to F.6). The summary of t_{90} and the final response magnitude after 1 hour of Hg exposure is shown in Figures 6.10a and 6.10b, respectively.

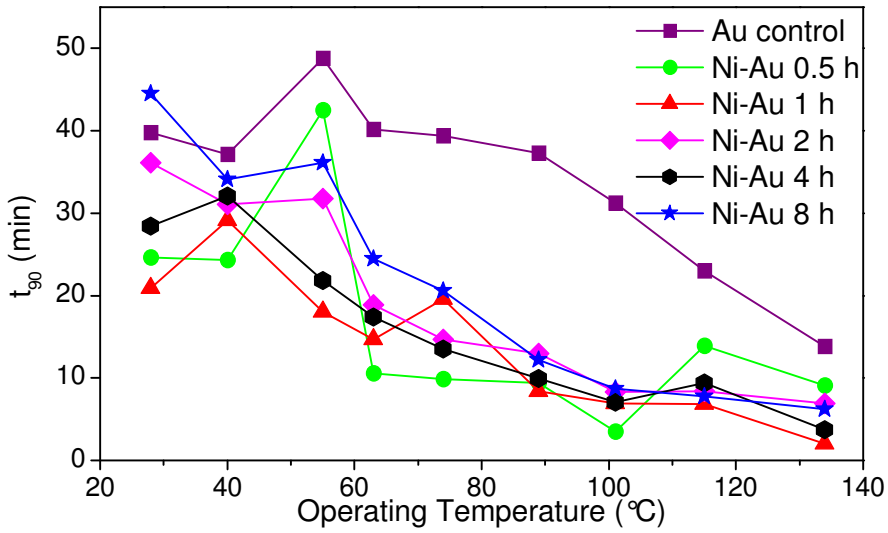

a) Influence of temperature on t_{90}

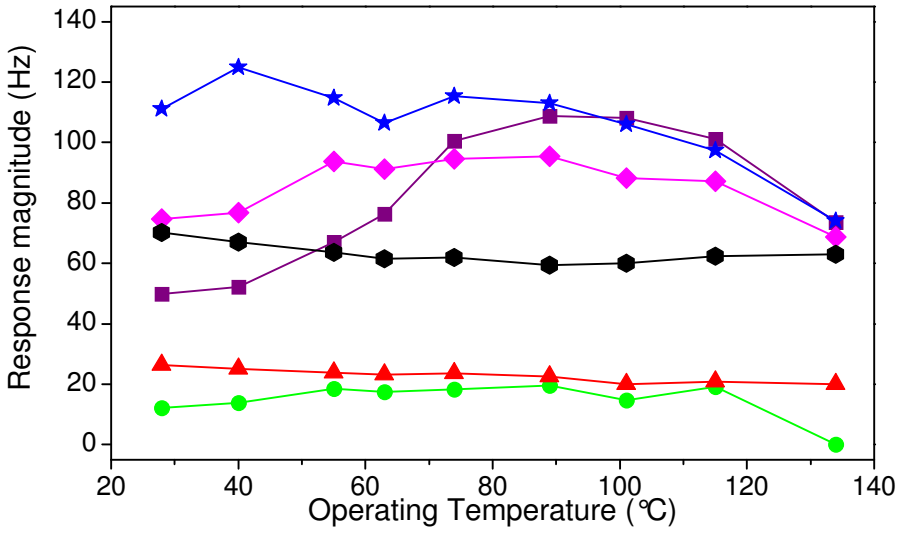

b) Influence of temperature on response magnitude

Figure 6.10: QCM data showing the influence of operating temperature on the t_{90} and response magnitude of the sensors when exposed to 1.02 mg/m^3 Hg pulses.

A common balance between the response time and response magnitude is found to occur at an operating temperature of 89℃. In Figure 6.10a it is observed that the t_{90} is generally reduced with increasing operating temperature for all QCMs with the all the GR QCMs having lower t_{90} than the Au control at 89℃. At this temperature the t_{90} values of the GR

modified sensors is found to be around ¼ of the control Au QCM indicating the modified sensors are 4 times faster in producing 90% of their total response due to Hg exposure than that of the non-modified Au control QCM. It can be observed from Figure 6.10b that only the response magnitude of the 8 h GR and Au control QCMs are influenced by operating temperature. The 8 h GR QCM is found to be the optimum sensor having reached the highest response magnitude compared to all other sensors tested for each Hg pulse at an operating temperature of 89°C while attaining relatively low t_{90} (quick response times towards the tested Hg concentrations). The 1 h GR QCM was found to have the lowest t_{90} however also had the lowest response magnitude from all the sensors tested. The response rate curves of the GR QCMs towards Hg vapour are shown in Appendix F, Figures F.3 through to F.6 and is summarised as follows. The maximum response rate magnitudes of all the GR sensors in general are observed to increase with increasing temperature, similar to the Au control QCM. Furthermore, the maximum response rate magnitudes of the sensors towards Hg vapour are observed to increase with increasing GR reaction time, however a reduction in signal to noise ratio was observed for the 8 h GR QCM.

6.4.4 Influence of GR reaction time on QCM Response Magnitude and Recovery

The response magnitude as well as the ratio of desorption (Δf_d) to that of the Hg sorption (Δf_s) at the operating temperature of 89°C and largest Hg concentration of 10.55 mg/m^3 is shown in Table 6.1.

Table 6.1: Sensor data for all GR , Au thin films and Au-rough based QCMs demonstrating Hg sorption, desorption and Hg desorption to sorption ratio observed at Hg vapour concentration of 10.55 mg/m^3 and an operating temperature of 89°C.

QCM electrode	*Hg sorption (Hz)*	*Hg desorption (Hz)*	*Hg desorption to Hg sorption ratio*
0.5 h GR	32.7	30.7	0.939
1 h GR	46.4	45	0.970
2 h GR	186.7	179	0.959
4 h GR	122.6	119	0.971
8 h GR	230.6	229	**0.993**
100 nm Au	213.1	200.4	0.940
150 nm Au	208.1	195.4	0.940
200 nm Au	195.4	175.6	0.899
Au-rough	**271.2**	**260.7**	0.961

All the tested QCMs presented in chapter 3 through to chapter 6 are shown for comparative reasons. The maximum and minimum values for each column are indicated by a **bold** and underlined font, respectively. It is observed that the 8 h GR QCM had the second highest sorption capacity towards Hg (after the Au-rough QCM) while having the highest Hg desorption to sorption ratio than any other QCM tested so far. The highest desorption response magnitude observed for the Au-rough QCM is due to the high Hg sorption (or Hg surface coverage) which occurred before the one hour recovery period. The 0.5 h GR QCM is observed to have the lowest response magnitude and the minimum Hg desorption/Hg sorption ratio making it inadequate as a potential Hg vapour sensor.

6.4.5 Influence of GR reaction time and Operating Temperature on QCM Sensitivity and Limit of Detection

The sensitivity and limit of detection (LOD) of each QCM was calculated for 28 and 89℃ following the procedure described in Chapter 4, Section 4.4.4.2 in order to determine the influence of operating temperature on these parameters of the GR sensors. A summary of the calculated parameters is presented in Table 6.2.

Table 6.2: Calculated sensitivity and limit of detection for all GR and Au control QCMs for operating temperature of 28 and 89℃

QCM electrode	Detection limit (mg/m^3)		Sensitivity [$Hz/(mg/m^3)$]	
	28℃	89℃	28℃	89℃
200 nm Au control	0.031	0.108	28.7	38.8
0.5 h GR	**0.126**	<u>0.103</u>	<u>2.66</u>	<u>5.91</u>
1 h GR	0.058	0.138	8.69	10.2
2 h GR	0.020	0.147	25.1	39.6
4 h GR	0.022	0135	25.1	27.0
8 h GR	0.014	0.128	43.3	49.4

It is observed that the 2, 4 and 8 h GR QCMs outperform the LOD of the Au control QCM at 28℃. However, only the 0.5 h GR QCM has better LOD than the Au control QCM at 89℃ but with reduced response magnitude as was observed in Table 6.1. The sensitivity of the GR QCM towards Hg vapour are observed to increase with increasing reaction time at 28℃, with only the 8 h GR QCM outperforming the Au control sensor. However, when exposing Hg at 89℃, similar trend is observed for all the GR QCMs except for the 2 h GR QCM. The 2 and 4 h GR QCMs were both observed to outperform the Au control sensor at 89℃. In general it is observed that an increase in operating temperature increases the LOD of the

sensors while increasing their sensitivities towards Hg vapour. Fortunately, the increased LOD at 89℃ of each sensor is below the lowest tested Hg vapour concentration (1.02 mg/m^3) indicating all sensors can be tested towards Hg concentration range of 1.02 to 10.55 mg/m^3 at 89℃.

6.4.6 Influence of Hg in the Presence of Interferent Gases on the Galvanically Replaced QCMs

Three selected sensors, namely the 1, 4 and 8 h GR QCMs were further tested towards Hg vapour in the presence of H_2O and NH_3 due to their highest Hg desorption abilities as well as the 8 h GR QCM having the highest Hg sorption capacity. The pulse sequence for all the GR and Au control QCMs towards Hg vapour exposure with/without the presence of interferent gases at 89℃ is shown in Figure 6.11. A reduced response magnitude is observed when the selected sensors (shown in Figure 6.11) are exposed to Hg in the presence of the interferent gas species compared to Hg exposure alone.

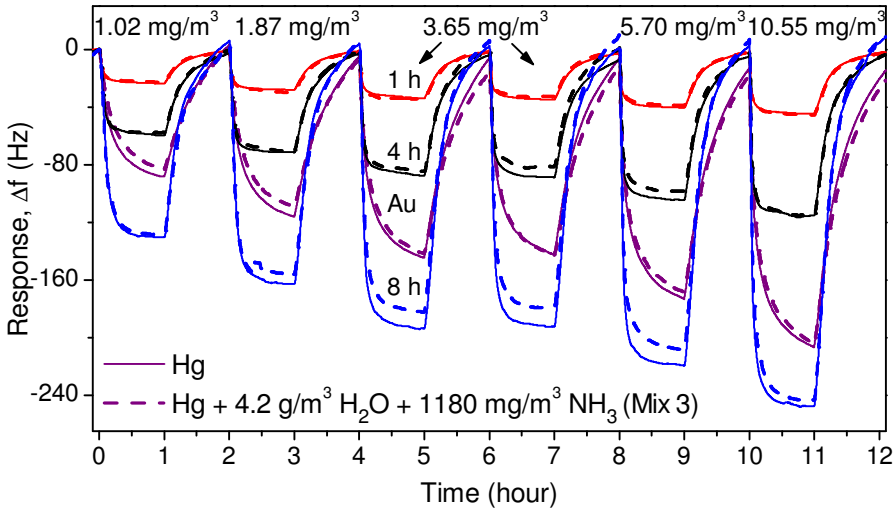

Figure 6.11: GR and Au control sensors response dynamics towards Hg in the presence of interferent gases (mix 3) at 89℃.

The sensor response curves for the 1, 4 and 8 h GR QCMs towards Hg vapour with and without the presence of interferent gases at the operating temperature of 89℃ are shown in Figures 6.12, 6.13 and 6.14, respectively. Set 1 through to Set 5 refers to Hg exposure in the absence of interferent gases. Each set comprised of 1 pulse of each Hg concentration (1.02, 1.87, 3.65, 5.70 and 10.55 mg/m^3) as explained in Chapter 2, Section 2.5.

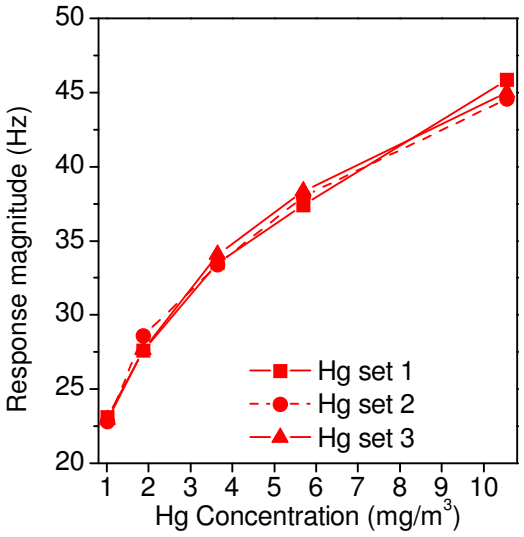

a) Hg exposure

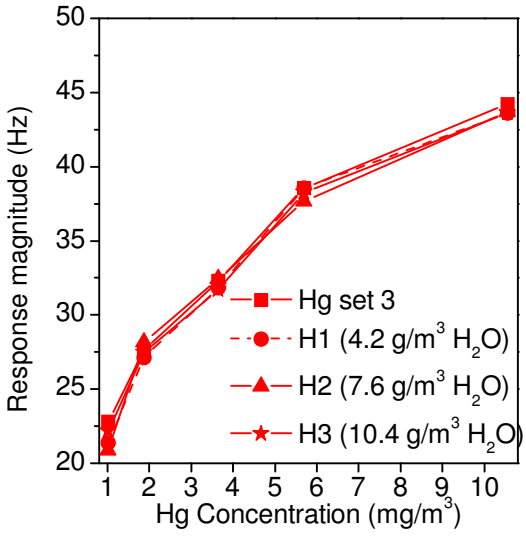

b) Hg exposure in the presence of humidity

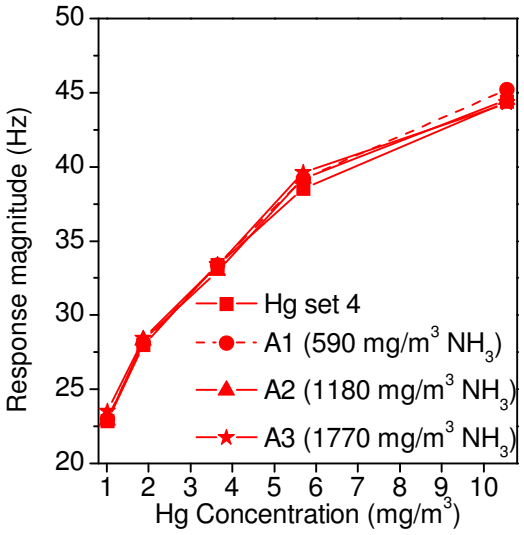

c) Hg exposure in the presence of ammonia

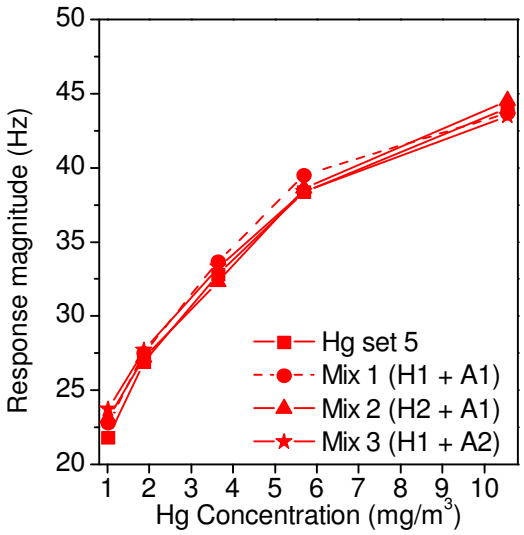

d) Hg exposure in the presence of both humidity and ammonia

Figure 6.12: QCM data – 1 h GR QCM exposed to Hg vapour concentrations ranging from 1.02 to 10.55 mg/m^3 at an operating temperature of 89℃ with and without the presence of interferent gases.

In Figure 6.12, it is observed that the effect of Hg exposure (Figure 6.12a) as well as Hg in the presence humidity (Figure 6.12b), ammonia (Figure 6.12c) or mixtures of both humidity and ammonia (Figure 6.12d) has little effect on the response magnitude of the 1 h GR QCM sensor.

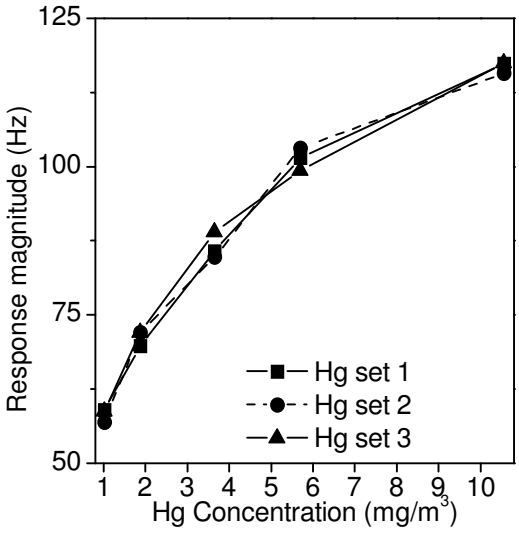

a) Hg exposure

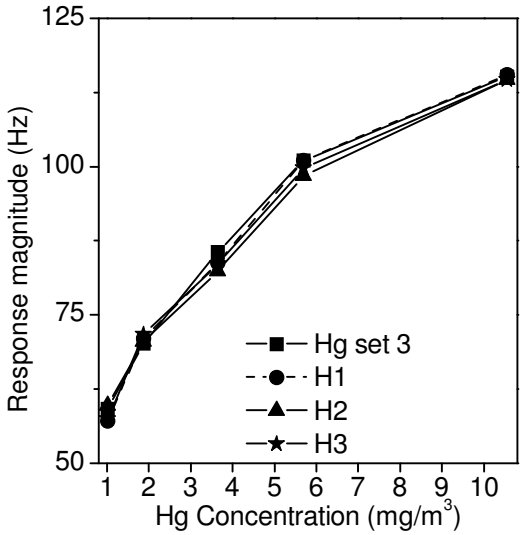

b) Hg exposure in the presence of humidity

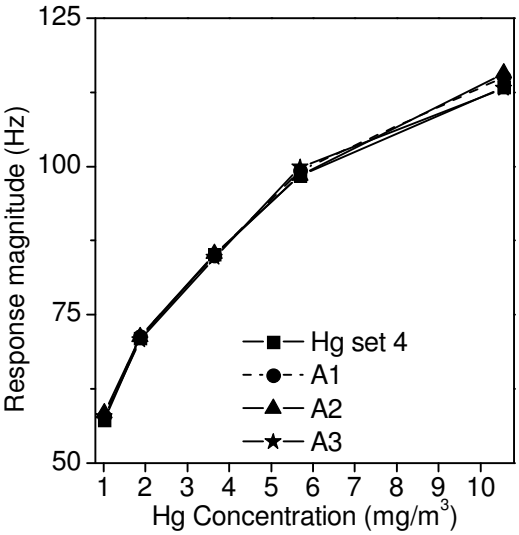

c) Hg exposure in the presence of ammonia

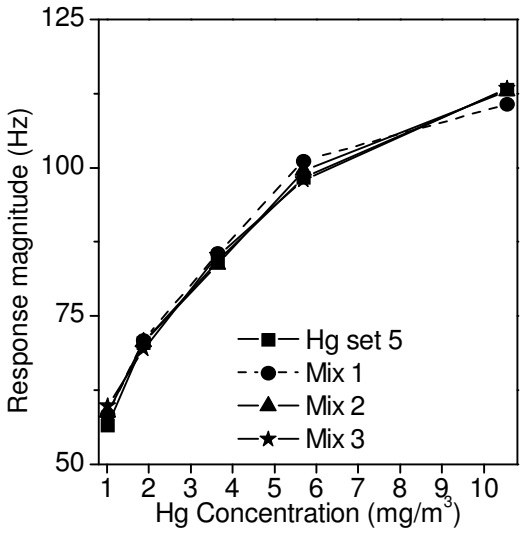

d) Hg exposure in the presence of both humidity and ammonia

Figure 6.13: QCM data – 4 h GR QCM exposed to Hg vapour concentrations ranging from 1.02 to 10.55 mg/m^3 at an operating temperature of 89°C with and without the presence of interferent gases.

It is also observed in Figure 6.13 that the effect of Hg exposure (Figure 6.13a) as well as Hg in the presence humidity (Figure 6.13b), ammonia (Figure 6.13c) or mixtures of both humidity and ammonia (Figure 6.13d) has little effect on the response magnitude of the 4 h GR QCM sensor. However, it can be observed that the 4 h GR QCM has a higher response magnitude towards Hg vapour than that of the 1 h GR QCM for all tested Hg vapour concentrations (1.02, 1.87, 3.65, 5.70 and 10.55 mg/m^3) at an operating temperature of 89°C.

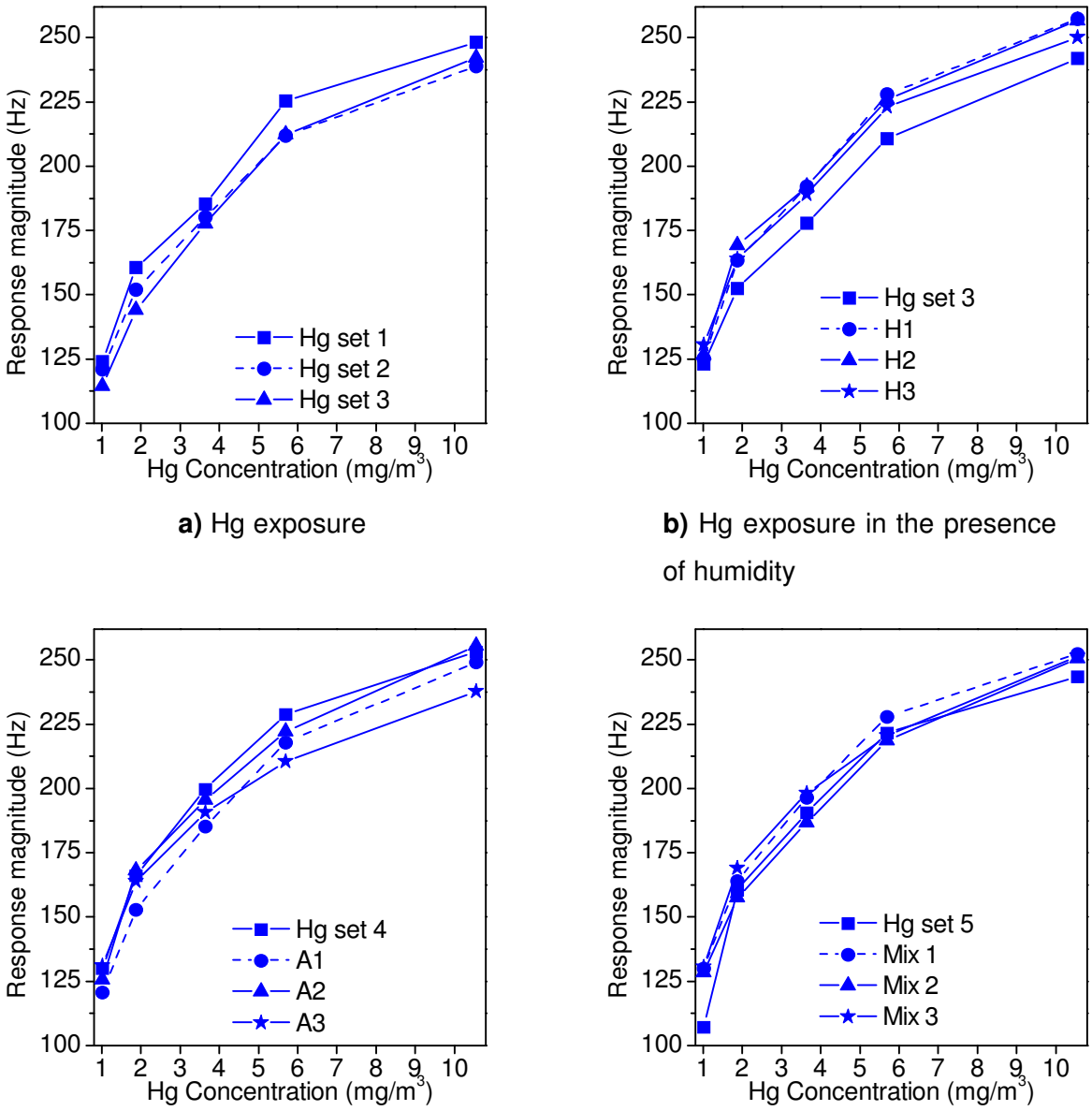

a) Hg exposure

b) Hg exposure in the presence of humidity

c) Hg exposure in the presence of ammonia

d) Hg exposure in the presence of both humidity and ammonia

Figure 6.14: QCM data – 8 h GR QCM exposed to Hg vapour concentrations ranging from 1.02 to 10.55 mg/m^3 at an operating temperature of 89℃ with and without the presence of interferent gases.

From Figure 6.14, It is observed that the QCM undergoing 8 h GR reaction period produced poor repeatability in response magnitude when exposed to Hg in the presence of interferent gases when compared to the performance of the 1 and 4 h GR QCMs (see Figures 6.12 and 6.13). The 8 h GR QCM was found to have higher response magnitude over the 1 and 4 h GR QCMs and also had the highest Hg desorption ability than all other sensors tested so far (indicated by bold font in Table 6.1). However the 8 h GR sensor's performance as Hg vapour sensor in the presence of interferent gases tested is found to be poor relative to the 1 and 4 GR sensors. It is observed that the presence of humidity produces a slight

increase in response magnitude resulting in reduced dynamic range in the sensor response magnitude between Hg concentrations (Figure 6.14b). The presence of ammonia on the other hand, is observed to produce a reduced response magnitude compared to that of Hg exposure alone as shown in Figure 6.14c.

Ammonia and humidity are well known to adsorb on gold[138,139] as well as oxides of nickel and other transition metals[349,350]. Since the GR reaction QCM electrodes are all shown to contain both Au and NiO, it is reasonable to assume that both ammonia and humidity do adsorb on these surfaces. The introduction of humidity may have produced increased response magnitude due to affinity of the molecules to NiO while no adsorption of Hg is expected on these sites. The reduction in response magnitude due to the introduction of ammonia may be due to competition for adsorption sites on the surface of the Au nanostructures between Hg and NH_3 as both are known to adsorb on Au.[78,138-140] Approximately 12 NH_3 molecules are required to adsorb on the one adsorption site where Hg would normally adsorb, for the response magnitude of the sensor to replicate that of one Hg atom since one Hg atom is ~12 times heavier than one NH_3 molecule. This however seems not to be the case as the response magnitude of the sensor is observed to reduce indicating less than 12 NH_3 molecules are adsorbed in one Hg sorption site.

6.5 Hg Diffusion Bahaviour in GR Surfaces

In order to study the diffusion behaviour of Hg in the GR QCM electrodes, SIMS depth profiling was performed on the Control nickel and the 1 h GR and 4 h GR QCM electrodes as shown in Figure 6.15. The 1 and 4 h GR QCMs were selected as they were little affected by Hg in the presence of H_2O, NH_3 and both H_2O and NH_3 mixture. The Y-axis in Figures 6.15b and Figure 6.15c are the same as that of Figure 6.15a. In this axis, the element counts normalised with that of Cs^+ ion counts have been plotted. The bottom X-axis represent the sputtering time where the measurement of the crater depth using surface profiler revealed 100 seconds refers to ~11 nm depth in the sample and is shown in the top X-axis. SIMS normalised counts of ~10^{-5} refer to no Au present on the surface as the Ni control QCM electrode underwent no GR reaction.

From the SIMS data presented in Figure 6.15, as expected, no Hg signal was observed in the Ni control substrate (Figure 6.15a). By comparing Figure 6.15b and 6.15c it was observed that the height of the Au nanostructures also increases with increasing GR reaction time. That is, for the 1 h GR reaction time electrode (Figure 6.15b), the Au signal starts to decrease following ~100 seconds of sputtering period compared to ~400 seconds for the 4 h GR reaction time (Figure 6.15c). The fact that the Ni counts is constantly increasing to the point where the Au count reaches to around 10^{-5} supports the argument that the Au

structures have grown in height. That is, although the etching rate of Ni is different to that of Au, the Cs^+ ion beam is thought to be able to sputter off increasing amount of Ni from the surface as the Au structures height decreases during sputtering. The size of the Au nanostructures was also observed to increase with increasing GR reaction time as was observed from the SEM images in Figure 6.1. These observations indicate that both size and height of the nanostructures increase with increasing GR reaction time.

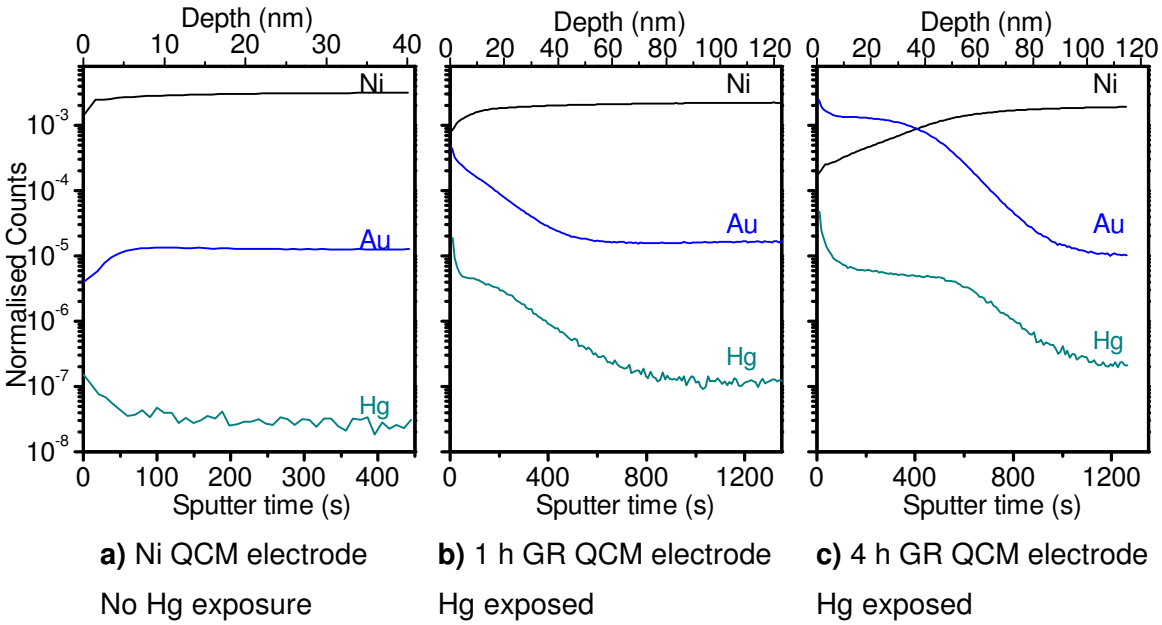

Figure 6.15: SIMS data showing lack of Hg accumulation between the Au nanostructures and Ni film. A sputter time of 100s refers to 11 nm in the X-axis.

The Hg signal is observed to follow the trend of that of Au signal indicating Hg has diffused through the gold and is available throughout the gold nanostructures (Figures 6.15b and 6.15c). It is interesting to observe that a hump was not present in the 1 and 4 h GR QCMs indicating absence of any Hg accumulation between the Au and Ni layers, as was otherwise observed in between that of 20, 30 and 40 nm Au ultra-thin films and the SiO_2 barrier layer in chapter 5. This may be due to the GR Au nanostructures having non-continuous, island type structures (similar to the 10 nm Au ultra-thin non-continuous film) rather than a continuous film (similar to the 40 nm Au ultra-thin films in Chapter 5, Figure 5.4). The non-continuous nature of the GR electrodes would potentially allow diffused Hg in the boundary layer between Ni and Au to escape from the nanostructures' surfaces and sides. This would also explain the high Hg desorption ability of the GR reaction modified Ni-Au system as evidenced by the QCM results in table 6.1. Therefore, the non-continuous and thin nature of the GR Au nanostructures makes them excellent surface for selective Hg vapour sensing in the presence of interferent gases with excellent desorption kinetics during recovery period.

6.6 Summary

It is shown for the first time that the novel choice of Ni-Au hybrid nano-structures can be grown directly on QCM substrates for Hg vapour sensing applications using galvanic replacement reactions. The Ni-Au system was chosen based on the fact Ni has a low affinity towards Hg vapour as opposed to Au which is known to readily undergo Hg sorption. This approach was used to create nanostructures containing large number of surface defects (i.e. Hg sorption sites). The thin and non-continuous nature of developed Au nanostructures was thought to lead to quicker response, large response magnitude and recovery as well as reduced Hg diffusion than thicker continuous films of Au alone. This approach was found to fulfil its purpose where higher Hg sorption and therefore sensor response magnitudes were observed when compared to the Au control QCM. Furthermore, upon the recovery phase, the GR QCMs were observed to exhibit between 93 to 100% desorption of the adsorbed amalgamated Hg compared to the Au control QCM where less than 90% regeneration was observed. The QCM sensor electrodes modified using GR reaction times of 1 h and 4 h showed small response magnitudes or sorption capacity towards Hg vapour but interestingly showed to be little affected by interferent gases (H_2O and NH_3). The QCM electrode undergoing 8 h GR reaction showed high response magnitude, sorption and desorption capacity, however was found to be affected by the presence of the interferent gases much the same as a continuous film of Au (which will be presented in Chapter 7). This indicated that the GR reaction period, otherwise the amount of Au deposited on Ni surface, influences the QCM based Hg vapour sensor's performance towards the interferent gases. SIMS data showed no accumulation of Hg at the Ni-Au boundary of these modified sensors as was otherwise the case for the evaporated thin Au films presented in chapter 5. This is thought to be the reason for the sensors high Hg desorption and lower drift during Hg sensing. The 1 and 4 h GR sensors developed in this work have great potential to be used as online Hg vapour sensors in the presence of interferent gases such as H_2O and NH_3, thus making them highly relevant to some industrial applications.

6.7 References

(1) Bansal, V.; Jani, H.; Plessis, J. D.; Coloe, P. J.; Bhargava, S. K. *Adv. Mater.* **2008**, *20*, 717-723.
(2) Bond, G. C. *Catalysis Today* **2002**, *72*, 5-9.
(3) Sun, Y.; Mayers, B. T.; Xia, Y. *Nano Lett.* **2002**, *2*, 481-485.
(4) Sun, Y.; Xia, Y. *Journal of the American Chemical Society* **2004**, *126*, 3892-3901.
(5) Liang, H. P.; Guo, Y. G.; Zhang, H. M.; Hu, J. S.; Wan, L. J.; Bai, C. L. *Chem. Commun.* **2004**, 1496-1497.
(6) Liang, H.-P.; Wan, L.-J.; Bai, C.-L.; Jiang, L. *The Journal of Physical Chemistry B* **2005**, *109*, 7795-7800.
(7) Shukla, S.; Priscilla, A.; Banerjee, M.; Bhonde, R. R.; Ghatak, J.; Satyam, P. V.; Sastry, M. *Chem. Mat.* **2005**, *17*, 5000-5005.
(8) Selvakannan, P. R.; Sastry, M. *Chem. Commun.* **2005**, 1684-1686.
(9) Viyannalage, L. T.; Vasilic, R.; Dimitrov, N. *J. Phys. Chem. C* **2007**, *111*, 4036-4041.
(10) Vasilic, R.; Dimitrov, N. *Electrochemical and Solid-State Letters* **2005**, *8*, C173-C176.
(11) Vasilic, R.; Viyannalage, L. T.; Dimitrov, N. *Journal of the Electrochemical Society* **2006**, *153*, C648-C655.
(12) Brankovic, S. R.; Wang, J. X.; Adzic, R. R. *Surface Science* **2001**, *474*, L173-L179.
(13) Mrozek, M. F.; Xie, Y.; Weaver, M. J. *Analytical Chemistry* **2001**, *73*, 5953-5960.
(14) Lipi´nski, L.; Szmyrka-Grzebyk, A.; Manuszkiewicz, H. *Measurement Science and Technology* **2000**, *11*, 738-742.
(15) Sabri, Y. M.; Ippolito, S. J.; Tardio, J.; Atanacio, A. J.; Sood, D. K.; Bhargava, S. K. *Sensors and Actuators B: Chemical* **2009**, *137*, 246-252.
(16) Cherstiouk, O.; Gavrilov, A.; Plyasova, L.; Molina, I.; Tsirlina, G.; Savinova, E. *Journal of Solid State Electrochemistry* **2008**, *12*, 497-509.
(17) Green, T. A. *Gold Bulletin* **2007**, *40*, 105-114.
(18) Inukai, J.; Sugita, S.; Itaya, K. *Journal of Electroanalytical Chemistry* **1996**, *403*, 159-168.
(19) George, M. A.; Glaunsinger, W. S. *Thin Solid Films* **1994**, *245*, 215-224.
(20) Fiermans, L.; Hoogewijs, R.; Vennik, J. *Surface Science* **1975**, *47*, 1-40.
(21) Haseeb, A. S. M. A.; Chakraborty, P.; Ahmed, I.; Caccavale, F.; Bertoncello, R. *Thin Solid Films* **1996**, *283*, 140-144.
(22) Aravinda, C. L.; Mayanna, S. M.; Bera, P.; Jayaram, V.; Sharma, A. K. *Journal of Materials Science Letters* **2002**, *21*, 205-208.
(23) Jiang, P.; Zhou, J.-J.; Li, R.; Gao, Y.; Sun, T.-L.; Zhao, X.-W.; Xiang, Y.-J. *Journal of Nanoparticle Research* **2006**, *8*, 927-934.
(24) Qian, L.; Ming, M.; Yuqing, Z. H. A. *Chinese Journal of Catalysis* **2006**, *27*, 1111-1116.
(25) George, M. A.; Glaunsinger, W. S.; Thundat, T.; Lindsay, S. M. *Journal of Microscopy* **1988**, *152*, 703-713.
(26) Jin, Y.; Dong, S. *The Journal of Physical Chemistry B* **2003**, *107*, 12902-12905.
(27) Bilic, A.; Reimers, J. R.; Hush, N. S.; Hafner, J. *The Journal of Chemical Physics* **2002**, *116*, 8981-8987.
(28) Kay, B. D.; Lykke, K. R.; Creighton, J. R.; Ward, S. J. *The Journal of Chemical Physics* **1989**, *91*, 5120-5121.
(29) Cain, S. R.; Matienzo, L. J.; Emmi, F. *The Journal of Physical Chemistry* **2002**, *94*, 4985-4990.
(30) Fox, C. G.; Alder, J. F. *Analyst* **1989**, *114*, 997-1004.
(31) Surplice, N. A.; Brearley, W. *Surface Science* **1975**, *52*, 62-74.
(32) Levlin, M.; Ikavalko, E.; Laitinen, T. *Fresenius Journal of Analytical Chemistry* **1999**, *365*, 577-586.

Chapter VII

QCM Based Hg Vapour Sensor Enhancement by Surface Modification using Gold Electrodeposition

In this chapter the novel idea of growing well adhered Au nanospikes on QCM electrodes by electrodeposition is presented. Two nanospike QCMs were tested towards Hg vapour in the presence of various interferent gases. The high response magnitude of the nanospike QCM sensor towards Hg vapour was found to be not just to the increased surface area alone but is also due to their rich (111) crystallographic orientation and the presence of nodules and other surface defects that act as Hg sorption sites. The nanospike QCM was also found to be selective towards Hg vapour in the presence of interferent gases (humidity and ammonia) and had much higher sensitivity and lower detection limits compared to that of an Au control QCM. The nanospike QCM was further tested for its long term, 50 day stability towards Hg in the presence humidity and ammonia. The long term testing was designed to simulate some of the industrial conditions. The developed nanospike based Hg vapour sensor was found to have enhanced sensitivity and selectivity towards Hg vapour in the presence of the interferent gases tested over the 50 day testing period. Moreover, a separate nanospike sensor was tested in a specially designed industrial chamber towards Hg vapour in the presence of additional interferent gases including VOCs that are known to have high affinity with Au. It was found that the nanospike QCMs maintained their selectivity towards Hg vapour. As a result, the technique to fabricate nanospike based QCMs was patented and the nanospike QCM was set aside for future onsite testing at the industry partners refineries.

7.1 Introduction

In this chapter, the electrodeposition of Au nanostructures directly on to QCM electrodes is presented in order to increase the sensitivity of the sensor towards Hg vapour by increasing the effective surface area and number of defect sites at the surface. Upon observing the diffusion and accumulation behaviour of Hg in Au ultra-thin films, it was realised that either a thin non-continuous or thick continuous type films with a large number of surface defects (or Hg sorption sites) is required (see Chapter 5). In Chapter 6, the thin and non-continuous type Au films were formed directly on Ni based QCM electrodes which successfully enhanced Hg selectivity and recovery characteristics, however they were found to have only ~27% higher sensitivity than the Au control QCM when operated at 89°C. In this chapter, a shape-controlled approach is employed to obtain increased sensitivity towards Hg vapour by the formation of thick and continuous Au films with large number of surface defect sites. The Au surface defect sites can act as Hg sorption sites[93] resulting in the enhancement of the QCM response magnitude towards Hg vapour.

Amongst the strategies for the growth of shape-controlled Au nanostructures directly onto a Au surface,[351] electrodeposition is particularly promising. It allows controlled growth by setting parameters such as applied potential, electrolyte concentrations, pH and deposition temperature, thus leading to a diversity of metal nano-architectures.[352-354] The process uses an electrical current to reduce Au^{3+} cations from the electrolyte. The Au^{3+} cations deposit on the Au electrodes of the QCM (at the cathode), while elemental Au is oxidized to Au^{3+} from the counter Au electrode (at the anode) and dissolved into the electrolyte as follows:

$$Au^{3+}_{(aq)} + 3e^- \rightarrow Au^{0}_{(s)} \quad \text{(Cathode)} \qquad \text{Equation 7.1}$$

$$Au^{0}_{(s)} \rightarrow Au^{3+}_{(aq)} + 3e^- \quad \text{(Anode)} \qquad \text{Equation 7.2}$$

Some of the structures synthesised using the electrochemical deposition of gold include gold clusters with dentritic structures, dendritic rods, nano-sheets, nano-triangles, flowerlike and pinecone-like nano-structures.[351,355-358] Additives such as Pb^{2+} ions,[359,360] Pb^{4+} ions,[351,358] I^- ions,[361] cysteine,[361-363] and poly-vinylpyrrolidone (PVP)[364,365] have been employed during electrodeposition to produce Au nanostructures with spherical, pin-like, porous, and flower-like morphologies.[360-362,365] These additives generally bind preferentially to a particular crystallographic face of the growing Au crystal, thus promoting other crystal faces to grow faster leading to shape anisotropy.

The electrodeposition of gold on a polished Au surface introduces microscopic roughness[366,367] and therefore defects,[313,342,368] while also increasing the effective surface area of the film. Therefore it is postulated that an electrodeposited nanostructures with a high

surface area and many surface defect sites will significantly improve the Hg sorption capacity of a surface, thus leading to a significantly large response magnitude than a non-modified Au surface. This is based on the findings presented in Chapter 3, Section 3.2.5 and Chapter 5, Section 5.3. Additionally, the nanoscopic roughness and the steps and defect sites introduced in Au nanostructures during electrodeposition changes the surface energy by either improving or reducing the wetting ability of the surface towards different chemicals.[367,369] Therefore the surfaces wetting ability towards Hg or water vapour may be altered, which could be particularly advantageous for sensing Hg in the presence of humidity by increasing the selectivity of Hg over humidity.

7.2 Experimental Setup

In order to modify the Au electrode based QCMs for Hg vapour sensing, electrodeposition of Au nanostructures directly onto the Au electrodes of a QCM was performed. Following a thorough literature review, it was found that Noort et al.[351,358] had electrodeposited Au dendrite nanostructures (also referred to as Au black) on Au based QCM electrodes to enhance sensitivity by increasing the Au surface area. However, as Au black does not have high thermal stability, this technique was altered to form a surface with larger nanostructures that were rigidly adhered to the surface. In order to prevent the formation of Au black, the deposition parameters were customised by using an order of magnitude lower concentration of the ions in the electrolyte and using Pb^{2+} instead of Pb^{4+} as the shape directing additive.

Prior to the electrodeposition process, optically polished AT-cut QCM substrates were first e-beam deposited with 10 nm of Ti and 100 nm of Au on both sides of the QCM (see Chapter 2, Section 2.2). The electrodeposition of Au nanostructures on the QCM electrodes was then performed in an electrolyte solution (total volume 75 mL) containing hydrogen tetrachloroaurate (III) hydrate (2.718 g L^{-1}) and lead (II) acetate (0.177 g L^{-1}) (Sigma-Aldrich, Australia). A schematic of the two electrode electrodeposition process is shown in Figure 7.1a. A potential of -2 V was applied at room temperature, between an Au-QCM crystal (cathode) and an Au foil (anode) spaced 25 mm apart, for different electrodeposition times of 15, 30, 45, 60, 90, 120 and 150 seconds. In order to study the growth of the deposited nanostructures, each deposition period was performed on a separate QCM, totalling seven electrodeposited QCMs. The potential was applied using an Agilent arbitrary waveform generator (Model 33220A) and the current was recorded using a Keithley digital multimeter (Model 2001). The 150 second deposition period provided homogeneous nanostructures resembling nanospikes type shapes (see the SEM images presented in Section 7.3.1) having the largest amount of Au nanostructures deposited on the surface while still maintaining a high Q-factor. Due to time constraints, only the 150 second

nanospike based QCM was selected to be tested towards Hg vapour. This QCM is referred to as the nanospike QCM from this point on.

The cyclic voltammetry (CV) trace for the electrolyte was later performed using a three electrode system (CH Instruments, CHI 760C) in order to study the electrochemical properties of the ions in the electrolyte and is shown in Figure 7.1b. The CV trace shows the Au oxidation and reduction regions as well as the Pb under potential deposition (UPD) regions. UPD is a phenomenon in electrodeposition that usually refers to the reduction of a metal cation at a potential less negative than the equilibrium potential for the reduction of that particular metal.[370] The CV trace provided insight into the range of currents and voltages that may be used to form the nanospike structures and confirmed that the voltage applied during the 2 electrode depositions would not have reduced Pb ions in the electrolyte solution on the QCM surface.

The customised deposition technique of the nanostructures was patented as they were found to have a unique morphology and crystallographic orientation with high selectivity towards Hg vapour in the presence of interferent gases (as will be discussed in this chapter). Furthermore, the electro-catalytic and surface enhanced Raman scattering activities of the developed nanostructures was also studied. However, this is beyond the scope of this work and these results are published elsewhere.[370,371]

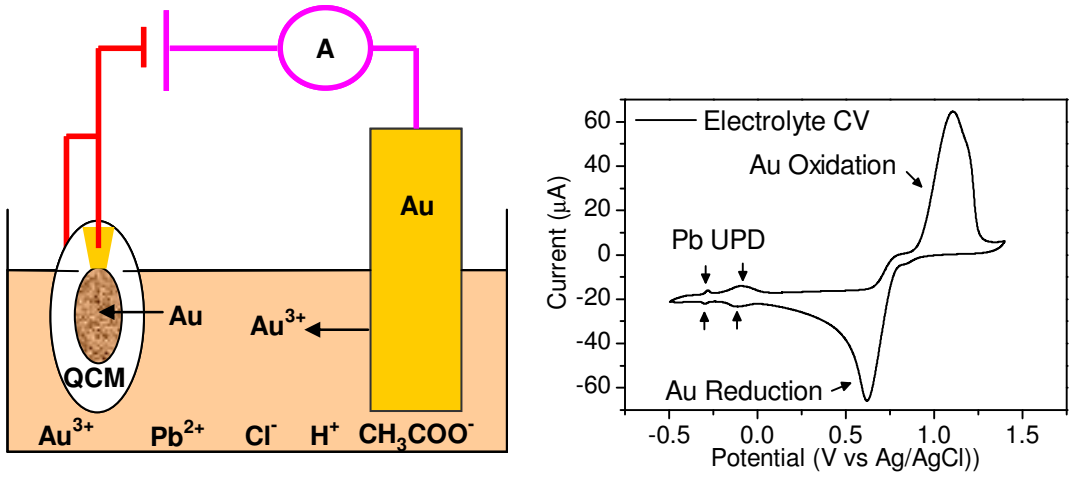

a) Electrodeposition setup **b)** Cyclic voltammeter

Figure 7.1: Electro-deposition set-up showing all the ions present in the electrolyte and the electrolyte cyclic voltammeter measurement (CV). The Pb UPD and the Au oxidation and reduction regions are indicated by arrows.

7.2.1.1 Mass of Gold Nanospikes

The mass of Au electrodeposited on the 100 nm Au film based QCM electrodes under a constant potential of -2V between the anode and the cathode for specific time points of 15 to

150 seconds was calculated using Sauerbrey's and Faraday's equations and is shown in Figure 7.2.

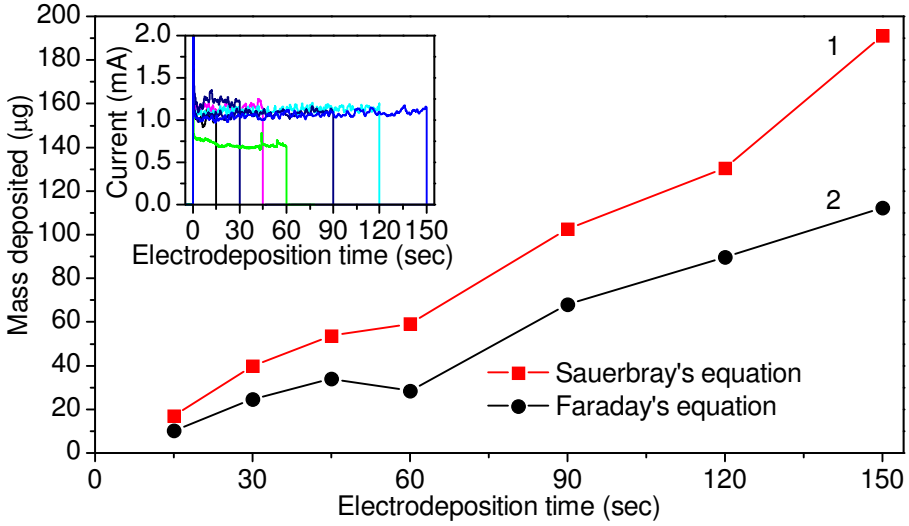

Figure 7.2: Sauerbrey's (curve 1) and Faraday's (curve 2) equation comparison of the mass deposited on the QCM gold electrodes at various electrodeposition time points. The inset shows the current curves for the different surfaces obtained during electrodeposition at -2V potential.

Curve 1 (square boxes) is the calculated mass of gold deposited on the QCM using Sauerbrey's equation. This was calculated by measuring the sensor response (in Hz) before and after electro-deposition[174,198] and using the QCM mass sensitivity of 4.39 ng.Hz^{-1}.cm^{-2}. In curve 2 (circles) the deposited gold mass was calculated electrochemically using Faraday's equation.[372] The calculation involved the integration of the current (I) versus time (t) curves shown in the inset of Figure 7.2. Although both curves 1 and 2 follow the same trend, the Sauerbrey method was consistently found to result in higher mass deposition than the values calculated by Faraday's equation. Fleming et al.[372] observed a similar trend where the Sauerbrey equation also resulted in evaluating a higher mass than Faraday's equation. Although Fleming's group compared the deposition of azurine (copper containing protein) on self assembled monolayers (SAMs) coated gold QCM electrodes using the two equations, the reasoning for the higher evaluated mass using Sauerbrey's equation may also be valid in this study. It was reasoned that the Sauerbrey relationship used to calculate the mass deposited on the QCM assumes that there is no variation in the energy dissipated at the oscillating surface and so assumes that the adsorbed layer is a thin, homogeneous layer that is rigidly attached and its motion coupled to the oscillating surface.[372,373] Other factors that produced non-mass loading perturbations in frequency signal output of the QCM sensor include high mass loading, interfacial slippage, surface roughness, surface stress, non-uniform mass distribution and ambient temperature changes.[374,375] Therefore the Sauerbrey equation would over-estimate the mass of the deposited nanostructures on the QCM.

For the purpose of this study however, it must be determined whether the total deposited mass on QCM substrate would produce a non-linear relationship between the QCM response and Hg sorption during Hg vapour sensing. That is, it is well known that Sauerbrey's equation is linear and accurate only up to total electrode mass loads of ~2% of the mass of quartz substrate.[204,210] The deposited mass of Au nanospikes on the QCM Au electrode (following 150 seconds of electrodeposition period) is estimated to be 191.1 µg (the higher mass obtained from Sauerbrey's equation) as shown in Figure 7.2. Combining this value with the mass of the 10 nm Ti adhesion layer (2.27 µg) and 100 nm Au films (97.1 µg) on both sides of the crystal, a total calculated mass of 290.47 µg (2.27 + 97.1 + 191.1 µg) is obtained. Fortunately, the total estimated mass deposited on the quartz wafers is found to be less than 386 µg (2% of mass of quartz substrate, i.e. 19.3 mg) including the original e-beamed seed layer formed (191.1 µg + 99.38 µg), which is well within the 2% margin for Sauerbrey's equation to be valid during Hg sensing (as discussed in Chapter 1, Section 1.2.6.2). Furthermore, the Q-factor of the nanospike QCM was recorded to be 7028 and was well above the acceptable value of 3000 required for oscillation to occur in the experimental setup.

7.2.1.2 Electrochemical Surface Area of Gold Nanospikes

The influence of Au film surface area on Hg sorption capacity can be realized by calculating the electrochemical surface area. The total geometric surface area of the two Au electrodes of the QCM was calculated to be ~0.32cm^2 (given that each of the two electrodes had a diameter of 4.5 mm). The electrochemical surface area was determined by calculating the charge required for reducing the monolayer of oxide as described by Rand and Woods[274]. The electrochemical/geometrical surface area ratio of the Au control film (100 nm Au-polished) was found to be ~1.5 cm^2/cm^2 as presented in Chapter 4, Section 4.3.1. Similarly, from the integration of the cyclic voltammetric response region shown in Appendix G.1, the electrochemical/geometrical surface area ratio of nanospikes was determined to be ~4.73 cm^2/cm^2 or ~3 times the Au control QCM electrode. Therefore the nanospike QCM is expected to produce at least 3 times the response magnitude than the Au control QCM when exposed towards the same Hg vapour concentration. In addition, the response magnitude is expected to be even higher because the process of electrodeposition forms rough surfaces[356,376] with a high number of nodules and other surface defects[313,342,368] which act as Hg sorption sites.[90]

7.3 Gold Nanospikes Sensitive Layer Characterisation

In this section, the secondary electron microscopy (SEM), energy-dispersive X-ray (EDX) spectroscopy and X-ray diffraction (XRD) characterisations of the electrodeposited nanostructures are presented.

7.3.1 Surface Morphology – SEM

SEM characterisation of the electrodeposited nanostructures on QCM electrodes was performed in order to determine the size and shape of the resulting nanostructures. Figure 7.3a shows the SEM image of a 100 nm Au film e-beam deposited onto a QCM substrate. The SEM image clearly indicates a relatively flat surface with well-dispersed Au clusters. Figures 7.3b through to 7.3h show the representative SEM images of Au-coated QCM crystals after subsequent electrodeposition of Au from a solution containing $AuCl_4^-$ ions in the presence of Pb^{2+} ions for (b) 15 sec, (c) 30 sec, (d) 45 sec, (e) 60 sec, (f) 90 sec, (g) 120 sec and (h) 150 sec, respectively. From the SEM images, it appears that during the initial phase of Au electrodeposition, pre-existing Au nanoclusters of the e-beam-deposited gold film (a) act as nucleation centres for the growth of Au nanoparticles (b and c), which further start growing outwardly in a network-like structure of Au nanospikes as the reaction continues for up to 60 sec (d and e). When the electrodeposition of Au is continued for 90 sec and 120 sec, the whole surface of the QCM crystal is found to be uniformly covered with well-defined Au nanospikes with prismatic tapering ends (f and g). A further increase in deposition time to 150 sec results in larger nanospikes with the appearance of sharp nodular structures (h).

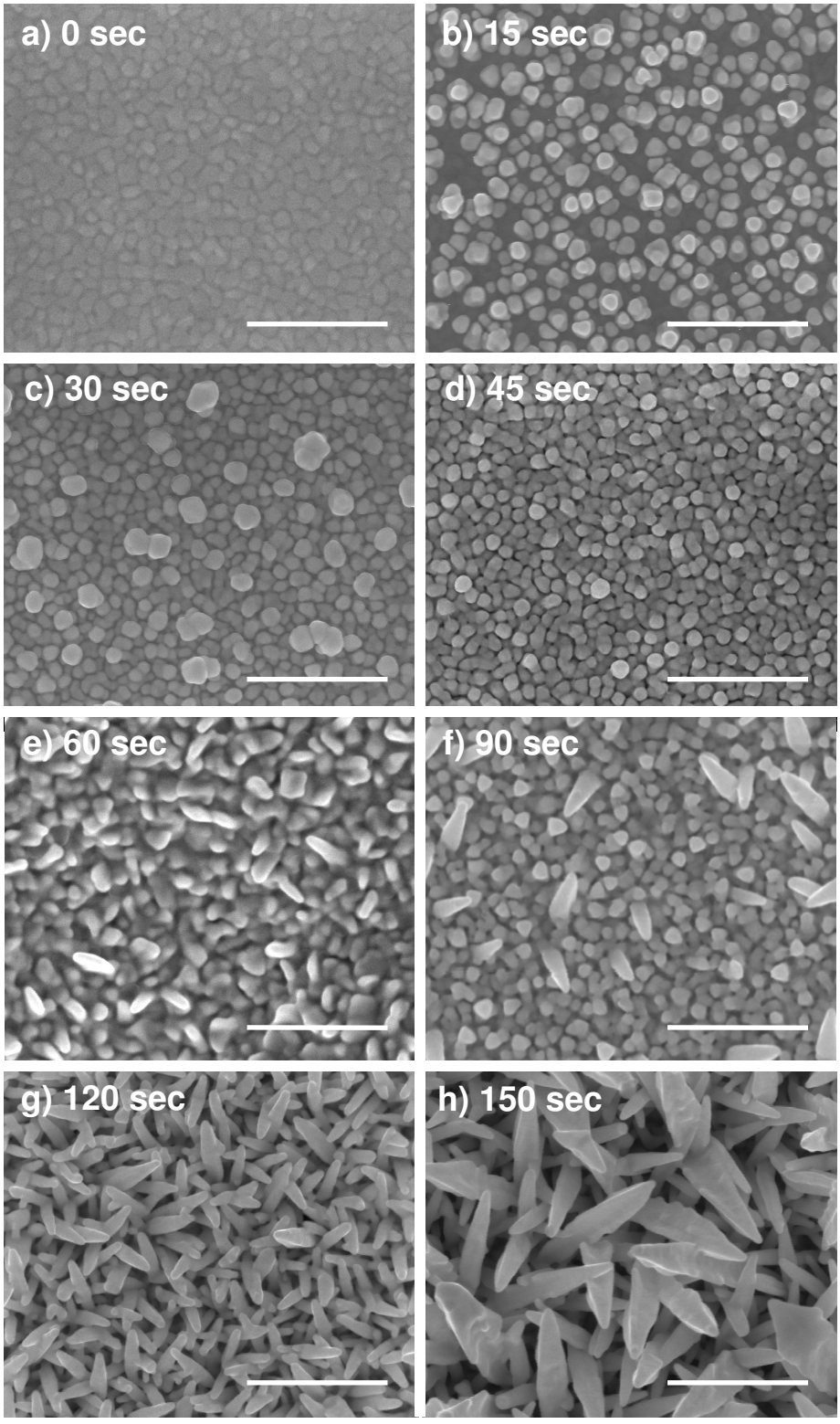

Figure 7.3: Images a) to h) represent SEM micrographs of electrodeposited gold thin films with deposition times of 0 to 150 seconds (as labelled). Scale bars represent 500nm.

Side-view SEM images of the QCM edges taken on a 40° angle indicate that the majority of nanospikes are between 0.8 to 1 µm in length with a base thickness of ~50 nm and a tip thickness of ~10 nm (Figures 7.4a and 7.4b). Notably, both faces of the QCM crystals (electrodes) showed an extremely uniform coverage of the aforementioned structures, as can be seen in a lower-magnification SEM image of the nanospikes obtained after 150 sec of electrodeposition Figure 7.4c.

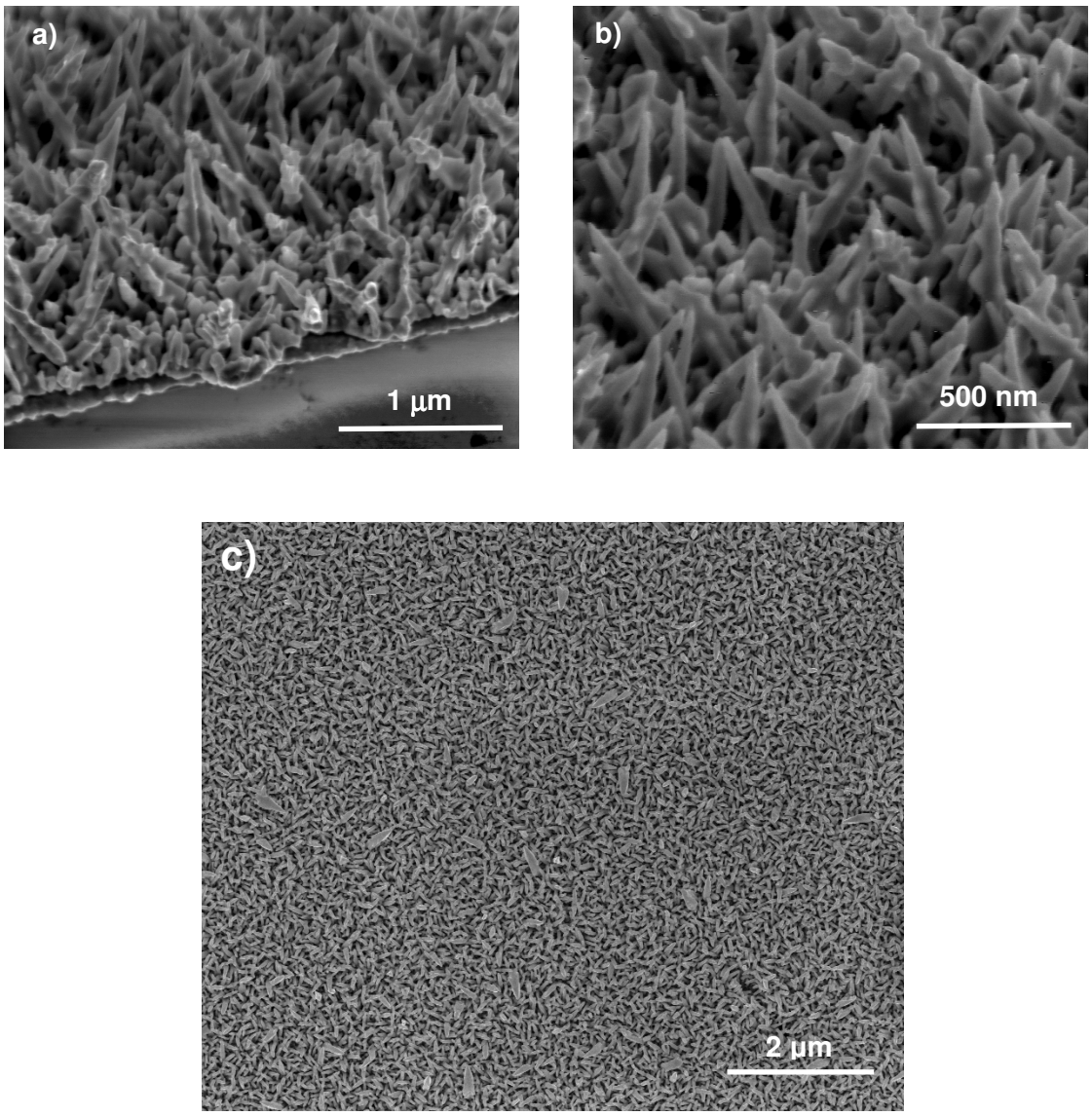

Figure 7.4: a) and b) SEM showing the dimensions of Au nanospikes in a 40° angular side-view image of a QCM edge; c) low magnification SEM image showing the extremely uniform coverage of Au nanospikes obtained after 150 sec of electrodeposition time.

7.3.1.1 Thermal Stability of the Nanospikes

Although it is extremely difficult to achieve, for most of the applications including Hg sensing in industrial streams it is important that the nanostructures are formed on a rigid substrate and are thermally and mechanically stable. For Hg vapour sensing applications a thermal stability to at least 150°C is required, as this is the minimum temperature reported to desorb

Hg from Au films.[249] Therefore the heating of a nanospike QCM was performed in order to deduce whether they are thermally stable at 150℃ for short periods of time. This is substantially higher than the normal operating temperature of 89℃ used in sensing experiments presented later in this chapter. After observing no significant morphological change following heat treatment at a temperature of 150℃ for 10 hours under nitrogen atmosphere (Figure 7.5a), the nanospike QCM was annealed at 220℃ for a further 48 hours under dry nitrogen atmosphere (Figure 7.5b). The nanospikes showed some morphology change only at the extreme condition of 220℃ for 48 hours, indicating that the nanospikes are thermally stable nano-structures, especially for Hg vapour sensing applications.

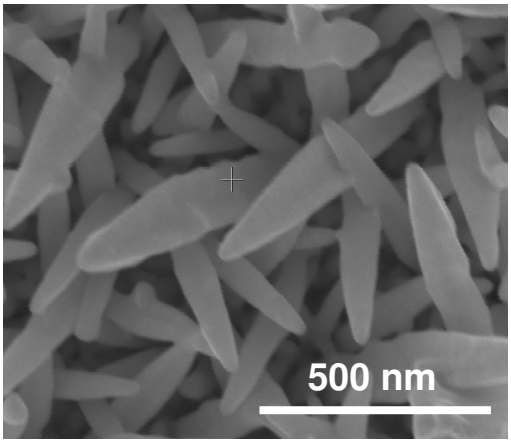

a) 150℃ for 10 hours

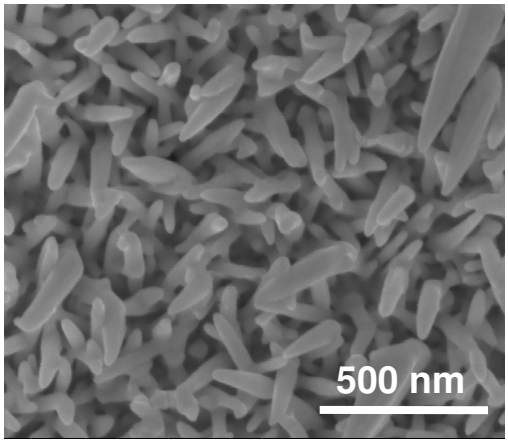

b) 220℃ for 48 hours

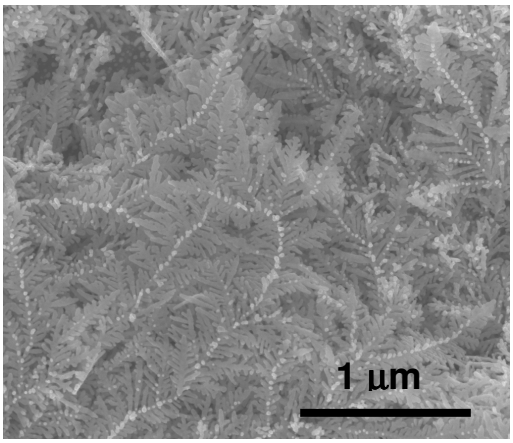

c) Before heat treatment

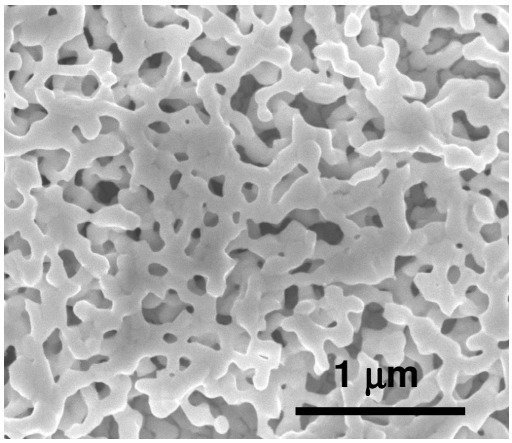

d) 150℃ for 10 hours

Figure 7.5: SEM of Au nanospikes following heat treatment at (a) 150℃ for 10 hours then (b) 220℃ for 48 hours, compared with Au dendritic structures (c) before and (d) after heat treatment at 150℃ for 10 hours.

In a similar experiment, dendritic nanowire-like structures (referred to as 'nanodentrites') were grown on gold coated quartz substrates following the method used by Noort et al.[358] and heat treated at 150℃ for 10 hours under N_2 atmosphere. The SEM images of nanodentrites before and after heat treatment are shown in Figures 7.5c and 7.5d,

respectively. It is observed that these dendrites, although reported widely as having high surface area were found to melt and undergo significant morphology change. This demonstrates their unsuitability at high temperatures (≥150℃). This also clearly demonstrates the thermal superiority of Au nanospikes over widely reported Au nanodendrites in the literature. Notably, these high surface area Au nanodendrites could not be successfully used for Hg sensing even at room temperature, because the growth of compact Au nanodendrites onto the QCM crystal significantly dampened its Q-factor, thus making it impossible for the QCM to oscillate and rendering the sensor unusable.

7.3.1.2 Adherence – Scratch Test

In another experiment, a separate nanospike QCM electrode was lightly scratched by a pair of metal tweezers as a mechanical adherence test of the nanospikes on the Au QCM electrodes (Figure 7.6). Surprisingly the nanospikes were found to have collapsed or squashed to the surface rather than detach from the surface. This was a clear demonstration of the rigid adherence of these deposited Au nanospikes on the QCM Au electrodes.

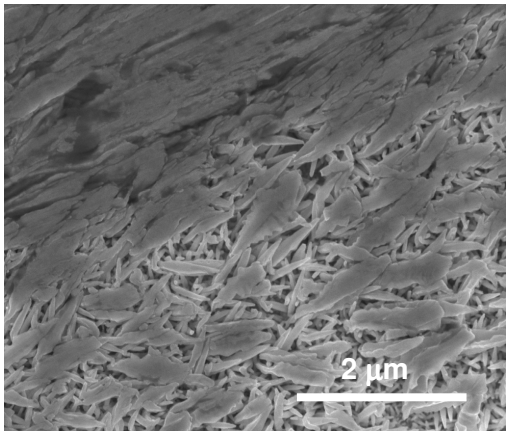

Figure 7.6: SEM image showing rigid adherence of nanospikes on the Au electrode.

7.3.2 Surface Chemical Composition – EDX

All seven electrodeposited Au nanostructure QCMs were analysed for the presence of Pb using energy-dispersive X-ray (EDX) spectroscopy since Pb^{2+} ions were employed as a shape-directing additive in the electrolyte in this study. However, the presence of Pb could not be detected in any of the electrodeposited nanostructures. For clarity purposes only the EDX measurements for the 150 sec electrodeposited nanospike QCM is shown in Figure 7.7.

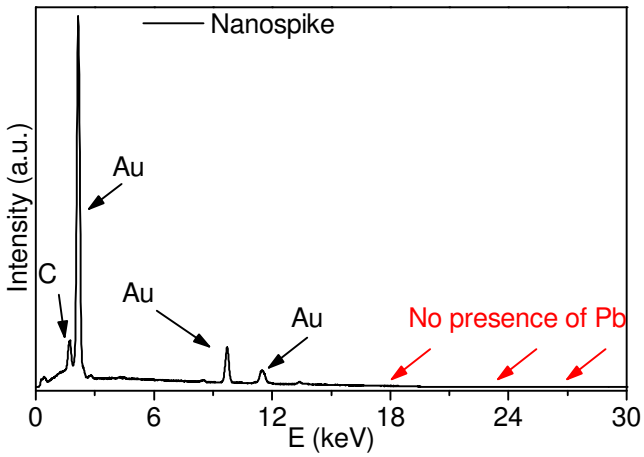

Figure 7.7: EDX spectra of the Au nanospikes, showing no observed Pb peaks.

It should be noted that Pb^{2+} ions may have been reduced in the form of Pb^{0} during the deposition process. However, any deposited Pb^{0} would most likely be galvanically oxidized back to to Pb^{2+} by the $AuCl_4^-$ ions in the electrolyte. Further confirmation of galvanic replacement reaction of Pb during electrodeposition of Au is required; however this is beyond the scope of this thesis.

7.3.3 Crystallography – XRD

In order to study the crystal orientation of the electrodeposited nanospikes, the nanospike and the Au control (100 nm e-beam deposited Au) QCM electrodes were characterised using X-ray diffraction (XRD). The XRD analysis of the electrodeposited samples reveals the preferential growth of face centred cubic (fcc) Au nanospikes along the (111) crystallographic plane as shown in Figures 7.8. It is clear from the XRD patterns that during the Au electrodeposition under the conditions employed here, a significant enhancement of the (111) peak is observed as the reaction time progresses to 150 sec. The growth of nanospikes along the (111) crystallographic plane is also evident from the intensity ratios of the (111) and (200) diffraction peaks following the different electrodeposition periods as shown in the inset of Figure 7.8. The intensity ratio of the (111) and (200) diffraction peaks following the 150 sec electrodeposition period is observed to be ~32. When compared with the standard Au JCPDS file reference (30 versus 3),[377] this is an order of magnitude enhancement in the peak ratio for the nanospikes produced after 150 sec of electrodeposition. These observations confirm that these Au nanospikes bulk are primarily dominated by (111) facets and is not the dominant exposed facet.

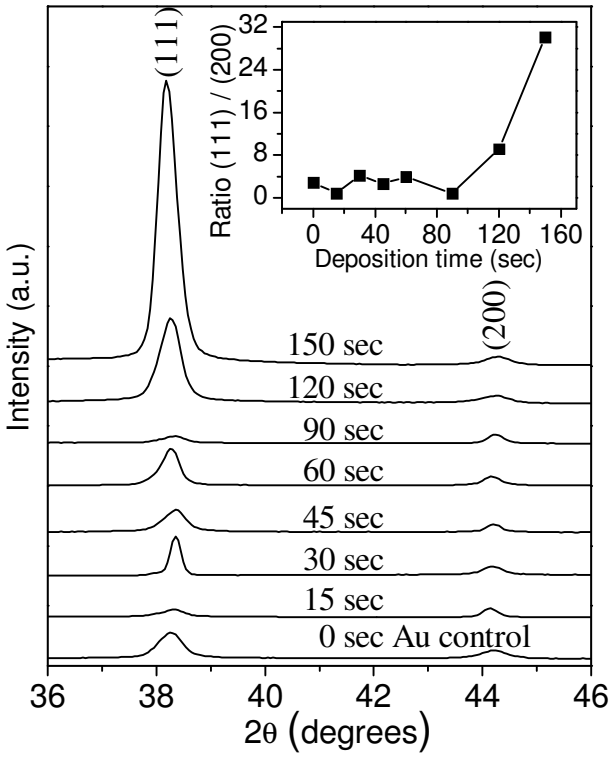

Figure 7.8: XRD patterns of 100 nm Au film e-beam deposited on to a QCM, followed by Au electrodeposition in the presence of Pb^{2+} ions for 15, 30, 45, 60, 90, 120 and 150 sec. The inset graph shows the peak intensity ratios of (111) to (200) crystal planes against deposition time, the XRD patterns for which are shown in the main figure.

The growth mechanism of (111) dominated fcc structures based on the differential binding ability of available ions and additives to different crystallographic planes, leading to preferential growth along the (111) plane, has been previously proposed.[378] In this study, it is highly possible that the preferential binding affinity of $AuCl^{4-}$ and Pb^{2+} ions to different crystallographic planes of gold plays an important role in the growth of Au nanospikes. Previous experimental and theoretical studies have suggested that Pb^{2+} ions bind preferentially to different Au crystallographic facets in the order (110) ≥ (100) > (111), with the least affinity towards the (111) crystallographic facet.[379,380] Conversely, the $AuCl^{4-}$ ions have stronger affinity towards the Au (111) facet.[378] Therefore, it is expected that under the conditions employed here, adsorption of Pb^{2+} onto Au (110) and (100) will restrict the growth along these planes, while strong electrodeposition growth will be promoted along Au (111) plane due to the strong binding affinity of $AuCl^{4-}$ ions to the (111) plane which leads to their reduction at (111) facets. It is possible that the other ions present during the reaction (chloride and acetate ions) may also play some role in determining the final morphology of Au nanostructures.[381-386] However, the amount of free chloride ions produced in situ during the electrodeposition of Au from $AuCl^{4-}$ will be very low at the $AuCl^{4-}$ concentration level used in this study.[370,387] More so, the role of these ionic impurities can be considered negligible

due to the significantly higher binding affinity of $AuCl^{4-}$ ions to Au (111) in comparison with those of other ions.[378]

7.4 Hg Sensing Performance of Nanospike Based QCM

A nanospike QCM was tested toward Hg vapour concentrations ranging from 1.02 to 10.55 mg/m^3 and operating temperatures ranging from 28 to 134°C with and without the presence of H_2O, NH_3 and their mixtures at different levels. The nanospike QCM was tested towards Hg vapour in the presence of interferent gases using the test patterns described in Chapter 2, Section 2.5. The influence of operating temperature and the presence of interferent gases on the response of the developed nanospike QCM during Hg sensing is presented in the following subsections.

7.4.1 Influence of Operating Temperature on Response Magnitude

The influence of operating temperature on QCM sensor response was studied by using the temperature profile testing sequence described in Chapter 2, Section 2.5.2. The response curves for the sensors at operating temperatures of 28 and 89°C are shown in Figures 7.9a and 7.9b, respectively. The operating temperature of 28°C is shown as it is the closest tested temperature to room temperature. In addition, 89°C was chosen as the ideal Hg vapour sensing operating temperature based on a trade-off between sensor response magnitude, recovery, dynamic range and temperature stability (see Chapter 4, Sections 4.4.2 to 4.4.5). It is also just below the temperature often used by industries when performing Hg monitoring procedures.[146]

It is evident from Figure 7.9 that at both 28°C and 89°C, the Au nanospike QCM shows significantly higher response magnitudes towards all the Hg vapour concentrations in comparison with that of the Au control QCM. For instance, the Au nanospike QCM is observed to have ~4.9 and ~2.8 times the response magnitude of the Au control QCM when exposed to 10.55 mg/m^{-3} Hg at 28°C and 89°C, respectively. As was discussed in Section 7.2.2, if Au surface area increase was the only reason for the increase in response magnitude, the increase in response magnitude of the Au nanospike QCM was expected to be ~3 times of the Au control QCM. However, the nanospike QCM showed ~4.9 times the response magnitude of the Au control QCM at 28°C, indicating that the increase in response magnitude is not due to increase in surface area alone. The microscopic roughness, steps and defect sites introduced during the electrodeposition process may have influenced surface tension and thus the wetting ability[367] of nanospikes towards Hg vapour, resulting in the sensor having a higher response magnitude than the Au control.

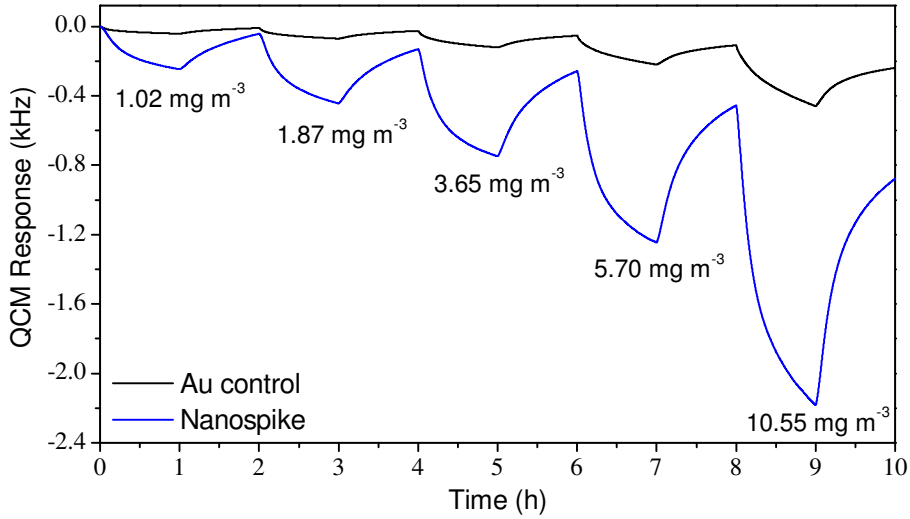

a) 28℃

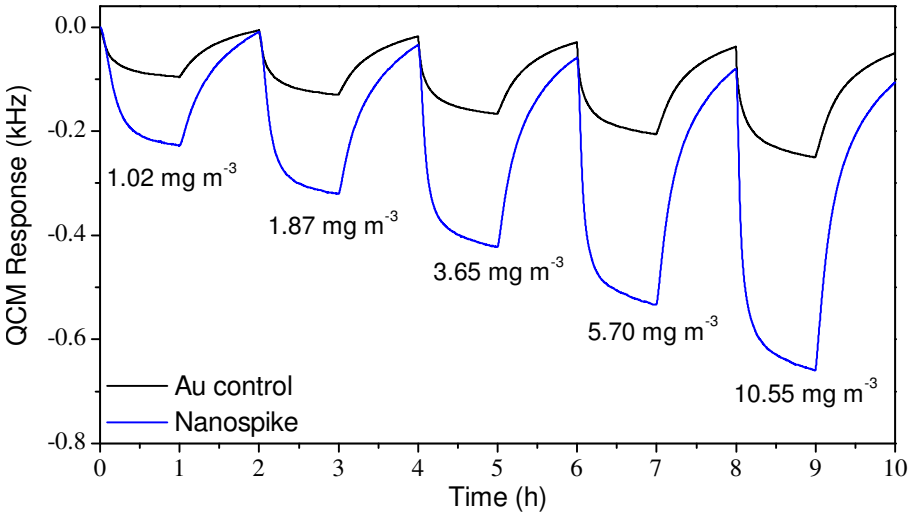

b) 89℃

Figure 7.9: Sensor response of 100 nm e-beam deposited Au film (curve 1) and electrodeposited nanospikes (curve 2) towards Hg pulse sequence, with Hg concentrations ranging from 1.02 to 10.55 mg/m^3 at operating temperatures of 28 and 89℃.

The drift, noise and response time of the nanospike QCM and Au control QCMs were also calculated at 28 and 89℃. At 28℃ both sensors had negligible noise and drift before Hg exposure, which is most likely due to the well known zero temperature coefficient and temperature stability of AT-cut quartz QCMs at around room temperature.[301] However, before Hg exposure at 89℃, the drift and noise of the Au control QCM was found to be 0.28 Hz/h and ±0.59 Hz respectively. The spikes on the other hand had similar drift but with only ±0.08 Hz noise. When operated at 89℃ and Hg concentration of 10.55mg/m^3, the nanospike QCM is observed to achieve a 90% response (t_{90}) in ~18.5 minutes; more than 10 minutes quicker then the Au control QCM. However, at 28℃ the t_{90} for the nanospike and Au control

QCMs was 40 and 49 minutes, respectively. It is therefore clear that the noise and response time of the nanospike QCM are reduced by increasing the operating temperature. However, this incurs a trade-off of reduced response magnitudes towards Hg vapour.

7.4.1.1 Temperature Profile

Figure 7.10 shows the response magnitude of the nanospikes based Hg sensor for various Hg vapour concentrations and operating temperatures (the temperature profile sequence described in Chapter 2, Section 2.5.2). The response magnitude of the Au control sensor (100 nm Au electrode based QCM) at different operating temperatures was presented in Chapter 4, Figure 4.6a. It is observed that the nanospike QCM outperformed the non-modified Au control QCM in terms of response magnitude at all operating temperatures. Furthermore, it is observed that the nanospike QCM does not have a cubic type temperature profile curve as was observed for the Au control QCM shown in Chapter 4, Figure 4.6a. The response magnitude of the nanospike QCM and dynamic range is observed to decrease with increasing operating temperature (Figure 7.10a).

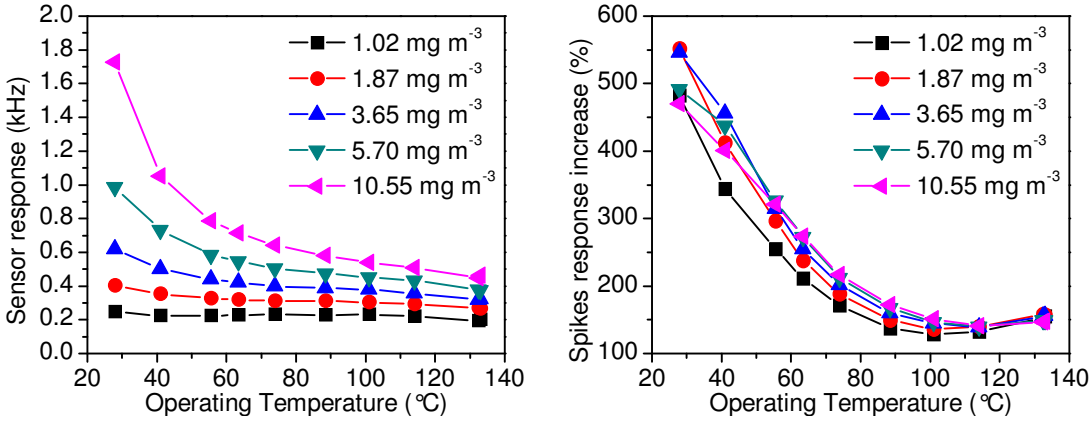

a) Nanospike temperature profile **b)** Increase in response magnitude

Figure 7.10: Temperature profile of the nanospike QCM and the increase in response magnitude of the nanospike QCM over the Au control QCM with operating temperature.

In order to compare the Hg sorption capacity of the nanospikes at different operating temperatures, the response magnitude of the nanospike QCM was compared to the Au control QCM (Figure 7.10b). It is observed that with increasing temperature, the increased response magnitude of the nanospike over the control Au QCM decreases dramatically. The highest response magnitude increase of the nanospike over the control QCM is observed at the lowest operating temperature of 28℃ and Hg concentrations of 1.87 and 3.65 mg/m^3. The change in response magnitude enhancement of the nanospike over the Au control QCM confirms that the Hg sorption capacity of the nanospikes is not only due to its higher surface area but is also dependent on morphology and operating temperature.

7.4.1.2 Sensitivity and Limit of Detection

The response magnitude of the nanospike and Au control QCMs towards the tested Hg concentrations (ranging from 1.02 to 10.55 mg/m^3) at operating temperatures of 28 and 89℃ is extracted from Figure 7.9 and presented in Figure 7.11. It is observed that the QCMs' response magnitude towards the various tested Hg vapour concentrations is more linear at 28℃ than at 89℃. In fact, when lines of best fit were drawn for each curve, the coefficient of determination (R^2 values) for the control Au was found to 0.9803 and 0.9172 at the operating temperatures of 28 and 89℃, respectively. The nanospike QCM data had R^2 values of 0.9979 and 0.9158 at 28 and 89℃, respectively. The non-linear response magnitude versus Hg concentration curves at the higher operating temperature may be attributed to the tendency of Hg vapour to remain in the gas phase rather than adsorb or amalgamate on the Au electrodes, resulting in both sensors reaching saturation.

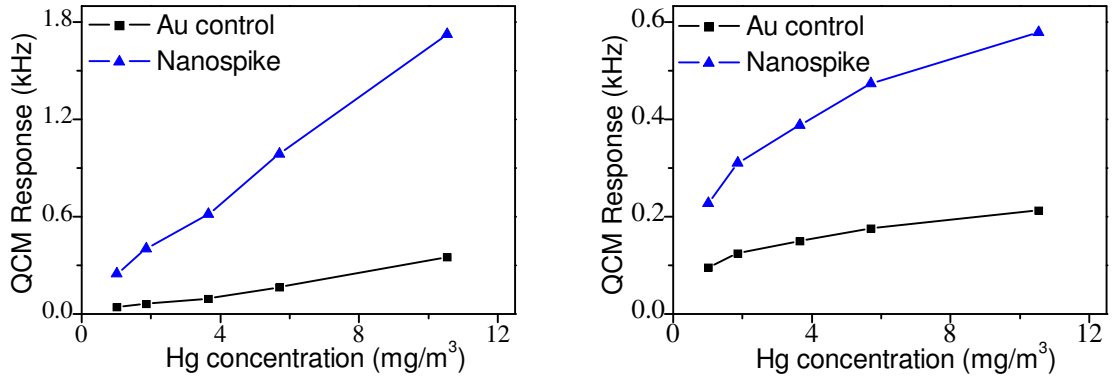

a) 28℃ **b)** 89℃

Figure 7.11: Sensor response magnitudes showing the linearity of the response magnitudes of the respective surfaces towards different concentrations of Hg vapour at operating temperatures of 28 and 89℃. Data extracted from Figure 7.9.

The sensitivity and limit of detection (LOD) of the nanospike QCM at 28 and 89℃ were calculated and compared for the two operating temperatures using the method described in Chapter 4, Section 4.4.4.2. The sensitivity of the nanospike QCM towards Hg vapour at operating temperatures of 28 and 89℃ was calculated to be 155 and 179.2 Hz/(mg/m^3), respectively. This indicates that the sensitivity of the nanospike QCM towards Hg vapour is little affected by operating at the higher operating temperatures. The limit of detection of the nanospike QCM towards Hg vapour at the operating temperature of 28℃ and 89℃ was calculated to be 0.006 and 0.316 mg/m^3, respectively. Therefore, this indicates that ~52 fold increase in LOD of the nanospike QCM is obtained by increasing the operating temperature from 28 to 89℃. Furthermore, the sensitivity of the nanospike QCM was observed to be ~5.4 and ~4.7 times the Au control QCM at 28 and 89℃, respectively.

7.4.2 Sensor Repeatability

In addition to the response magnitude, another important parameter that determines a sensor's performance is its reproducibility (precision) over a period of time. The precision of the sensors may be estimated by calculating the coefficient of variation (*COV*) , which describes the spread of the response magnitude data for a given Hg vapour concentration as shown in Equation 7.3,

$$COV = \frac{\sigma}{\bar{x}} \times 100\% \qquad \text{Equation 7.3}$$

where σ is the standard deviation and $\bar{x}$ is the mean of the sensor response magnitudes. Figure 7.12 shows the response magnitude of the nanospike and Au control QCMs over a 72 hour testing period (four repeated cycles of the sequence shown in Figure 7.9) and illustrates the stability of the nanospike over the Au control QCM during a 3 day continuous testing period at an operating temperature of 89°C. The maximum COV of the nanospike and Au control QCMs towards Hg vapour over the 3 day testing period was observed to be ~1.6 and 3.6%, respectively. This shows a good repeatability of the nanospike QCM and indicates that the precision of both sensors can be enhanced or maintained by calibrating the sensors every 3 days.

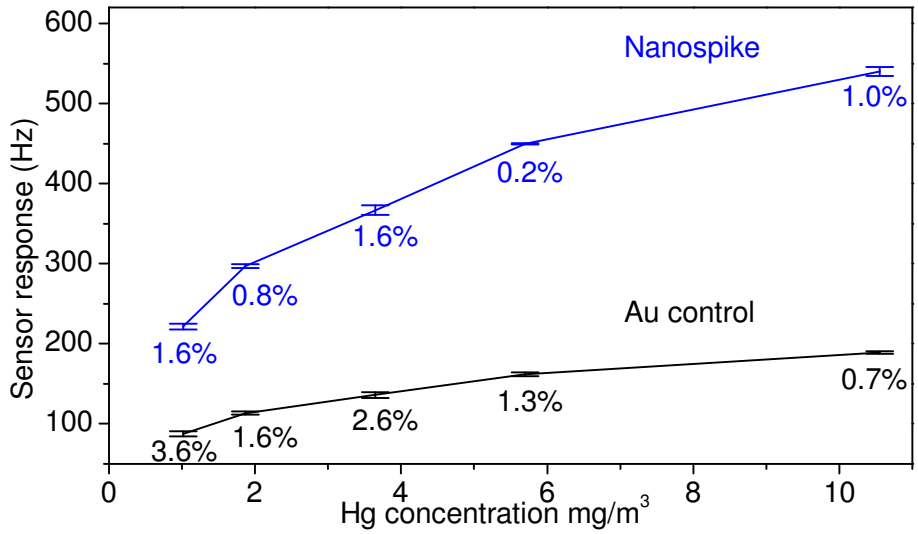

Figure 7.12: Degradation of nanospike and Au control QCMs over a 3 day testing period. The COV (in percentage, %) is shown for each Hg vapour concentration at 89°C.

It is noteworthy that the currently commercially available, highly accurate and precise, Hg vapour sensor based on gold film resistivity (Jerome 431-X) can measure Hg concentrations of up to only 0.99 mg/m^3 with a precision of ± 5 % at 0.10 mg/m^{-3} and at an operating temperature up to only 40°C.[388] This clearly shows the superiority of these nanospike based Hg vapour sensors over existing sensor technologies in high Hg vapour concentrations and temperature ranges.

7.4.3 Influence of Humidity Interference

In order to study the influence of humidity on sensor response, the nanospike and the Au control QCMs were exposed to Hg in the presence of humidity at various operating temperatures and concentrations using the pulse sequence shown in Figure 7.9. Both sensors were tested at various humidity concentrations between 0 to 10.4 g/m^3 of H_2O vapour at operating temperatures of 40, 55, 75 and 89ºC. Figures 7.13a and b show the response magnitude of the Au control and nanospike QCMs, respecitively, at the tested mercury vapour concentrations (1.02, 1.87, 3.65, 5.70 and 10.55 mg/m^3).

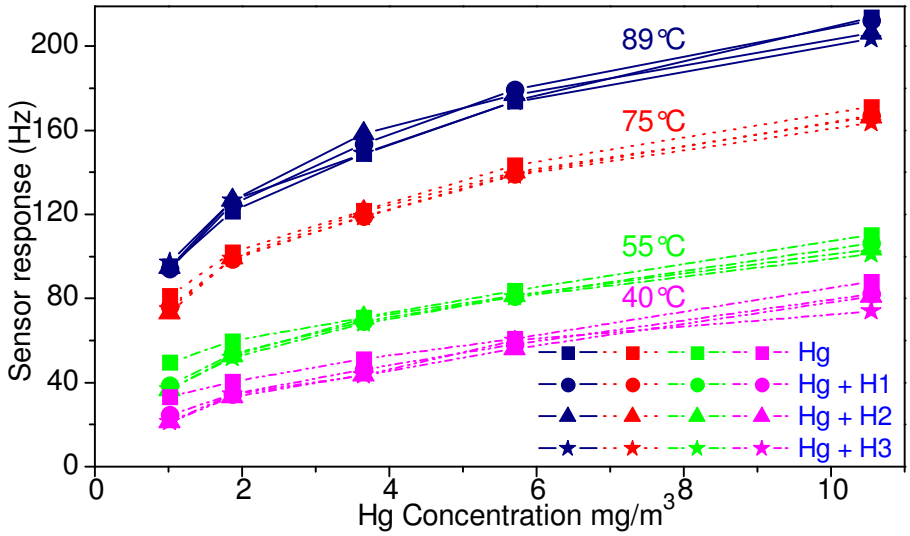

a) Au control (non-modified) QCM

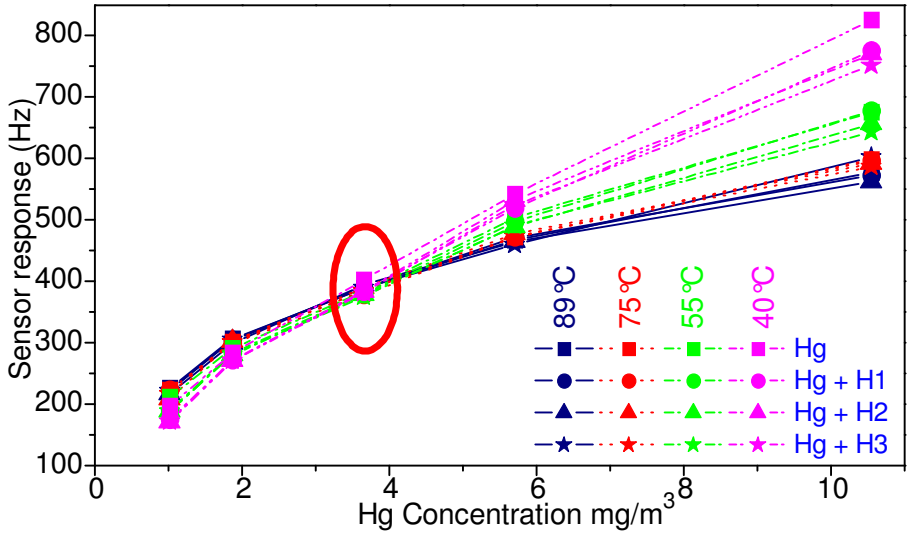

b) Nanospike (modified) QCM

Figure 7.13: Effect of humidity and temperature on Au control and the nanospike QCMs.

The nanospike QCM is shown to be only marginally affected by the changing humidity conditions at every tested operating temperature. For example, at operating temperatures of 75 and 89ºC, the response magnitude deviation of the modified QCM towards 3.65 mg/m^3 of

mercury is less than 0.3% over all the tested humidity levels for both temperatures (as indicated by the circled data). However, at Hg vapour concentration of 10.55 mg/m^3 humidity fluctuations cause approximately ±1.5, ±1.2, ±2.4 and ±3.5% variations in response magnitudes (COV) for operating temperatures of 89, 75, 55 and 40ºC, respectively. Therefore the operating temperature for minimal humidity interference over the full mercury concentration range is observed to be at 89ºC, with the trade-off being a lower response magnitude at the higher operating temperature. The results indicate that modifying the QCM surface via electrodeposition significantly reduces the effect of humidity and temperature fluctuations.

7.4.4 Influence of Ammonia Interference

The response magnitude of the Au control and nanospike QCMs towards Hg vapour in the presence of ammonia under different operating temperatures are shown in Figures 7.14. The results are highly encouraging, as varying ammonia concentrations (ranging from 847 to 2541 mg/m^3) have only a minimal effect on the final response magnitude of the nanospikes QCM. At an operating temperature of 89ºC, the variation in response magnitude for the nanospike QCM is found to be less than ±1.2% when exposed to Hg concentration of 10.55 mg/m^3 with and without the presence of ammonia interferent gas at various levels. This value is similar to the response magnitude variation observed when the nanospike QCM was exposed to Hg in the presence of humidity (see Section 7.4.3).

From the results, it is concluded that the surface morphology of the electrodeposited nanospikes may be more selective towards Hg, which effectively reduces the ability of NH_3 molecules to compete with Hg for active Au sites. Even though the Au control based QCM shows reasonable performance in the presence of ammonia, the response magnitude is considerably lower (~2.8 times), leading to a lower signal to noise (S/N) ratio. Furthermore, no operating temperature dependence is shown between 75 and 89ºC; it is observed that a temperature variation of 14℃ does not have significant effect on the precision of the nanospike QCM resulting in similar Δf values at both operating temperatures of 75 and 89℃. The nanospike QCM is observed to perform well around Hg concentration of 3.65 mg/m^3 at 89℃.

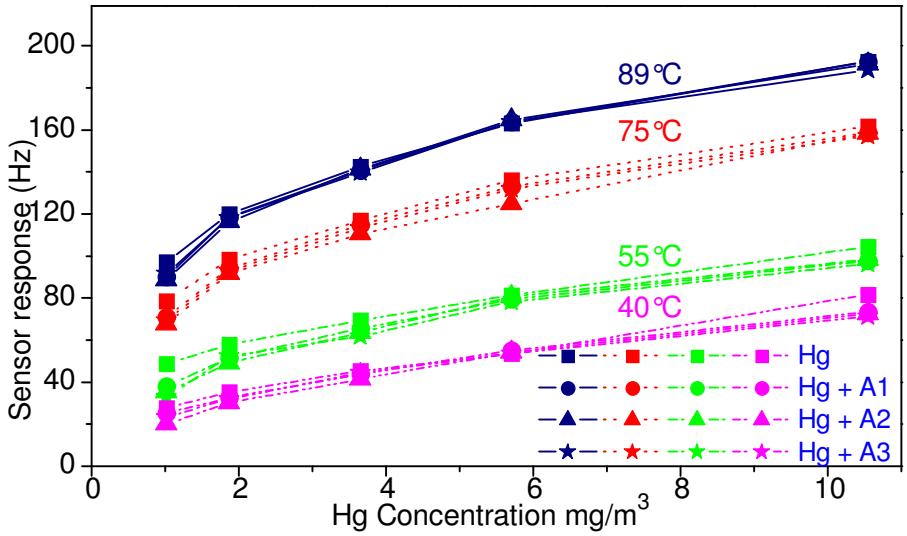

a) Au control (non-modified) QCM

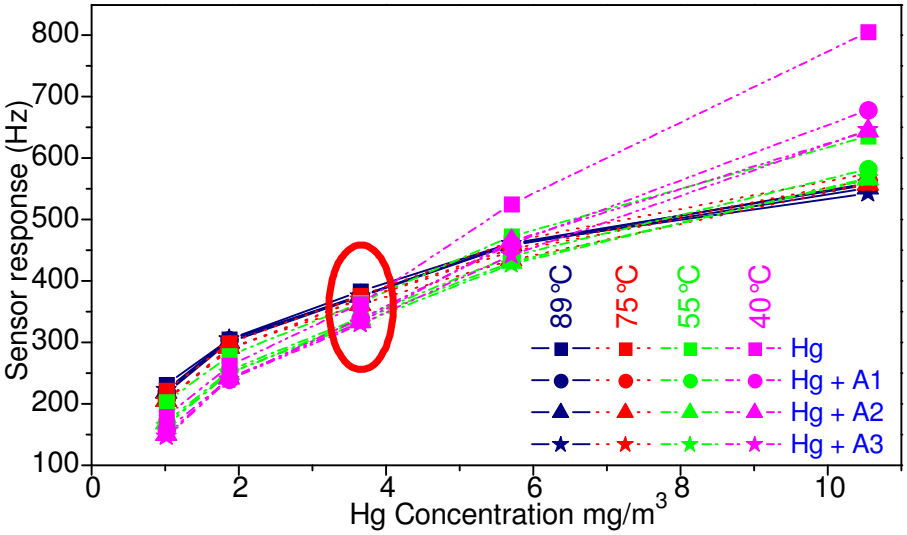

b) Nanospike (modified) QCM

Figure 7.14: Response magnitude of the Au control and nanospike QCMs towards Hg in the presence of ammonia at different operating temperatures.

7.4.5 Influence of Humidity and Ammonia Interference

To study the influence of Hg in the presence of both ammonia and humidity on sensor response magnitude, the Au control and nanospike QCMs were exposed to different levels of mixed interferent gas species at 89℃ (mix concentration levels 1 to 3, described in Chapter 2, Section 2.6.3). The effect of the presence of both ammonia (concentration range of 847 to 2541 mg/m^3) and humidity (concentration range of 4.2 to 10.4 g/m^3) at 89℃ is shown in Figure 7.15. It may be observed that the nanospike QCM has a large response magnitude, a large dynamic range between various Hg vapour concentrations and is not affected by the presence of ammonia and humidity interferent gas levels when compared to the Au control QCM. For example, the nanospike and Au control QCMs are observed to deviate by 11.4 Hz (6.8%) and 3.8 Hz (0.8%) when exposed to a Hg concentration of

5.7 mg/m^3 in the presence of mix 3 (4.2 g/m^3 H_2O and 1694 mg/m^3 NH_3). The results show the better selectivity of the nanospike QCM towards Hg in the presence of ammonia and humidity over the Au control QCM when operated at 89°C.

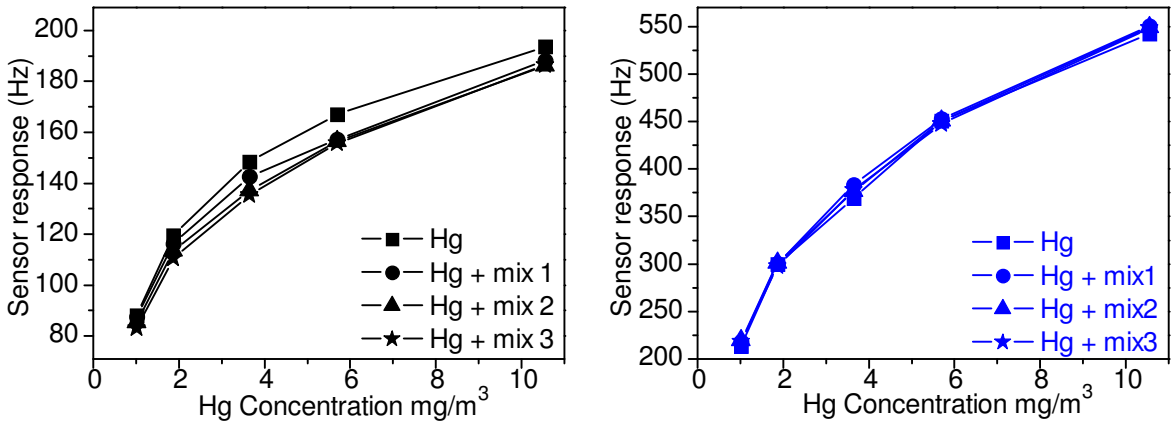

a) Au control (non-modified) QCM **b)** Nanospike (modified) QCM

Figure 7.15: Effect of ammonia and humidity (mix levels 1 to 3) on modified and non-modified QCMs.

7.5 Long Term Sensor Performance

In order to determine the long term stability of the nanospike QCM, both the Au control and nanospike QCM were tested towards Hg vapour with and without the presence of interferent gases over an additional 50 day period at 89°C. Two types of pulse sequences (described in Chapter 2, Section 2.6) were used throughout the 50 day testing period. The purpose of the first pulse sequence was to study the sensor memory, that is, the effect of previous exposures of Hg towards subsequent Hg vapour concentrations with and without the presence of interferent gases. As an example, the data gathered for the nanospike QCM from the memory effect test sequence where only the Hg concentration (x_n) was varied is shown in Figure 7.16. The operating temperature was kept constant at 89°C during the entire 50 day period. This test sequence was performed four times towards Hg vapour with and without the presence of humidity and ammonia mixture at various levels as described in Chapter 2, Section 2.5.4.

The purpose of the second pulse sequence was to study the effect on sensor memory of changing the interferent gas concentration levels while exposing constant Hg concentration pulses. Figure 7.17 shows the data gathered for the nanospike QCM at a Hg concentration of 3.65 mg/m^3 (or x_3) with the interferent gas levels being varied at every Hg pulse. This test sequence was performed 5 times for the five Hg vapour concentrations tested (ranging from 1.02 to 10.55 mg/m^3) as explained in Chapter 2, Section 2.5.5.

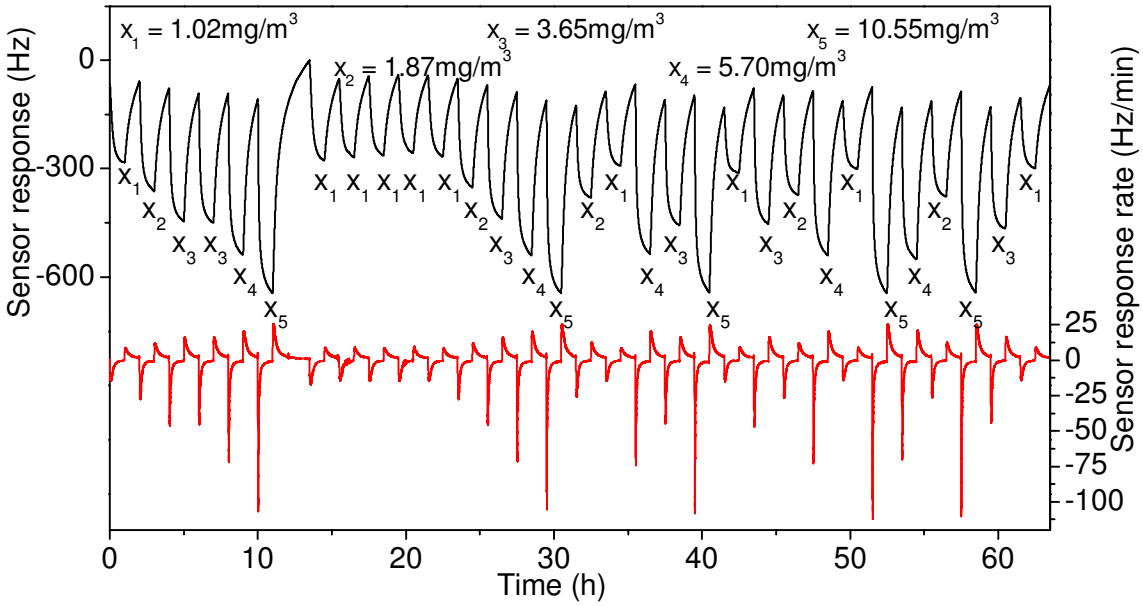

Figure 7.16: Response of the nanospike QCM during a memory effect testing sequence. The top curve (left axis) is the QCM response and the bottom curve (right axis) is the QCM response rate data.

The change in frequency (Δf) and the rate of change of the frequency ($\Delta f/\Delta t$) were calculated for each test sequence. Although not all possible permeations were undertaken, the tests were designed to acquire a spread of data which represented as many possible combinations with comparable pulses in the restricted time frame. The comparable pulses were used to gather degradation data (i.e. reduction in response magnitude versus age of the sensor) over a 50 day period.

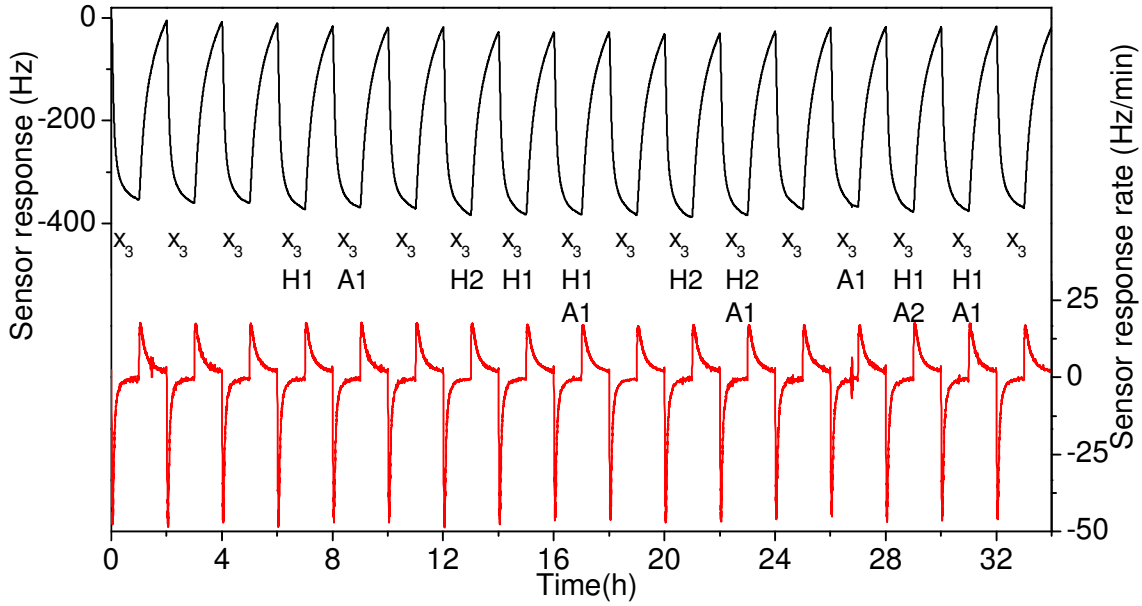

Figure 7.17: Response of nanospike QCM for x_3 Set W (x_3 = 3.65 mg/m^3 Hg).

The response magnitude and response rate data of both the Au control and nanospike QCMs for each testing procedure used are shown (as box plots) in Appendix G (Figure G.2 and G.3 and Table G.1). A summary of the performance of each sensor over the entire 50 day period is shown in Figure 7.18. The number of data points, n, for each of the five tested Hg vapour concentration ranges from 42 to 62.

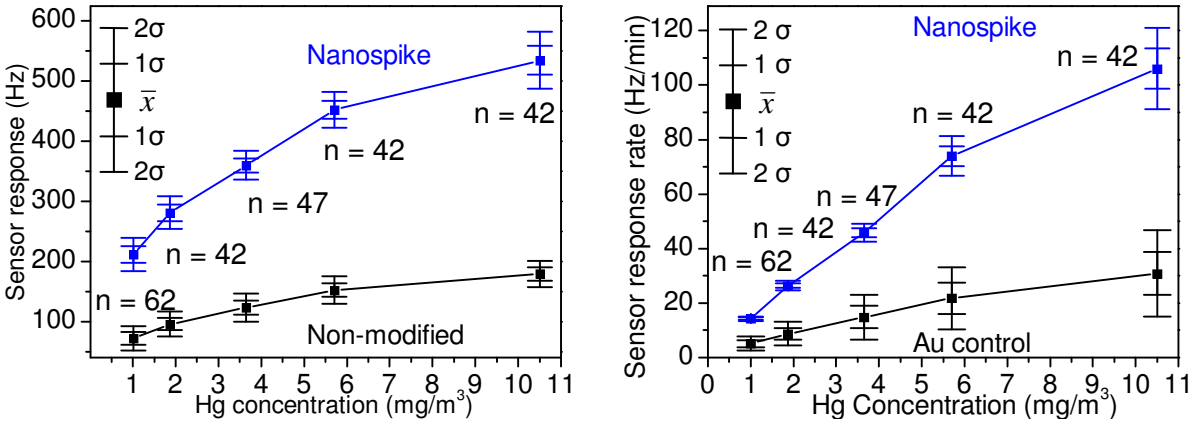

a) Statistically calculated Δf **b)** Statistically calculated $\Delta f/\Delta t$

Figure 7.18: Statistically calculated change in oscillation frequency and rate of change in oscillation frequency for both the Au control and nanospike QCMs.

Although the sensors have been through many types of different pulse sequences involving Hg exposure with and without the presence of interferent gases, their performance is observed to be exceptional throughout the 50 day testing period. What is more interesting is that the data spread in Figure 7.18 shows that the nanospike QCM significantly outperforms the Au control QCM in terms of increased response magnitude and dynamic range for both the Δf and $\Delta f/\Delta t$ data. Significant overlap in error bars for the non-modified QCM values are observed when compared to the nanospike QCM values. For example, for Au control QCM, a Δf of 90Hz could either be read as Hg concentration of 1.01, 1.87 or 3.65mg/m^3 if a certainty of 2σ is required or reported.

Furthermore, analysis of the data taken at comparable points during the course of the 50 day testing period revealed that the response magnitude of the nanospike QCM degraded approximately 9% while the non-modified degraded by up to 23.3%. This data is summarised in Table 7.1.

Table 7.1: QCM data showing response magnitude and degradation for both the Au control and nanospike QCMs tested over a 50 day period.

Day	Response of nanospike QCM to 10.5mg/m^3 of Hg	Response of Au control QCM to 10.5mg/m^3 of Hg	Degradation % of nanospikes	Degradation % of control Au
1	579.7 Hz	213.0 Hz	0.0	0.0
15	527.7 Hz	184.2 Hz	-9.0	-13.5
29	532.3 Hz	163.4 Hz	-8.2	-23.3
50	544.9 Hz	168.6 Hz	-6.0	-20.8

The response characteristics of the Au control sensor showed a considerable reduction in response magnitude with the Au control QCM having ~23% lower response magnitude for Hg on day 29 when compared to that of day 1 of the 50 day testing period. The nanospike QCM appears to be more stable with only a 6% reduction in affinity towards Hg on day 50 when compared to day 1. Therefore, the nanospike QCM seems to be extremely well suited for on-line elemental mercury sensing. The results presented are considered a critical step forward in the attempt to obtain an accurate on-line mercury sensor system capable of determining elemental mercury vapour concentrations in the presence of fluctuating temperature and humidity and ammonia concentrations, which are commonly found in alumina refinery gas streams.

7.5.1 Surface Morphology Change Following Long Term Testing

The SEM images of the two surface electrodes (Au control and nanospike QCMs) following the 50 day Hg exposure tests are shown in Figure 7.19.

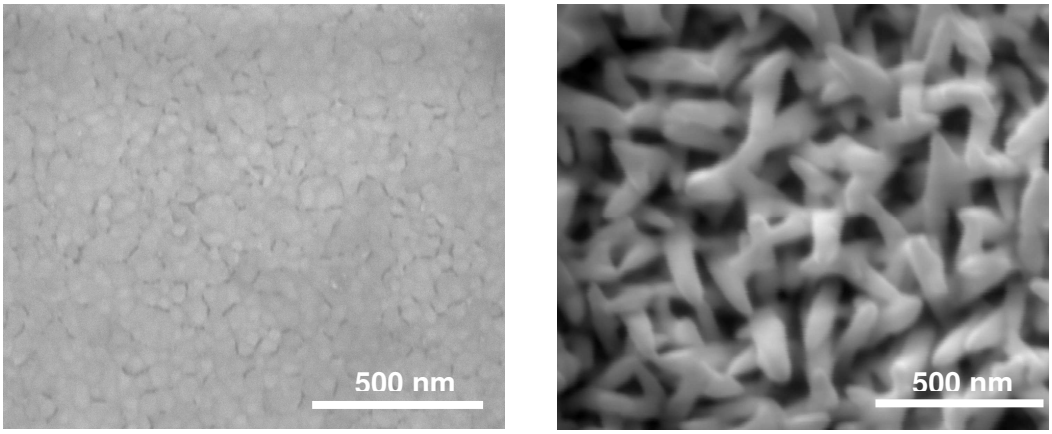

a) Au control (100 nm Au thin film) **b)** Nanospikes (modified)

Figure 7.19: SEM images of Au control and nanospike QCM electrodes following 50 day testing period towards Hg vapour with and without the presence of interferent gases.

At the conclusion of the 50 day test, the Au control surface (non-modified) is observed to have less defined boundaries between the nanoclusters (Figure 7.19a). The surface of the control QCM Au electrode before Hg exposure (Figure 7.2a) consisted of gold nanoclusters coalesced together which were separated by considerably deep grain boundaries. This also agrees with the literature[78,87,96,302] where for example Yang et al.,[302] exposed Hg to Au films at room temperature and observed that Hg exposure to Au forms amalgams which can partially fill the small grain boundaries in order to accommodate the extra Hg inside the Au film. Similarly, the Au nanospikes in Figure 7.2h are observed to be well defined with sharp edges before exposing them to Hg vapour. Although they keep their shape following mercury exposure in the presence of interferent gases over the 50 day test period (Figure 7.19b), the edges are observed to be less defined, which may be due to the etching of Au in adsorbed/amalgamated Hg and the initial exposure to higher operating temperatures during the temperature profile experiment, which was presented in Section 7.4.1.1.

7.5.2 Hg Accumulation and Sensor Lifetime

Given some assumptions, the sensor life time may be estimated. One such assumption is that the sensor lifetime is completed when all available Au on the QCM electrodes is completely converted to Au-Hg amalgam. There are many possible amalgam crystal structures that may occur in the Au-Hg system,[69] however from the Au-Hg phase diagram[389] Au_2Hg is found to be the richest in Hg content (ration of Hg to Au ~1/3 by mass) and is the most stable phase below temperatures of 122°C.[390,391] Therefore, for the purpose of calculating the nanospike QCM lifetime, it is assumed that the only amalgam that is formed between the Au nanospikes and Hg is the stable Au_2Hg amalgam. By monitoring the QCM response over the 50 day testing period using Sauerbrey's equation, it was determined that the amount of Hg per surface area on the nanospike QCM electrodes at the conclusion of the test was 3091.2 ng/cm^2. This results in 4673.9 ng of Hg when the electrochemical surface area of 1.512 cm^2 is taken into account. When taking the electrochemical surface area of the nanospikes into account, the total Hg amalgamated on the QCM Au evaluates to be 4673.9 ng. Given that there is 288.2 µg of Au on the QCM (e-beam Au seed layer and electrodeposited Au calculated in Section 7.2.1.1), the ratio of Hg to Au on the QCM electrodes would be ~1/62 given all the 4673.9 ng of amalgamated Hg is present in the film. Assuming constant accumulation of Hg by the Au films over time (Hg:Au ratio of ~1/62 per 50 days of continuous Hg testing), to reach a Hg to Au content of ~1/3 would take approximately 2.83 years, which is thus the estimated lifetime of the nanospike QCM. However, the response magnitude and Q-factor are the ultimate factors determining the usefulness of the nanospike QCM, and may reduce the sensor lifetime to much less than 2.83 years.

7.6 Preliminary Industrial Trial Testing

Due to the promising results obtained during the 50 day testing period, a separate nanospike QCM was exposed to Hg vapour in the presence of additional interferent gases using a specially designed and built industrial chamber described in Chapter 2, Section 2.1.1. The industrial chamber was used in this second phase of the project in order to meet with the HAZOP and HAZARD specifications required by the industry partners. The additional gases chosen to be tested were based on the combination of chemicals that are most commonly found in alumina refinery stacks[44,392,393] as well as those chemicals that contain functional groups which have strong interactions with Au.[136-144,261,394] The nanospike QCM was tested towards Hg in the presence of the contaminant gases listed in Table 7.2. It should be noted that the water vapour in this testing phase of the project was 23.5 g/m^3 which is higher than the humidity content present in plant streams once a 1 in 4 dilution is considered. This water vapour concentration is ~4 times more than the concentrations used for the tests conducted in Section 7.4. This high level of humidity was generated using a relative humidity generator (V-Gen from InstruQuest).

Table 7.2: Interferent gases levels in the mixture (P_i) to which the QCMs were exposed.

Interferent gas (P_i)	**Concentration**
Humidity	23.5 g/m^3
Ammonia	270 mg/m^3
Acetaldehyde	560 mg/m^3
Acetone	18 mg/m^3
DMDS	6 mg/m^3
MEK	100 mg/m^3

The response graph of the Au control and nanospike QCMs towards a Hg concentration of 1.87 mg/m^3 at an operating temperature of 90°C are shown in Figure 7.20a and 7.20b, respectively. It may be observed that although both QCMs respond relatively well to Hg in the presence of contaminant gases tested, the nanospike QCM response contains a relatively high S/N than the Au control QCM. Similar data was obtained for all Hg vapour concentrations tested (1.02, 1.87, 3.65, 5.70 and 10.55 mg/m^3).

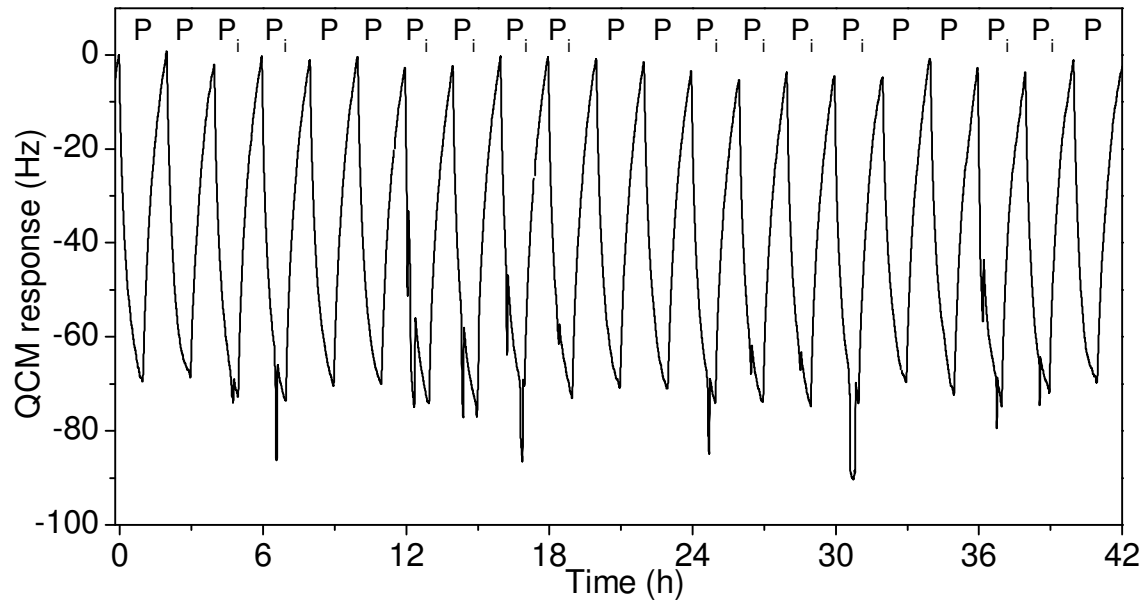

a) Au control

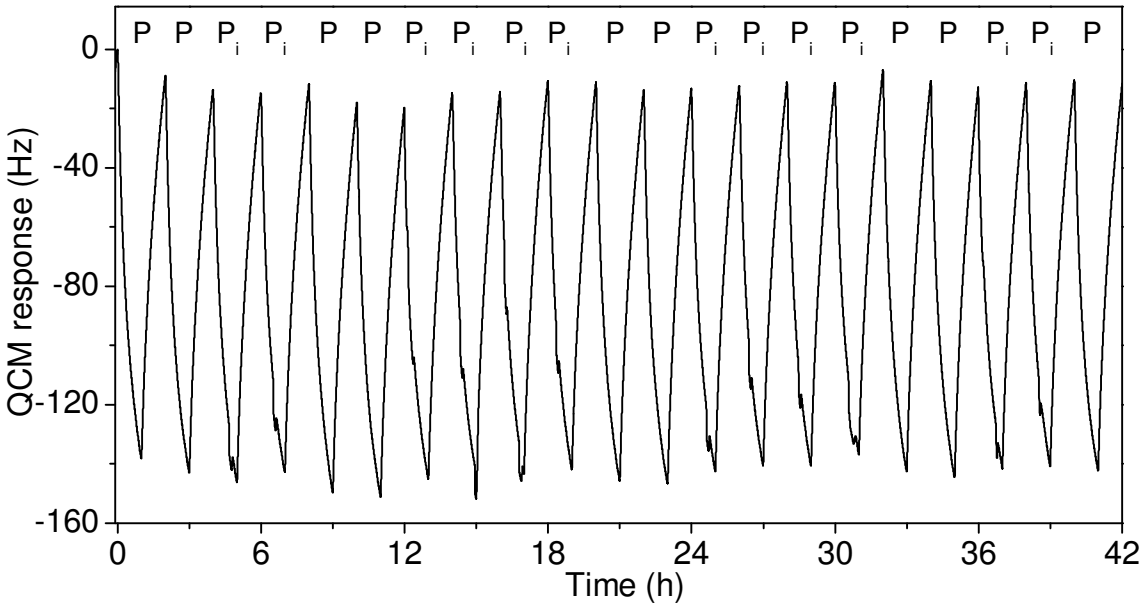

b) Nanospike

Figure 7.20: Response dynamics of Au control and Nanospike QCMs towards Hg concentration of 1.87 mg/m^3 at 89°C in the presence of contaminant gases.

A summary of the performance of both sensors towards the five Hg vapour concentrations is presented in Figure 7.21. The number of data points, n, collected for each Hg vapour concentration is also shown. It is observed that there is a high separation (dynamic range) between the response magnitudes of the different Hg vapour concentrations for the nanospike when compared to the Au control QCM. This clearly demonstrates the ability of the nanospike QCM to differentiate between the different Hg concentrations in the presence of contaminant gases. It is worth noting that the response magnitude of the nanospike QCM in the industrial chamber is lower than that observed in the laboratory chamber (see Figure

7.18a). This may be due to the different experimental parameters that were used in the preliminary industrial trial testing and the 50 day testing period (see Section 7.4 and 7.5). That is, the nanospike QCM used in the preliminary industrial trial testing was pre-treatment by heating the QCM to 170℃ for a 2 week period in a specially designed stainless steel industrial chamber that had a volume of 0.1L. The nanospike QCM presented in Section 7.4 and 7.5, however, was pre-treated at a lower temperature of 134℃ for a shorter period of time (1 day) inside a Teflon laboratory chamber that had a volume of 0.5L.

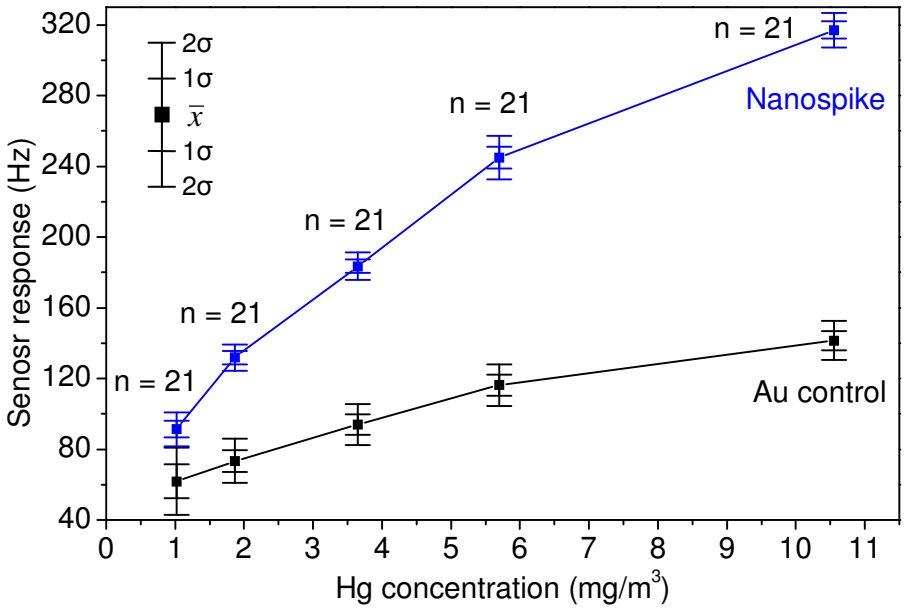

Figure 7.21: Statistically calculated change in oscillation frequency for both the Au control and nanospike QCMs. Note the significant overlap in error bars for the response magnitude values of the Au control QCM when compared to the nanospike QCM.

The sensitivity and LOD of the QCMs at 89℃ in the industrial chamber was calculated using the methods outlined in Chapter 4, Section 4.4.4.2 and is presented in Table 7.3. The COV is given as a percent figure, and represents the precision/selectivity of the sensor. The sensitivity is given as a/x_n where a is constant and x_n (where n = 1 to 5) represents Hg concentration, where n = 1, 2, 3, 4 and 5 refers to Hg vapour concentrations of 1.02, 1.87, 3.65, 5.70 and 10.55 mg/m^3, respectively.

Table 7.3: Sensitivity and detection limit of the Au control and nanospike QCMs at an operating temperature of 89℃ in laboratory and industrial testing chambers.

	Laboratory chamber			**Industrial chamber**		
Hg sensor	**Sensitivity a/x_n [Hz/(mg/m^3)]**	**Detection limit (µg/m^3)**	**CV (%)**	**Sensitivity a/x_n [Hz/(mg/m^3)]**	**Detection limit (µg/m^3)**	**CV (%)**
Au control	40.2	171	9.6	34.7	45.31	7.8
Nanospike	149.2	316	4.5	96.9	30.72	2.8

In the laboratory chamber, it was found that the Hg vapour sensitivity of the nanospike and the Au control QCMs was Hg concentration dependent; the nanospike is observed to have ~4 times the sensitivity of Au control QCM towards Hg vapour. In the industrial chamber, the nanospike QCM was observed to have better selectivity towards Hg vapour (low COV) and ~3 times the sensitivity of the Au control QCM. Although the response magnitude and sensitivity of the nanospike has reduced in the industrial chamber due to the chamber's differing size, shape and construction (shown in Chapter 2), both the Au control and nanospike QCMs are observed to attain the advantage of lower COV and LOD. This indicates that using the nanospike QCM in the industrial chamber results in better selectivity and the detection of lower Hg concentrations (down to 30.72 $\mu g/m^3$) with a 95% confidence level, as shown in Table 7.3. Overall, the nanospike Hg sensing data presented here indicates that the nanospike QCMs could be used in a plant trial as a potential online Hg vapour sensor for industrial effluent streams.

7.7 Summary

It is clearly evident from the mercury sensing studies that Au nanospikes directly electrodeposited onto a QCM sensor can act as an excellent selective Hg vapour sensor in the presence of various interferent gases. The Hg vapour sensing capability of this system at an operating temperature of 89°C towards Hg vapour in the presence of interferent gases is extremely relevant to industrial effluent streams. To the best of the Author's knowledge, no commercial sensor currently available in the market is capable of dealing with the interferent gases tested during the preliminary industrial trial testing phase of this PhD program.

The developed Au nanospikes based QCM was clearly shown to have a quick response time and large response magnitude due to the large surface area and presence of nodules and other surface defects, which act as Hg sorption sites on the QCM. The deposited Au nanospikes were observed to be highly (111) orientated, uniform and rigidly adhered to the QCM Au electrode with the deposited mass not exceeding the linear region of the Sauerbrey equation. The nanospike QCM tested in the Teflon laboratory chamber was found to outperform the Au control QCM and had ~4 times the sensitivity and ~10 minutes faster response time (t_{90}) at an operating temperature of 89°C. Although the nanospike QCM had ~5.4 times the sensitivity of the Au control QCM at 28°C, data showed that selectivity towards Hg vapour may be enhanced by operating at 89°C.

The nanospike sensor was tested towards a range of Hg vapour concentrations (1.02 to 10.55 mg/m^3) in the presence of H_2O and NH_3 interferent gases at various levels over a 50 day period at an operating temperature of 89°C. The Hg pulse sequence during the long term

testing was developed to partially simulate industrial stream conditions. Due to the trade off between response magnitude and dynamic range decreasing when operating temperature increases, the operating temperature of 89℃ was selected and kept constant during the 50 day testing period. The nanospike QCM was found to have high selectivity towards Hg vapour in the presence of humidity and ammonia with a reduction of only 6 % in response magnitude compared to the 20.8% reduction of the Au control based QCM following the 50 day testing period. Furthermore, the high dynamic range and low COV observed from the data collected over the 50 day testing period indicated that the nanospikes are highly sensitive and selective towards Hg vapour and may produce a more accurate result with high precision when calibrated prior to use. That is, although a single calibration on the first day of the 50 day testing produced excellent results with a Hg concentration reporting within ±7% with a 95% confidence interval, if a calibration was conducted every 3 days, a reading within ±1.6% would be possible.

Due to the promising results, a separate nanospike QCM sensor was fabricated and an industrial trial test was performed in the specially designed and built stainless steel chamber. The sensor was tested towards Hg vapour in the presence of ammonia, humidity and additional interferent gases that are commonly found in alumina refinery stacks as well as those which contain functional groups which have strong affinity for Au (acetaldehyde, acetone, dimethyl disulphide and methyl ethyl ketone). The nanospike QCM was observed to maintain its high response magnitude, sensitivity and dynamic range relative to the Au control based QCM. The high selectivity and sensitivity of the nanospike QCM towards Hg vapour has resulted in financial support from industrial partners to undergo a plant trail with the nanospike QCM in the near future. Furthermore, the electrodeposition conditions at which the nanospikes are formed have been patented; due to the high potential for the nanospike QCM to be used as online Hg vapour sensor (see Appendix A for patent details).
Future efforts are also directed towards the growth of Au nanospikes directly onto other sensing platforms including the surface acoustic wave (SAW) platform[99], so that sensors that detect ultra-low concentrations of chemical and biological species can be developed. These surfaces are also being investigated for (electro)-catalysis applications and as potential surface enhanced Raman scattering (SERS) substrates. The vast potential commercial implications of Au nanospikes for real-world sensing and catalysis applications cannot be overemphasized.

7.8 References

(1) Veiga, M. M.; Maxson, P. A.; Hylander, L. D. *Journal of Cleaner Production* **2006**, *14*, 436-447.
(2) Reisch, M. In *Business* 2008; Vol. 86, p 22-23.
(3) Goldman, R. L.; Shannon, M. W. *Pediatrics* **2001**, *108*, 197-205.
(4) Rong, Y.; David Tee, L.; Joo Hwa, T. *Environmental Science and Pollution Research International* **2003**, *10*, 399-407.
(5) Palomares, E.; Vilar, R.; Durrant, J. R. *Chem. Commun.* **2004**, 362-363.
(6) Laudal, D. L.; French, N. B. In *Conference On Air Quality II: Mercury* 2000; Vol. 2, p 1-16.
(7) Lockley, I. *Emission Reduction program*, 2007.
(8) Sabri, Y. M.; Ippolito, S. J.; Bhargava, S. K. *Light Metals 2009* **2009**, 37-42.
(9) Government, A.; Department of the Environment, W., Heritage and the Arts, Ed.; National Pullutant Inventory: 2009; Vol. 2007-2008.
(10) Morency, J. *Filtration & Separation* **2002**, *39*, 24-26.
(11) Germani, M. S.; Zollert, W. H. *Environmental Science & Technology* **1988**, *22*, 1079-1085.
(12) Fthenakis, V. M.; Lipfert, F. W.; Moskowitz, P. D.; Saroff, L. *Journal of Hazardous Materials* **1995**, *44*, 267-283.
(13) Dobbs, C.; Armanios, C.; McGuiness, L.; Bauer, G.; Ticehurst, P.; Lochore, J.; Irons, R.; Ryan, R.; Adamek, G. In *7th International Alumina Quality Workshop* Perth, Western Australia, 2005, p 199-204.
(14) Shao, R.; Tan, E. L.; Grimes, C. A.; Ong, K. G. *Sensors Letters* **2007**, *5*, 6.
(15) Windham, R. L. *Analytical Chemistry* **1972**, *44*, 1334-1336.
(16) Sabri, Y. M.; Ippolito, S. J.; Tardio, J.; Sood, D. K.; Bhargava, S. K.; Mullett, M.; Harrison, I.; Rosenberg, S. In *8th International Alumina Quality Workshop* Darwin, Australia, 2008, p 260-266.
(17) Caron, J. J. *Surface Acoustic Wave Continuous Emissions Monitor for Total Mercury*, Sensor Research and Development Corporation, 2001.
(18) Schweyer, M. G.; Andle, J. C.; McAllister, D. J.; Vetelino, J. F. *Sensors and Actuators B: Chemical* **1996**, *35*, 170-175.
(19) Laudal, D. L.; Thompson, J. S.; Pavlish, J. H.; Brickett, L. A.; Chu, P. *Fuel Processing Technology* **2004**, *85*, 501-511.
(20) Holmes, M.; Pavlish, J.; EERC, Ed. North Dakota, 2004; Vol. 2009.
(21) Canstein, H. V.; Kelly, S.; Li, Y.; Wagner-Dobler, I. *Applied and Environmental Microbiology* **2002**, *68*, 2829-2837.
(22) Schrope, M. *Nature news* **2001**, *409*, 124-124.
(23) Smith, R. P. *Nature* **2005**, *436*, 779-779.
(24) Stokstad, E. *Science* **2004**, *303*, 34-.
(25) Boyd, A. S.; Seger, D.; Vannucci, S.; Langley, M.; Abraham, J. L.; King, L. E. J. *Journal of the American Academy of Dermatology* **2000**, *43*, 81-90.
(26) Graeme, K. A.; Pollack, C. V. *The Journal of emergency medicine* **1998**, *16*, 45-56.
(27) Baughman, T. A. *Environmental Health Perspectives* **2006**, *114*, 147-152.
(28) Trasande, L.; Landrigan, P. J.; Schechter, C. *Environmental Health Perspectives* **2005**, *113*, 590-596.
(29) LaMontagne, A. D.; Steenland, N. K.; Kelsey, K. *Ethylene oxide*; fourth ed.; Lippincott & Wilkins: Philadelphia, 2007.
(30) Morris, T. A. PhD by Research, The University of Alabama, 2004.
(31) Laudal, D. L.; Brown, T. D.; Nott, B. R. *Fuel Processing Technology* **2000**, *65-66*, 157-165.
(32) Bergan, T.; Gallardo, L.; Rodhe, H. *Atmospheric Environment* **1999**, *33*, 1575-1585.
(33) Pacyna, E. G.; Pacyna, J. M.; Pirrone, N. *Atmospheric Environment* **2001**, *35*, 2987-2996.
(34) Kalac, P.; Niznanská, M.; Bevilaqua, D.; Stasková, I. *Science of The Total Environment* **1996**, *177*, 251-258.

(35) Mukherjee, A. B.; Melanen, M.; Ekqvist, M.; Verta, M. *The Science of The Total Environment* **2000**, *259*, 73-83.
(36) Slemr, F.; Scheel, H. E. *Atmospheric Environment* **1998**, *32*, 845-853.
(37) Shetty, S. K.; Lin, C.-J.; Streets, D. G.; Jang, C. *Atmospheric Environment* **2008**, *42*, 8674-8685.
(38) Pacyna, E. G.; Pacyna, J. M. *Water, Air, & Soil Pollution* **2002**, *137*, 149-165.
(39) Sjöholm, M.; Weibring, P.; Edner, H.; Svanberg, S. *Opt. Express* **2004**, *12*, 551-556.
(40) Swain, E. B.; Jakus, P. M.; Rice, G.; Lupi, F.; Maxson, P. A.; Pacyna, J. M.; Penn, A.; Spiegel, S. J.; Veiga, M. M. *AMBIO: A Journal of the Human Environment* **2007**, *36*, 45-61.
(41) Government, A. *Mercury & compounds Emissions - All sources: Australia*, National Pollutant Inventory, 2006-2007.
(42) Alcoa *Environmental Review and Management Program*, Alcoa, 2005.
(43) Kockman, D.; Horvat, M.; Jacimovic, R.; Gibicar, D. *RMZ - Materials and Geoenvironment* **2005**, *52*, 71-74.
(44) Mullett, M.; Tardio, J.; Bhargava, S.; Dobbs, C. *Journal of Hazardous Materials* **2007**, *144*, 274-282.
(45) Lacerda, L. D. *Water, Air, & Soil Pollution* **1997**, *97*, 247-255.
(46) Johnson, J. *Chemical and Engineering News* **2001**, *79*, 18-19.
(47) Powers, R. A. *Proceedings of the IEEE* **1995**, *83*, 687-693.
(48) Pavlish, J. H.; Sondreal, E. A.; Mann, M. D.; Olson, E. S.; Galbreath, K. C.; Laudal, D. L.; Benson, S. A. *Fuel Processing Technology* **2003**, *82*, 89-165.
(49) Camargo, J. A. *Nature* **1993**, *365*, 302-302.
(50) Hirokatsu Akagi, Y. F., Eigo Takabatake, *Photochemistry and Photobiology* **1977**, *26*, 363-370.
(51) Pak, K.-R.; Bartha, R. *Appl. Environ. Microbiol.* **1998**, *64*, 1987-1990.
(52) Bidone, E. D.; Castilhos, Z. C.; Cid de Souza, T. M.; Lacerda, L. D. *Bulletin of Environmental Contamination and Toxicology* **1997**, *59*, 194-201.
(53) Carpi, A. *Water, Air, & Soil Pollution* **1997**, *98*, 241-254.
(54) Vallee, B. L.; Ulmer, D. D. *Annual Review of Biochemistry* **1972**, *41*, 91-128.
(55) Gillis, A. A.; Miller, D. R. *The Science of The Total Environment* **2000**, *260*, 191-200.
(56) Schroeder, W. H.; Munthe, J. *Atmospheric Environment* **1998**, *32*, 809-822.
(57) Hacon, S.; Rochedo, E. R.; Campos, R.; Rosales, G.; Lacerda, L. D. *Water, Air, & Soil Pollution* **1997**, *97*, 91-105.
(58) Scallan, K. F., University of California, 2007.
(59) Levlin, M.; Ikävalko, E.; Laitinen, T. *Fresenius' Journal of Analytical Chemistry* **1999**, *365*, 577-586.
(60) Guminski, C. *Journal of the Less Common Metals* **1991**, *168*, 329-334.
(61) McNerney, J. J.; Buseck, P. R.; Hanson, R. C. *Science* **1972**, *178*, 611-612.
(62) Granite, E. J.; Pennline, H. W.; Hargis, R. A. *Industrial & Engineering Chemistry Research* **2000**, *39*, 1020-1029.
(63) Braman, R. S.; Johnson, D. L. *Environmental Science & Technology* **1974**, *8*, 996-1003.
(64) Yan, T. Y. *Industrial & Engineering Chemistry Research* **1994**, *33*, 3010-3014.
(65) Diggs, T. H.; Ledbetter, J. O. *American Industrial Hygiene Association Journal* **1983**, *44*, 606 - 608.
(66) Reed, C. E.; Kanazawa, K. K.; Kaufman, J. H. *Journal of Applied Physics* **1990**, *68*, 1993-2001.
(67) Dumarey, R.; Dams, R.; Hoste, J. *Analytical Chemistry* **1985**, *57*, 2638-2643.
(68) Schroeder, W. H.; Hamilton, M. C.; Stobart, S. R. *REV. ANALYT. CHEM.* **1985**, *8*, 179-209.
(69) Be'er, A.; Lereah, Y.; Frydman, A.; Taitelbaum, H. *Physica A: Statistical Mechanics and its Applications* **2002**, *314*, 325-330.
(70) Guminski, C.; Galus, A.; Hirayama, C. In *Solubility Data Series: Metals in Mercury*; Warsaw, U. O., Ed.; Pergamon Press: Warsaw, Poland, 1986; Vol. 25, p 258-384.
(71) Strachan, J. F.; Harris, N. L. *Journal of the Institute of Metals* **1956**, *85*, 17-24.

(72) Sunier, A. A.; Gramkee, B. E. *Journal of the American Chemical Society* **1929**, *51*, 1703-1708.
(73) Sunier, A. A.; Weiner, L. G. *Journal of the American Chemical Society* **1931**, *53*, 1714-1721.
(74) Sunier, A. A.; White, C. M. *Journal of American Chemical Society* **1930**, *52*, 1842-1850.
(75) Mees, G. *Journal of the American Chemical Society* **1938**, *60*, 870-871.
(76) Anderson, J. T. *The Journal of Physical Chemistry* **1932**, *36*, 2145-2165.
(77) Brown, J. B. *Journal of Chemical Education* **1960**, *37*, 415.
(78) Levlin, M.; Ikavalko, E.; Laitinen, T. *Fresenius Journal of Analytical Chemistry* **1999**, *365*, 577-586.
(79) Rex, M.; Hernandez, F. E.; Campiglia, A. D. *Analytical Chemistry* **2006**, *78*, 445-451.
(80) Ruys, D. P.; Andrade, J. F.; Guimaraes, O. M. *Analytica Chimica Acta* **2000**, *404*, 95-100.
(81) Battistoni, C.; Bemporad, E.; Galdikas, A.; Kaciulis, S.; Mattogno, G.; Mickevicius, S.; Olevano, V. *Applied Surface Science* **1996**, *103*, 107-111.
(82) Morris, T.; Szulczewski, G. *Langmuir* **2002**, *18*, 5823-5829.
(83) Morris, T.; Szulczewski, G. *Langmuir* **2002**, *18*, 2260-2264.
(84) Morris, T.; Sun, J.; Szulczewski, G. *Analytica Chimica Acta* **2003**, *496*, 279-287.
(85) Kobiela, T.; Nowakowski, B.; Dus, R. *Applied Surface Science* **2003**, *206*, 78-89.
(86) Nowakowski, R.; Kobiela, T.; Wolfram, Z.; Dus, R. *Applied Surface Science* **1997**, *115*, 217-231.
(87) Fialkowski, M.; Grzeszczak, P.; Nowakowski, R.; Holyst, R. *The Journal of Physical Chemistry B* **2004**, *108*, 5026-5030.
(88) Brosset, C.; Iverfeldt, Å. *Water, Air, & Soil Pollution* **1989**, *43*, 147-168.
(89) Sabri, Y. M.; Ippolito, S. J.; Tardio, J.; Atanacio, A. J.; Sood, D. K.; Bhargava, S. K. *Sensors and Actuators B: Chemical* **2009**, *137*, 246-252.
(90) George, M. A. PhD by research, Arizona State University, 1991.
(91) Aiyer, H. N.; Kawazoe, T.; Lim, J.; Echigo, Y.; Ohtsu, M. *Nanotechnology* **2001**, *12*, 368-371.
(92) Be'er, A.; Hecht, I.; Taitelbaum, H. *Physical Review E* **2005**, *72*, 031606.
(93) George, M. A.; Glaunsinger, W. S. *Thin Solid Films* **1994**, *245*, 215-224.
(94) George, M. A.; Glaunsinger, W. S.; Thundat, T.; Lindsay, S. M. *Thin Solid Films* **1990**, *189*, 59-72.
(95) Nowakowski, R.; Pielaszek, J.; Dus, R. *Applied Surface Science* **2002**, *199*, 40-51.
(96) Yang, X. M.; Tonami, K.; Nagahara, L. A.; Hashimoto, K.; Wei, Y.; Fujishima, A. *Surface Science* **1994**, *319*, L17-L22.
(97) Scheide, E. P.; Taylor, J. K. *American Industrial Hygiene Association Journal* **1975**, *36*, 897 - 901.
(98) Stobinski, L.; Dus, R. *Surface Science* **1993**, *298*, 101-106.
(99) Haskell, R. L. B.; Caron, J. J.; Duptisea, M. A.; Ouellette, J. J.; Vetelino, J. F. In *Ultrasonics Symposium, 1999. Proceedings*; IEEE: Orono, ME, 1999; Vol. 1, p 429-434 vol.1.
(100) Chaurasia, H. K.; Huizinga, A.; Voss, W. A. G. *Journal of Physics D: Applied Physics* **1975**, *8*, 214-218.
(101) Drelich, J.; White, C. L.; Xu, Z. *Environ. Sci. Technol.* **2008**, *42*, 2072-2078.
(102) Kalb, G. W. *Atomic Absorption Newsletter* **1970**, *9*, 4.
(103) Larjava, K.; Laitinen, T.; Vahlman, T.; Artmann, S.; Siemens, V.; Broekaert, J. A. C.; Klockow, D. *International journal of environmental analytical chemistry* **1992**, *49*, 73 - 85.
(104) Larjava, K.; Laitinen, T.; Kiviranta, T.; Siemens, V.; Klockow, D. *International journal of environmental analytical chemistry* **1993**, *52*, 65-73.
(105) Jansen, H. J. F.; Freeman, A. J.; Weinert, M.; Wimmer, E. *Physical Review B* **1983**, *28*, 593.
(106) Mott, N. F. *Philosophical Magazine* **1961**, *6*, 287 - 309.
(107) Dowben, P. A. *Surface Science Reports* **2000**, *40*, 151-247.

(108) Miedema, A. R.; Dorleijn, J. W. F. *Philosophical Magazine Part B: Physics of Condensed matter: Statistical Mechanics, Electronics, Optical and Magnetic Properties* **1981**, *43*, 251-272.
(109) Schmutzler, R. W.; Hensel, F. *Journal of Non-Crystalline Solids* **1972**, *8-10*, 718-721.
(110) El-Hanany, U.; Warren, W. W. *Physical Review Letters* **1975**, *34*, 1276.
(111) Even, U.; Jortner, J. *Physical Review Letters* **1972**, *28*, 31.
(112) Hensel, F. *Berichte der Bunsengesellschaft fur Physikalische Chemie* **1976**, *80*, 786-789.
(113) Cheshnovski, O.; Even, U.; Jortner, J. *Solid State Communications* **1977**, *22*, 745-748.
(114) Gaston, N.; Schwerdtfeger, P. *Physical Review B (Condensed Matter and Materials Physics)* **2006**, *74*, 024105-12.
(115) Ballone, P.; Galli, G. *Physical Review B* **1989**, *40*, 8563.
(116) Steckel, J. A. *Physical Review B (Condensed Matter and Materials Physics)* **2008**, *77*, 115412.
(117) Bloch, A. N.; Rice, S. A. *Physical Review* **1969**, *185*, 933.
(118) Kutana, A.; Giapis, K. P. *Nano Lett.* **2006**, *6*, 656-661.
(119) Chandra, S.; Di Marzo, M.; Qiao, Y. M.; Tartarini, P. *Fire Safety Journal* **1996**, *27*, 141-158.
(120) Henn, A. R. *Biophysical Chemistry* **2003**, *105*, 533-543.
(121) Lennard-Jones, J. E.; Corner, J. *Transactions of the Faraday Society* **1940**, *36*, 1156-1162.
(122) Joseph McGuire, E. L., Robert D. Sproull, *Surface and Interface Analysis* **1990**, *15*, 603-608.
(123) Rhee, S. K. *Journal of the American Ceramic Society* **1970**, *53*, 386-389.
(124) Granite, E. J. In *Annual International Pittsburgh Coal Conference* Pittsburgh, 2003; Vol. 20, p 983-1010.
(125) Abollino, O.; Giacomino, A.; Malandrino, M.; Piscionieri, G.; Mentasti, E. *Electroanalysis* **2008**, *20*, 75-83.
(126) Clevenger, W. L.; Smith, B. W.; Winefordner, J. D. *Critical Reviews in Analytical Chemistry* **1997**, *27*, 1-26.
(127) Temmerman, E.; Vandecasteele, C.; Vermeir, G.; Leyman, R.; Dams, R. *Analytica Chimica Acta* **1990**, *236*, 371-376.
(128) Sánchez Uría, J. E.; Sanz-Medel, A. *Talanta* **1998**, *47*, 509-524.
(129) Blanco, R. M.; Villanueva, M. T.; Uría, J. E. S.; Sanz-Medel, A. *Analytica Chimica Acta* **2000**, *419*, 137-144.
(130) Das, A. K.; de la Guardia, M.; Cervera, M. L. *Talanta* **2001**, *55*, 1-28.
(131) Logar, M.; Horvat, M.; Akagi, H.; Pihlar, B. *Analytical and Bioanalytical Chemistry* **2002**, *374*, 1015-1021.
(132) Tong, X.; Barat, R. B.; Poulos, A. T. *Review of Scientific Instruments* **2002**, *73*, 2392-2397.
(133) Granite, E. J.; Pennline, H. W. *Industrial & Engineering Chemistry Research* **2002**, *41*, 5470-5476.
(134) Weissberg, B. G. *Economic Geology* **1971**, *66*, 1042-1047.
(135) Sholupov, S.; Pogarev, S.; Ryzhov, V.; Mashyanov, N.; Stroganov, A. *Fuel Processing Technology* **2004**, *85*, 473-485.
(136) Rocha, T. A. P.; Gomes, M. T. S. R.; Duarte, A. C.; Oliveira, J. A. B. P. *Analytical Communication* **1998**, *35*, 415-416.
(137) Richton, R. E.; Farrow, L. A. *The Journal of Physical Chemistry* **2002**, *85*, 3577-3581.
(138) Bilic, A.; Reimers, J. R.; Hush, N. S.; Hafner, J. *The Journal of Chemical Physics* **2002**, *116*, 8981-8987.
(139) Kay, B. D.; Lykke, K. R.; Creighton, J. R.; Ward, S. J. *The Journal of Chemical Physics* **1989**, *91*, 5120-5121.
(140) Surplice, N. A.; Brearley, W. *Surface Science* **1975**, *52*, 62-74.
(141) Nuss, H.; Jansen, M. *Angewandte Chemie* **2006**, *45*, 4369-4371.
(142) de Vooys, A. C. A.; Mrozek, M. F.; Koper, M. T. M.; van Santen, R. A.; van Veen, J. A. R.; Weaver, M. J. *Electrochemistry Communications* **2001**, *3*, 293-298.

(143) Mirsky, V. M.; Vasjari, M.; Novotny, I.; Rehacek, V.; Tvarozek, V.; Wolfbeis, O. S. *Nanotechnology* **2002**, *13*, 175-178.
(144) Meyer, R.; Lemire, C.; Shaikhutdinov, S. K.; Freund, H. *Gold Bulletin* **2004**, *37*, 72-124.
(145) Caron, J. J. O., ME), Haskell, Reichl B. (Veazie, ME), Freeman, Carl J. (Rockville, MD), Vetelino, John F. (Orono, ME); Sensor Research and Development Corp. (Orono, ME): United States, 1999.
(146) Levlin, M.; Niemi, H. E. M.; Hautojärvi, P.; Ikävalko, E.; Laitinen, T. *Fresenius' Journal of Analytical Chemistry* **1996**, *355*, 2-9.
(147) Kvietkus, K.; Xiao, Z.; Lindqvist, O. *Water, Air, & Soil Pollution* **1995**, *80*, 1209-1216.
(148) Skreblin, M.; Byrne, A. R. *Vestnik Slovenskega Kemijskega Drustva* **1991**, *38*, 16.
(149) Mazzolai, B.; Mattoli, V.; Raffa, V.; Tripoli, G.; Accoto, D.; Menciassi, A.; Dario, P. *Sensors and Actuators A: Physical* **2004**, *113*, 282-287.
(150) Mazzolai, B.; Mattoli, V.; Raffa, V.; Tripoli, G.; Accoto, D.; Menciassi, A.; Dario, P. In *Sensors and Microsystems, Proceedings of the Italian Conference*; 8 ed. *Trento, Italy,*, 2003; Vol. 8, p 369-375.
(151) Morris, T.; Kloepper, K.; Wilson, S.; Szulczewski, G. *Journal of Colloid and Interface Science* **2002**, *254*, 49-55.
(152) Dimasi, E.; Tostmann, H.; Ocko, B. M.; Huber, P.; Shpyrko, O. G.; Pershan, P. S.; Deutsch, M.; Berman, L. E. In *Materials Research Society Symposium Proceedings* 2000; Vol. 590, p 183-188.
(153) Butler, M. A.; Ricco, A. J.; Baughman, R. J. *Journal of Applied Physics* **1990**, *67*, 4320-4326.
(154) Chah, S.; Yi, J.; Zare, R. N. *Sensors and Actuators B: Chemical* **2004**, *99*, 216-222.
(155) Hughes, R. C.; Ricco, A. J.; Butler, M. A.; Martin, S. J. *Science* **1991**, *254*, 74-80.
(156) Ryan, M. A.; Homer, M. L.; Shevade, A. V.; Lara, L. M.; Yen, S.-P. S.; Kisor, A. K.; Manatt, K. S. *ECS Meeting Abstracts* **2008**, *16*, 431-439.
(157) RA-915+, I.
(158) Lumex 2008.
(159) Gochfeld, M. *Ecotoxicology and Environmental Safety* **2003**, *56*, 174-179.
(160) Holland, K. New York, 2005; Vol. 2009.
(161) Ritchie, K. A.; Burke, F. J. T.; Gilmour, W. H.; Macdonald, E. B.; Dale, I. M.; Hamilton, R. M.; McGowan, D. A.; Binnie, V.; Collington, D.; Hammersley, R. *British Dental Journal* **2004**, *197*, 625-632.
(162) Kramer, C. 2001; Vol. 2008.
(163) Arizona Instruments LLC Arizona, 2007; Vol. 2009, p mercury sensors.
(164) Wu, J. M.; Huang, H. S.; Livengood, C. D. *Development of a sorbent-based technology for control of mercury in flue gas*, 1996.
(165) Loredo, J.; Soto, J.; Álvarez, R.; Ordóñez, A. *Environmental Monitoring and Assessment* **2007**, *130*, 201-214.
(166) Monitor, T. V. M. V. 2006, p Mercury sensor.
(167) Choi, H. K.; Lee, S. H.; Kim, S. S. *Fuel Processing Technology* **2009**, *90*, 107-112.
(168) Mercury Instruments USA 2009; Vol. 2009.
(169) Wängberg, I.; Edner, H.; Ferrara, R.; Lanzillotta, E.; Munthe, J.; Sommar, J.; Sjöholm, M.; Svanberg, S.; Weibring, P. *The Science of The Total Environment* **2003**, *304*, 29-41.
(170) Ferrara, R.; Mazzolai, B. *The Science of The Total Environment* **1998**, *215*, 51-57.
(171) Ippolito, S. J.; Trinchi, A.; Powell, D. A.; Wlodarski, W. In *Solid State Gas Sensing*; Comini, E., Faglia, G., Sberveglieri, G., Eds.; Springer Science+Business Media, LLC: Brescia, Italy, 2009; Vol. 1, p 329.
(172) Ballantine, D. S.; Wohltjen, H. *Analytical Chemistry* **1989**, *61*, 704A-715A.
(173) Ward, M. D.; Buttry, D. A. *Science* **1990**, *249*, 1000-1007.
(174) Sauerbrey, G. *Zeitschrift für Physik A Hadrons and Nuclei* **1959**, *155*, 206-222.
(175) Martin, S. J.; Granstaff, V. E.; Frye, G. C. *Analytical Chemistry* **1991**, *63*, 2272-2281.
(176) Kanazawa, K. K.; Gordon, J. G. *Analytical Chemistry* **1985**, *57*, 1770-1771.
(177) Martin, S. J.; Frye, G. C.; Ricco, A. J.; Senturia, S. D. *Analytical Chemistry* **1993**, *65*, 2910-2922.

(178) Dong, Y. *Sensors and Actuators B: Chemical* **2005**, *108*, 622-626.
(179) Smith, A. L.; Shirazi, H. M. *Thermochimica Acta* **2005**, *432*, 202-211.
(180) Smith, A. L.; Shirazi, H. M.; Mulligan, S. R. *Biochimica et Biophysica Acta (BBA) - Protein Structure and Molecular Enzymology* **2002**, *1594*, 150-159.
(181) Al Kobaisi, M. Doctor of Philosophy, Royal Melbourne Institue of Technology University, 2008.
(182) Janshoff, A.; Galla, H.-J.; Steinem, C. *Angewandte Chemie* **2000**, *39*, 4004-4032.
(183) Beil, F. W.; Blick, R. H.; Wixforth, A. *Physica E: Low-dimensional Systems and Nanostructures* **2004**, *21*, 1106-1110.
(184) Schweyer, M. G.; Weaver, J. T.; Andle, J. C.; McAllister, D. J.; French, L.; Vetelino, J.; Height, J. J. In *Frequency Control Symposium, 1997., Proceedings of the 1997 IEEE International* 1997, p 147-155.
(185) Venema, A.; Nieuwkoop, E.; Vellekoop, M. J.; Ghijsen, W. J.; Barendsz, A. W.; Nieuwenhuizen, M. S. *IEEE Transactions on Ultrasonics, Ferroelectrics and Frequency Control* **1987**, *34*, 148-155.
(186) Thiele, J. A.; da Cunha, M. P. *Sensors and Actuators B: Chemical* **2006**, *113*, 816-822.
(187) Arnau, A.; Ferrari, V.; Soares, D.; Perrot, H. In *Piezoelectric Transducers and Applications*; Springer Berlin Heidelberg: 2008, p 117-186.
(188) Arnau, A. *Sensors* **2008**, *8*, 370-411.
(189) O'Sullivan, C. K.; Guilbault, G. G. *Biosensors and Bioelectronics* **1999**, *14*, 663-670.
(190) James, D.; Scott, S. M.; Ali, Z.; O'Hare, W. T. *Microchimica Acta* **2005**, *149*, 1-17.
(191) Cheeke, J. D. N.; Wang, Z. *Sensors and Actuators B: Chemical* **1999**, *59*, 146-153.
(192) Khlebarov, Z. P.; Stoyanova, A. I.; Topalova, D. I. *Sensors and Actuators B: Chemical* **1992**, *8*, 33-40.
(193) Fox, C. G.; Alderm, J. F. *Analyst* **1989**, *114*, 997-1004.
(194) Ali, Z. *Journal of thermal analysis and calorimetry* **1999**, *55*, 397-412.
(195) Tsionsky, V.; Gileadi, E. *Langmuir* **1994**, *10*, 2830-2835.
(196) Flitti, F.; Far, A.; Guo, B.; Bermak, A. *Journal of Sensors* **2008**, *2008*, 1-6.
(197) Buck, R. P.; Lindner, E.; Kutner, W.; Inzelt, G. *Pure & Applied Chemistry* **2004**, *76*, 1139-1160.
(198) Zimmermann, B.; Lucklum, R.; Hauptmann, P.; Rabe, J.; Büttgenbach, S. *Sensors and Actuators B: Chemical* **2001**, *76*, 47-57.
(199) Sagmeister, B. P.; Graz, I. M.; Schwödiauer, R.; Gruber, H.; Bauer, S. *Biosensors and Bioelectronics* **2009**, *24*, 2643-2648.
(200) Bender, J. W.; Krim, J. In *Microscale Diagnostic Techniques* 2005, p 227-259.
(201) Herrmann, F.; Jakoby, B.; Rabe, J.; Büttgenbach, S. *Sensors Update* **2001**, *9*, 105-160.
(202) Ballato, A.; Gualtieri, J. G. *Ultrasonics, Ferroelectrics and Frequency Control, IEEE Transactions on* **1994**, *41*, 834-844.
(203) Lakin, K. M.; Wang, J. S. *Applied Physics Letters* **1981**, *38*, 125-127.
(204) Granstaff, V. E.; Martin, S. J. *Journal of Applied Physics* **1994**, *75*, 1319-1329.
(205) Behling, C.; Lucklum, R.; Hauptmann, P. *Sensors and Actuators A: Physical* **1997**, *61*, 260-266.
(206) Thanner, H.; Krempl, P.; Selic, R.; Wallnöfer, W.; Worsch, P. *Journal of Thermal Analysis and Calorimetry* **2003**, *71*, 53-59.
(207) Bechmann, R. *Journal of Scientific Instruments* **1952**, *29*, 73-76.
(208) Shockley, W.; Curran, D. R.; Koneval, D. J. *The Journal of the Acoustical Society of America* **1967**, *41*, 981-993.
(209) Behling, C.; Lucklum, R.; Hauptmann, P. *Sensors and Actuators A: Physical* **1998**, *68*, 388-398.
(210) Mecea, V. M. *Sensors and Actuators A: Physical* **1994**, *40*, 1-27.
(211) Lu, C.-S.; Lewis, O. *Journal of Applied Physics* **1972**, *43*, 4385-4390.
(212) Ippolito, S. J. PhD by research, RMIT university, 2006.
(213) Ho, M. H.; Guilbault, G. G.; Scheide, E. P. *Analytica Chimica Acta* **1981**, *130*, 141-147.
(214) Konash, P. L.; Bastiaans, G. J. *Analytical Chemistry* **1980**, *52*, 1929-1931.

(215) Grate, J. W.; Martin, S. J.; White, R. M. *Analytical Chemistry* **1993**, *65*, 987A-996A.
(216) Benes, E.; Gröschl, M.; Burger, W.; Schmid, M. *Sensors and Actuators A: Physical* **1995**, *48*, 1-21.
(217) Auge, J., University of Magdeburg, 1995.
(218) Janata, J.; Josowicz, M.; DeVaney, D. M. *Analytical Chemistry* **1994**, *66*, 207-228.
(219) Bethea, T.; Cady-Sawyer, K.; Ettenson, L.; Harris, K.; Mandl, D.; Martynowicz, K.; Raeisghasem, A.; Westman, D. Columbia, USA, 2005.
(220) Fox, B. S.; Mason, K. J.; McElroy, F. C. *Journal of ASTM International (JAI)* **2005**, *2*, 11.
(221) Meischen, S. J.; VanPelt, V. J.; Zarate, E. A. In *95th Proceedings of the Air & Waste Management Association's Annual Conference & Exhibition* 2002, p 1364-1378.
(222) Magnuson, J. K.; Anderson, T. N.; Lucht, R. P.; Vijayasarathy, U. A.; Kalyan, A. In *23rd Proceedings - Annual International Pittsburgh Coal Conference (2006)* Pittsburgh, 2006; Vol. 14, p 1-14.
(223) Appel, D.; Grassi, J. H.; Kita, D.; Socha, J. United States, 2008.
(224) Raffa, V.; Mazzolai, B.; Mattoli, V.; Mondini, A.; Dario, P. *Sensors and Actuators B: Chemical* **2006**, *114*, 513-521.
(225) McNerney, J. J.; Buseck, P. R. *Gold Bulletin* **1973**, *6*, 106-107.
(226) Jerome411X.
(227) Shevade, A.; Blanco, M.; Goddard, W.; Ryan, M.; Homer, M.; Taylor, C.; Jewell, A.; Kisor, A.; Yen, S.-P.; Manatt, K.; Zhou, H.; Pelletier, C.; Lewis, C. *ECS Meeting Abstracts* **2006**, *601*, 1243-1243.
(228) Ryan, M. A.; Homer, M. L.; Zhou, H.; Mannat, K.; Manfreda, A.; Kisor, A. K.; Shevade, A. V.; Yen, S.-P. S. In *International Conference on Environmental Systems*; Jet Propulsion Laboratory, National Aeronautics and Space Administration: Rome, Italy, 2005, p 1-8.
(229) Ryan, M. A.; Shevade, A. V.; Zhou, H.; Homer, M. L. *MRS Bulletin* **2004**, *29*, 714.
(230) Huang, S. W.; Neoh, K. G.; Shih, C. W.; Lim, D. S.; Kang, E. T.; Han, H. S.; Tan, K. L. *Synthetic Metals* **1998**, *96*, 117-122.
(231) Choudary, B. M.; Madhi, S.; Chowdari, N. S.; Kantam, M. L.; Sreedhar, B. *Journal of the American Chemical Society* **2002**, *124*, 14127-14136.
(232) Weibring, P.; Andersson, M.; Edner, H.; Svanberg, S. *Applied Physics B: Lasers and Optics* **1998**, *66*, 383-388.
(233) Edner, H.; Ragnarson, P.; Wallinder, E. *Environmental Science & Technology* **2002**, *29*, 330-337.
(234) Toth, J. J.; Wittman, R.; Schenter, R. E.; Cooper, J. A. *Nuclear Instruments and Methods in Physics Research Section A: Accelerators, Spectrometers, Detectors and Associated Equipment* **2007**, *572*, 1102-1105.
(235) D'ottone, L. K. B., FL, US) United States, 2006.
(236) Adams, J. D.; Rogers, B.; Manning, L.; Hu, Z.; Thundat, T.; Cavazos, H.; Minne, S. C. *Sensors and Actuators A: Physical* **2005**, *121*, 457-461.
(237) Thundat, T.; Wachter, E. A.; Sharp, S. L.; Warmack, R. J. *Applied Physics Letters* **1995**, *66*, 1695-1697.
(238) Fadel, L.; Dufour, I.; Lochon, F.; Francais, O. *Sensors and Actuators B: Chemical* **2004**, *102*, 73-77.
(239) Hu, Z.; Thundat, T.; Warmack, R. J. *Journal of Applied Physics* **2001**, *90*, 427-431.
(240) Berger, R.; Delamarche, E.; Lang, H. P.; Gerber, C.; Gimzewski, J. K.; Meyer, E.; Güntherodt, H. J. *Applied Physics A: Materials Science & Processing* **1998**, *66*, S55-S59.
(241) Marie, R.; Jensenius, H.; Thaysen, J.; Christensen, C. B.; Boisen, A. *Ultramicroscopy* **2002**, *91*, 29-36.
(242) Butler, M. A.; Ricco, A. J. *Applied Physics Letters* **1988**, *53*, 1471-1473.
(243) Manganiello, L.; Rios, A.; Valcarcel, M. *Analytical Chemistry* **2002**, *74*, 921-925.
(244) Yao, S.; Tan, S.; Nie, L. *Fenxi Huaxue* **1986**, *14*, 6.
(245) Casilli, S.; Malitesta, C.; Conoci, S.; Petralia, S.; Sortino, S.; Valli, L. *Biosensors and Bioelectronics* **2004**, *20*, 1190-1195.

(246) Rogers, B.; Bauer, C. A.; Adams, J. D. *Micro-Electro-Mechanical Systems* **2003**, *5*, 663-666.
(247) Gomes, M. T. S. R.; Oliveira, M. O.; Oliveira, J. A. B. P. *Langmuir* **1999**, *15*, 8780-8782.
(248) Bristow, Q. *Journal of Geochemical Exploration* **1972**, *1*, 55-76.
(249) Scheide, E. P.; Taylor, J. K. *Environ. Sci. Technol.* **1974**, *8*, 1097-1099.
(250) Scheide, E. P. *Physics Teacher* **1977**, *15*, 47-51.
(251) McCammon, C. S. J.; Woodfin, J. W. *American Industrial Hygiene Association Journal* **1977**, *38*, 378-386.
(252) Scheide, E. P.; Warnar, R. B. *American Industrial Hygiene Association Journal* **1978**, *39*, 745-749.
(253) Mogilevski, A. N.; Mayorov, A. D.; Stroganova, N. S.; Stavrovski, D. B.; Galkina, I. P.; Spassov, L.; Mihailov, D.; Zaharieva, R. *Sensors and Actuators A: Physical* **1991**, *28*, 35-39.
(254) Spassov, L.; Yankov, D. Y.; Mogilevski, A. N.; Mayorov, A. D. *Review of Scientific Instruments* **1993**, *64*, 225-227.
(255) Caron, J. J.; Haskell, R. B.; Benoit, P.; Vetelino, J. F. *IEEE transactions on ultrasonics, ferroelectrics, and frequency control* **1998**, *45*, 1393-1398.
(256) Haskell, R. B. Masters, University of Maine, 2003.
(257) Mercer, T. T. *Analytical Chemistry* **1979**, *51*, 5.
(258) Hirvonen, J. K.; Weisenberger, W. H.; Westmoreland, J. E.; Meussner, R. A. *Applied Physics Letters* **1972**, *21*, 37-39.
(259) Cox, H. H. J.; Deshusses, M. A. *Chemical Engineering Journal* **2002**, *87*, 101-110.
(260) McNamara, J. D.; Wagner, N. J. *Gas Separation & Purification* **1996**, *10*, 137-140.
(261) Finklea, H. O.; Avery, S.; Lynch, M.; Furtsch, T. *Langmuir* **2002**, *3*, 409-413.
(262) Himmelhaus, M.; Buck, M.; Grunze, M. *Applied Physics B: Lasers and Optics* **1999**, *68*, 595-598.
(263) Thome, J.; Himmelhaus, M.; Zharnikov, M.; Grunze, M. *Langmuir* **1998**, *14*, 7435-7449.
(264) Aliganga, A. K. A.; Wang, Z.; Mittler, S. *The Journal of Physical Chemistry B* **2004**, *108*, 10949-10954.
(265) Li, D.; Ma, M. *Sensors and Actuators B: Chemical* **2000**, *69*, 75-84.
(266) Joyner, R. W.; Roberts, M. W. *Journal of the Chemical Society Faraday Transactions 1* **1973**, *69*, 1242-1250.
(267) Atkins, P. W. *Physical Chemistry*; 2nd ed.; Oxford University Press: Oxford, Great Britain, 1982.
(268) Nott, B. R. *Water, Air, & Soil Pollution* **1995**, *80*, 1311-1314.
(269) Nilsson, S.; Klett, O.; Svedberg, M.; Amirkhani, A.; Nyholm, L. *Rapid Communications in Mass Spectrometry* **2003**, *17*, 1535-1540.
(270) Hoogvliet, J. C.; van Bennekom, W. P. *Electrochimica Acta* **2001**, *47*, 599-611.
(271) Sexton, B. A.; Feltis, B. N.; Davis, T. J. *Sensors and Actuators A: Physical* **2008**, *141*, 471-475.
(272) Ali, M. B.; Bessueille, F.; Chovelon, J. M.; Abdelghani, A.; Jaffrezic-Renault, N.; Maaref, M. A.; Martelet, C. *Materials Science and Engineering: C* **2008**, *28*, 628-632.
(273) Moody, N. R.; Adams, D. P.; Medlin, D.; Headley, T.; Yang, N.; Volinsky, A. *International Journal of Fracture* **2003**, *120*, 407-419.
(274) Rand, D. A. J.; Woods, R. *Journal of Electroanalytical Chemistry* **1971**, *31*, 29-38.
(275) García-Sánchez, A.; Contreras, F.; Adams, M.; Santos, F. *Environmental Geochemistry and Health* **2006**, *28*, 529-540.
(276) Li, J.; Herrero, E.; Abruña, H. D. *Colloids and Surfaces A: Physicochemical and Engineering Aspects* **1998**, *134*, 113-131.
(277) Schoettel, G.; Vittal, J. J.; Puddephatt, R. J. *Journal of the American Chemical Society* **1990**, *112*, 6400-6402.
(278) Scott, J. E.; Ottaway, J. M. *Analyst* **1981**, *106*, 1076-1081.
(279) McDonagh, C.; Bowe, P.; Mongey, K.; MacCraith, B. D. *Journal of Non-Crystalline Solids* **2002**, *306*, 138-148.

(280) Bohets, H.; Vanhoutte, K.; De Maesschalck, R.; Cockaerts, P.; Vissers, B.; Nagels, L. J. *Analytica Chimica Acta* **2007**, *581*, 181-191.
(281) Crank, J. *The Mathematics of Diffusion*; Oxford University Press, London, England, 1975; Vol. 2nd edition.
(282) Richaud, R.; Lachas, H.; Healey, A. E.; Reed, G. P.; Haines, J.; Jarvis, K. E.; Herod, A. A.; Dugwell, D. R.; Kandiyoti, R. *Fuel* **2000**, *79*, 1077-1087.
(283) Krata, A.; Bulska, E. *Spectrochimica Acta Part B: Atomic Spectroscopy* **2005**, *60*, 345-350.
(284) Ping, L.; Dasgupta, P. K. *Analytical Chemistry* **1989**, *61*, 1230-1235.
(285) Takaya, M.; Joeng, J. Y.; Ishihara, N.; Serita, F.; Kohyama, N. *Industrial Health* **2006**, *44*, 287-290.
(286) Marins, R. V.; de Andrade, J. B.; Pereira, P. A. d. P.; Paiva, E. C.; Paraquetti, H. H. M. *Journal of Environmental Monitoring* **2000**, *2*, 325-328.
(287) Moreno, F. N.; Anderson, C. W. N.; Stewart, R. B.; Robinson, B. H. *Environmental and Experimental Botany* **2008**, *62*, 78-85.
(288) Ford, R. R.; Pritchard, J. *Transactions of the Faraday Society* **1971**, *67*, 216-221.
(289) George, M. A.; Glaunsinger, W. S.; Thundat, T.; Lindsay, S. M. *Journal of Microscopy* **1988**, *152*, 703-713.
(290) Inukai, J.; Sugita, S.; Itaya, K. *Journal of Electroanalytical Chemistry* **1996**, *403*, 159-168.
(291) Butt, H.-J.; Graf, K.; Kappl, M. In *Physics and Chemistry of Interfaces* 2004, p 177-205.
(292) Meghea, A.; Rehner, H.; Peleanu, I.; Mihalache, R. *Journal of Radioanalytical and Nuclear Chemistry* **1998**, *229*, 105-110.
(293) Jones, R. G.; Perry, D. L. *Surface Science* **1978**, *71*, 59-74.
(294) Jones, R. G.; Perry, D. L. *Surface Science* **1979**, *82*, 540-548.
(295) Jones, R. G.; Perry, D. L. *Vacuum* **1981**, *31*, 493-498.
(296) Singh, N. K.; Jones, R. G. *Surface Science* **1990**, *232*, 229-242.
(297) Levine, H. S.; MacCallum, C. J. *Journal of Applied Physics* **1960**, *31*, 595-599.
(298) Yoshida, Z. *Bulletin of the Chemical Society of Japan* **1981**, *54*, 562-567.
(299) Aylward, G. H.; Findlay, T. J. V. *SI Chemical Data*; John Wiley & Sons, 2002; Vol. 5.
(300) Buffat, P.; Borel, J. P. *Physical Review A* **1976**, *13*, 2287.
(301) Lucklum, R.; Eichelbaum, F. In *Piezoelectric Sensors* 2007, p 3-47.
(302) Yang, X.; Tonami, K.; Nagahara, L. A.; Hashimoto, K.; Wei, Y.; Fujishima, A. *Chemistry Letters* **1994**, *11*, 2059-2062.
(303) Sakai, G.; Baik, N. S.; Miura, N.; Yamazoe, N. *Sensors and Actuators B: Chemical* **2001**, *77*, 116-121.
(304) Hsieh, J. C.; Liu, C. J.; Ju, Y. H. *Thin Solid Films* **1998**, *322*, 98-103.
(305) Lucklum, R.; Behling, C.; Hauptmann, P. *Analytical Chemistry* **1999**, *71*, 2488-2496.
(306) Schramm, U.; Roesky, C. E. O.; Winter, S.; Rechenbach, T.; Boeker, P.; Schulze Lammers, P.; Weber, E.; Bargon, J. *Sensors and Actuators B: Chemical* **1999**, *57*, 233-237.
(307) Cavicchi, R. E.; Suehle, J. S.; Kreider, K. G.; Gaitan, M.; Chaparala, P. *Sensors and Actuators B: Chemical* **1996**, *33*, 142-146.
(308) Sakai, G.; Matsunaga, N.; Shimanoe, K.; Yamazoe, N. *Sensors and Actuators B: Chemical* **2001**, *80*, 125-131.
(309) Bakker, E.; Pretsch, E.; Buhlmann, P. *Analytical Chemistry* **2000**, *72*, 1127-1133.
(310) Hahm, J.-i.; Lieber, C. M. *Nano Lett.* **2003**, *4*, 51-54.
(311) Zheng, G.; Patolsky, F.; Cui, Y.; Wang, W. U.; Lieber, C. M. *Nat Biotech* **2005**, *23*, 1294-1301.
(312) Dryzek, J.; Czapla, A. *Journal of Materials Science Letters* **1986**, *5*, 1269-1270.
(313) Green, T. A. *Gold Bulletin* **2007**, *40*, 105-114.
(314) Miller, J. C.; Miller, J. N. *Statistics for Analytical Chemistry*; 3rd ed.; Ellis Horwood Limited: West Sussex, 1993.
(315) Li, J.; Abruna, H. D. *The Journal of Physical Chemistry B* **1997**, *101*, 2907-2916.
(316) Jain, R. K. *Cancer and Metastasis Reviews* **1990**, *9*, 253-266.

(317) Wei, G. C. T.; Wuensch, B. J. *Journal of the American Ceramic Society* **1976**, *59*, 295-299.
(318) Buttry, D. A.; Ward, M. D. *Chem. Rev.* **1992**, *92*, 1355-1379.
(319) Zierhut, A.; Leopold, K.; Harwardt, L.; Worsfold, P.; Schuster, M. *Journal of Analytical Atomic Spectrometry* **2009**, *24*, 767-774.
(320) Huang, D.; Liao, F.; Molesa, S.; Redinger, D.; Subramanian, V. *Journal of the Electrochemical Society* **2003**, *150*, G412-G417.
(321) Akita, T.; Okumura, M.; Tanaka, K.; Kohyama, M.; Haruta, M. *Journal of Materials Science* **2005**, *40*, 3101-3106.
(322) Akhter, J. I.; Ahmed, E.; Ahmad, M. *Materials Chemistry and Physics* **2005**, *93*, 504-507.
(323) Porter, D. A.; Easterling, K. E. *Phase Transformations in Metals and Alloys*; 2nd Edition ed.; CRC Press, 1992.
(324) Mehrer, H. *Diffusion in Solids*; 1 ed.; Springer, 2007.
(325) Avallone, E. A.; Baumeister, T.; Sadegh, A.; Marks, L. S. *Marks' Standard Handbook for Mechanical Engineers*; 11 ed.; McGraw-Hill Professional, 2006.
(326) Caron, J.; Freeman, C. J. *Surface Acoustic Wave Mercury Vapor Sensor*, Sensor Research and Development Corporation, 1998.
(327) Sanemasa, I. *Bulletin of the Chemical Society of Japan* **1975**, *48*, 1795-1798.
(328) Bansal, V.; Jani, H.; Plessis, J. D.; Coloe, P. J.; Bhargava, S. K. *Adv. Mater.* **2008**, *20*, 717-723.
(329) Bond, G. C. *Catalysis Today* **2002**, *72*, 5-9.
(330) Sun, Y.; Mayers, B. T.; Xia, Y. *Nano Lett.* **2002**, *2*, 481-485.
(331) Sun, Y.; Xia, Y. *Journal of the American Chemical Society* **2004**, *126*, 3892-3901.
(332) Liang, H. P.; Guo, Y. G.; Zhang, H. M.; Hu, J. S.; Wan, L. J.; Bai, C. L. *Chem. Commun.* **2004**, 1496-1497.
(333) Liang, H.-P.; Wan, L.-J.; Bai, C.-L.; Jiang, L. *The Journal of Physical Chemistry B* **2005**, *109*, 7795-7800.
(334) Shukla, S.; Priscilla, A.; Banerjee, M.; Bhonde, R. R.; Ghatak, J.; Satyam, P. V.; Sastry, M. *Chem. Mat.* **2005**, *17*, 5000-5005.
(335) Selvakannan, P. R.; Sastry, M. *Chem. Commun.* **2005**, 1684-1686.
(336) Viyannalage, L. T.; Vasilic, R.; Dimitrov, N. *J. Phys. Chem. C* **2007**, *111*, 4036-4041.
(337) Vasilic, R.; Dimitrov, N. *Electrochemical and Solid-State Letters* **2005**, *8*, C173-C176.
(338) Vasilic, R.; Viyannalage, L. T.; Dimitrov, N. *Journal of the Electrochemical Society* **2006**, *153*, C648-C655.
(339) Brankovic, S. R.; Wang, J. X.; Adzic, R. R. *Surface Science* **2001**, *474*, L173-L179.
(340) Mrozek, M. F.; Xie, Y.; Weaver, M. J. *Analytical Chemistry* **2001**, *73*, 5953-5960.
(341) Lipi´nski, L.; Szmyrka-Grzebyk, A.; Manuszkiewicz, H. *Measurement Science and Technology* **2000**, *11*, 738-742.
(342) Cherstiouk, O.; Gavrilov, A.; Plyasova, L.; Molina, I.; Tsirlina, G.; Savinova, E. *Journal of Solid State Electrochemistry* **2008**, *12*, 497-509.
(343) Fiermans, L.; Hoogewijs, R.; Vennik, J. *Surface Science* **1975**, *47*, 1-40.
(344) Haseeb, A. S. M. A.; Chakraborty, P.; Ahmed, I.; Caccavale, F.; Bertoncello, R. *Thin Solid Films* **1996**, *283*, 140-144.
(345) Aravinda, C. L.; Mayanna, S. M.; Bera, P.; Jayaram, V.; Sharma, A. K. *Journal of Materials Science Letters* **2002**, *21*, 205-208.
(346) Jiang, P.; Zhou, J.-J.; Li, R.; Gao, Y.; Sun, T.-L.; Zhao, X.-W.; Xiang, Y.-J. *Journal of Nanoparticle Research* **2006**, *8*, 927-934.
(347) Qian, L.; Ming, M.; Yuqing, Z. H. A. *Chinese Journal of Catalysis* **2006**, *27*, 1111-1116.
(348) Jin, Y.; Dong, S. *The Journal of Physical Chemistry B* **2003**, *107*, 12902-12905.
(349) Cain, S. R.; Matienzo, L. J.; Emmi, F. *The Journal of Physical Chemistry* **2002**, *94*, 4985-4990.
(350) Fox, C. G.; Alder, J. F. *Analyst* **1989**, *114*, 997-1004.
(351) van Noort, D.; Mandenius, C. F. *Biosensors & Bioelectronics* **2000**, *15*, 203-209.
(352) Tian, Y.; Liu, H. Q.; Deng, Z. F. *Chem. Mat.* **2006**, *18*, 5820-5822.
(353) Natter, H.; Hempelmann, R. *Z. Phys. Chem.* **2008**, *222*, 319-354.

(354) O'Mullane, A. P.; Ippolito, S. J.; Sabri, Y. M.; Bansal, V.; Bhargava, S. K. *Langmuir* **2009**, In press, Accepted, doi: la-2008-039016.R1.
(355) Sabri, Y. M.; Bansal, V.; Ippolito, S. J.; Bhargava, S. K. *Adv. Mater.* **2009**, Under Review.
(356) Zhang, H.; Xu, J.-J.; Chen, H.-Y. *The Journal of Physical Chemistry C* **2008**, *112*, 13886-13892.
(357) Li, Y.; Shi, G. *The Journal of Physical Chemistry B* **2005**, *109*, 23787-23793.
(358) van Noort, D.; Rani, R.; Mandenius, C.-F. *Microchimica Acta* **2001**, *136*, 49-53.
(359) Toyama, S.; Takei, O.; Tsuge, M.; Usami, R.; Horikoshi, K.; Kato, S. *Electrochemistry Communications* **2002**, *4*, 540-544.
(360) Bonroy, K.; Friedt, J.-M.; Frederix, F.; Laureyn, W.; Langerock, S.; Campitelli, A.; Sara, M.; Borghs, G.; Goddeeris, B.; Declerck, P. *Analytical Chemistry* **2004**, *76*, 4299-4306.
(361) El-Deab, M. S.; Sotomura, T.; Ohsaka, T. *Electrochimica Acta* **2006**, *52*, 1792-1798.
(362) Gao, F.; El-Deab, M. S.; Okajima, T.; Ohsaka, T. *Journal of the Electrochemical Society* **2005**, *152*, A1226-A1232.
(363) El-Deab, M. S.; Sotomura, T.; Ohsaka, T. *Journal of the Electrochemical Society* **2005**, *152*, C730-C737.
(364) Huang, S.; Ma, H.; Zhang, X.; Yong, F.; Feng, X.; Pan, W.; Wang, X.; Wang, Y.; Chen, S. *The Journal of Physical Chemistry B* **2005**, *109*, 19823-19830.
(365) Duan, G.; Cai, W.; Luo, Y.; Li, Z.; Li, Y. *Applied Physics Letters* **2006**, *89*, 211905.
(366) Toyama, S.; Someya, M.; Takei, O.; Ohtake, T.; Usami, R.; Horikoshi, K.; Ikariyama, Y. *Chemistry Letters* **2001**, *30*, 160-161.
(367) Notsu, H.; Kubo, W.; Shitanda, I.; Tatsuma, T. *Journal of Materials Chemistry* **2005**, *15*, 1523-1527.
(368) Peppler, K.; Polleth, M.; Meiss, S.; Rohnke, M.; Janek, J. *Zeitschrift für Physikalische Chemie* **2006**, *220*.
(369) Wenzel, R. N. *The Journal of Physical and Colloid Chemistry* **1949**, *53*, 1466-1467.
(370) O'Mullane, A. P.; Ippolito, S. J.; Sabri, Y. M.; Bansal, V.; Bhargava, S. K. *Langmuir* **2009**, *25*, 3845-3852.
(371) Plowman, B.; Ippolito, S. J.; Bansal, V.; Sabri, Y. M.; O'Mullane, A. P.; Bhargava, S. K. *Chem. Commun.* **2009**, *7*, 5039-5041.
(372) Fleming, B. D.; Praporski, S.; Bond, A. M.; Martin, L. L. *Langmuir* **2008**, *24*, 323-327.
(373) Rodahl, M.; Hook, F.; Krozer, A.; Brzezinski, P.; Kasemo, B. *Review of Scientific Instruments* **1995**, *66*, 3924-3930.
(374) A. Sannino, S. P., L. Giotta, L. Valli, A. Maffezzoli, *Journal of Applied Polymer Science* **2007**, *106*, 3040-3050.
(375) Marx, K. A. In *Piezoelectric Sensors* 2007, p 371-424.
(376) Zhang, X.; Shi, F.; Niu, J.; Jiang, Y.; Wang, Z. *Journal of Materials Chemistry* **2008**, *18*, 621-633.
(377) Sun, X.; Dong, S.; Wang, E. *Langmuir* **2005**, *21*, 4710-4712.
(378) Cao, L.; Zhu, T.; Liu, Z. *Journal of Colloid and Interface Science* **2006**, *293*, 69-76.
(379) Schultze, J. W.; Dickertmann, D. *Surface Science* **1976**, *54*, 489-505.
(380) Rojas, M. I.; Dassie, S. A.; Leiva, E. P. M. *Zeitschrift fuer Physikalische Chemie* **1994**, *185*, 33-50.
(381) Wu, Q.; Barkey, D. *Journal of the Electrochemical Society* **2000**, *147*, 1038-1045.
(382) Lamb, V. A.; Johnson, C. E.; Valentine, D. R. *Journal of the Electrochemical Society* **1970**, *117*, 291C-318C.
(383) Kondo, K.; Murakami, H. *Journal of the Electrochemical Society* **2004**, *151*, C514-C518.
(384) Carneval, G.; Cusminsky, J. B. d. *Journal of the Electrochemical Society* **1981**, *128*, 1215-1221.
(385) McIntyre, J. D. E.; Peck, W. F. *Journal of the Electrochemical Society* **1976**, *123*, 1800-1813.
(386) Chang, B.-Y.; Ahn, E.; Park, S.-M. *The Journal of Physical Chemistry C* **2008**, *112*, 16902-16909.
(387) Guo, S.; Wang, L.; Wang, E. *Chem. Commun.* **2007**, 3163-3165.

(388) (ESCO), E. S. C. I.
(389) Okamoto, H.; Massalski, T. *Journal of Phase Equilibria* **1989**, *10*, 50-58.
(390) Rolfe, C.; Hume-Rothery, W. *Journal of the Less Common Metals* **1967**, *13*, 1-10.
(391) Berndt, A. F.; Cummins, J. D. *Acta Crystallographica, Section B: Structural Crystallography and Crystal Chemistry* **1970**, *26*, 864-7.
(392) Forster, P. G.; Grocott, S. C. In *Proceedings of the 4th International Alumina Quality Workshop* Darwin, N.T., 1996, p 478-487.
(393) Mullett, M. E. Master of Applied Science, RMIT University, 2005.
(394) Tanida, K.; Hoshino, M. *The Rigaku Journal* **1990**, *7*, 35-40.
(395) Worden, S. *Journal of Design History* **2009**, doi:10.1093/jdh/epn039.
(396) Tan, R. B. H.; Khoo, H. H. *Journal of Cleaner Production* **2005**, *13*, 607-618.
(397) Hetherington, D. *The Full-Cost Economics of Climate Change - Aluminium: A Case Study*, Per Capita Australia Limited, 2008.
(398) Frost, M.; Parton, K. In *Australian Agriculture and Resource Economics Society* Cairns, Australia, 2009, p 1-17.
(399) Mollard, W.; Richmond, S.; Haine, I.; Penney, K. *Australian Commodities* **2005**, *12*, 126-142.
(400) Hind, A. R.; Bhargava, S. K.; Grocott, S. C. *Colloids and Surfaces A: Physicochemical and Engineering Aspects* **1999**, *146*, 359-374.
(401) Fthenakis, V. M.; Kim, H. C.; Wang, W. *Life Cycle Inventory Analysis in the Production of Metals Used in Photovoltaics*, Brookhaven National Laboratory, 2007.
(402) Waite, D. T.; Snihura, A. D.; Liu, Y.; Huang, G. H. *Chemosphere* **2002**, *49*, 341-351.

Chapter VIII

Conclusions and Future Work

In this chapter, the summary of the work presented in this thesis and the potential avenues for future work are discussed

8.1 Summary of Work

The sustainability of many industries around the world is reliant on attempts to detect and reduce anthropogenic Hg vapour emissions due to their environmental and health impacts that have resulted in stringent government regulations for pollution control. Currently available commercial technologies to measure elemental Hg vapour are mostly based on CVAAS instruments which are costly, time consuming, labor intensive, limited to time-average applications and suffer from undesired photochemical reactions from interferent gases, thus making them impractical for many industrial applications.

The novel idea of employing nano-engineered gold sensitive layers on quartz crystal microbalance electrodes to selectively sense Hg vapour is presented in this PhD thesis. To the best of Author's knowledge, no work had been published using nanostructured Au based QCMs for the detection of mercury in harsh industrial environments at the time the thesis was started. Systematic experiments were used to achieve the final objective of producing a nanomaterial based selective Hg vapour sensor in the presence of NH_3 and H_2O interferent gas species. The industrial conditions imposed by the industrial partners, namely BHP Billiton and ALCOA Australia, on the experiments included Hg vapour concentrations ranging from 1 to 10 mg/m^3 at temperatures of 20 to 80°C with various levels of interferent gases (NH_3 and H_2O). According to the industry partners, these were the most problematic gases when current commercially available Hg vapour sensors are used to perform spot sampling measurements in alumina refineries.

The findings towards the development of QCMs with modified Au electrode based Hg vapour sensors are discussed in the following subsections.

8.1.1 Gravimetric Based Hg Vapour Sensor

In the critical literature review undertaken in Chapter 1, it was shown that the qualities of the QCM made it the ideal choice of transducer over other gravimetric based sensors for high concentration Hg vapour sensing applications. Furthermore, topics such as Hg and Au interaction, the effects of mercury on human health and the environment, major industrial sources of Hg emissions and the currently available technologies for measuring Hg vapour in laboratory and industrial applications were discussed.

8.1.2 Importance of Experimental Set-up

The designed, built and controlled mercury vapour gas calibration system was presented in Chapter 2. The certified permeation tubes generating Hg vapour were recalibrated in the built system using a method similar to EPA method 101A for verification. The system was

purposely designed to operate continuously and at a high pressure of 1220 mbar to overcome a series of shortfalls (with other system designs). The increased pressure also facilitated more gas-solid collisions, helping to increase the relatively low QCM transducer sensitivity. The importance of maintaining different sub-system temperatures and pressures in order to achieve repeatable Hg concentrations at many different operating chamber conditions (temperature and interferent gas concentrations) was also discussed.

8.1.3 Hg Interaction with Metal Films

In Chapter 3, QCMs employing optically polished and mechanically roughened substrate morphologies with either Au, Ag, Ni and Ti thin film sensitive layers were tested towards Hg vapour in order to study the interaction of Hg on the different film types and morphologies. It was found that the Au-rough based QCM had the highest Hg sorption capacity and desorption rate, the fastest response time and maintained a higher sticking probability than Au-polished, Ag-rough and Ag-polished QCMs. As expected, the Ti and Ni electrode based QCMs did not show a response towards Hg vapour. By digesting and analysing the sensors using ICPMS, it was found that the Au-rough contained 16% less by mass Hg amalgam than the Ag-rough film, indicating that better regeneration occurs when the film has a higher number of surface defects and grain boundaries. SIMS depth profiling performed on a duplicate set of QCMs exposed to Hg vapour confirmed that Ag films retained a higher portion of the adsorbed/amalgamated Hg than the Au films following a recovery period of 5 hours. Overall, the Au-rough based QCM was found to be the better sensor for Hg vapour sensing compared to Au-polished, Ag-polished and Ag-rough QCMs. However, the introduction of interferent gases was found to have detrimental effects on the Au-rough electrode QCM, so it was necessary to better understand Hg interaction with Au films prior to Au surface modification to develop a more Hg selective material.

8.1.3.1 Influence of Au Film Thickness

In Chapter 4, optically polished Au QCMs of film thicknesses between 40 and 200 nm were exposed to various Hg vapour concentrations (1.02, 1.87, 3.65, 5.70 and 10.55 mg/m^3) at different operating temperatures (28, 40, 55, 63, 74, 89, 101, 114 and 134°C) in order to better understand Hg interaction with Au-polished thin films. It was found that not only Au film thickness but parameters such as Hg vapour concentration, Hg exposure period, operating temperature and Hg surface coverage all influenced the Hg sorption and desorption characteristics of thin Au films. The temperature profiles of the QCM response magnitudes were observed to be a cubic type curve for all the Au-polished based QCMs. This indicated that using an operating temperature of 89°C instead of near-room temperature resulted in increased response time and better recovery, but in reduced QCM response magnitude and dynamic range during Hg vapour sensing.

8.1.3.2 Hg Sorption and Diffusion Behaviour in Ultra-thin Films

In order to study Hg sorption and diffusion behaviour in ultra-thin films of Au sensitive layers with thicknesses 10, 20, 30 and 40 nm, forty specially fabricated QCMs were exposed to Hg vapour at various operating conditions before performing SIMS depth profiling. The Au ultra-thin sensitive layers were separated from the Au electrodes by a 20 nm SiO_2 boundary layer to stop further diffusion of Hg vapour beyond the ultra-thin Au films and into the QCM Au electrode. By extrapolating the QCM response magnitudes towards Hg vapour to zero Au film thickness it was possible to differentiate between the adsorbed and absorbed Hg on the ultra-thin Au sensitive layers. The ratio of adsorbed to absorbed Hg on Au films was found to decrease with increased Hg vapour concentration and to increase with increased operating temperature. The higher Hg sorption capacity of the 10 nm Au surface was attributed to the mobility of Au nanoclusters on SiO_2 films resulting in the exposure of non-amalgamated Au to Hg vapour.

SIMS depth profiles of the ultra-thin Au films showed that Hg vapour behaved similarly to the behaviour of liquid Hg on Au substrates that has been reported in literature. SIMS depth profiling of all 40 QCMs showed Hg diffusion in the films and Hg accumulation between the Au ultra-thin film and the SiO_2 barrier layer in all tested films, except for the 10 nm film when operated at 28°C. The findings suggested that in order to reduce Hg accumulation in Au and increase sensor recovery, a non-continuous Au film needed to be fabricated and used as the Hg sensitivity layer. On the other hand, the thicker and continuous Au films were observed to undergo larger response magnitudes. This was possibly due to the reduced concentration gradient of Hg through the Au film depth resulting in a higher diffusion factor, leading to repeatable amount of Hg sorption capacity and good sensor repeatability. Based on these results, two different surface modification techniques were employed to develop sensors with high recovery and response magnitudes.

8.1.4 Use of Galvanic Replacement Reaction to Enhance Sensor Recovery

In Chapter 6, Au-Ni hybrid nanostructures were fabricated directly on to specially fabricated QCM Ni electrodes by employing galvanic replacement (GR) reactions to improve sensor recovery. The surfaces produced by the GR reaction method resulted in Au nano-islands on the QCM Ni electrodes. Hg exposure tests showed 93 to 100% desorption or regeneration of the GR sensors compared to < 90% for an Au control when operated at 89°C. SIMS depth profiling analysis showed no evidence of accumulation of Hg at the Au/Ni boundary layer, which is thought to be the reason for the near-full regeneration of these modified sensors. In addition, the 1 h and 4 h GR QCMs showed good selectivity towards Hg vapour when tested in the presence of humidity, ammonia or a mixture of both at different concentration levels. However, low response magnitudes (leading to lower dynamic range between Hg vapour

concentrations) were observed for all the developed Ni-Au hybrid nanostructures when compared to a 150 nm Au control QCM. Furthermore, XPS analysis showed NiO on the surface, which may capture some VOCs during Hg sensing in industrial effluents thus potentially reducing the selectivity of the Ni-Au hybrid nanostructures QCMs. In order to increase QCM response magnitude and overcome the NiO issues, the thick continuous Au nanostructured films on QCMs were pursued.

8.1.5 Use of Electrodeposition to Enhance Sensor Response Magnitude

In order to develop a sensor with a high response magnitude towards Hg vapour, a protocol was established to synthesize Au nanospikes directly onto QCM Au electrodes as presented in Chapter 7. This protocol has since been patented. The nanospike QCM had a 4.90 times greater response magnitude than the Au control QCM when exposed to a Hg concentration of 10.55 mg/m^3 at an operating temperature of 28°C. The high response towards Hg vapour of the nanospike QCM was confirmed not to be due to surface area increase alone but also due to their rich (111) plane orientation and increased surface defect sites over evaporated thin films. Furthermore, the nanospike QCM showed good selectivity towards Hg in the presence of humidity and ammonia interferent gases. The nanospike QCMs also maintained very good selectivity and higher response magnitude when tested towards Hg vapour with and without the presence of interferent gases for a continuous 50 day period at 89°C. This long term test was conducted in order to duplicate scenarios which may occur if the sensors are used in online industrial streams.

Additionally, a separate Au nanospike QCM was then tested towards Hg vapour in the presence of additional interferent gases that may be present in some alumina refinery effluent gases that have high affinity towards Au. These preliminary industrial trial tests were conducted in a testing chamber with a significantly smaller volume that was specially designed and built by the author in accordance with the industrial partners' HAZARD and HAZOP specifications. The interferent gases tested were acetaldehyde, acetone, dimethyl disulphide, methyl ethyl ketone, ammonia and humidity. The nanospike based sensor maintained its higher response, selectivity and dynamic range compared to the Au control QCM when exposed to Hg vapour in the presence of the interferent gases at 89°C and was therefore selected to be tested onsite in an industrial trial in the near future.

8.1.6 Performance Comparison of the Developed Nano-engineered Sensors

The performance of Au based QCMs tested as potential Hg vapour sensors in this dissertation are presented in Table 8.1. The bold and underlined data represents the maximum and minimum values in each column, respectively. It may be observed that the nanospikes QCMs produced the highest sensitivity of 149.2 Hz/(mg/m^3), the maximum Hg

sorption rate of 123.8 Hz/min and the quickest response time of 1.9 minutes (using the rate data) than all the other sensors tested in this work. The ratio of Hg desorption to that of sorption is observed to be only slightly lower than the 8 h GR QCM. However it was observed that the nanospike based QCMs were more selective towards Hg vapour in the presence of the six tested interferent gases whereas the 8 h GR QCM was badly influenced by the presence of ammonia and humidity. Although the response magnitude of the nanospikes in the preliminary plant trial was observed to reduce, it was also observed to maintain very high selectivity and a higher response magnitude than the Au control QCM, making it an ideal candidate as an online Hg vapour sensor for industrial effluent streams.

Table 8.1: QCM data for all sensors tested demonstrating Hg sorption, desorption and the observed Hg desorption to sorption ratio. The data presented are for Hg concentration of 10.55 mg/m^3 at an operating temperature of 89℃ (unless otherwise specified)

	Non-modified Hg Vapour Sensors									
QCM electrode	Hg sorption (Hz)	Hg desorption (Hz)	Hg desorption to Hg sorption ratio	t_{90} (min)	Max sorption rate (Hz/min)	Time to reach max sorption rate (min)	Detection limit (mg/m^3)		Sensitivity [Hz/(mg/m^3)]	
							28℃	89℃	28℃	89℃
100 nm Au	213.1	200.4	0.940	29.0	68.7	0.5	0.035	0.171	28.8	40.2
150 nm Au	208.1	195.4	0.940	36.6	65.9	0.6	0.026	0.137	30.8	45.1
200 nm Au	195.4	175.6	0.899	38.4	65.1	0.9	0.031	0.108	28.7	38.8
Au-Rough	271.2	260.7	0.961	12.6	75.1	1.3	0.012	0.311	71.3	69.1
	Modified Hg Vapour Sensors									
0.5 h GR	32.7	30.7	0.939	7.6	23.2	0.6	**0.126**	0.103	2.66	5.91
1 h GR	46.4	45	0.970	9.9	47.0	0.5	0.058	0.138	8.69	10.2
2 h GR	186.7	179	0.959	8.3	85.9	1.2	0.020	0.147	25.1	39.6
4 h GR	122.6	119	0.971	8.5	63.9	0.8	0.022	0135	25.1	27.0
8 h GR	230.6	229	**0.993**	7.0	84.6	1.1	0.014	0.128	43.3	49.4
Nanospike	**576.4**	**553.3**	0.960	18.6	**123.8**	**1.9**	0.006	**0.316**	**155**	**149.2**
Nanospike (in preliminary industrial trial test)	317.0	314.4	0.992	**39.6**	41.1	2.1	-	0.031	-	96.9

8.2 Conclusions

Due to their high sensitivity and long term stability in the presence of interferent gases when operated at 89°C, the nanospikes, 1, 2 and 4 h GR QCMs developed in this work offer extensive commercialization opportunities. This dissertation shows the development of low-cost, selective and sensitive elemental mercury vapour detectors by the integration of Au nanostructures as the sensitive layer on QCM electrodes. The proposed detection methodology and design, using the nanospikes QCM for example, offers many advantages over the current commercially available Hg vapour sensors, such as:

- The need to pre-concentrate Hg is omitted, thus sensing is faster, requires less material and avoids potential errors associated with memory effects.
- The sensor recovery methodology does not require any heating or acid dissolution while the sensor is still able to reproduce similar response magnitudes for identical Hg vapour concentration with and without the presence of interferent gases.
- The system is cost effective. The cost of AAS, AFS, AES or ICPMS systems, for example, range from tens to hundreds of thousands of dollars. Currently, industries pay ~$AU 10,000 per sample to detect the Hg concentration in each stream with the results being revealed a little over 2 weeks later. The cost of 1 modified QCM as described may be within tens of dollars, with the additional advantage of having online measurements within 3 to 10 minutes of the 1 hour Hg exposure period (using sorption rate data). The associated plumbing (i.e. mass flow controllers and sensor testing chamber) and electronics (i.e. frequency counters and computers) may be further engineered to make them significantly smaller and cheaper than the current commercially available sensors used by industries. For example, a testing chamber housing one QCM may be designed with the sensor signal being relayed to a single remote computer operating from industry laboratories that communicates to a multiplexed frequency counter.
- The modified QCM showed only 6% degradation in response magnitude following 50 days of Hg exposure in the presence of interferent gases at an operating temperature of 89°C. No calibration was performed after the first day of testing. Calibration of the sensors requires nothing more than exposure to five Hg concentrations lasting a total of 14 hours and are required about 4 times a year to get Hg readings at least within ±7% with 95% confidence. Additionally this procedure has the potential to be computer automated, requiring minimal user intervention.
- Because the sensors are gravimetric based rather than resistive, and because most VOCs present in Hg emitting industries generally have lower molecular weights and lower affinity for Au than Hg vapour, they are significantly less prone to interfere or cause memory effects on the modified QCMs.

In summary, this PhD research program has produced significant contributions to the fields of surface modification of gold and Hg vapour sensing. The author's achievements throughout this work include one provisional patent, six published refereed journal articles, various news articles, and ABC (Australian Broadcasting Corporation) radio interview, conference proceedings, presentations and posters. A full list of the author's achievements throughout this work may be found in Appendix A.

8.3 Ongoing Future Work

Throughout the course of this PhD program several areas of interest that have tremendous research potential have been identified. Further research should embrace the following investigations:

- Formation of the nanostructures described on SAW sensors, which may also be made into hand held instruments for lower Hg vapour concentration monitoring.
- Under potential deposition of Pb during Au electrodeposition should be further investigated to better understand the growth mechanism of the nanospikes.
- HR-TEM studies should be performed to demonstrate the nature of the exposed Au facets along the nanospike walls and whether these exposed facets play any role in terms of sensor performance (e.g. Hg sorption and/or desorption)
- The QCMs should undergo synthetic testing against other interferent gases including VOCs which are present in other industries, such as those in coal-fired power generation.
- The deposition of various types of self-assembled monolayers to reduce the sorption of any potential interferent gases on the sensitive layer.
- The decrease in the composition of NiO on the galvanically replaced electrodes observed from XPS data is not well understood and needs to be further investigated by XPS depth profiling.

Finally, the direct growth of (111)-oriented nanostructures on an appropriate sensing platform may also provide immense future opportunities towards detection of ultra-low concentrations of other chemical and biological species. The author's developed nanostructures may also be investigated for their performance of (111)-oriented Au nanospikes as well as the galvanically replaced nanostructures for electrocatalysis, biosensing, surface enhanced Raman scattering (SERS) and various other applications. The vast potential implications of Au nanospikes and galvanically replaced nanostructured materials for sensing and various other applications cannot be overemphasized.

Appendices

Appendix A

Author's Achievements

Inside Cover Page in PCCP Journal (2009)

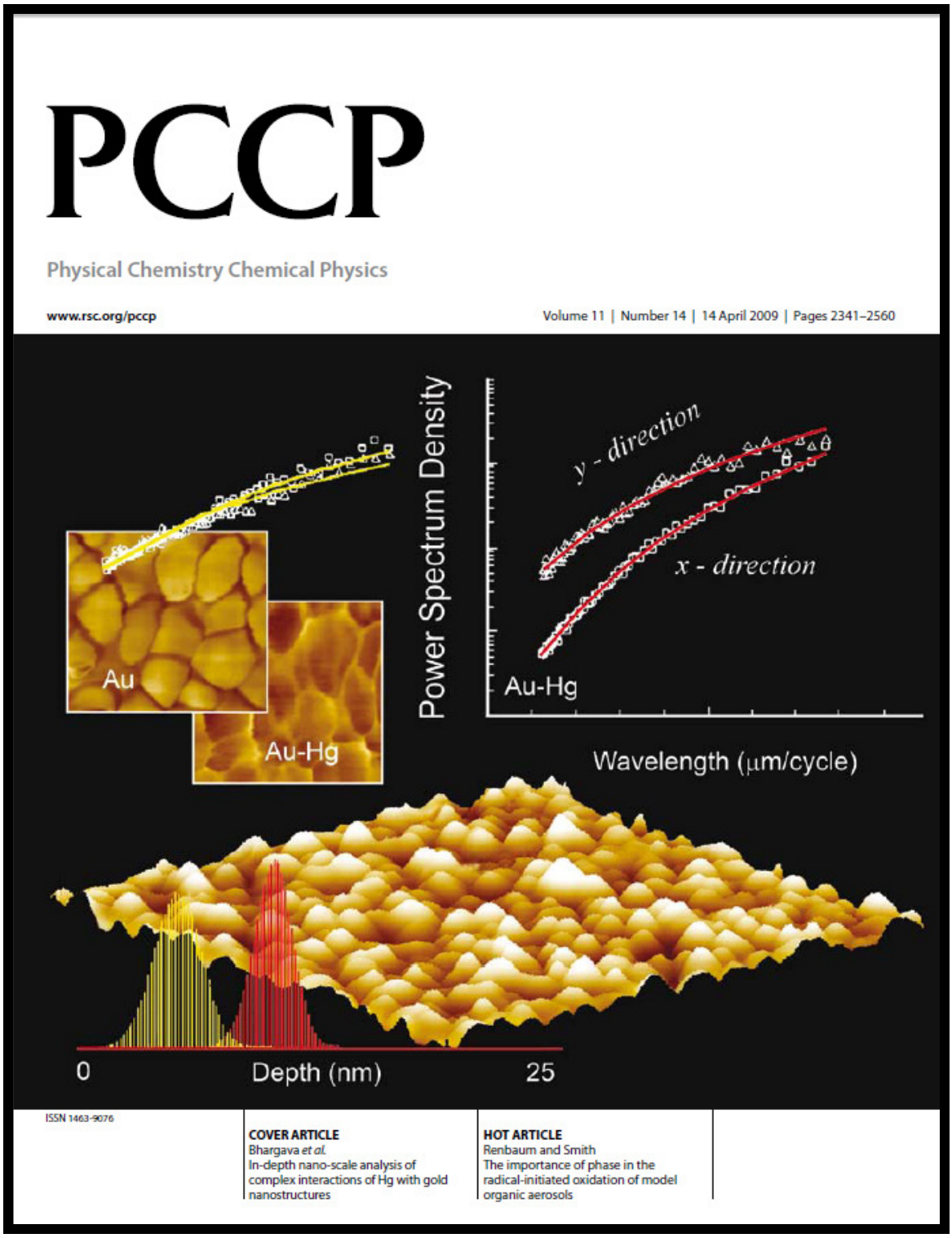

Provisional Patent

Provisional Patent "Electrodeposited gold nanostructures: for sensing mercury vapour in the presence of volatile organic compounds found in industrial effluent streams" filed 1st July 2008 (Patent No: 2008903362). This was upgraded to a PCA patent on 01/06/2009 having patent number 2009902459.

Refereed Journal Articles

1) Sabri, Y. M.; Ippolito, S. J.; Tardio, J.; Atanacio, A. J.; Sood, D. K.; Bhargava, S. K. Mercury diffusion in gold and silver thin film electrodes on quartz crystal microbalance sensors ***Sensors and Actuators B: Chemical,*** **2009**, *137*, 246-252.

2) Sawant, P. D.; Sabri, Y. M.; Ippolito, S. J.; Bansal, V.; Bhargava, S. K. In-depth nano-scale analysis of complex interactions of Hg with gold nanostructures using AFM based power spectrum density method ***Physical Chemistry Chemical Physics,*** **2009**, *11*, 2374-2378. **Selected for Inside Cover Page**.

3) O'Mullane, A. P.; Ippolito, S. J.; Sabri, Y. M.; Bansal, V.; Bhargava, S. K. Premonolayer Oxidation of Nanostructured Gold: An Important Factor Influencing Electrocatalytic Activity ***Langmuir,*** **2009**, *25*, 3845-3852.

4) Sabri, Y. M.; Ippolito, S. J.; Bhargava, S.K. Mercury Vapor Sensor for Alumina Refinery Processes, ***Light Metals 2009***, 37-42.

5) Sabri, Y. M.; Bansal, V.; Ippolito, S. J.; O'Mullane, A. P.; Bhargava, S. k. Template-less, Surfactant-free, Rapid and Simple Electrochemical Fabrication of Gold Nanospikes-Decorated Ultrahigh Response QCM Sensors **Environmental Science and Technology**, **2010**, Communicated.

6) Ippolito, S. J.; Plowman, B.; Bansal, V.; Sabri, Y. M.; O'Mullane, A. P.; Bhargava, S. k. Gold nanospikes formed through a simple electrochemical route with high electrocatalytic and surface enhanced Raman scattering activity **Chemical Communications**, **2009**, 7, 5039-5041.

Peer Reviewed Conference Proceedings & Presentations

1) Sabri, Y. M.; Ippolito, S. J.; Tardio, J.; Hussein, A.; O'Mullane, A. P.; Bhargava, S. K.; *APCOT*, Australia, 2010, Full manuscript and presentation. Full manuscript will be published in the journal of Sensors and Actuators A: Physical by the conference

2) Sabri, Y. M.; Ippolito, S. J.; Tardio, J.; O'Mullane, A. P.; Bansal, V.; Bhargava, S. K.; *APCOT*, Australia, 2010, Full manuscript and presentation. Full manuscript will be published in the journal of Sensors and Actuators A: Physical by the conference

3) Sabri, Y. M.; Kojima, R.; Ippolito, S. J.; Kaner, R. B.; Wlodarski, W.; Kalantar-zadeh, K.; Bhargava, S. K.; *IMCS*, Australia, 2010, Poster presentation. Full manuscript will be published in the journal of Sensors Letters by the conference

4) Sabri, Y. M.; Ippolito, S. J.; Tardio, J.; O'Mullane, A. P.; Bansal, V.; Bhargava, S. K.; *International Conference on Nanoscience and Nanotechnology (ICONN 2010)*, NSW, Aust, Febraury 25 – 29. Abstract and presentation

5) Sabri, Y. M.; Ippolito, S. J.; Tardio, J.; Sood, D. K.; Bhargava, S. K.; Mullett, M.; Harrison, I.; Rosenberg, S.; *8th International Alumina Quality Workshop* Darwin, Australia, 2008, p 260-266. Full manuscript and presentation

6) Sabri, Y. M.; Ippolito, S. J.; Bhargava, S. K.; Sood, D. K.; Bansal, V.; 12th international meeting on chemical sensors, columbus, Ohio, USA July 13 – 16 2008. Full manuscript and presentation

7) Sabri, Y. M.; Ippolito, S. J.; Bhargava, S. k.; Sood, D. K.; Tardio, J.; 12th international meeting on chemical sensors, columbus, Ohio, USA July 13 – 16 2008. Full manuscript and presentation

8) Bhargava, S. K.; Bansal, V.; Jani, H.; Sabri, Y.; Ippolito, S. J. 2008 International Conference on Nanoscience and Nanotechnology (ICONN 2008), Melb, VIC, Aust, Febraury 25 – 29. Abstract and presentation

9) Sabri, Y. M.; Ippolito, S. J.; Tardio, J.; Sood, D. K.; Bhargava, S. K. In *Nanoscience and Nanotechnology, 2008. ICONN 2008. International Conference on* 2008, p 71-74. Full manuscript and presentation. The manuscript is available from http://ieeexplore.ieee.org/stamp/stamp.jsp?tp=&arnumber=4639248&isnumber=4639211

10) Sabri, Y. M.; Sood, D. K.; Bhargava, S. K.; Ippolito, S. J.; 15th AINSE Conference on Nuclear and Complementary Techniques of Analysis (NCTA), Melbourne University, Melb, VIC, Aust, November 21 – 23 2007. pp.287-291. Full manuscript and poster

11) Dhawan, D.; Sabri, Y.; Bhargava, S.; Sood, D.; Kalantar-Zadeh, K. In *Micro- and Nanotechnology: Materials, Processes, Packaging, and Systems III*; 1 ed.; SPIE: Adelaide, Australia, 2006; Vol. 6415, p 641514-8. Full manuscript only

12) Sood, D. K.; Sabri, Y. M.; Bhargava, S. K.; Andrienko, I.; Wlodarski, W.; Evans, P. J.; 14th AINSE Conference on Nuclear and Complementary Techniques of Analysis & 19th Vacuum Society of Australia Congress (NCTA/VSA), Wellington, NZ, November 19 – 22; 2005. Full manuscript and presentation

Media Citations

1. Research on "Measuring Mercury with Nanotechnology" has been covered by reputed international scientific websites and magazines From May **2009**.

ABC National – Science Show 2 May 2009-05-05 - Mercury released as coal is burnt in power stations

http://www.abc.net.au/rn/scienceshow/stories/2009/2558479.htm

Stories of Australian Science 2010 - "Measuring mercury with a Midas touch"

http://www.scienceinpublic.com/stories/2009/measuring-mercury

AtoZofNano – "Using Nanotechnology to Measure Mercury"

http://www.azonano.com/details.asp?ArticleId=2395

AtoZofNano – Nanotechnology Thought Leader Series – Suresh Bhargava

http://www.azonano.com/experts.asp?iExpertID=70

The Age – “Mercury Falling” (19-11-2009)
http://www.theage.com.au/national/education/mercury-falling-20091119-iocb.html

RMIT Front page - “Measuring Mercury with Nanotechnology”
http://www.rmit.edu.au/browse;ID=xwzx3dxlgxzi

Australian Financial Review (RMIT insert) - “Midas Touch”

Nanotechnology Now - “Measuring Mercury with Nanotechnology”
http://www.nanotech-now.com/news.cgi?story_id=33383

Nanowerk – “Pioneering nanotechnology sensor can precisely measure mercury”
http://www.nanowerk.com/news/newsid=10860.php

Nano techwire.com - “Measuring Mercury with Nanotechnology”
http://nanotechwire.com/news.asp?nid=7979&ntid=&pg=1

Science Alert – “Gold nano-hairs find mercury”
http://www.sciencealert.com.au/news/20092805-19203.html

Nanotechnology & development news - “Measuring Mercury with Nanotechnology”
http://www.merid.org/NDN/more.php?id=1930

R&Dmag – “Gold spikes take accurate measure of industrial mercury”
http://www.rdmag.com/News/2009/05/Gold-spikes-take-accurate-measure-of-industrial-mercury/

ICHemE – “21st century chimney sweeping: RMIT forest of nano-gold captures mercury”
http://www.tce-today.co.uk/tcetoday/NewsDetail.aspx?nid=11791

Also Mentioned in:
Gold – “Gold used in US Army DNA research”
http://www.utilisegold.com/news/2009/06/02/story/12162/gold_used_in_us_army_dna_research

2. Research on Mercury vapor sensing using modified Au surfaces incorporated on QCM transducers was covered by reputed newspaper (*Financial Review*) in 3rd of June **2009** edition.
3. “Measuring mercury with a Midas touch” was published in the 2010 edition of *Stories of Australian Science* magazine.

4. Two radio interviews were conducted, namely Australian Broadcasting Corporation (ABC) radio and Triple R Broadcasters Melbourne (3RRR) radio in the years **2009** and **2010**, respectively.

Research Fellowships

Australian Institute of Nuclear Science and Engineering (AINSE) Award (Award No: AINGRA06164P) Totalling $13406.00 – Granted in 2006

Australian Institute of Nuclear Science and Engineering (AINSE) Award (Award No: AINGRA08104P) Totalling $18,130.00 – Granted in 2007

Australian Institute of Nuclear Science and Engineering (AINSE) Travel Grant Totalling $500.00 – Granted in 2008

Student Awards

Particle & Surface Science Award (Includes $500 Award) for producing the best results using the micromeritics system. The award was received twice in consecutive years of 2007 and 2008.

Student supervision

During the research candidature, the author was also involved in the supervision of three students from final year undergraduates and the supervision of one honours student.

Appendix B:

Alumina Industry and the Bayer process

In 2005, Australia was the largest producer and exporter of alumina producing 30% of the world's alumina.[395] Australian Aluminium/alumina export was estimated to be over A$7.2 billion in the financial year 1999-2000[396] to A$10 billion in 2005-2006 financial year with over A$3.8 billion from alumina alone.[397] in 2006-2007, alumina/aluminium was second after coal in the top eight commodities with 5.5% of the total commodities exported.[398] The Australian alumina export is estimated to reach over A$4.7 billion by the year 2010.[399] The alumina refinery industry is constantly trying to minimize the adverse environmental impacts of the Bayer process to maintain its environmental responsibilities while having its substantial contribution to the Australian economy. The Bayer process is used for refining bauxite to smelting grade alumina (Al_2O_3), the raw material for aluminium manufacturing.[400]

The Bayer process being the means of obtaining alumina from bauxite has not much changed since the first plant opened in 1893.[401] Generally, the Bayer process can be considered in four stages:

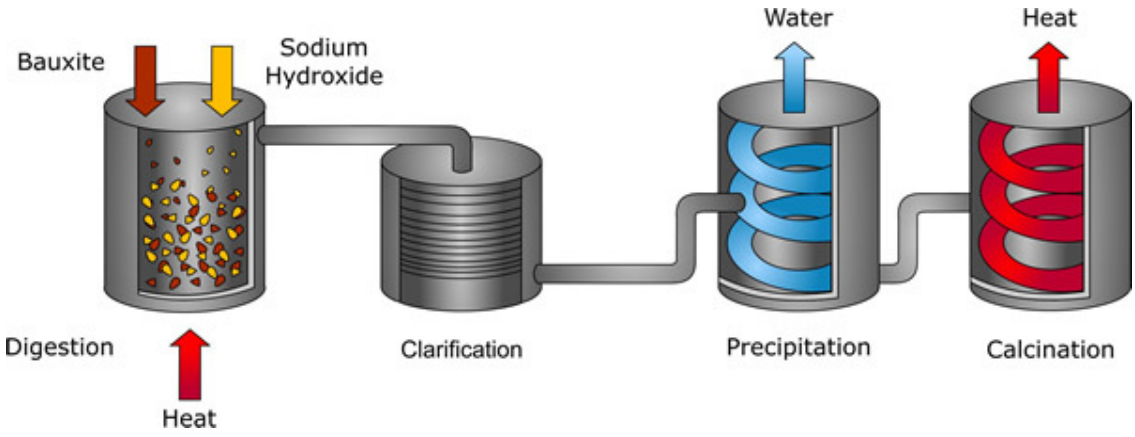

1. Digestion:

In this stage, the bauxite is washed, ground, and dissolved in caustic soda (sodium hydroxide) under high pressure and temperature conditions. The hydrated alumina is selectively removed from the other (insoluble) oxides by transferring it into a solution of sodium hydroxide (caustic soda) according to the following reaction:

$Al_2O_3.xH_2O + 2NaOH = 2NaAlO_2 + (x+1)H_2O$

The digestion is completed within a digester, typically operated at between 200 and 240℃ and can involve pressures of around 30 atm. The concentration of caustic soda can be as high as 10%.

2. Clarification:

The removal of residues from the liquor stream after the digestion stage is complete.

After the digestion, the liquor (containing the dissolved Al_2O_3) must be separated from the insoluble bauxite residues (containing iron, silicon, and titanium), purified as much as possible and filtered before it is delivered to a decomposer. These residues sink gradually to the bottom of the tank and are removed. They are known colloquially as "red mud". Bauxite residues (also known as red mud) are by-products of the Bayer Process. The amount of residues generated, per tonne of alumina produced, varies depending on the type of bauxite used, from 0.3 tonnes for high-grade bauxite to 2.5 tonnes for very low grade. The red mud is thickened and washed so that the caustic soda can be removed and recycled.

3. Precipitation: The removal of crystals of alumina hydrate from the caustic solution of the liquor stream.

After clarification, the clear sodium aluminate solution is pumped into a huge tank called a precipitator. In this stage, crystalline alumina trihydrate is extracted from the digestion liquor by the following hydrolysis reaction:

$2NaAlO_2 + 4H_2O = Al_2O_3.3H_2O + 2NaOH$

This is basically the reverse of the digestion process. Fine particles of alumina are added to seed the precipitation of pure alumina particles as the liquor cools. The particles sink to the bottom of the tank and are removed. The liquor is recycled back to digestion.

4. Calcination: The removal of water crystallization from the alumina hydrate after precipitation.

In this stage, the alumina trihydrate crystals are passed through a rotary calcination kiln or a fluidized calciner at 1100℃ to drive off the chemically combined water. The final product is a fine white anhydrous aluminum oxide powder called alumina. This is the basic material from which aluminum is made.

B.1 Hg in the Bayer Process

Bauxite contains trace amounts of mercury which may accumulate in the Bayer liquor, alumina hydrate and oxalate in the processing of bauxite.[13] The digestion and

evaporation steps of the Bayer process involve flash evaporation/cooling. This produces as stream that is cooled in heat exchangers. This leaves a vapour that is in equilibrium with the condensate. Significant concentrations of VOCs and Hg are present in this vapour phase. The digestion and evaporation processes are reducing due to the dissolved organic species, which can act as reducing agents within the liquor stream. Gases exiting these streams include ammonia, water and various VOCs (i.e. acetone, 2-butanone etc.) with the balance being nitrogen.[392] The Hg emissions to air from Bayer refineries are almost 100% elemental mercury from studies of emissions for Alcoa Bayer refineries.[13] Elemental Hg in the gaseous phase is in steady state with the concentration in the condensate according to Henry's law.[327,402] The mercury concentration will therefore depend on the temperature but typical mercury concentrations range from 3 – 30 mg/m^3 at temperatures of 20 – 80°C. Hg emissions from Bayer refineries differ significantly from refinery to refinery. Some refineries have significant mercury emissions from digestion and calciners due to mercury in the alumina hydrate while other refineries have a significantly higher portion of the Hg emissions from the digestion vent gases or oxalate kiln.[13] Hg emissions are also found, in small quantities, from the liquor burner and boilers.[8]

Appendix C

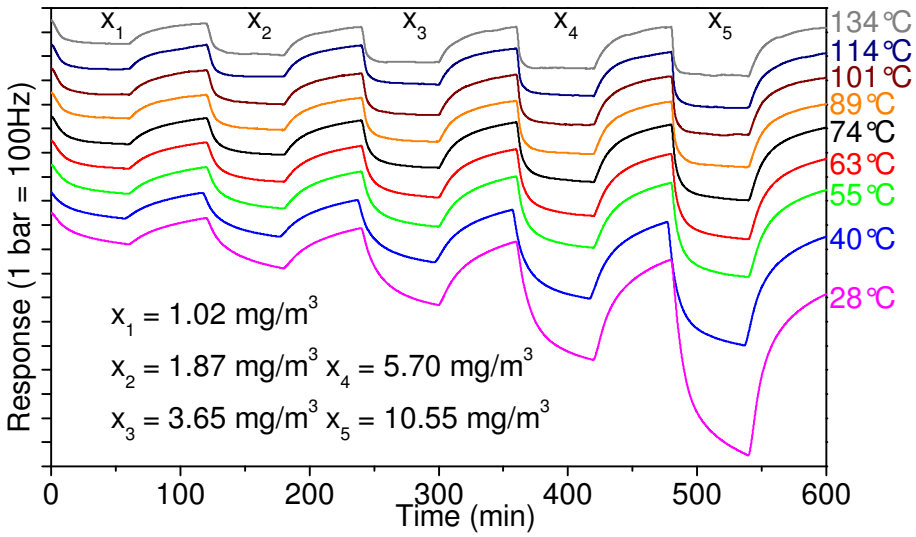

Figure C.1: Response curves for Au-rough QCM exposed to various Hg vapour concentrations at various operating temperatures.

Appendix D:

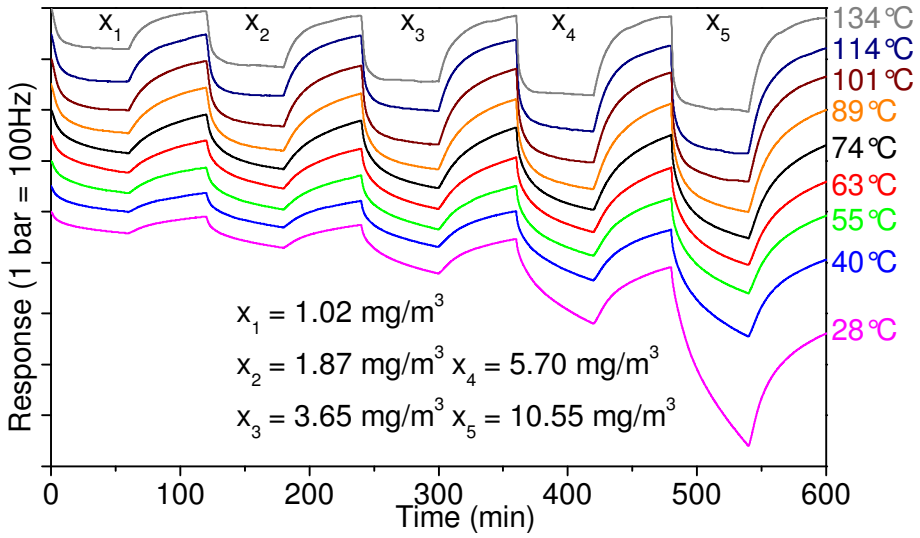

Figure D.1: Response curves for 100 nm Au film (optically polished) QCM exposed to various Hg vapour concentrations at various operating temperatures.

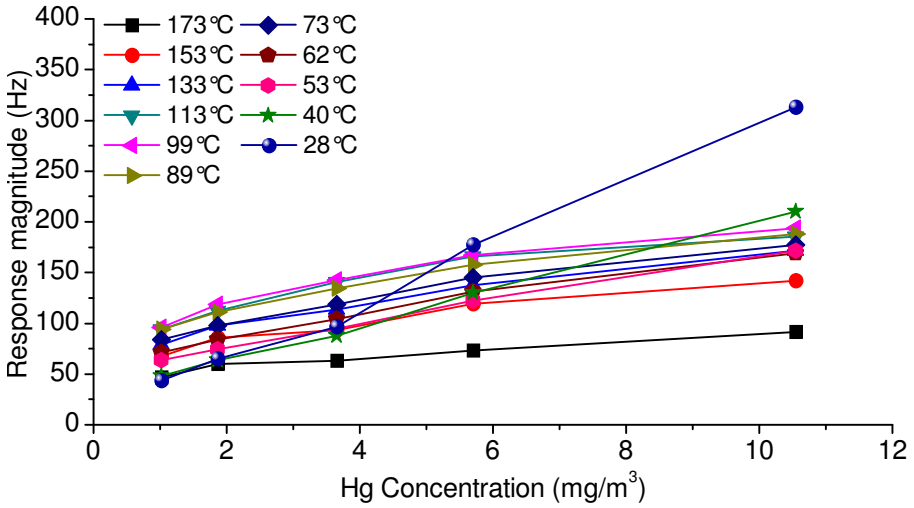

a) Duplicate 100 nm Au-polished QCM

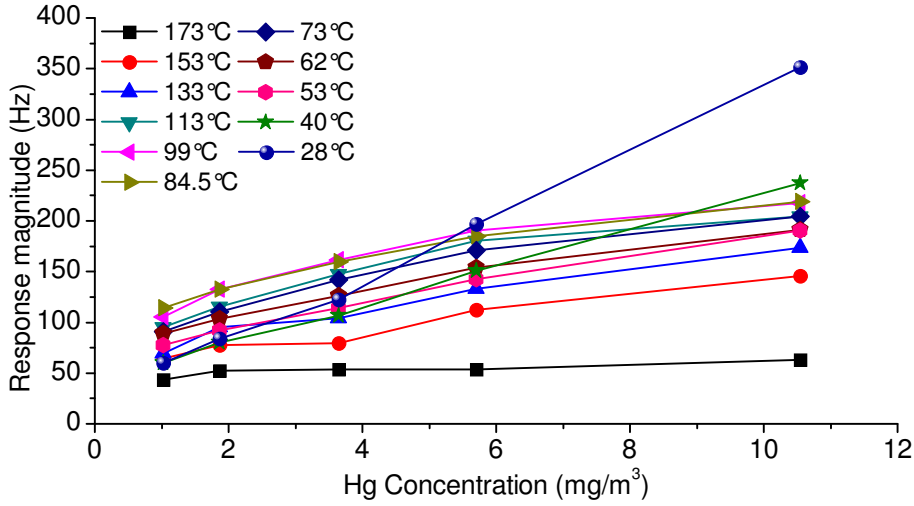

b) 150 nm Au-polished QCM

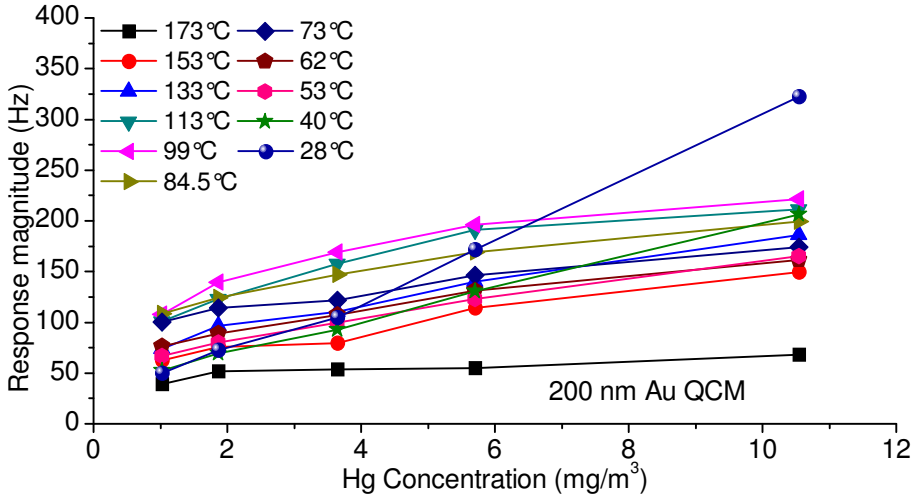

c) 200 nm Au-polished QCM

Figure D.2: QCM data representing Hg sorption isotherm for thin Au films

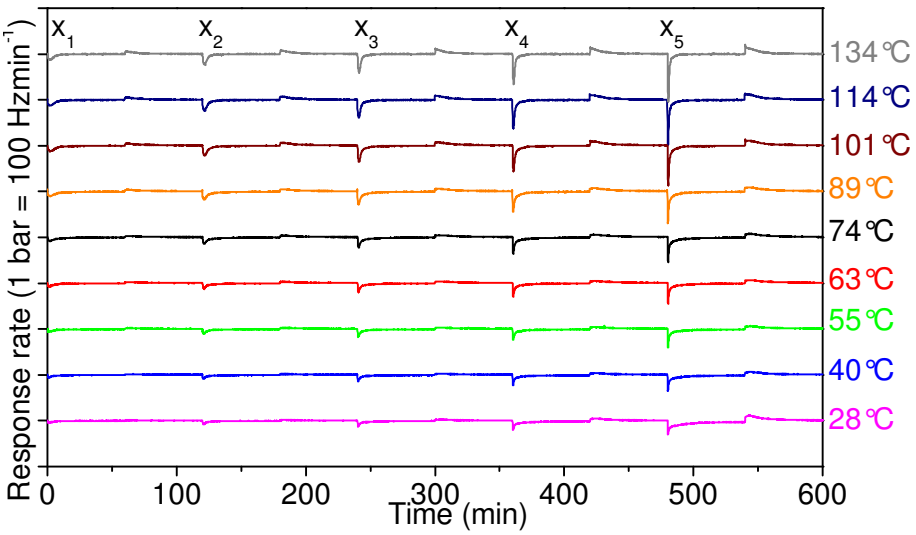

a) Au-Polished

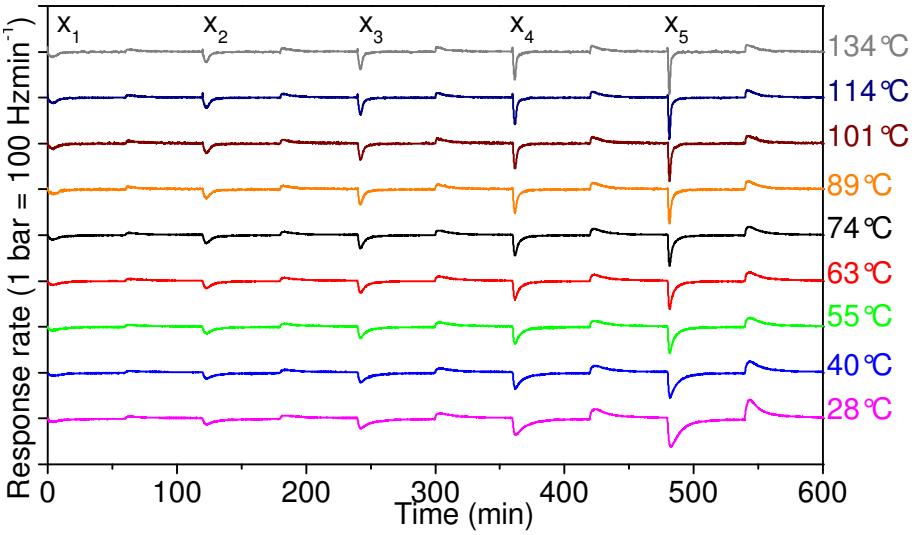

b) Au-Rough

Figure D.3: QCM response rate representing Hg sorption and desorption rates at all operating temperatures and Hg concentrations tested.

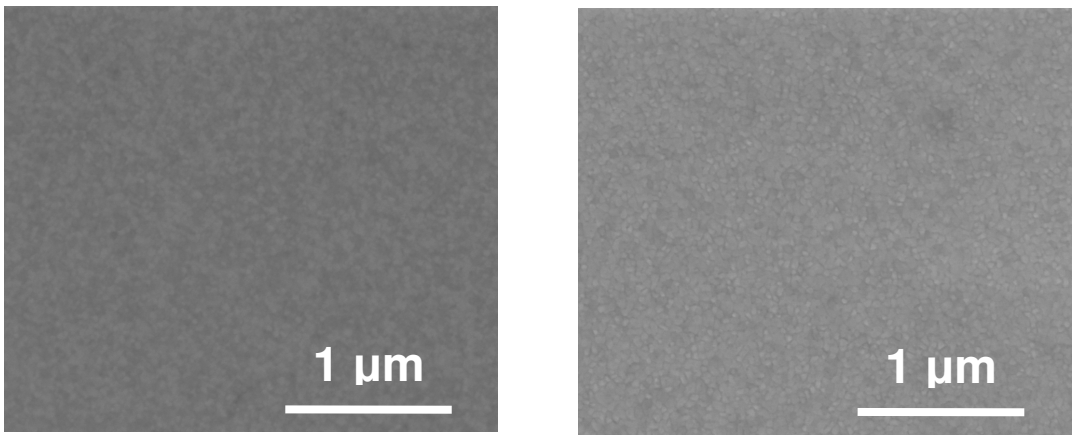

a) 50 nm **a)** 100 nm

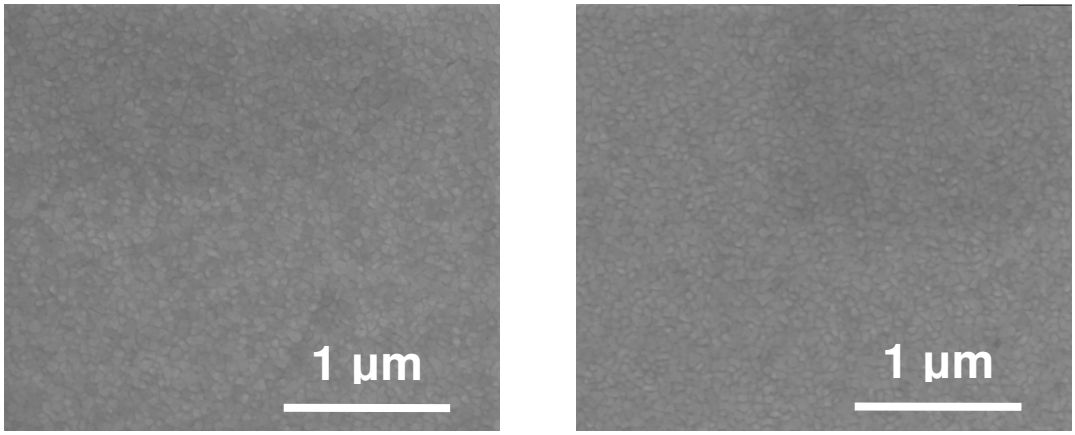

a) 150 nm **a)** 200 nm

Figure D.4: SEM images of Au thin films deposited on QCM prior to Hg exposure

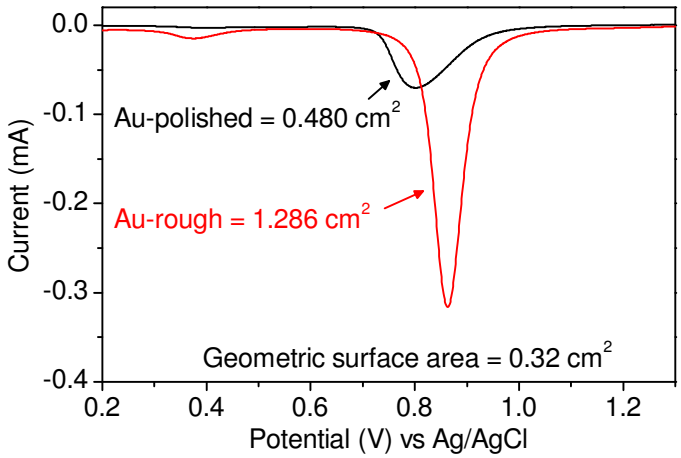

Figure D.5: Electrochemical surface area of Au-polished and Au-rough based QCM electrodes

Appendix E

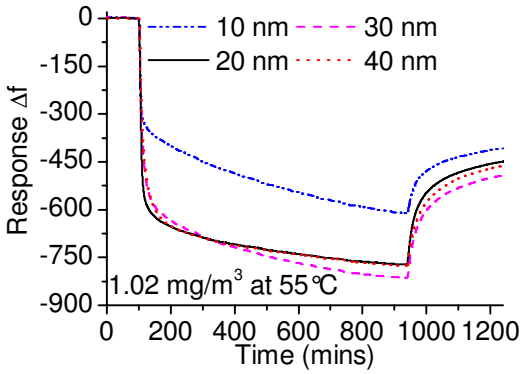

a) Dynamic response for 14 hour Hg exposure and 5 hour recovery period

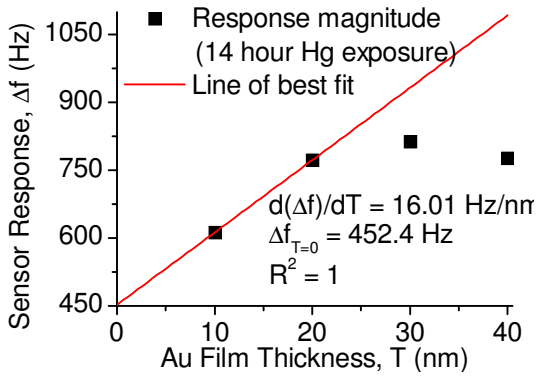

b) ETZT method applied following 14 hour of Hg exposure

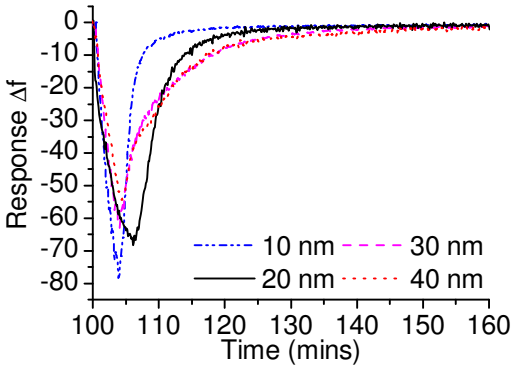

c) Sorption rate (1st hour)

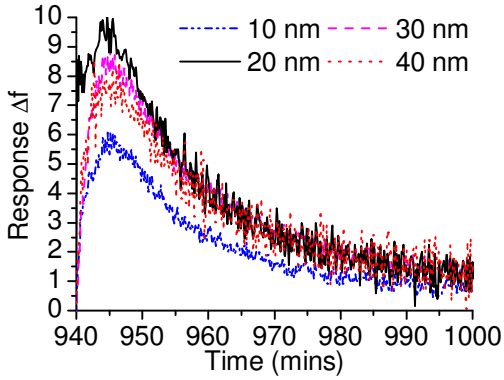

d) Desorption rate (1st hour)

Figure E.1: Dynamic response, ETZT graphic representation, Hg sorption and desorption rate profiles of QCM sensors with electrode film thicknesses of 10, 20, 30, and 40 nm when exposed towards 1.02 mg/m^3 Hg at 55℃.

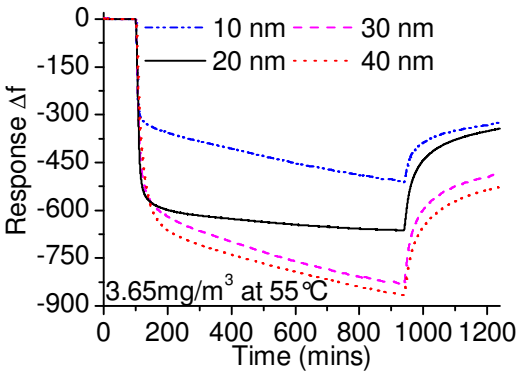

a) Dynamic response for 14 hour Hg exposure and 5 hour recovery period

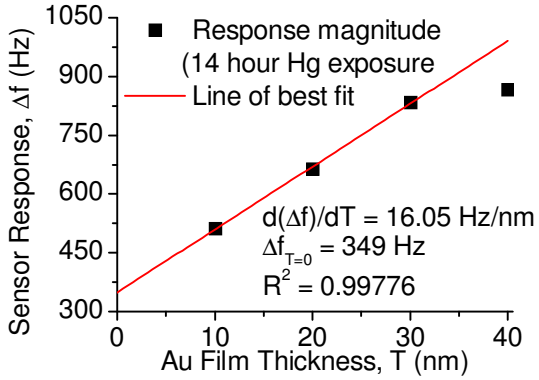

b) ETZT method applied following 14 hour of Hg exposure

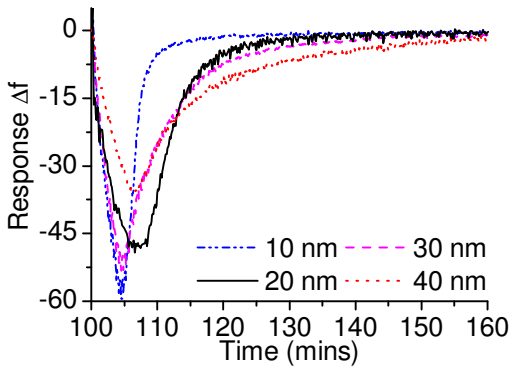

c) Sorption rate (1st hour)

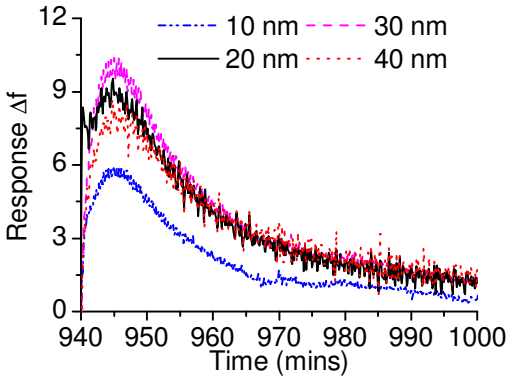

d) Desorption rate (1st hour)

Figure E.2: Dynamic response, ETZT graphic representation, Hg sorption and desorption rate profiles of QCM sensors with electrode film thicknesses of 10, 20, 30, and 40 nm when exposed towards 3.65 mg/m^3 Hg at 55℃.

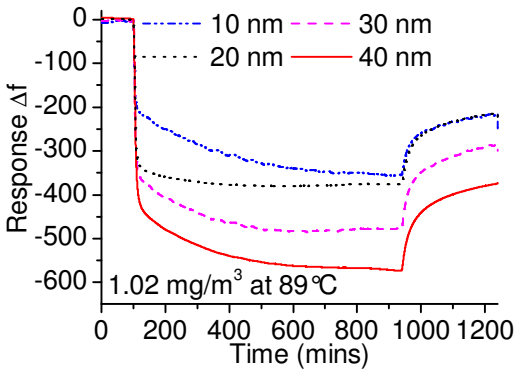

a) Dynamic response for 14 hour Hg exposure and 5 hour recovery period

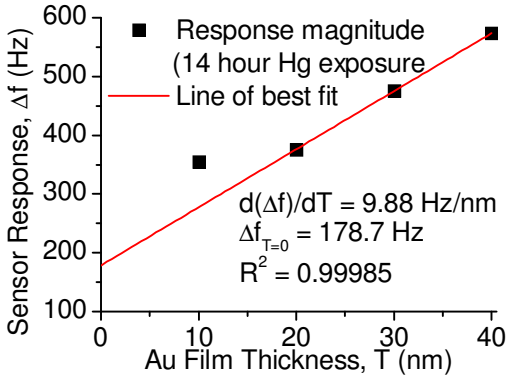

b) ETZT method applied following 14 hour of Hg exposure

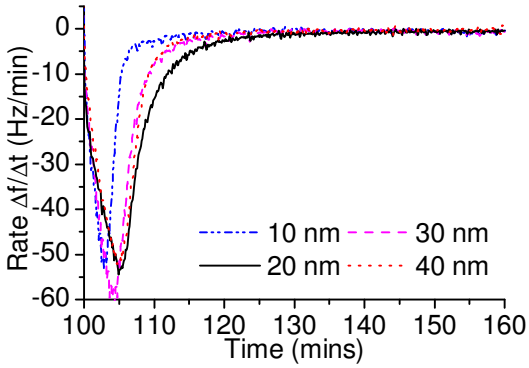

c) Sorption rate (1st hour)

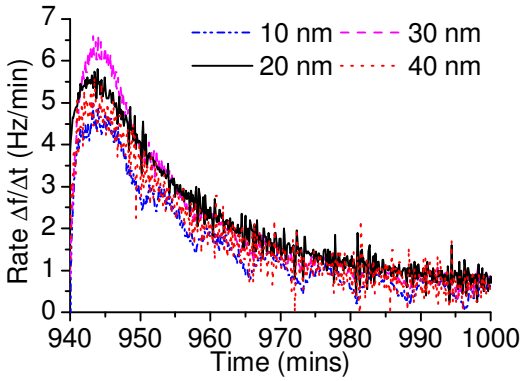

d) Desorption rate (1st hour)

Figure E.3: Dynamic response, ETZT graphic representation, Hg sorption and desorption rate profiles of QCM sensors with electrode film thicknesses of 10, 20, 30, and 40 nm when exposed towards 1.02 mg/m^3 Hg at 89℃.

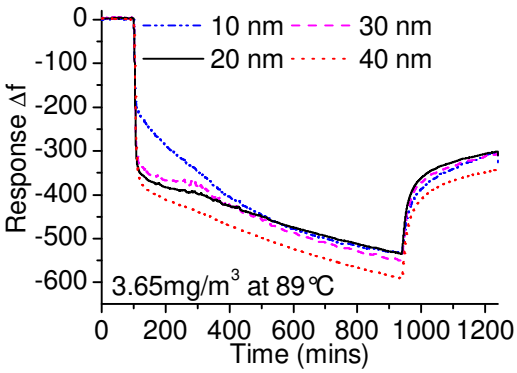

a) Dynamic response for 14 hour Hg exposure and 5 hour recovery period

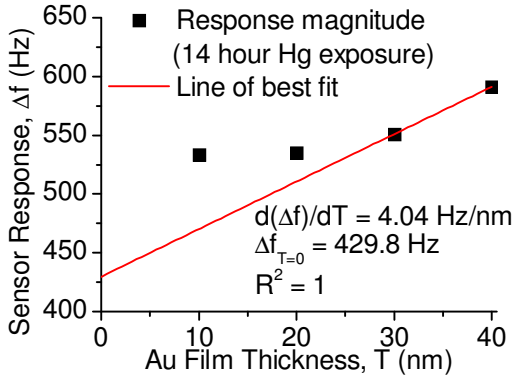

b) ETZT method applied following 14 hours of Hg exposure

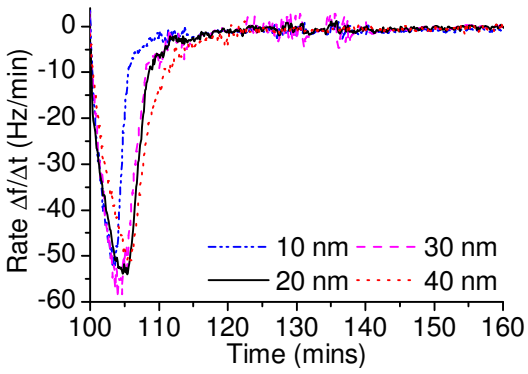

c) Sorption rate (1st hour)

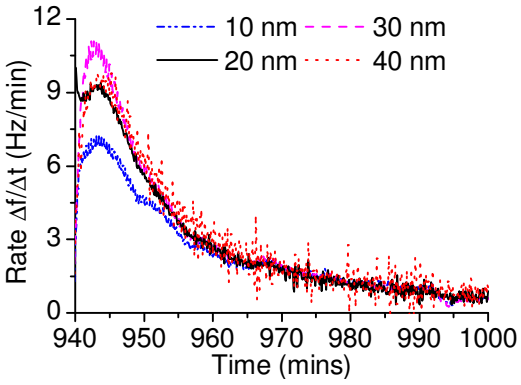

d) Desorption rate (1st hour)

Figure E.4: Dynamic response, ETZT graphic representation, Hg sorption and desorption rate profiles of QCM sensors with electrode film thicknesses of 10, 20, 30, and 40 nm when exposed towards 3.65 mg/m^3 Hg at 89℃.

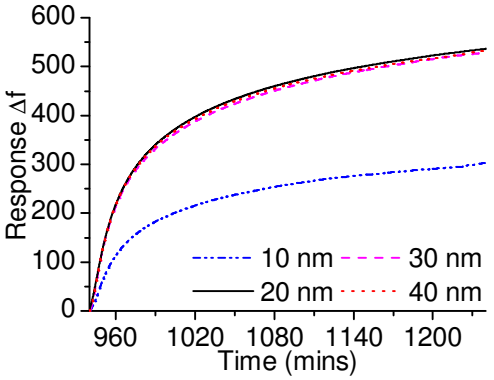

a) 1.02 mg/m^3 Hg at 28℃

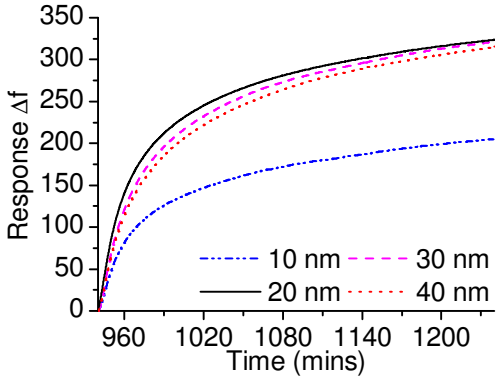

b) 1.02 mg/m^3 Hg at 55℃

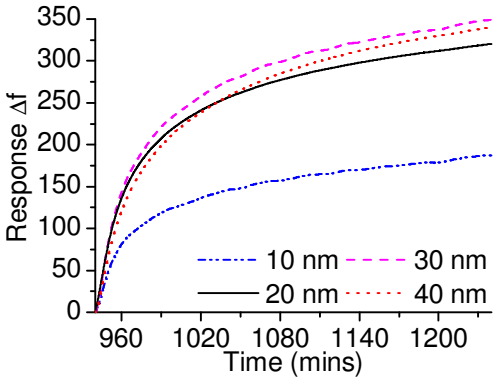

c) 3.65 mg/m^3 Hg at 55℃

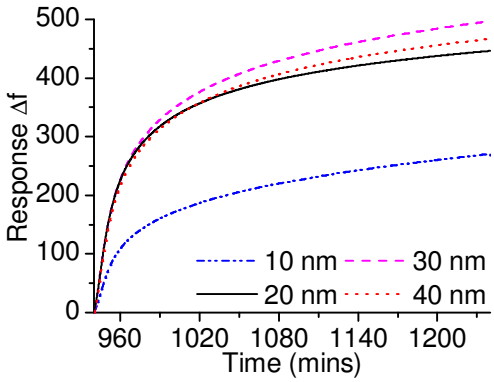

d) 10.55 mg/m^3 Hg at 55℃

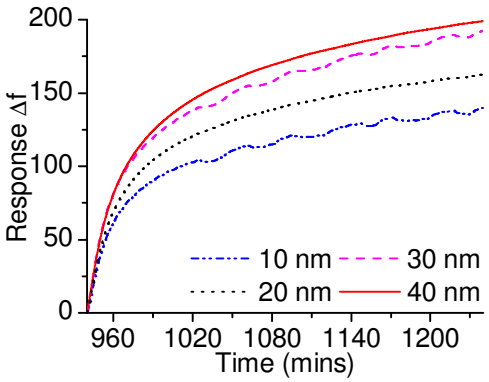

e) 1.02 mg/m^3 Hg at 89℃

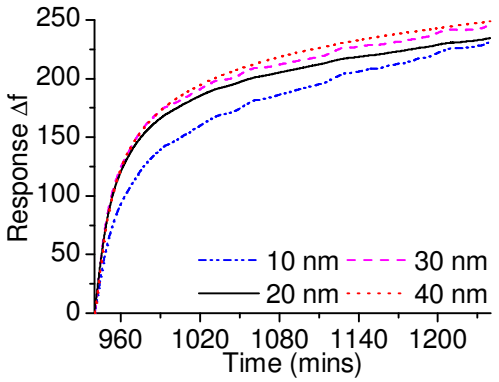

f) 3.65 mg/m^3 Hg at 89℃

Figure E.5: Dynamic response of Hg desorption profiles of QCM sensors with electrode film thicknesses of 10, 20, 30, and 40 nm when exposed towards dry nitrogen for 5 hours following 14 hour Hg exposure period.

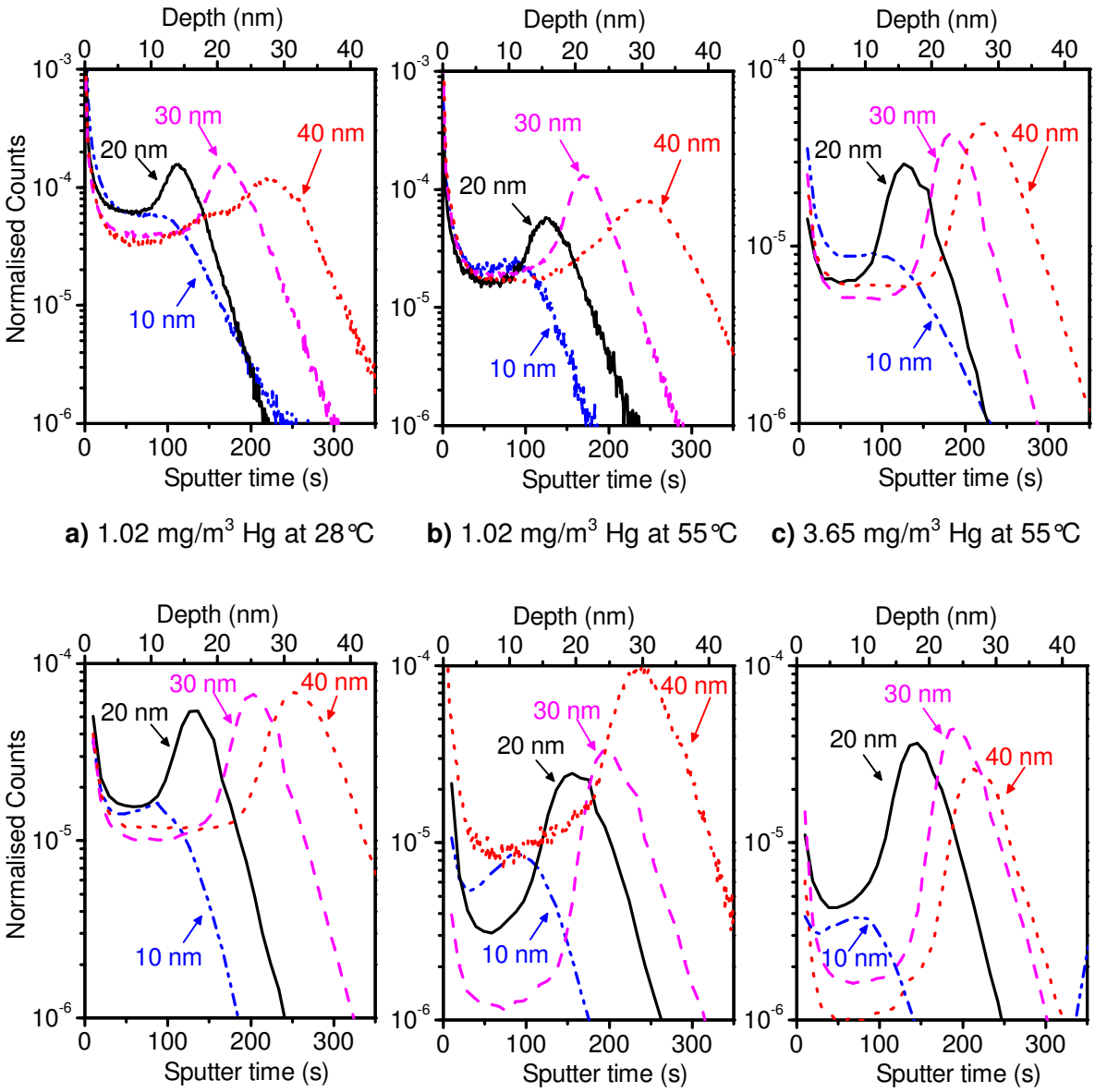

a) 1.02 mg/m^3 Hg at 28℃ **b)** 1.02 mg/m^3 Hg at 55℃ **c)** 3.65 mg/m^3 Hg at 55℃

d) 10.55 mg/m^3 Hg at 55℃ **e)** 1.02 mg/m^3 Hg at 89℃ **f)** 3.65 mg/m^3 Hg at 89℃

Figure E.6: SIMS depth profile of the ultra thin Au films following 14 hours of Hg exposure and 5 hours of recovery period using dry nitrogen at various operating temperatures and Hg concentrations.

Appendix F

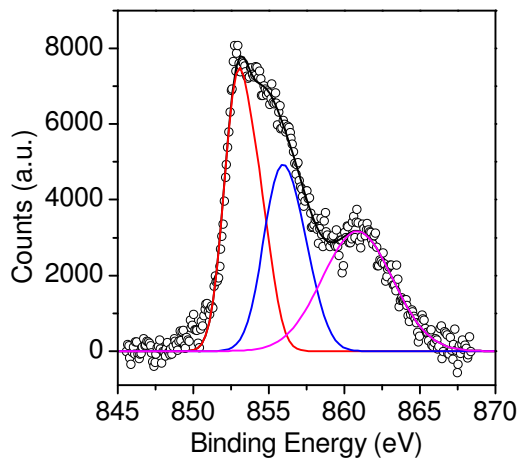

a) Ni

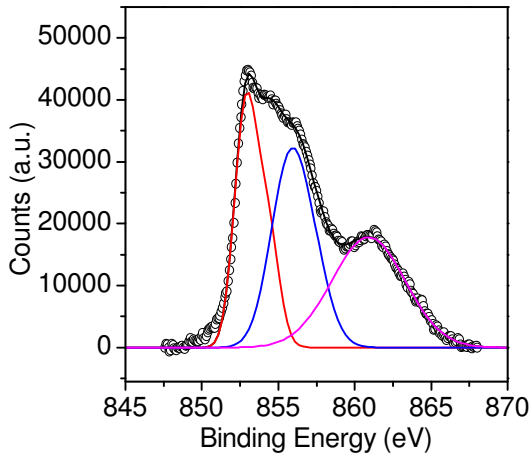

b) 0.5 h GR

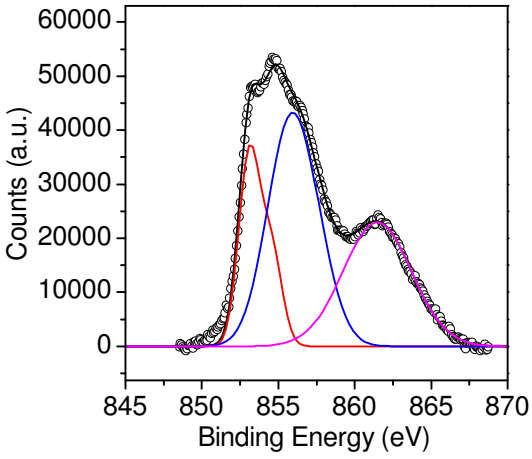

c) 1 h GR

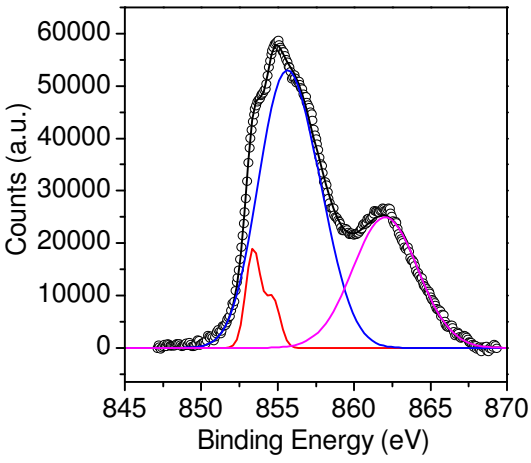

d) 2 h GR

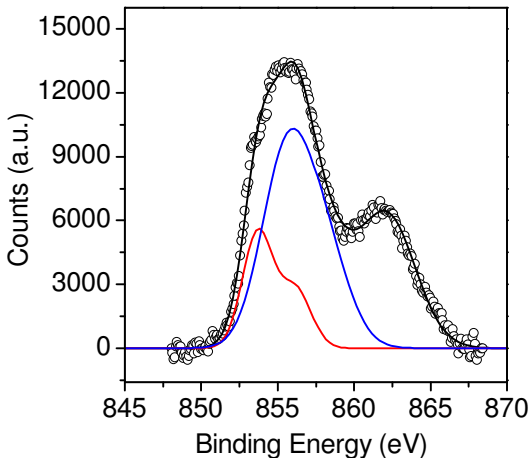

e) 4 h GR

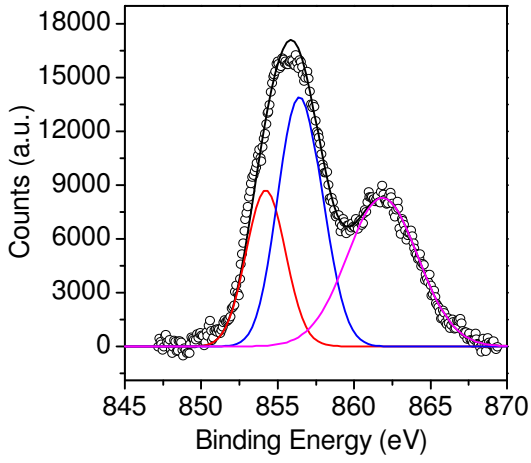

f) 8 h GR

Figure F.1: XPS spectra (Ni 2P core level region) for the Ni-Au GR QCM electrodes. The deconvoluted peak areas were used to estimate the NiO to Ni ratio and presented in chapter 6 Figure 6.6b

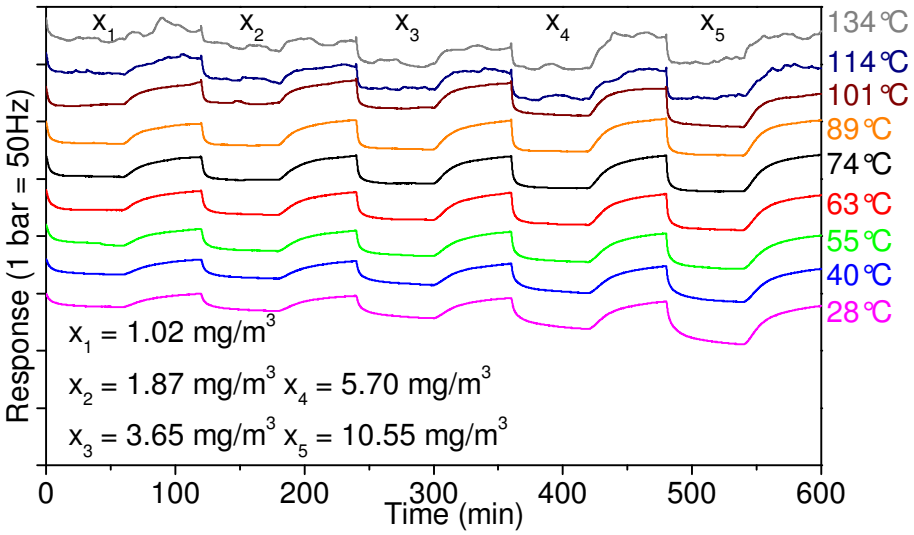

a) Sensor response

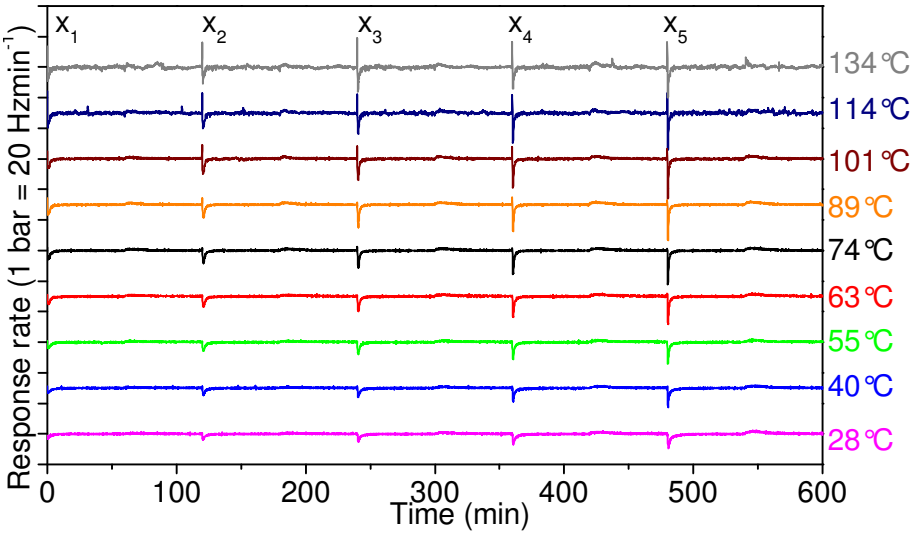

b) Sensor response rate

Figure F.2: 0.5 h GR QCM response (top) and response rate (bottom) at various Hg vapor concentrations and operating temperatures.

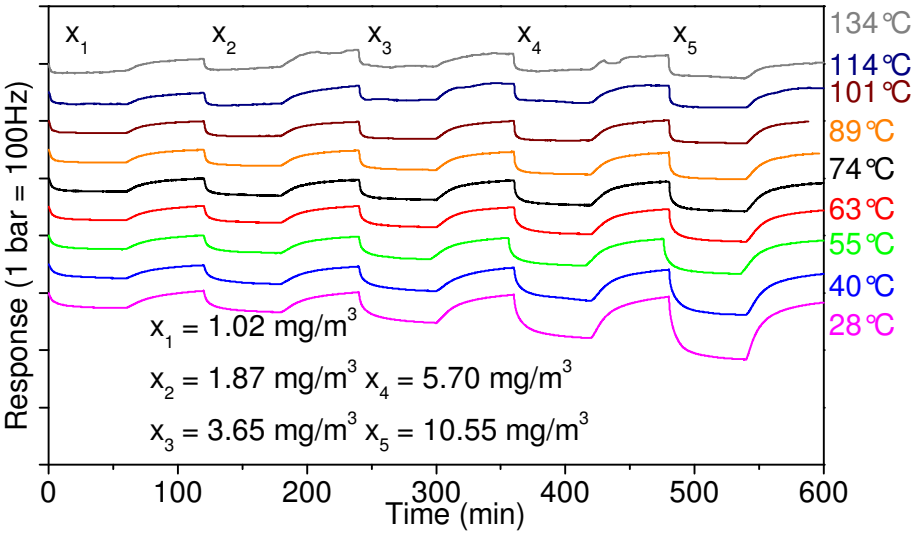

a) Sensor response

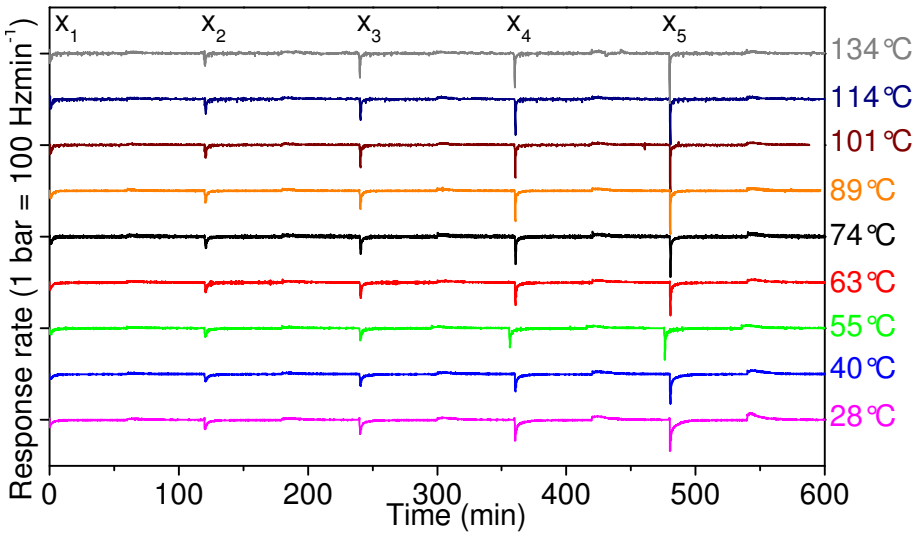

b) Sensor response rate

Figure F.3: 1 h GR QCM response (top) and response rate (bottom) at various Hg vapor concentrations and operating temperatures.

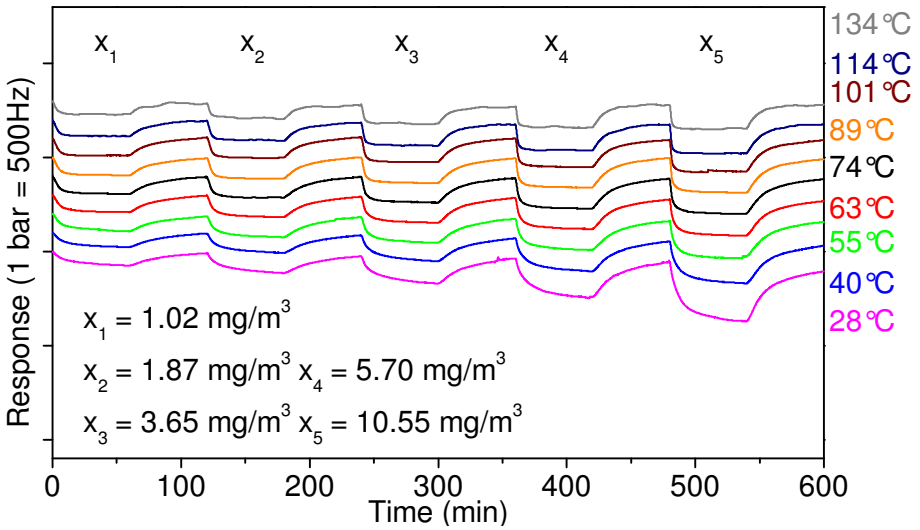

a) Sensor response

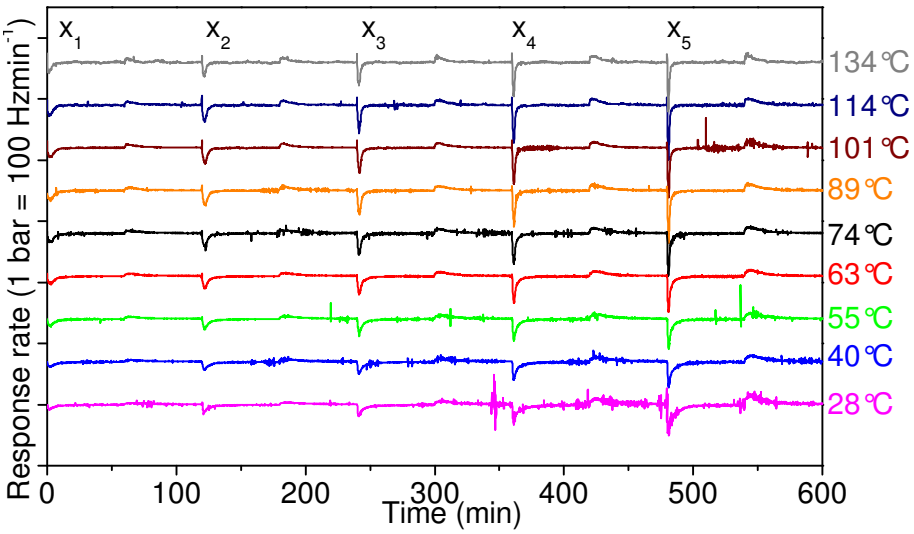

b) Sensor response rate

Figure F.4: 2 h GR QCM response (top) and response rate (bottom) at various Hg vapor concentrations and operating temperatures.

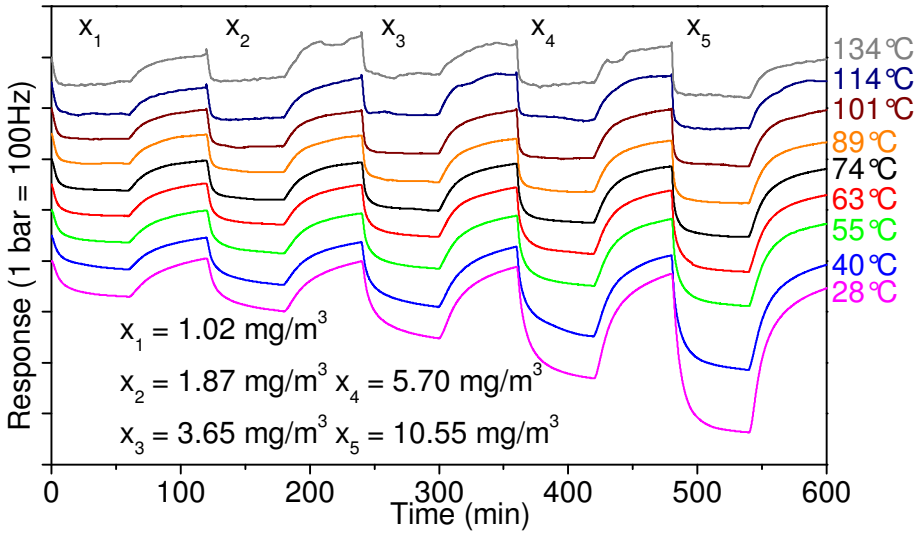

a) Sensor response

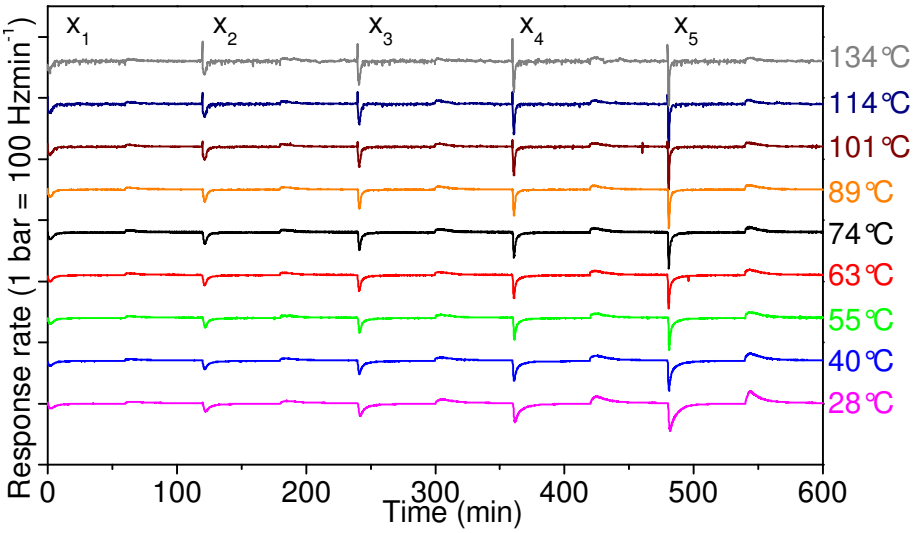

b) Sensor response rate

Figure F.5: 4 h GR QCM response (top) and response rate (bottom) at various Hg vapor concentrations and operating temperatures.

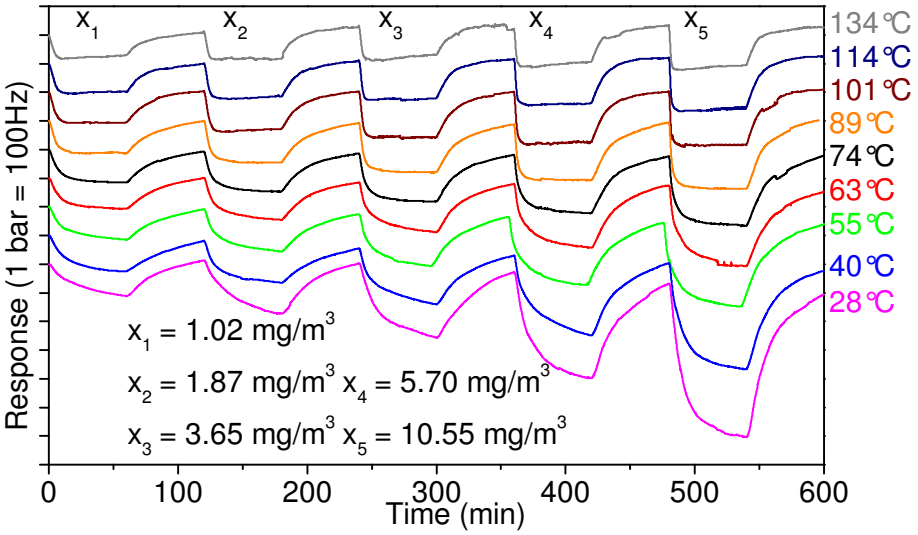

a) Sensor response

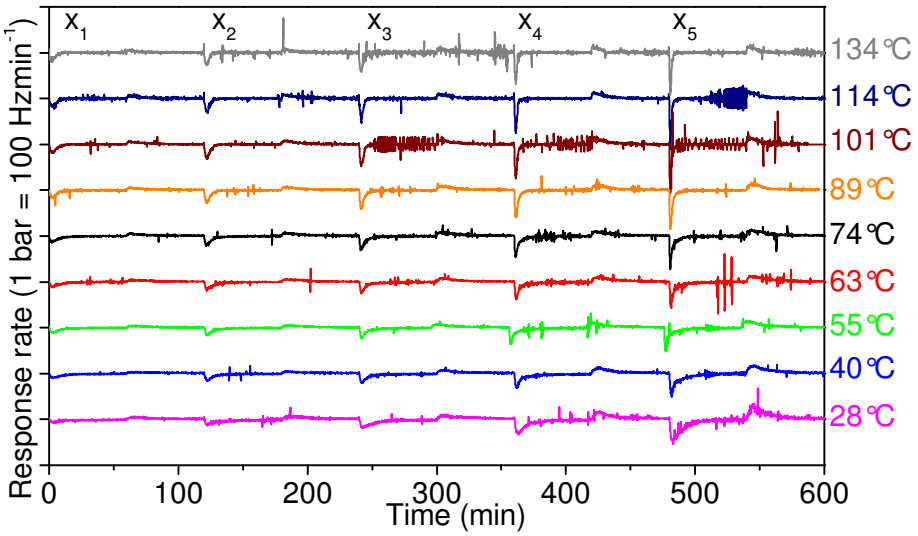

b) Sensor response rate

Figure F.6: 8 h GR QCM response (top) and response rate (bottom) at various Hg vapor concentrations and operating temperatures.

Appendix G

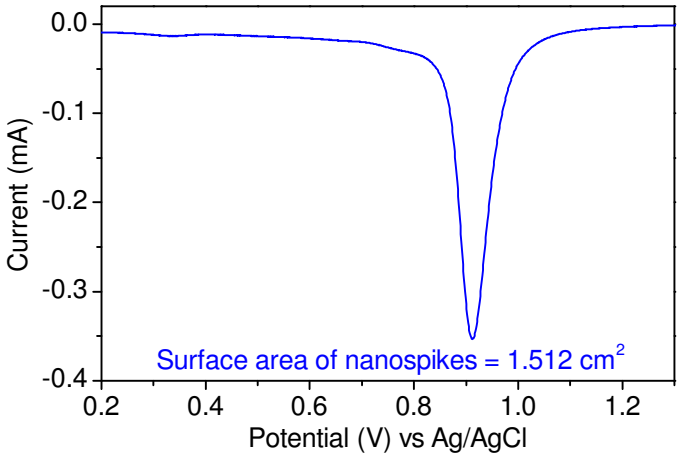

Figure G.1: CV at 100 mVs^{-1} in 0.5 M H_2SO_4 in order to determine the electrochemical surface area of nanospikes on the QCM electrodes

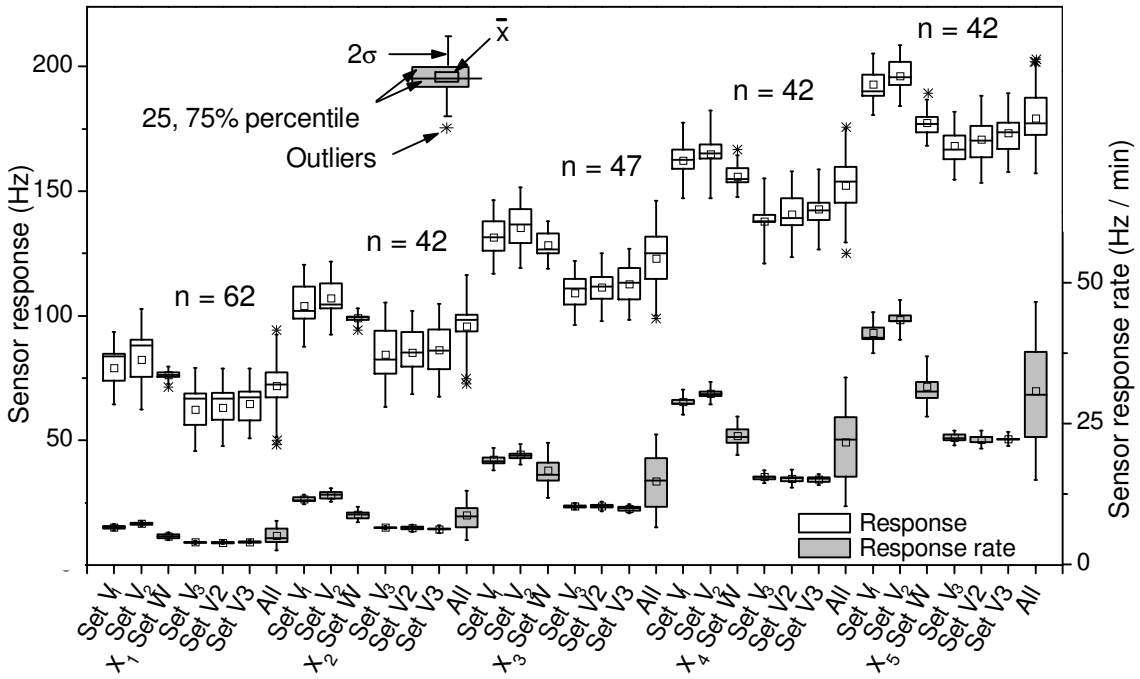

Figure G.2: Box plot of control Au QCM (100 nm Au thin film) sensor using data gathered over a 50 day testing period. The pulse sequence for each test may be found in Chapter 2, Section 2.5.

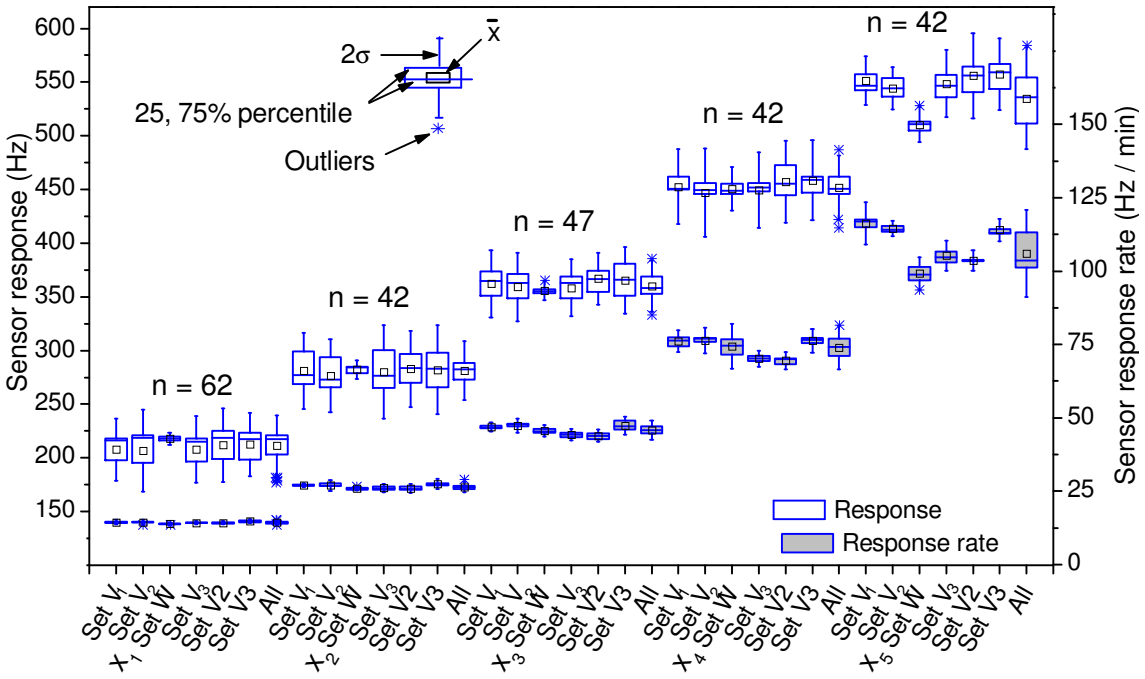

Figure G.3: Box plot of modified QCM (Au nanospikes) sensor using data gathered over a 50 day testing period. The pulse sequence for each test may be found in Chapter 2, Section 2.5.

Box plots with 25% and 75% quartiles were chosen to represent all data points collected, where the whiskers represent two standard deviation (2σ) and the asterisks (*) represent the outlier values. The last box in each Hg concentration set represents all data collected for that concentration. The sample set size, *n*, refers to this same box, which is labelled with the suffix *All*. X_n (where n = 1 to 5) represents Hg concentrations 1.02, 1.87, 3.65, 5.70 and 10.55 mg/m^3. Each 'set' of test patterns have been thoroughly explained in chapter 2.

Table G.1: Summary of the QCM data over a 70 day testing period for Au control and nanospikes. The percent values in brackets represent the coefficient of variation (*COV*) describing how spread out the data is, and is given by $COV = \frac{\sigma}{\bar{x}} \times 100\%$.

Modified by electro-deposition (nanospikes)

Δf data						
Hg Concentration	**Number of data points, n**	**Mean, $\bar{x}$ (Hz)**	**σ (Hz) and *COV* in (%)**	**Median (Hz)**	**Minimum (Hz)**	**Maximum (Hz)**
1.01	62	211.7	**13.9 (6.6%)**	217.6	177.0	229.3
1.87	42	281.2	**13.7 (4.9%)**	282.4	254.5	306.0

3.65	47	360.0	**11.8 (3.3%)**	358.0	333.2	385.6
5.70	42	452.0	**14.9 (3.3%)**	450.8	414.0	487.1
10.5	42	534.9	**23.8 (4.4%)**	536.0	496.6	584.3
Δf/ Δt data						
Hg Concentration	**Number of data points**	**Mean (Hz/min)**	**σ (Hz) and *COV* in (%)**	**Median (Hz/min)**	**Minimum (Hz/min)**	**Maximum (Hz/min)**
1.01	62	14.3	**0.42 (3.0%)**	14.3	13.4	15.3
1.87	42	26.4	**0.84 (3.2%)**	26.3	25.3	29.0
3.65	47	45.8	**1.60 (3.5%)**	45.8	42.7	49.0
5.70	42	74.0	**3.68 (5.0%)**	74.3	67.5	81.6
10.5	42	106.1	**7.43 (7.0%)**	103.7	93.6	120.7

Non-modified (Au control)

Δf data						
Hg Concentration	**Number of data points, n**	**Mean, $\bar{x}$ (Hz)**	**σ (Hz) and *COV* in (%)**	**Median (Hz)**	**Minimum (Hz)**	**Maximum (Hz)**
1.01	62	72.0	**10.3 (14%)**	72.6	48.3	94.2
1.87	42	95.7	**10.4 (11%)**	98.5	72.6	116.4
3.65	47	123.1	**11.5 (9.3%)**	125	99	143.6
5.70	42	152.3	**11.4 (7.5%)**	153.8	125.1	175.7
10.5	42	179.2	**11.0 (6.1%)**	177.4	161.3	202.9
Δf/ Δt data						
Hg Concentration	**Number of data points**	**Mean, $\bar{x}$ (Hz/min)**	**σ (Hz) and *COV* in (%)**	**Median (Hz/min)**	**Minimum (Hz/min)**	**Maximum (Hz/min)**
1.01	62	5.1	**1.29 (25%)**	4.7	3.7	7.6
1.87	42	8.7	**2.18 (25%)**	8.6	5.8	12.9
3.65	47	14.8	**4.12 (28%)**	14.9	9.3	21.2
5.70	42	21.7	**5.69 (26%)**	22.2	14.3	31.8
10.5	42	30.8	**7.91 (25%)**	30.2	21.0	45.5

Table G.1 further highlights the significance of the nanospikes QCM when compared to the non-modified Au control sensor. It is clear that the standard deviation of the sensors appear to be near identical in magnitude, however the larger response magnitude of the electro-deposited sample means that COV is at least 1.4 and up to 8 times higher for the Au control QCM.